
Electronic Thesis and Dissertation Repository

1-15-2015 12:00 AM

Cluster Fluid Dynamics in Down Flow Reactors: Experimental and Modeling Study

Angel Virgilio Lanza Soto
The University of Western Ontario

Supervisor
Dr. Hugo I. de Lasa
The University of Western Ontario

Graduate Program in Chemical and Biochemical Engineering
A thesis submitted in partial fulfillment of the requirements for the degree in Doctor of Philosophy
© Angel Virgilio Lanza Soto 2015

Follow this and additional works at: <https://ir.lib.uwo.ca/etd>

 Part of the [Catalysis and Reaction Engineering Commons](#), [Petroleum Engineering Commons](#), and the [Transport Phenomena Commons](#)

Recommended Citation

Lanza Soto, Angel Virgilio, "Cluster Fluid Dynamics in Down Flow Reactors: Experimental and Modeling Study" (2015). *Electronic Thesis and Dissertation Repository*. 2659.
<https://ir.lib.uwo.ca/etd/2659>

This Dissertation/Thesis is brought to you for free and open access by Scholarship@Western. It has been accepted for inclusion in Electronic Thesis and Dissertation Repository by an authorized administrator of Scholarship@Western. For more information, please contact wlsadmin@uwo.ca.

Cluster Fluid Dynamics in Down Flow Reactors: Experimental and Modeling Study

(Thesis format: Monograph)

by

Angel Virgilio Lanza Soto

Graduate Program in Engineering
Department of Chemical and Biochemical Engineering

A thesis submitted in partial fulfillment
of the requirements for the degree of
Doctor of Philosophy

The School of Graduate and Postdoctoral Studies
The University of Western Ontario
London, Ontario, Canada

© Angel Virgilio Lanza Soto 2015

Abstract

Gas–solid concurrent downers possess unique features when compared to other gas–solid systems. Establishing their fluid dynamic properties requires both experimental measurements of gas–solid flow properties and computational modeling.

Measuring gas–solid flow properties such as cluster solid concentrations, individual cluster slip velocities, and cluster sizes, involves the use of specialized optical equipment, as well as a rigorous data analysis methodology. In addition, the modeling of the fluid dynamics of gas–solid flows in downer units offers special challenges such as establishing a proper drag model, cluster configuration and sizes, sphericity, boundary conditions, among other issues.

In this PhD dissertation, the fluid dynamics of gas–solid flows in downer reactor units are analyzed in the context of a wide range of operating conditions. To accomplish this, local cluster particle characteristics are determined for the first time, using two separate downer units and a significantly enhanced data analysis. This involves individual cluster signals recorded by the CREC–GS–Optiprobos and a method for setting the data baseline using solid mass balances. The proposed methodology allows the calculation of individual cluster slip velocities, agglomerate particle sizes, individual particle cluster size distributions, and cluster drag coefficients.

Gas–solid flows in downers are simulated in the present PhD dissertation, using a Computational Particle Fluid Dynamics (CPFD) Numerical Scheme. The CPFD model includes particles represented as clusters. This model is validated with experimental data obtained from the two independent downer units which have different downer–column internal diameters (a 1 inch ID and a 2 inch ID). CPFD simulations are implemented using average particle cluster sizes as obtained experimentally. Experimentally observed time–averaged axial and radial velocities, solid concentration profiles, and cluster particle acceleration regions are successfully simulated by a CFPD model. These findings support: a) a narrow distribution of particle cluster catalyst residences, b) the characteristic particle “forward” mixing, and c) the relatively flat radial solid concentrations and solid cluster velocities.

It is found that CPFD simulations agree well with experimentally determined particle cluster velocity and the solid void fraction in the downer core region, with this being the case for all the operating conditions studied.

Keywords

Gas–Solid Fluid Dynamics, Downer Reactor Units, Cluster Fluid Dynamics, Computational Particle Fluid Dynamics (CPFD), Barracuda®, Fluid Catalytic Cracking (FCC), Fluidization, Concurrent Down Flow.

Dedication

*This dissertation is dedicated to the memory of my beloved father, **Angel Virgilio Lanza González (1929–2005)**, who has been a source of encouragement and inspiration to me throughout my life.*

*Esta tesis está dedicada a la memoria de mi querido padre, **Angel Virgilio Lanza González (1929–2005)**, quien ha sido una fuente de estímulo e inspiración para mí a lo largo de mi vida.*

Acknowledgments

I wish to express my sincere gratitude to everyone who made this doctoral study possible.

First of all, I would like to thank my advisor, Dr. Hugo Ignacio de Lasa, for his endless guidance during my research and study at The University of Western Ontario. He was always available and willing to help. His recognized expertise, perpetual energy, and enthusiasm in research, extremely motivated me in my studies.

I recognize that this research would not have been possible without the financial assistance of The Natural Sciences and Engineering Research Council of Canada (NSERC), and the Ontario Graduate Scholarship (OGS) I was awarded. I express my gratitude to those agencies that allowed me to pursue my PhD studies.

Thanks to Jose Munoz and Pastor Solano, the laboratory technicians, for helping me during the long hours in the laboratory. Thank you to Florencia de Lasa for helping me in the editing of the final version of all my publications. I am also very thankful to my laboratory and office mates, Ashraful Islam, Gureet Chandhok, Isabela Reiniati, Jahirul Mazumder, Patricio Valades, Quddus Rezwanul, and Saad Al-Bogami, for the good times, refreshing work breaks, and fun lunch environment. I am especially grateful to my friends Vanessa Rodgher, Enrique Salaices and Jesus Moreira, for all the support, advice and caring that they provided me during this dissertation.

My deepest gratitude goes to my family for their unconditional love throughout my life. Not a single word can fully describe how thankful I am to my Mother, Nancy Soto. I owe her everything; she has always been extremely supportive. It is impossible to thank her adequately for everything she has done for me.

I am also indebted to my clever and beautiful wife, Yira Aponte, whose love, patience, understanding and unconditional support allowed me to finish this journey. She already has my heart so I will just give her a heartfelt “thanks”. Lastly, I wish to thank my daughter Samantha and my unborn baby Victoria just for being the driving-force in my life.

Table of Contents

Abstract.....	ii
Dedication.....	iv
Acknowledgments.....	v
Table of Contents.....	vi
List of Tables.....	x
List of Figures.....	xii
List of Appendices.....	xx
Nomenclature.....	xxi
Chapter 1.....	1
1 Introduction.....	1
Chapter 2.....	10
2 Literature Review.....	10
2.1 Downer Reactor Units.....	10
2.2 Hydrodynamics of Downers.....	11
2.2.1 Axial Flow Sections.....	12
2.2.2 Axial Distribution of Pressure.....	13
2.2.3 Radial Flow Sections.....	15
2.3 Feeders/Distributors.....	16
2.4 Cyclones/Separators.....	19
2.5 Cluster Formation in Downers, Radial and Axial Distribution.....	22
2.6 Computational Fluid Dynamics.....	24
2.7 Measurements of Solids Concentration in a Downer.....	27
2.8 Heat Transfer in Downer Reactors.....	29
2.9 Some Industrial Application of Downer Reactor Units.....	31

2.9.1	Application of Downers in Fluid Catalytic Cracking (FCC)	31
2.9.2	Application of Downers in Pyrolysis of Biomass and Coal	39
2.10	Conclusions	40
Chapter 3	43
3	Scope of the Research	43
3.1	Overall Objectives	43
3.2	Accomplishment of Research Objectives	44
Chapter 4	46
4	Experimental Equipments and FCC Catalyst.....	46
4.1	Chemical Reactor Engineering Centre Gas–Solid Optical Probe (CREC–GS–Optiprobe).....	46
4.2	Gas–solid Co–current Flow Downer Units	53
4.2.1	One inch Internal Diameter Downer Unit.....	53
4.2.2	Two inch Internal Diameter Downer unit.....	55
4.3	FCC Catalyst Particles Used.....	57
4.4	Conclusions.....	58
Chapter 5	60
5	Methodology Proposed for Signal Analysis	60
5.1	Baseline Concept and its Importance for Signal Analysis.....	60
5.2	Baseline Setting Methodology.....	63
5.3	Conclusions.....	68
Chapter 6	70
6	Experimental Results Obtained with the 1 inch Internal Diameter Downer Unit.....	70
6.1	Baseline Reference Factor from Experimental Results	71
6.2	Cluster Slip Velocity from Experimental Data.....	73
6.3	Radial Solid Concentration Profiles.....	75

6.4 Cluster Size and Cluster Slip Velocity Calculations.....	77
6.5 Particle Cluster Size Distribution Results.....	78
6.6 Mechanistic Model for the Cluster Drag Coefficient Calculation	84
6.7 Conclusions.....	93
Chapter 7.....	94
7 Computational Particle Fluid Dynamics Modeling of the One inch Internal Diameter Downer unit.....	94
7.1 Computational Method	94
7.1.1 Gas Phase Model.....	95
7.1.2 Particle Phase Model.....	96
7.1.3 Coupling Gas and Particle Phases.....	98
7.1.4 Turbulence model	99
7.1.5 Experimental Set–up and Simulation Conditions.....	99
7.2 Discretization Sensitivity Analysis	102
7.3 Boundary Conditions and Input Values	109
7.4 Drag Model	112
7.5 Particle Cluster Sizes and Sphericity	113
7.6 Results and Discussion	114
7.7 Conclusions.....	123
Chapter 8.....	125
8 Experimental Results and CPFD Simulations Obtained with the Two Inch Internal Diameter Downer Unit.....	125
8.1 Baseline Reference Factor from Experimental Results	126
8.2 Cluster Slip Velocity from Experimental Data.....	128
8.3 Radial Solid Concentration Profiles.....	130
8.4 Cluster Size and Cluster Slip Velocity Calculations.....	132
8.5 Particle Cluster Size Distribution Results.....	134

8.6 Computational Particle Fluid Dynamics Modeling of the Downward Gas–Solid Flow.....	138
8.6.1 Computational Method.....	138
8.6.2 Experimental Set–up and Simulation Conditions.....	139
8.6.3 Discretization Sensitivity Analysis.....	139
8.6.4 Boundary Conditions and Input Values.....	145
8.6.5 Drag Model.....	147
8.6.6 Particle Cluster Sizes and Sphericity.....	147
8.7 Results and Discussion.....	147
8.8 Conclusions.....	157
Chapter 9.....	159
9 Conclusions and Recommendations.....	159
9.1 Conclusions.....	159
9.2 Recommendations.....	161
References.....	162
Appendices.....	177
Curriculum Vitae.....	188

List of Tables

Table 1–1: Some application areas for gas–solid Circulating Fluidized Bed systems using downers.	4
Table 2–1: Yields of conventional FCC and HS–FCC (Abul–Hamayel, 2004).	36
Table 6–1: Operating conditions used in the 1 inch internal diameter downer unit.	70
Table 6–2: Baseline reference factor experimental results.	72
Table 6–3: Operating conditions and number of clusters studied.	79
Table 6–4: Operating conditions and number of clusters considered for cluster size distribution study.	81
Table 7–1: Particle discretization analysis. Operating condition: $U_g=1.68$ m/s, $G_s=82$ kg/m ² s.	104
Table 7–2: Mesh discretization details	107
Table 7–3: Operating conditions used in this study.	110
Table 7–4: Input parameters in the CPFDF Simulation.	111
Table 7–5: Average particle cluster size and sphericity.	114
Table 8–1: Operating conditions used in the 2 inch internal diameter downer unit.	126
Table 8–2: Baseline reference factor experimental results.	127
Table 8–3: Operating conditions and number of clusters studied	134
Table 8–4: Particle discretization analysis. Operating condition: $U_g=1.5$ m/s, $G_s=34$ kg/m ² s.	141
Table 8–5: Mesh discretization details	143

Table 8–6: Input parameters in the CPFD Simulation..... 146

Table 8–7: Average particle cluster size and sphericity. 147

List of Figures

Figure 1–1: Circulating Fluidized Bed typical configuration.....	2
Figure 2–1: Axial gas–solid flow structure in downers (Zhu et al., 1995).....	13
Figure 2–2: Axial distribution of pressure gradient. Effects of solids flux and gas velocity (Zhu et al., 1995).....	13
Figure 2–3: Gas/solid distributor section of the downer unit used by Brust and Wirth (2004).	17
Figure 2–4: Setup of the gas/solid distributor used by Lehner and Wirth (1999). In this Figure the units are reported in mm.	18
Figure 2–5: Three distributor designs used by Johnston et al. (1999).....	19
Figure 2–6: Inertial separator designed by Huard et al. (2010).....	21
Figure 2–7: Short–contact cyclone reactor designed by Zhang et al. (2013).....	21
Figure 2–8: Configurations of downer reactors, United States patents in the literature, part 1/2.	32
Figure 2–9: Configurations of downer reactors, United States patents in the literature, part 2/2.	33
Figure 2–10: Comparison between Co–Current Upflow (CCU) and Co–Current Downflow (CCDF) in gasoline and coke production.	34
Figure 2–11: Comparison of downer and riser based on High–Severity FCC Process (Abul–Hamayel, 2004).	37
Figure 2–12: Industrial demonstration of a downer reactor (Jinan Refinery, SINOPEC).....	38

Figure 4-1: Schematics of the emitter side of a CREC–GS–Optiprobe showing the region of high light intensity (Nova et al., 2004a).	47
Figure 4-2: Operating principle of the CREC–GS–Optiprobos (Nova et al., 2004b).	48
Figure 4-3: Fiber–optic configuration system for cross–correlation analysis (Nova et al., 2004b).	49
Figure 4-4: CREC–GS–Optiprobe beam profile characterization results.	51
Figure 4-5: Curve fitting analysis of the beam profile.....	52
Figure 4-6: Schematic diagram of the one inch internal diameter downer unit showing the fiber optic port, adapted from Nova (2005).	54
Figure 4-7: Schematic diagram of the two inch internal diameter downer unit.	56
Figure 4-8: Scaled representation of the 2 inch internal diameter downer unit.....	57
Figure 4-9: Volume weighted particle size distribution of FCC particles used in the present study.....	58
Figure 5–1: CREC–GS–Optiprobe signals for the upper and lower probes: conditions, 1 inch downer, $G_s=60.2 \text{ kg/m}^2/\text{s}$, $U_g=1.29 \text{ m/s}$, $r/R=0.1$	61
Figure 5–2: Example of the cross–correlation sequence R_{xy} for one cluster, 2 inch downer, $G_s=50 \text{ kg/m}^2/\text{s}$, $U_g=1.5 \text{ m/s}$, $r/R=0$	66
Figure 6–1: Baseline reference factor as a function of the solid mass flux.....	72
Figure 6–2: Baseline reference factor as a function of the superficial gas velocity.	73
Figure 6–3: Radial cluster slip velocity profiles. Figures (a) to (d) show lower, lower intermediate, higher intermediate, and higher solid mass flux respectively.....	74

Figure 6–4: Radial cluster solid concentration profiles. Figures from (a) to (d), show results of the upper optiprobe; (e) to (h) show results of the lower optiprobe. Four groups are presented, lower, lower intermediate, higher intermediate, and higher solid mass flux.....	76
Figure 6–5: Slip velocities of particles as a function of number of particles in the 1 inch internal diameter downer unit. Operating condition: $U_g=0.95$ m/s, $G_s=10$ kg/m ² /s. Data points included: 899 clusters.....	77
Figure 6–6: Cluster slip velocity distribution: $U_g=1.16$ m/s, $G_s=106$ kg/m ² /s.	78
Figure 6–7: Individual particle cluster size distributions at various solid fluxes and gas velocities.	82
Figure 6–8: Distribution of the number of particles in clusters for $U_g=2.5$ m/s, $G_s=91.2$ kg/m ² /s.	82
Figure 6–9: Individual particle cluster size distribution averages.	83
Figure 6–10: Individual particle cluster size distribution weighted averages for all operational conditions studied.	83
Figure 6–11: Individual cluster size distribution averages at $r/R=0$ radial position.....	84
Figure 6–12: Main forces acting on single particles.....	85
Figure 6–13: Cluster drag coefficient dependence with Reynolds number according with Equation (6–12).	87
Figure 6–14: Change of the CD with Re. Solution Points for Equations (6–12) and (6–13).	88
Figure 6–15: Maximum and minimum cluster drag coefficients estimated with Haider and Levenspiel (1989) correlation.	91
Figure 6–16: Maximum and minimum cluster drag coefficients estimated with Ganser (1993) correlation.	91

Figure 6–17: Theoretical and experimental cluster slip velocities for various cluster lengths. Experimental data are reported in color zones. Color zones represent fractions of the 20,667 total clusters population sharing the same cluster slip velocity and number of particles. 92

Figure 7–1: Particle Size Distribution (PSD) for the FCC particles of the present study. ... 101

Figure 7–2: Inlet particle velocity sensitivity analysis. 101

Figure 7–3: Effect of particle resolution on the calculated cluster particle velocity at the center line of the downer unit. Operating condition: $U_g=1.68$ m/s, $G_s=82$ kg/m²s. Note: four different grids with n_p changing from 30–30,000 were used in the calculations. 105

Figure 7–4: Effect of particle resolution on particle volume fraction at the center line in the downer unit. Operating condition: $U_g=1.68$ m/s, $G_s=82$ kg/m²s. Note: four different grids with n_p changing from 30–30,000 were used in the calculations. 105

Figure 7–5: Effect of particle resolution on pressure in a downer unit of this study. Operating condition: $U_g=1.68$ m/s, $G_s=82$ kg/m²s. Note: four different grids with n_p changing from 30–30,000 were used in the calculations. 106

Figure 7–6: Effect of spatial resolution on cluster particle velocity at the center line of the downer unit. Operating condition: $U_g=1.68$ m/s, $G_s=82$ kg/m²s. Note: $n_p=3,000$, 7x7x557 and 9x9x702 grids were used in the calculations..... 107

Figure 7–7: Effect of spatial resolution on particle volume fraction at the center line of the downer unit. Operating condition: $U_g=1.68$ m/s, $G_s=82$ kg/m²s. Note: $n_p=3,000$, 7x7x557 and 9x9x702 grids were used in the calculations..... 108

Figure 7–8: Effect of spatial resolution on pressure. Operating condition: $U_g=1.68$ m/s, $G_s=82$ kg/m²s. Note $n_p=3,000$, 7x7x557 and 9x9x702 grids were used in the calculations. 108

Figure 7–9: X–Y Grids used in the CPFD simulations. 109

Figure 7–10: Drag coefficients for various drag models including non–spherical particles. 112

Figure 7–11: Simulated average pressure profile along the downer. Operating condition: $U_g=2.53$ m/s; $G_s=76$ kg/m ² s.....	115
Figure 7–12: Average pressure gradient profile along the downer. Operating conditions: $U_g=2.53$ m/s; $G_s=76$ kg/m ² s.....	116
Figure 7–13: Average axial velocity profile along the downer. Operating conditions: $U_g=2.53$ m/s; $G_s=76$ kg/m ² s.....	116
Figure 7–14: Radial profiles for a) cluster particle velocity profile, and b) particle void fraction profile. Axial position of the CREC–GS–Optiprobe $z=0.15$ m, (1/2).	118
Figure 7–15: Radial profiles for a) cluster particle velocity profile, and b) particle void fraction profile. Axial position of the CREC–GS–Optiprobe $z=0.15$ m, (2/2).	119
Figure 7–16: Comparison of between CPFDF simulations and experimental results for cluster particle velocity and particle volume fraction. a) Cluster particle velocity (m/s), b) Particle volume fraction.	120
Figure 7–17: Comparison between CPFDF simulations and experimental results omitting the data in the near wall region. (a) Cluster particle velocity (m/s), (b) Particle volume fraction.	121
Figure 7–18: (a) Radial velocity profile, (b) Particle volume fraction. Operating conditions: $U_g=2.53$ m/s; $G_s=76$ kg/m ² s.....	122
Figure 8–1: Baseline reference factor as a function of the solid mass flux.....	127
Figure 8–2: Baseline reference factor as a function of the gas velocity.....	128
Figure 8–3: Radial cluster slip velocity profiles. Figures (a) to (c) show lower, intermediate, and higher gas velocity, respectively.	129
Figure 8–4: Radial cluster solid concentration profiles. Figures from (a) to (c), show results of the upper optiprobe; (d) to (f) show results of the lower optiprobe. Three groups are presented, lower, intermediate, and higher gas velocity.....	131

Figure 8–5: Slip velocities of particles as a function of the number of particles in the 2 inch internal diameter downer unit. Operating condition: $U_g=1.5$ m/s, $G_s=34$ kg/m ² s. Data points included: 533 clusters.	132
Figure 8–6: Cluster slip velocity distribution. For N=1 to 2, 250 clusters are considered; For N=7 to 8, 43 clusters are accounted. Operating condition: $U_g=1.5$ m/s, $G_s=34$ kg/m ² s.	133
Figure 8–7: Individual particle cluster size distributions at various solid fluxes and gas velocities.	135
Figure 8–8: Distribution of the number of particles in clusters for $U_g=1.5$ m/s, $G_s=34$ kg/m ² s.	136
Figure 8–9: Individual particle cluster size distribution averages.	136
Figure 8–10: Individual particle cluster size distribution weighted averages for all operational conditions studied.	137
Figure 8–11: Individual cluster size distribution averages at $r/R=0.9$ radial position.	137
Figure 8–12: Effect of particle resolution on the calculated cluster particle velocity at the center line of the downer unit. Operating condition: $U_g=1.5$ m/s, $G_s=34$ kg/m ² s. Note: five different grids with n_p changing from 30–300,000 were used in the calculations.	141
Figure 8–13: Effect of particle resolution on particle volume fraction at the center line in the downer unit. Operating condition: $U_g=1.5$ m/s, $G_s=34$ kg/m ² s. Note: five different grids with n_p changing from 30–300,000 were used in the calculations.	142
Figure 8–14: Effect of particle resolution on pressure in a downer unit of this study. Operating condition: $U_g=1.5$ m/s, $G_s=34$ kg/m ² s. Note: five different grids with n_p changing from 30–300,000 were used in the calculations.	142
Figure 8–15: Effect of spatial resolution on cluster particle velocity at the center line of the downer unit. Operating condition: $U_g=1.5$ m/s, $G_s=34$ kg/m ² s. Note: $n_p=30,000$, 11x11x453 and 13x13x518 grids were used in the calculations.	143

Figure 8–16: Effect of spatial resolution on particle volume fraction at the center line of the downer unit. Operating condition: $U_g=1.5$ m/s, $G_s=34$ kg/m ² s. Note: $n_p=30,000$, 11x11x453 and 13x13x518 grids were used in the calculations.....	144
Figure 8–17: Effect of spatial resolution on pressure. Operating condition: $U_g=1.5$ m/s, $G_s=34$ kg/m ² s. Note: $n_p=30,000$, 11x11x453 and 13x13x518 grids were used in the calculations.	144
Figure 8–18: Simulated average pressure profile along the downer. Operating condition: $U_g=1.5$ m/s, $G_s=34$ kg/m ² s.....	148
Figure 8–19: Average pressure gradient profile along the downer. Operating condition: $U_g=1.5$ m/s, $G_s=34$ kg/m ² s.....	149
Figure 8–20: Average axial velocity profile along the downer. Operating condition: $U_g=1.5$ m/s, $G_s=34$ kg/m ² s.....	149
Figure 8–21: Radial profiles for a) cluster particle velocity profile, and b) particle volume fraction profile. Low gas velocities. Axial position of the CREC–GS–Optiprobes $z=0.30$ m.	151
Figure 8–22: Radial profiles for a) cluster particle velocity and b) particle volume fraction. Intermediate gas velocities. Axial position of the CREC–GS–Optiprobes $z=0.30$ m.....	152
Figure 8–23: Radial profiles for a) cluster particle velocity and b) particle volume fraction. High gas velocities. Axial position of the CREC–GS–Optiprobes $z=0.30$ m.....	153
Figure 8–24: Comparison between CPDF simulations and experimental results for cluster particle velocity and particle volume fraction. (a) Cluster particle velocity (m/s), and (b) Particle volume fraction.....	154
Figure 8–25: (a) Radial velocity profile, (b) Particle volume fraction. Operating condition: $U_g=1.5$ m/s, $G_s=34$ kg/m ² s.....	155

Figure 8–26: Comparison of the CPF_D simulations and experimental data for the cluster void fraction and the cluster velocity based on the deviations (error %) at $r/R=0.9$ of the downer units studied. 156

List of Appendices

Appendix A: Fluid Catalytic Cracking (FCC) Catalyst.....	177
Appendix B: Camera Beam Profiler.....	181
Appendix C: Beam Profiler Software.....	182

Nomenclature

A	Downer reactor internal area, m^2
A_c	Cluster cross-section area, m^2
A_s	Single particle cross-section area, m^2
\mathbf{a}_s	Particle acceleration vector $(a_{p_x}, a_{p_y}, a_{p_z})$, m/s^2
C_d	Drag coefficient
d_s	Particle diameter, m
D_s	Drag coefficient at a particle location
f_d	Drag force, N
f_b	Buoyancy force, N
f_g	Force of gravity, N
\mathbf{F}	Rate of momentum exchange between phases, N/m^3
\mathbf{F}_s	Particle drag force, N
f	Particle distribution function (PDF)
f_D	Particle distribution function with collision damping
G_s	Solid mass flux, $kg/m^2 \cdot s$
\mathbf{g}	Gravitational acceleration, m/s^2
h	Downer length, m; or Characteristic dimension of the sensing region (focal point), m
K	Drag expression constant
K_1, K_2	Functions of ψ
l_o	Object distance, m
l_i	Image distance, m
m	Total number of cluster detected above the baseline for a specific time
m_s	Particle mass, kg
Mw_g	Gas molecular weight, g/mol
n	Baseline reference factor

N	Number of particles in a cluster having the same average diameter of 84.42 μm
n_p	Number of particles fed per average unit volume
p	Pressure, Pa
r	Downer radial position, m
R	Downer Internal Radio, m; or Universal gas constant, J/mol·K
Re	Reynolds number
R_{XY}	Cross–correlation sequence
r_{eq}	Equivalent cluster radio, m
S_{ij}	Rate of deformation, 1/s
T	Temperature, K
t	Time, s
U_{sg}	Superficial gas velocity, m/s
U_s	Terminal solid velocity, m/s
U_g	Gas velocity, m/s
U_{slip}	Slip velocity, m/s
\mathbf{U}_s	Particle velocity vector $(u_{p_x}, u_{p_y}, u_{p_z})$, m/s
V_p	Particle volume, m^3
V_ξ	Cell volume, m^3
V_c	Cluster volume, m^3
w_e	Effective weight force, N
X	Time series signal average, V
\mathbf{X}	Cluster time series, V
\mathbf{Y}	Cluster time series, V
\mathbf{x}	Particle spatial location vector (x_x, x_y, x_z) , m
z	Axial coordinate in the downer unit with $z=2$ m being the downer feeding point

Greek Symbols

δ_{ij}	The Dirac delta function
Δt_i	Sensor signal time length, s
ε_{cp}	Particle volume fraction at the close packing limit
ε_g	Gas volume fraction
ε_s	Particle volume fraction
μ_g	Gas dynamic viscosity, Pa·s
ξ	Cell number
ρ_s	Particle density, kg/m ³
ρ_g	Gas density, kg/m ³
σ	Standard deviation
τ_g	Gas stress tensor, N/m ²
τ_s	Particle normal stress tensor, N/m ²
τ_D	Collision damping time, s
ψ	Sphericity

Acronyms

CCD	Co-Current Downflow or Charge Coupled Device
CCU	Co-Current Upflow
CDCFB	Concurrent Downflow Circulating Fluidized Bed
CFB	Circulating Fluidized Beds
CFD	Computational Fluid Dynamics
CPFD	Computational Particle Fluid Dynamics
CREC-GS-Optiprobe	Chemical Reactor Engineering Centre Gas Solid Optiprobe
DEM	Discrete Element Method

ECT	Electrical Capacitance Tomography
FCC	Fluidized Catalytic Cracking
GRIN	Graded Refractive Index
GUI	Graphical User Interface
KTGF	Kinetic Theory of Granular Flow
LPG	Liquefied Petroleum Gas
MP-PIC	Multiphase Particle-In-Cell
VGO	Vacuum Gas Oil

Chapter 1

1 Introduction

Circulating Fluidized Beds, commonly designated with the CFB acronym, have been used as efficient gas–solid contact reactors in a broad range of applications. The origins of CFBs can be traced back to the 1940s. Starting in the 1960's to the 1970's CFBs have been the basis of a number of catalytic and non–catalytic processes for the manufacture of a variety of intermediate and consumer end products (Squires, 1994; Reh, 1971).

A typical configuration for gas–solid CFB systems includes the use of a riser: a tall reactor where the particles move upwards in contact with the gas phase. Following their circulation in the riser, solids flow through a system, usually involving: one or more cyclones, a standpipe, and a valve or seal. These external components constitute of a loop, allowing particles to be fed back into the riser unit. One should notice that individual particles circulate many times in this loop, while the fluid flows through the riser only once (Grace and Bi, 2003). A typical setup for a CFB is reported schematically in Figure 1–1.

When comparing CFB reactors with conventional bubbling fluidized bed reactors and other gas–solid contactors such as packed beds, CFB present several advantages such as: a) high gas throughputs, b) limited backmixing of gas, c) better temperature uniformity, d) flexibility in handling particles of widely differing sizes, densities, shapes and cohesivity, e) effective contact between gas and particles, f) limited gas bypassing with minimal mass transfer limitations, and g) opportunity for separate and complementary operation (e.g., catalyst regeneration or particle cooling) in the return loop.

Even though the predominant interest in CFB systems continues to be for gas–solid (two phase) contactors, in recent years, CFBs have also been used for liquid–solid systems and gas–liquid–solid (three–phase) systems. Furthermore, the technical literature also reports the case of internal circulating fluidized beds where the particles circulate around one or more loops within a main reactor space or vessel (Grace and Bi, 2003).

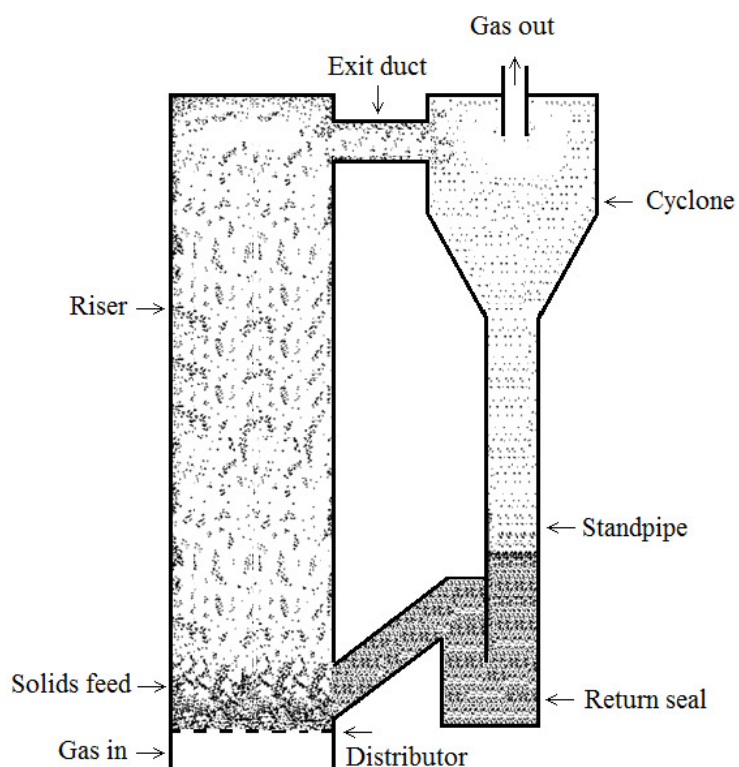


Figure 1–1: Circulating Fluidized Bed typical configuration.

One of the major applications of gas–solid CFB systems, using risers as the main reactor, can be found in Fluidized Catalytic Cracking (FCC) units. In these systems, it is imperative to simultaneously conduct the cracking reactions at the surface of the catalyst, limiting the coking of the catalyst (Chen, 2003).

Typical FCC units are composed of two reactors, a riser and a regenerator. It is in the cracking riser reactor, where almost all the endothermic cracking reactions, and coke deposition on the catalyst, takes place. The unit is completed with the catalyst regenerator component. It is in the catalyst regenerator, where the catalyst is reactivated by burning off the formed coke with air. One should mention that overall the catalyst serves the purpose of driving the conversion of vacuum gas oil while at the same time providing the heat carrying capacity required by the endothermic cracking reactions. It has been found, in more recent years, that the riser is a very efficient catalytic cracker. Thus, nowadays, most FCC units have been upgraded to have a cracking unit operating in the riser mode.

When examining the key operating variables for the commercial operation of gas–solid CFB riser systems, one can notice that they are bracketed into the following operational ranges ([Grace and Bi, 2003](#)): Superficial gas velocity: 2–12 m/s; net solid flux through the riser: 10–1000 kg/m²s; temperature: 20–950 °C; pressure: 100–2000 kPa; mean particle diameter: 50–500 µm; and overall riser height: 15–40 m.

While gas–solid CFB reactor systems, using risers, offer significant advantages over conventional bubbling fluidized bed reactors and packed beds, they may suffer from significant back mixing. Ideally, a uniform gas–solid suspension in the riser section is desirable, in which both the discrete and continuous phases move in plug flow mode. However, this regime is far from being achieved in some riser units and particularly, in the feeder section. As a result, a core–annulus model has been proposed with a flow structure inducing radial segregation of gas and solids. This flow structure reduces the overall contact between the two phases, diminishing the desired selectivity and leading to a non–uniform distribution of the desired product ([Zhu et al., 1995](#); [Wang et al., 1992](#)).

One should notice that the severe particle back mixing observed in risers is mainly the result of gas and solids moving upwards against the gravity. This, as a result, involves, an unfavorable hydrodynamics which can be largely overcome in a new gas–solid CFB configuration designated as “downer unit”.

Regarding downer units, gas and particulates move concurrently downwards, in the same direction as gravity. As a result one benefits from an enhanced and more uniform radial gas and a solid flow structure. Thus, in downer reactors, the flow structure involves a gas–solid suspension with individual particles relatively well distributed in a continuous gas phase, with this being true for a large range of operating conditions. In these types of diluted dispersed systems, the particle transport is governed by external field forces (e.g., gravity, buoyancy, drag, and electrical forces) acting on the particle surface or the surfaces of groups of particles ([Dang et al., 2014](#); [Koratiya et al., 2010](#); [Tuzla et al., 1998](#)).

These external field forces provide a relatively homogenous diluted particle flow displaying low solid hold-ups, short residence times and a relatively large loading ratio. Due to these properties, downers have attracted attention both in fundamental research and for practical applications. (Brust and Wirth, 2004; Zhu et al., 1995; Wang et al., 1992).

Commonly, a downer reactor consists of a vertical column with gas and solid distributors at the top and one or more gas–solid separators at the bottom. Typically, the downflow section is a straight vertical tubular conduit of constant diameter. For catalytic reactions, the reactor section is preferably manufactured to provide an inner surface which is as straight and smooth as possible.

Table 1–1: Some application areas for gas–solid Circulating Fluidized Bed systems using downers.

Applications	Reference
Thermal cracking of waste plastics derived oil	(Jiao et al., 1998)
Fluid Catalytic Cracking (FCC) to maximize refinery gasoline and/or propylene	(Jin et al., 2014; Chuachuensuk et al., 2013; Koratiya et al., 2010; Wu et al., 2009; Maadhah et al., 2008; Shaikh et al., 2008; Fujiyama et al., 2005; Abul–Hamayel, 2004; Deng et al., 2002; Talman et al., 1999)
Production of polymeric materials with superior physical properties	(Mei et al., 2006)
Coal pyrolysis (Coal gasification)	(Cheng and Wang, 2014; Cheng et al., 2014, 2013; Dong et al., 2012; Cheng et al., 2008; Kim et al., 2001)
Partial oxidation of n–butane to Maleic Anhydride (MAN)	(Vaishali et al., 2010)
Ozone decomposition	(Li et al., 2011)
Biomass pyrolysis	(Ding et al., 2012; Berg et al., 1989)
Carbon dioxide capture	(Kongkitisupchai and Gidaspow, 2013)

The published technical literature has shown that downer reactor units could have intrinsic advantages over riser units in fluid catalytic cracking processes (Koratiya et al., 2010; Deng et al., 2002). Using the downer unit, cracking reactions are driven in the downflow section, having a flow field with limiting phase segregation. Catalytic cracking reactions under those conditions of controlled phase contact enhances desired chemical reactions (Chuachuensuk et al., 2013; Koratiya et al., 2010; Wu et al., 2009; Maadhah et al., 2008; Shaikh et al., 2008; Fujiyama et al., 2005; Deng et al., 2002; Talman et al., 1999).

In this respect, one can foresee that in a downer reactor FCC plant, the catalyst and gas contact times could be better controlled with a significant reduction in overcracking and particle backmixing. It is thus expected that, the use of downer reactors could increase the desired intermediate chemical species in the cracking of vacuum gas oil such as gasoline, in this new approach the function of the downflow section is to complete the cracking reactions while providing a flow field which prevents phase segregation (Chuachuensuk et al., 2013; Koratiya et al., 2010; Wu et al., 2009; Maadhah et al., 2008; Shaikh et al., 2008; Fujiyama et al., 2005; Deng et al., 2002; Talman et al., 1999).

In a cold model laboratory downer, gas–solid downflow and solid circulation are usually achieved in a concurrent downflow circulating fluidized bed (CDCFB). Here, solids are separated from the gas stream at the bottom of the downer and are carried upwards in an accompanying riser to the top of the downer.

There have been, in recent years, valuable papers on downer fluid dynamics published in the technical literature. These articles chiefly consider slip velocity and solid concentration radial profiles while providing little reference regarding individual particle cluster properties (Abbasi et al., 2013; Islam et al., 2010; Islam, 2010; Qi et al., 2008; Nova et al., 2007, 2004b; Nova, 2005; Li et al., 2004; Manyele et al., 2003, 2002; Krol et al., 2000; Talman et al., 1999; Tuzla et al., 1998; Zhu et al., 1995; Wang et al., 1992).

To enhance the study of cluster particles, de Lasa et al. (1998) patented a novel optical fiber sensor. This sensor is a relatively simple and economical device. It has the potential of being able to measure local parameters, as required by the fluid dynamic characterization in gas–solid downer units. This sensor designated as the CREC–GS–Optiprobe uses a Graded Refractive Index (GRIN) lens. This GRIN lens creates a highly irradiated region at a few millimeters in front of the probe tip. As a result, particles reflect laser rays while moving through the highly irradiated region. These rays are captured by strategically located receiver optical fibers and are then converted to corresponding electrical signals. As a result, the CREC–GS–Optiprobe minimizes probe intrusion allowing for detailed resolution of particle phenomena.

Since the patent described above was implemented, de Lasa's research team has been considerably involved in experimental hydrodynamic studies in downer reactors using the patented fiber optical probe device. [Nova et al. \(2004a, 2004b\)](#) primarily discussed the novel CREC-GS-Optiprobe design principles, construction and experimental results. [Islam et al. \(2011b\)](#) discussed the CREC-GS-Optiprobe, its effective focal region estimation using geometrical optics. Furthermore, experimental data and time signal results have been analyzed in the CREC-labs using various statistical approaches. [Nova et al. \(2004b\)](#) reported particle cluster properties in downflow reactors. Clusters were characterized by relating signal "trains" which complied with the constraint of being in 5% of the highest peak. In addition, peak widths were measured at a reference level, crossing the signal at 50% of the height of the highest peak in the signal train. On the other hand, [Islam et al. \(2011a, 2010\)](#) proposed that signal peak widths could be calculated with a baseline set at the signal average plus three times the standard deviation ($x+3\sigma$). Due to the technical limitations of the data analysis ([Islam et al., 2011a, 2010](#); [Nova et al., 2004b](#)), it was not possible to correlate individual peak signals assigned to clusters.

Taking advantage of various data acquisition enhancements, [Lanza et al. \(2012\)](#) reported, for the first time, "individual cluster" information such as: a) cluster solid concentrations, b) individual cluster slip velocities, c) cluster sizes, and d) cluster drag coefficients. [Lanza et al. \(2012\)](#) developed a rigorous methodology setting the data baseline using the solid phase mass balance. Thus, using this approach, the baseline was selected for every operational condition in compliance with the solid mass balances. This approach provides a new data analysis method which circumvents the use of an arbitrary (empirical) and fixed data baseline level, as in prior studies. Additionally, [Lanza et al. \(2012\)](#) also proposed a mechanistic based method to calculate cluster drag coefficients, with this being a function of the cluster length and cluster particle size configuration of each particle cluster. To further characterize the gas-solid flow in downer units, [Lanza et al. \(2013\)](#) showed that particle clusters display asymmetric distributions with smaller particle clusters being the most dominant.

Mathematical modeling of gas–solid flow has recently received considerable attention because of issues of stability and formulation of well–posed governing equations (Cheng and Wang, 2014; Kim et al., 2011; Zhao et al., 2010; Andrews and O’Rourke, 1996). A promising mathematical technique is presented using the Computational Particle Fluid Dynamics approach (CPFD). In the CPFD method, the gas phase is treated as a fluid and is calculated using Eulerian computational grids, while the particle phase is modeled as discrete particles using Lagrangian numerical–particles. The fluid phase is described by mass and momentum conservation equations including the strong coupling to the particle phase. The particle phase is accounted for by using a particle probability distribution function. The particle momentum equation is based on a multiphase particle–in–cell (MP–PIC) method. In this regard, the use of CPFD, for downer simulations, may have significant advantages in describing the particle–fluid patterns and special flow features such as the inherent rotational flow properties.

Regarding the use of CPFD, to characterize the gas–solid flow in downers, Abbasi et al. (2012) reviewed the intrusion effects of the CREC–GS–Optiprobes in a downer reactor. These authors found that local axial gas and particle velocities, cluster sizes and particle volume fractions can be obtained by using the focal region of the CREC–GS–Optiprobes with essentially undisturbed measurements. Furthermore, based on CPFD, Abbasi et al. (2013) discussed multiphase flow patterns in a downflow reactor using three dimensional numerical simulation algorithms, with the following being described: a) local and time variations of fluid dynamic properties in downers, and b) circumferential solid fluxes, which both leading to particle motion with radial velocity components.

Thus, given the status of the development of downer models and the potential interest in scaling them up, one can acknowledge the significance of specific model validation using experimental data. As a result, in the present PhD dissertation, a gas–solid downflow comparative study is reported. Calculations are developed using the CPFD numerical scheme with an accurate cluster size distribution as reported in Lanza et al. (2013). The simulation conditions are selected in order that the calculated results could be directly compared with experimental results. It is observed that the successful comparison of

experimental and simulated results provides strong support for a phenomenologically based model for downer units.

During the development of the present PhD dissertation four articles were drafted, two of them were already published and the other two are going to be published in reputable chemical engineering journals as well. Professor H. de Lasa (supervisor) is co-author in all of them. He provided helpful recommendations throughout the whole research project and suggested key corrections to the draft versions of all four manuscripts. Additionally, Dr. M. Islam is co-author in the first three manuscripts. He performed the experiments in one of the two downer units studied. His unprocessed data was used for the elaboration of the first three papers. Regarding the present PhD dissertation, chapters are presented as follows:

Chapter 2 summarizes the literature review, relevant to the area of research. Chapter 3 of this thesis, outlines the main objectives of the research project and the accomplishment of the research objectives. Chapter 4 describes the experimental equipment and measurement methods used in this study.

Chapter 5 and partially Chapter 6 are based on a first publication, entitled "*Particle Clusters and Drag Coefficients in Gas-Solid Downer Units*". This article was published in Chemical Engineering Journal, volumes 200–202, pages 439–451, in June 2012. The PhD Candidate developed a new methodology for signal analysis, elaborated the computational program for his new data analysis method, estimated for the first time, “individual cluster” information such as: a) cluster solid concentrations, b) individual cluster slip velocities, and c) cluster sizes. He also proposed a mechanistic based method to calculate cluster drag coefficients in downer units, with this being a function of the cluster length and cluster particle size configuration of each particle cluster. He prepared the draft writing and implemented the corrections to the final manuscript.

The second part of Chapter 6 is based on a second publication, entitled "*Particle Cluster Size Distribution in Gas-Solid Downer Units*". This article was published in the in "The 14th International Conference on Fluidization – From Fundamentals to Products", Eds, ECI Symposium Series, http://dc.engconfintl.org/fluidization_xiv/33, volume (2013), in

May 2013. The PhD candidate calculated cluster size distributions based on the results obtained using his new methodology, proposed for cluster analysis, in downers reactor units. He implemented modifications to his computational programs to account for radial position influence on cluster size distribution. He also prepared the draft writing and implemented the corrections to the final manuscript.

Chapter 7 is based on a third publication, entitled "*Gas–Solid Fluid Dynamics in a Downflow Reactor: A CPFD Based Model*" This manuscript is still under revision. The PhD Candidate developed the Computational Particle Fluid Dynamics Simulations. He used the cluster size distribution and sphericity determined with his new methodology as an input for the simulations. He performed a discretization sensitivity analysis to obtain independent solutions. He determined all the computational parameters and compared them with the experimental data. He also prepared the draft writing and implemented the corrections of the final submitted version.

Chapter 8 is based on a four publication, entitled "*Cluster Fluid Dynamics in Gas–Solid Downflow Reactors: Experiments and CPFD Simulations*". This article is still under revision. The PhD Candidate designed and performed the experiments in a larger downer unit, implemented his methodology for data analysis, determined individual cluster properties and developed the Computational Particle Fluid Dynamics Simulations. He used the cluster size distribution and sphericity determined with his new methodology as an input for the simulations, He also performed a discretization sensitivity analysis to obtain independent solutions. He determined all the computational parameters and compared them with the experimental data. He also prepared the draft writing and implemented the corrections of the final submitted version. Finally, Chapter 8 is based on conclusions and recommendations for future work.

Chapter 2

2 Literature Review

In a down flow reactor, the flow direction of both the gas and the solids is downwards in the same direction as gravity. This hydrodynamics is a distinctive characteristic of this unit which makes it unique when compared to other gas–solid systems. The down flow unit, designated frequently as a “downer” provides a relatively homogenous dilute flow structure, nearly plug–flow for both phases, low solid hold–ups, short residence times and a relatively large solid/gas mass ratio. Due to these properties, downers attract the attention of researchers in both fundamental and applied technology areas. In this section, the hydrodynamics, feeders/distributors, cyclones/separators, cluster formation, numerical simulation, measurements of solid concentration, heat transfer, and applications of downer reactors are reported and discussed.

2.1 Downer Reactor Units

Down flow circulating fluidized beds, have attracted the interest of research engineering community, given their significant advantages when compared to other gas–solid systems such as riser units ([Arsenijević et al., 2014](#)).

One of the first designs of downer reactors, dates back to the early 1970s, when Stone and Webster began to develop a new type of reactor which consisted of a solid–gas feed mixer, a downflow reactor section and a specially designed one–quarter–turn cyclone for ultra fast gas–solid separation ([Gartside, 1983; 1989](#)). This reactor was reported to offer very short residence times (~200 ms), near plug flow and a high temperature reaction environment. However, its jets displayed very high velocities (over 100 m/s), leading to considerable catalyst attrition in the mixing zone.

In down flow units, the solid particle flow is assisted by gravity since particle flow and gas flow are in a direction coincident with gravity. Solid particles, as a result, experience a so–called “slip velocity” or difference between particle velocity and gas velocity, with the particle velocity being higher than that of the gas phase.

The slip velocity can, for a single particle, be estimated using the law of particle mechanics, which accounts for the balance of forces exerted on a particle. In this respect, in downers units, where there is a high population of particles moving simultaneously, particles may influence each other, while falling side-by-side or while travelling one behind the other. This condition may favor a drag force reduction, with a mass increment due to the consolidation of agglomerates. All this, may contribute to a rise in slip velocity. For instance, if two identical spheres fall one behind the other, with a separation distance smaller than a critical distance, their velocity may be increased by up to 50% (Islam, 2010; Nova, 2005; Krol et al., 2000).

2.2 Hydrodynamics of Downers

The main difference in the operation of risers and downers, lies in the fact that the flow direction is against or along the gravity force. As a result, the hydrodynamics in downer units show a unique flow structure across both the axial and radial directions.

The technical literature describes downers as having unique hydrodynamic characteristics (Wang et al., 1992). These distinctive hydrodynamic characteristics are described referring to three axial flow sections with different pressure drops as follows: a) inlet section, b) acceleration section and c) fully developed flow section.

Herbert et al. (1998) studied the axial pressure gradient profile in pilot scale downflow circulating fluidized beds and concluded that the system pressure gradient remained constant beyond the inlet section. Zhang (1999) obtained axial profiles of other measured variables such as solid holdup, solid velocity, solid mass flux and pressure loop in a downer system.

Deng et al. (2002), Zhang and Zhu (2000), and Zhang (1999) found that the radial distributions of particle velocities and solid fluxes in a downer reactor are quite uniform. This is also the case while compared to those in risers. Another group of researchers (Fan et al., 2008; Vaishali et al., 2008; Cao and Weinstein, 2000b), suggested that a non-uniform flow structure in the downer radial direction is still present with a

non-uniform property distribution. In this respect, [Lehner and Wirth \(1999\)](#) and [Wang et al. \(1992\)](#) claim that there is a dense ring of solid particles located near the unit wall.

In summary, in spite of the promise of downer reactor units, there are still issues that need to be clarified regarding the radial distribution of properties in downers.

2.2.1 Axial Flow Sections

In a downer reactor, gas and particles are fed from the top of the downer using gas and particle distributors. While particle velocities are initially close to zero, their contact gas is evolving at high velocity (somewhat in excess of the superficial velocity). Solids are then accelerated by both the combined effect of gas flow (drag) and gravity.

As a result, particles accelerate, until their velocity reaches the gas velocity. This segment is designated as the first acceleration section. As particle velocity increases in the first acceleration section, the actual average linear gas velocity decreases moderately due to the reduced solids concentration across the downer section ([Zhu et al., 1995](#); [Wang et al., 1992](#)).

Furthermore, after acquiring the same velocity of the gas phase, solids are further accelerated by gravity. This occurs while encountering drag forces exerted by the now slower moving gas phase. Therefore, particle velocity augments further, until the slip velocity between the particles display such as values, where gas drag forces fully counterbalance the gravitational force. This second segment is designated as a second acceleration section. In this section, particle velocity continues to augment, but at a reduced rate, compared with the increases observed in the first acceleration section. The reduction of gas velocity due to the change of solids concentration also remains small. One should mention that when the gravitational force balances the drag forces, both particle and gas velocities remain constant. This section (excluding any exit effect) is being designated as the constant velocity section. In this section, particles travel faster than gas, displaying a constant differential velocity designated as “slip velocity” ([Zhu et al., 1995](#); [Wang et al., 1992](#)). Figure 2–1 illustrates the three acceleration sections axially presented in a downer reactor.

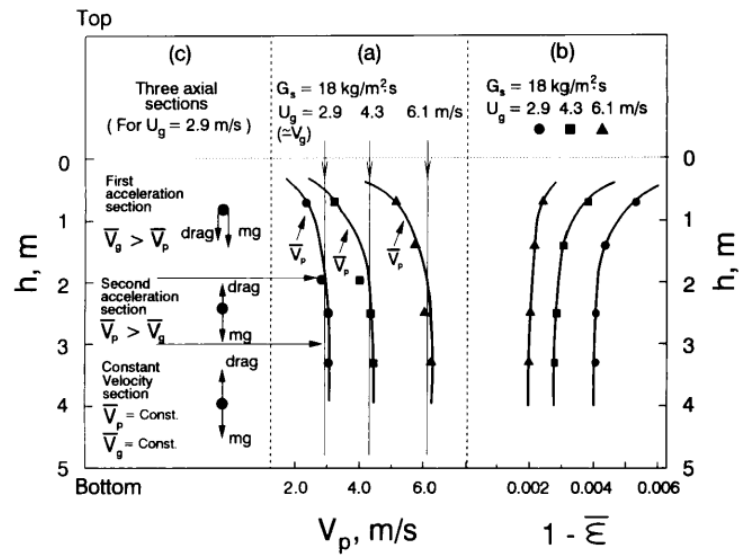


Figure 2–1: Axial gas–solid flow structure in downers (Zhu et al., 1995).

2.2.2 Axial Distribution of Pressure

The axial distribution of pressure gradient profiles reported by Wang et al. (1992) and redrawn as a function of solids and gas velocity by Zhu et al. (1995) are shown in Figure 2–2.

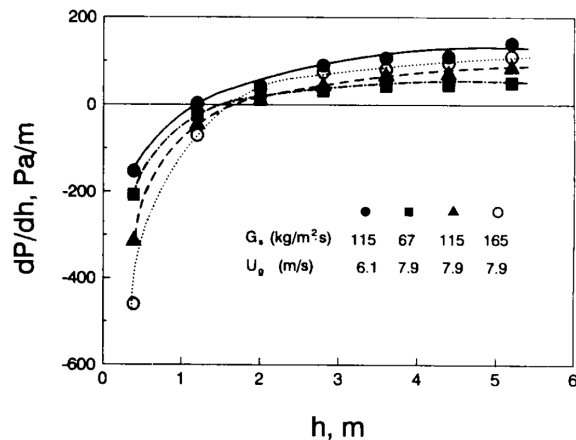


Figure 2–2: Axial distribution of pressure gradient. Effects of solids flux and gas velocity (Zhu et al., 1995).

It can be observed in Figure 2–2, that the pressure in the flow direction drops significantly in the first acceleration region. It is in this region, where the particle velocity

is smaller than the gas velocity. As a result, particles are accelerated by both gravitational and gas drag forces. In order to describe pressure changes, a momentum balance equation can be considered along the downer as follows:

$$\Delta p = p_2 - p_1 = \underbrace{\Delta L g \rho_s}_{\text{static head}} - \underbrace{\Delta p_{\text{acceleration}}}_{\text{energy loss}} - \underbrace{\Delta p_{\text{wall friction}}}_{\text{negligible}} \quad (2-1)$$

where p_1 and p_2 are the pressure at: point 1 at the downer top, and point 2 at the downer bottom, respectively. The $\Delta L g \rho_s$ term represents the pressure losses due to solid hold up static head, $\Delta p_{\text{acceleration}}$ accounts for the energy loss due to solids acceleration and $\Delta p_{\text{wall friction}}$ stands for the wall friction between point 1 and 2.

One should notice, that in the first acceleration section, the static head due to gravity is smaller than the one required to overcome the energy loss due to the drag exerted on particles. Thus, the Δp pressure change is negative.

In the second acceleration section, however, the particle velocity reaches the gas velocity. At this point, the pressure drop due to gravitational acceleration of particles, counterbalances the static head, resulting in a zero-drag free fall situation with zero pressure gradients. This zero drag point establishes the boundary between the first and second acceleration regions.

Beyond the point of zero drag, the Δp pressure gradient increases monotonically as particles are further accelerated by gravity. The increase in particle velocity continues until particles reach a point where the gas particle slip velocity is established, as a result of the upward drag force counterbalancing the gravitational force. At this point of the axial position, the pressure gradient becomes constant, with the pressure continuing to increase linearly in the flow direction.

The characteristics of axial flow structures in the various regions were reported by [Zhu et al. \(1995\)](#). This background information is important given that it allows one to select the location of particle flow measurements (i.e. measurements of particle flow in the constant velocity section).

2.2.3 Radial Flow Sections

The structure of the gas and solid flow, in the radial direction, is still a controversial topic, with various researchers reporting different views. Irrespective of these differences, there is agreement in the technical literature about downers leading to flows with smaller radial changes than risers.

The radial distributions of the local solid holdups and the pressure gradients along the downer column were studied by [Zhang et al. \(1999a, 1999b\)](#). These authors characterized the local and overall gas–solid flow structure, using a fibre optical solids concentration probe and a series of pressure transducers. They found that in the fully developed section, the radial solid holdup changes were as follows: a) Quite uniform in the central core region, and b) Decreased either quite quickly or slowly in near wall annular region with this depending upon solids circulation, These authors claim that the uniform radial distribution of the solid flow can provide an almost ideal plug flow condition in the downer, with this being one key advantage of downers over risers. These authors also suggested that the excellent radial uniformity in the core of the downers could be assigned to the gravitational force influence acting in the same direction than the particle flow as well as to a self–limiting mechanism preventing formation of large particle clusters.

On the other hand, [Cao and Weinstein \(2000a\)](#) studied radial solid density profiles in a downer using a X–ray imaging system. These authors found the existence of a core–annulus dilute flow surrounded by a denser wall region.

Furthermore, [Fan et al. \(2008\)](#) studied radial distribution profiles of ozone concentrations in a gas–solid concurrent down flow circulating fluidized bed (downer) to characterize the reactor performance. These authors reported that the radial ozone concentration distribution in a downer is quite flat in the fully developed region of the downer column. This is true except for a very narrow region of $r/R=0.8–0.97$ where there is a significant change in ozone concentration. This change was assigned to the faster reaction rate resulting from high catalyst concentration and solid segregation in the near wall region. It is in this zone, where it is claimed that particles fall faster than in the dilute core. [Fan et](#)

al. (2008) also reported that the significant fall of the ozone concentration near the reactor wall corresponds to higher superficial gas velocities at a given solid circulating rate. These authors pointed out that in the fully developed section, ozone decomposition is facilitated vis-a-vis the ozone conversion in the acceleration region due to the lateral particle migration. They suggested that a more systematic work should be done to understand the mass transfer in the near-wall region of the downer.

2.3 Feeders/Distributors

A major issue in the design of solid distributors of downer reactors is the gas and solid feeder design and operation. Downer feeders are characterized by ultra-short contact times (less than 1 s). The particulate phase needs to be rapidly dispersed in the gas flow. If this is not accomplished, a poor designed distribution at the downer entry, may cause fast reaction rates at some locations. In this respect, it is desirable that the inlet distributor of the downer provide a uniform distribution of phases from the very beginning with, quick solid acceleration and excellent control of gas-solids mixing. This will ensure that claimed advantages of downer reactors are implemented.

Cheng et al. (2008) mentioned that the major challenge to promote good initial gas-solid mixing comes from the gravity forces acting on the particles. At the entry, solids tend to drop immediately downward and cannot reflux or circulate. Recent studies on downer reactors have shown that a plug flow condition may not always be achieved in the fully developed section (Zhang et al. 1999a, 1999b). It has also been demonstrated that the design of the gas/solid distributors at the top of the reactor influences the flow pattern significantly (Johnston et al., 1999).

Given the interest in these matters, in the upcoming sections, the influence of the inlet distributor of downers on the gas-solid flow behavior is presented.

In this respect, Brust and Wirth (2004) studied experimentally the influence of the mixing behavior of gas/solid flows at the entrance section of a downer reactor, on the residence time distribution of the gas phase. They found that the residence time distribution of gas in a downer reactor is crucially effected by the operating mode of the gas/solid

distributor. The application of additional air improves the gas/solid mixing process at the outlet of the distributor. In fact, the operation of the unit at high gas/particle velocity ratio generates a strong backmixing of the solid material at the entrance region of the downer. This leads, as a consequence, to a wide residence time distribution of the gas. Nevertheless, they also reported that it is possible to operate the downer in plug-flow like conditions. To achieve this, researchers suggested that both high superficial gas velocities and low solid velocities are essential at the feeder inlet.

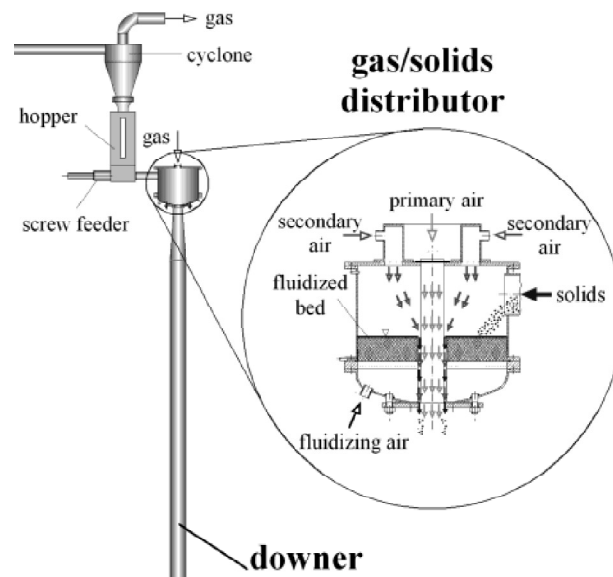


Figure 2–3: Gas/solid distributor section of the downer unit used by [Brust and Wirth \(2004\)](#).

A detailed design of the distributor used by [Lehner and Wirth \(1999\)](#) is shown in Figure 2–4. Solids are fed to a fluidized bed with a screw feeder. The main feature of the distributor consists of two concentric pipes, which are located at the center of the distributor.

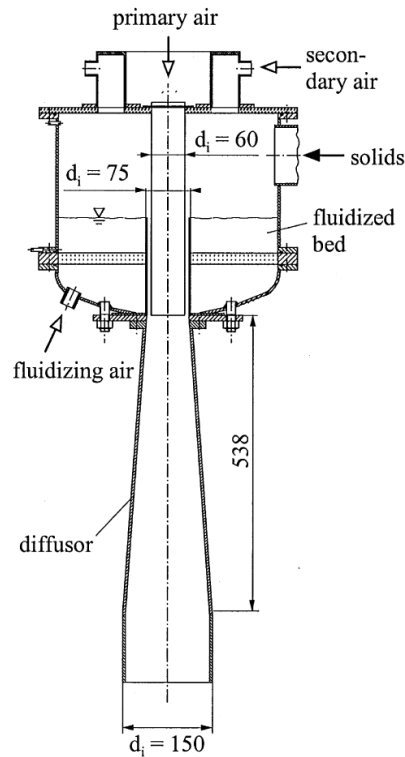


Figure 2–4: Setup of the gas/solid distributor used by [Lehner and Wirth \(1999\)](#). In this Figure the units are reported in mm.

Three distributor designs were used by [Johnston et al. \(1999\)](#) to test the gas/solid flow conditions at the entrance region of a downer unit. Pressure gauges were employed to measure the pressure gradient profiles, while fibre-optic probes were used to measure particle velocity and solids hold-ups. These authors found that the development of the axial gas/solid flow is highly dependent on the distributor type.

[Cheng et al. \(2008\)](#) reports a description of six of the representative inlet configurations of downer reactors found in the literature.

Regarding the effects of the distributor design on the hydrodynamics of a high-density downer reactor, they were considered by [Song et al. \(2005\)](#). These authors identified significant differences in local flow structure between low-density and high-density operating conditions in downers. They reported that as the gas velocity was raised from 0 to 6.0 m/s with the solids flux fixed around 400 kg/m²s, the solid hold-up profiles

became less uniform (denser near the wall and more dilute at the centre). These results are distinctively different from the ones found at low solids fluxes.

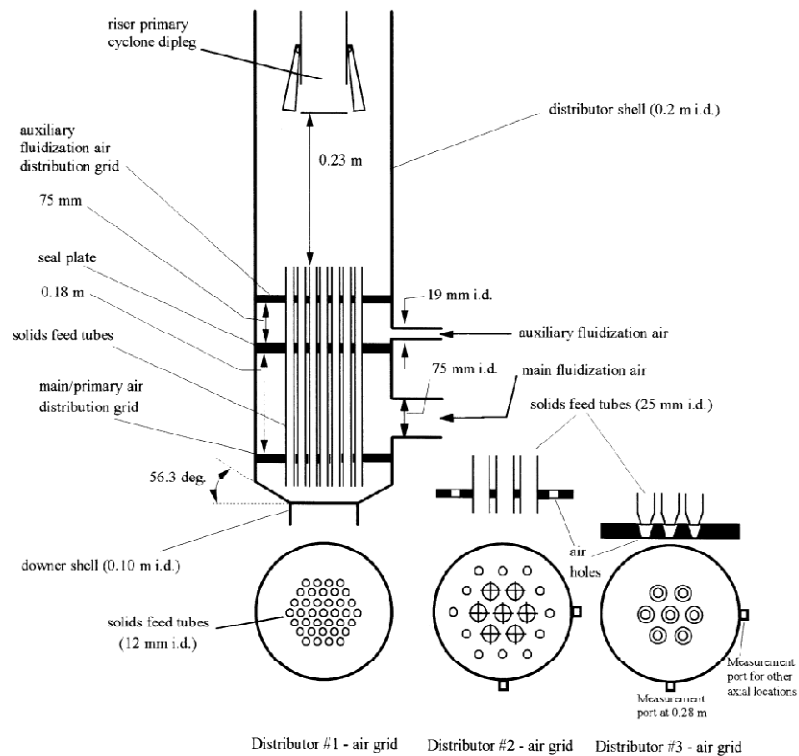


Figure 2–5: Three distributor designs used by Johnston et al. (1999).

Regarding the design of the downer inlet, one can notice that it has drawn much attention because of its strong potential impact on the overall reactor performance. This is especially important, given that in downers, the overall residence time can range from milliseconds to seconds. Thus, a good distribution of solids at the injection section is critical. Although many designs have been studied in the literature, more work has to be carried out to achieve reliable designs as may be required for large scale units in industry.

2.4 Cyclones/Separators

A cyclone is a device that separates particulate solids from a fluid stream by a radial centrifugal force exerted on the particles. Centrifugal forces separate the solid particles from the gas by driving the solids towards the cyclone wall. As a result, solid particles slide down towards the cyclone outlet, with solids being collected there. There are four

primary reasons for separating gases from solids in solid processing plants: 1) to minimize emissions for environmental purposes, 2) to protect other processing equipment (turbines, etc) from particle streams, 3) to avoid losing the solids, and 4) to stop unwanted gas–solid reactions from occurring.

Downer reactors typically accommodate short contact time fast reactions, especially those where an intermediate product is the desired product. Fast separation, is therefore, very critical. When the gas and solid residence/reaction time in the downer itself, is only a fraction of a second, a cyclone with solid residence times in the order of 1–2 s is still unacceptable. Non–traditional ultra fast and more efficient gas–solids separators are, therefore, needed to achieve quick separation.

In 2010, an integrated gas–solid inertial separator was designed by [Huard et al. \(2010\)](#) for implementation in a downer reactor used for the pyrolysis of biomass feedstock. In the case of a pyrolysis unit, product gases emerging from the pyrolysis reactor must be quickly separated from the heat–bearing solids in order to terminate the reaction, thereby stopping product overcracking and degradation. The separation process should also be efficient in terms of particulate removal from the product gas stream. This is important to prevent the additional product vapor reaction downstream of the separator and the solids contamination of the condensed oils. The stripping of the collected solids introduces an additional step in the overall separation process, which that is used to recover entrained product vapors from the solids exiting the separator. Regarding the proposed separator, these researchers reported: 1) excellent efficiencies in excess of 99.99% when separating silica sand from air, using swirl vane separator or cone deflector separator at solid loadings below 0.3 wt/wt; 2) good separation efficiencies of 98.50%, when the device was loaded with glass beads and FCC catalyst particles; 3) a 50% decrease in the separator pressure drop, at a solid load of 1.8 wt/wt using a 60° cone deflector. Figure 2–6. shows the inertial separator designed in this study.

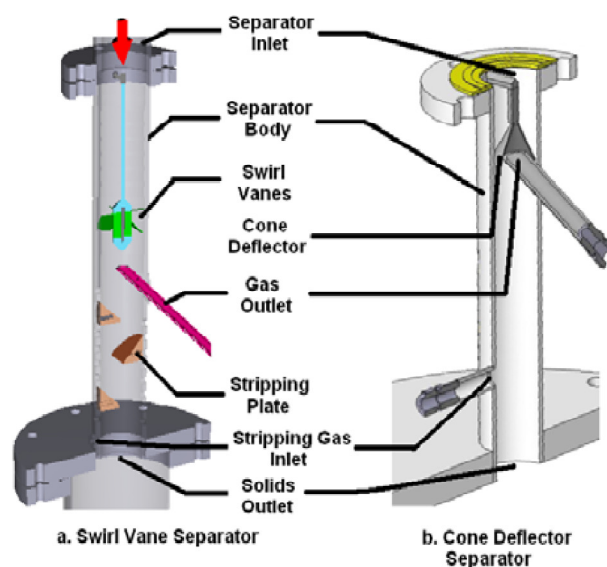


Figure 2–6: Inertial separator designed by [Huard et al. \(2010\)](#).

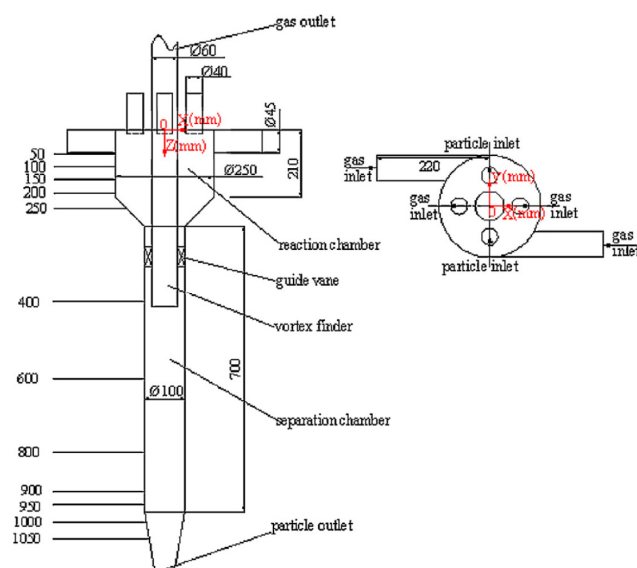


Figure 2–7: Short–contact cyclone reactor designed by [Zhang et al. \(2013\)](#).

A short–contact cyclone reactor for fluid catalytic cracking was designed by [Zhang et al., \(2013\)](#), see Figure 2–7. This reactor mainly includes two sections: a reaction chamber and a separation chamber. These researchers claimed that after the gas–solid flowed into a separation chamber, the gas phase could be separated from solids completely. The new

reactor had a good contact and separation effect. Simulated results were in reasonable agreement with the experimental findings.

One can then notice, that the gas–solid separator at the downer outlet plays a similarly significant role to the downer inlet design. The short, uniform contact times between catalysts and gas, require fast separation of gas and solids at the outlet to avoid consecutive reactions.

2.5 Cluster Formation in Downers, Radial and Axial Distribution

In a downer, the different phases (gas and solids) can aggregate to form transient structures. These structures can be grouped into two types, a dilute phase (more dispersed) and a cluster phase (more dense). These structures can be affected by the system boundaries and by their own interactions forming complex macro–structures characterized by mean radial and axial solids distributions. It is also known, that particle clusters may limit good multiphase mixing inside the system. Thus, particle clustering may have a negative effect on the system chemical reaction conversion. Therefore, the study of these transient flow structures in downers, can elucidate which mechanisms are important, for the control of flow behavior, and for the design, scale–up and overall control of downers.

Several researchers have performed experimental studies on the flow structures in downers. [Wang et al. \(1992\)](#) showed that in a downer, the particle concentration was uniform in the radial direction except for the position near the wall, where a dense phase zone existed. [Krol et al. \(2000\)](#) studied the cluster formation in down flow reactors by using a new optical sensor, the CREC–GS–Optic probe. These authors found that solids evolved as strings of particles and that the average cluster size ranged from 2 to 6 dp with a most probable string size of 3.5 dp. [Manyele et al. \(2003\)](#) reported that the flow non–uniformities in downers are mainly influenced by operating conditions (especially the gas velocity). Non–continuous trends of microscopic parameters were observed with increasing gas velocity and by flow development.

[Lu et al. \(2005\)](#) studied the flow structures in downers by a micro–video analysis of local voidage signals. The micro–video action shot showed that there were particle clustering phenomena in the downer and that the clusters existed mainly in the form of flocks and sticks. Through wavelet analysis of local voidage signals, a probability density of cluster sizes at different bed lengths was obtained. The probability density distributions of local voidage signals confirmed that the clusters in the downer were unstable and could not form a stable phase.

These researchers reported that the size of the clusters is augmented with an increase in the solid circulation rate and/or a decrease in the superficial gas velocity in the downer. This could be attributed to the fact that the higher the solid concentration is, the more easily the larger clusters can be formed. With an increasing number of particles in the cluster, the effective drag force that each particle sustains is reduced. This results in an increase of the cluster velocity ([Krol et al., 2000](#)). However, a further increase in the velocity of the cluster leads to a decrease in the cluster size. This is due to the dissipation and the break of clusters. On the other hand, increasing the solid circulation leads to an increase in the concentration of solids, followed by formation of larger clusters ([Karimipour et al., 2006](#)).

[Cheng et al. \(2008\)](#) reported a core–annulus system flow pattern in downers, at the annulus or wall region, where solid particles agglomerate and form particle clusters. It can be noticed that, the way to identify and characterize the important parameters of particle clusters, diameter and concentration, in the technical literature, is still in a development stage.

Cluster formation in downers has also been reported by simulation based works by several investigators ([Peng et al., 2013](#); [Chalermssinsuwan et al., 2012](#); [Khongprom et al., 2012](#); [Samruamphianskun et al., 2012](#); [Zhao et al., 2010](#); [Zhao et al., 2010](#); [Zhang et al., 2008](#)). [Zhao et al. \(2010\)](#) reported that Near the inlet, the particle distribution is dominated by the distributor design. Then, the particles disperse in the column, forming a homogeneous transit region. After that clusters start to form and modulate the gas–solid flow field until the fully developed state. They reported that clusters are composed of

loosely collected particles, and these particles have the same flow direction as the bulk flow so that no particle backmixing could be observed. One of the most recent publications on cluster formation in downers using computational fluid dynamics was presented by [Chalermssinsuwan et al. \(2013\)](#). These researchers calculated the particle cluster diameters and concentrations from two-dimensional CFD simulation results by using the concepts of kinetic theory of granular flow and statistic, in the CFB downer, a dilute core–annulus flow structure was reported. They claimed that the computer capacity remains the limitation for simulating a complex system. Although the two-dimensional model is proven to represent the three-dimensional system in their study, the three-dimensional model is more realistic than the two-dimensional model with higher computational effort.

2.6 Computational Fluid Dynamics

With the development of computing facilities nowadays, computer simulations have become an important experimentation complement in the study of multiphase hydrodynamics. In particular, various computational approaches and numerical schemes have been adopted to study flow characteristics in downer systems ([Ge et al., 2011](#)).

[Cheng et al. \(2001\)](#) reported a gas–turbulence solid–turbulence model to simulate the hydrodynamics in the entrance region of a downer. They showed that predicted profiles of local solid fractions and particle velocity display good agreement with the experimental results. [Bolkan et al. \(2003\)](#) integrated hydrodynamic features of circulating fluidized beds into a computer simulation of a downer reactor. They reported an empirical correlation when estimating average cluster sizes. They also presented a correlation for estimating the particle–wall friction factor. The hydrodynamic behavior of the gas–solid suspension, within the downer both in the developing–flow as well as in the downer fully developed flow regions, was successfully estimated.

Additionally, [Li et al. \(2004\)](#) reported another mathematical model to describe the hydrodynamics of the fully developed region in a downer reactor based on the energy–minimization and multi–scale (EMMS) principle. In this study, they

accomplished the following: a) a simulation of the influence of the friction coefficient, of the solid flow rate and of the superficial gas velocity on the flow pattern in the downer; b) a prediction of local solid concentration and gas/solid velocities; and c) a calculation of cluster size and local slip velocity.

In 2005, [Ropelato et al. \(2005\)](#) proposed a multiphase model to predict the hydrodynamics in downer reactors. The proposed model was based on an Eulerian–Eulerian Approach which included dissipation of turbulent kinetic energy. These authors claimed that CFD techniques provided powerful tools to simulate downer reactor inlet fluid dynamics as well as chemical process optimization.

In addition, based on the Eulerian–Eulerian Two–Fluid Continuum Approach, [Liu et al. \(2011\)](#) improved a unified second–order moment two–phase turbulence model to simulate the dense gas–particle flows in downers. These incorporated a coefficient of restitution into the Particle–Particle Collision Equation. Results were in agreement with experimental observations.

[Kim et al. \(2011\)](#) employed a k_1 – e_1 – k_2 – k_{12} two–fluid model based on the kinetic theory of granular flow (KTGF) to predict the flow behavior of gas and solids in downers. These researchers found that particles of small size as 70 μm in diameter apparently interact with the gas turbulence. The turbulence energy interaction between gas and solids was described by different k_{12} transport equations, while the particle dissipation by the large scale gas turbulent motion was taken into account through a drift velocity. Johnson–Jackson boundary condition was adopted to describe the influence of the wall on the hydrodynamics. The simulation results based on CFD model were compared with the experimental. Good agreement was obtained.

[Prajongkan et al. \(2012\)](#) calculated mass transfer coefficients and Sherwood numbers in a circulating fluidized bed downer using the concept of additive chemical reaction and mass transfer resistances. These researchers found that the mass transfer coefficients and Sherwood numbers had minimum values with both the increasing reaction rate constants and the increasing system height. System turbulences and dispersion coefficients were also studied in a Circulating Fluidized Bed (CFB) downer by [Chalermssinsuwan et al.](#)

(2012) using a Eulerian Computational Fluid Dynamics Model based on the concept of the kinetic theory of granular flow and statistics. Using this approach, these researchers found that in the CFB riser, a dense-core annulus flow structure was observed, while in the CFB downer, a dilute core-annulus flow structure was obtained. The particle cluster in the CFB riser had more heterogeneity movements than that in the CFB downer, which could be explained by the system flow direction. About the particle cluster dynamics, the particle cluster diameters and concentrations in the CFB riser were higher than in the CFB downer. The particle cluster dynamics were increased with decreasing system height, due to the accumulation of solid particles.

Furthermore, Computational Fluid Dynamics combined with the Discrete Element Method (CFD-DEM) have also been applied for studies of different multiphase flows (Lim et al., 2006). Zhang et al. (2008) used CFD-DEM to study particle cluster behavior in a riser/downer reactor. They reported that there are two types of clusters in a riser and downer: one is in the near wall region where the velocities of particles are low; the other is in the center region where the velocities of particles are high. With this method, various flow structures were predicted in the developing regions in the downer. CFD-DEM was also used by Zhao et al. (2010) to numerically simulate the flow behaviors in a downer with a newly designed distributor. They reported that uniformity of particle distribution was directly influenced by air supply conditions. The calculated particle and air velocity distributions as well as axial and radial distributions of solid holdups agreed quite well with the measurements using Electrical Capacitance Tomography (ECT). With the same approach, Zhao et al. (2010) studied the hydrodynamics in downers. They found distinct clustering phenomena in the downers. They reported that particles injected from the inlet, first streamed according to the inlet design, and then dispersed in the downer to a homogeneous state. After that, the clusters started to form, where the number of clusters and their sizes varied throughout the downer.

Shu et al. (2014) mentioned that there are a significant number of CFD studies in CFB downer reactor units. However, it is well-known that some parameters have an important impact on the results of CFD simulations of gas-solid flow as: a) drag correlations, b)

wall boundary condition, and c) parameters describing particle–particle collisions (restitution coefficient). These authors pointed out that it has long been recognized that proper determination of interphase drag forces is crucial for a successful simulation of a heterogeneous gas–solid flow. In particular, the restitution coefficient using the kinetic theory has a significant effect on the predicted hydrodynamics. Furthermore, these authors also mentioned that extensive numerical simulations have consistently shown that the hydrodynamics of gas–solid flow are sensitive to wall boundary conditions. In this respect, CFD in downers is a very active area of interest that continues attracting many researchers.

2.7 Measurements of Solids Concentration in a Downer

Several techniques have been reported in the technical literature in the last 30 years, to measure the solid concentration in gas–solid two–phase flows. These techniques can be classified as direct and indirect methods as well as, invasive and non–invasive (Yan, 1996). The most important advantage of non–invasive techniques is that the flow stream is maintained undisturbed by the sensor itself. However, one important limitation, is that they are usually restricted to monitoring overall properties such as solid concentration (Herbert et al., 1998).

Zheng and Liu (2010) pointed out that a significant number of studies in pneumatic conveying have concentrated in non–invasive and indirect measurements, acquiring solid concentration and velocity simultaneously. Nevertheless, these results for the industrial scale operations are still unsuitable. These authors reviewed the main limitations of non–invasive and indirect measurements with these being: spatial filtering, averaging, resolution, sensitivity, and tomography sensor structure. A detailed review of these issues can be found in Zheng and Liu (2010) and Yan (1996).

A common challenging task in all these methods, is to find an appropriate calibration which can provide data validation and confirmation of data reproducibility. Herbert et al. (1998) and Matsuno et al. (1983) proposed a similar calibration procedure. It suggests that although the methods are intrusive, the local characteristics of the gas–solid flow stream do not change significantly as a consequence of the disturbance caused by the

measuring equipment. However, [Herbert et al. \(1998\)](#) also mentioned, that it is likely that electrostatic charging of the fine catalyst particles may cause the particles to stick to the probe interfering with light transmission.

Given the valuable prospects for downer units, a better understanding of their fluid dynamics is of critical importance. In order to accomplish this, it is necessary to accurately measure gas–solid flow properties, such as particle velocity, particle cluster size and particle hold–up at the local level ([Tuzla et al., 1998](#)). With this goal in mind, one can find in the technical literature, measurements of particle properties using both non–intrusive and intrusive techniques. Among the non–intrusive techniques, one can cite: a) particle image velocimetry ([N. Dang et al., 2014](#); [T. Dang et al., 2014](#)), b) digital image analysis ([Pantzali et al., 2013](#)), c) laser doppler anemometry ([Pantzali et al., 2013](#)), d) electrical capacitance volume tomography ([Weber et al., 2013](#)), e) gamma–ray tomography ([Zhang et al., 2012](#)), f) automated radioactive particle tracking ([Zhang et al., 2012](#)), and g) ultrafast X–ray computed tomography ([Bieberle et al., 2012](#)). However, even though these techniques are not intrusive, calibrations are rather difficult. These techniques are also expensive, not easy to implement, require complex data analysis, and extensive computations ([Zhu et al., 2001](#)).

On the other hand, among the intrusive techniques, one can find: a) a fibre high speed photography method ([Qian et al., 2013](#)), b) optical fibre probes ([Li et al., 2013](#)), c) a dual–optical fibre density probe ([Zhang et al., 2003](#)), d) a Laser Doppler Velocimeter (LDV) system ([Zhang et al., 2003](#)), e) a capacitance probe ([Collin et al., 2009](#)). While the intrusive nature of these measurement techniques could interfere with the flow pattern in the reactor ([Werther, 1999](#)), these effects could, in practice, be minimized via adequate sensor designs.

In 1998, [de Lasa et al. \(1998\)](#) patented an optical fibre sensor. This sensor is a relatively simple and economical device. It has the potential of being able to measure local parameters, as required by the fluid dynamic characterization in gas–solid downer units. This sensor designated as the CREC–GS–Optiprobe uses a Graded Refractive Index (GRIN) lens. This GRIN lens creates a highly irradiated region at a few millimeters in

front of the probe tip. As a result, particles reflect laser rays while moving through the highly irradiated region. These rays are captured by strategically located receiver optical fibres and are then, converted to corresponding electrical signals. As a result, the CREC–GS–Optiprobe minimizes probe intrusion allowing for detailed resolution of particle phenomena.

2.8 Heat Transfer in Downer Reactors

Circulating Fluidized Bed (CFB) Downer Technology is being widely considered, especially for various gas–solid reactions such as catalytic cracking, combustion or other reactions. Some of them commonly require heat transfer during the reactions. A clear understanding of heat transfer behaviors in CFB downers will help to control the bed temperature and the energy exchange during the reaction. This is necessary for the proper design of CFB downer reactors. Two of the first studies of heat transfer in a downer reactor date back to 1999. At this time, [Yong et al. \(1999\)](#), and [Ma and Zhu \(1999\)](#) reported axial and radial distribution of heat transfer coefficients between the suspended surface and the gas–particle flow suspension at different operating conditions.

Heat transfer between gas–solid flow and heat transfer surfaces in a CFB downer comprises mainly of three components: 1) particle convection, 2) gas convection, and 3) radiation. At low temperatures, the radiation component can be neglected. Normally, particle convection is the primary heat transfer mechanism, given the large heat capacity of the solids, as compared to that of the gas. Gas convection may become important when the gas velocity is high and the solids hold–up is low.

[Ma and Zhu \(1999\)](#) pointed out that the heat transfer behavior in the downer is expected to be different from that in the riser. However, some of the influencing factors for the heat transfer may be the same in both the downer and the riser. These authors suggested that the heat transfer process in downers may be controlled by the hydrodynamics of the gas and solid mixture, in the vicinity of the heat transfer surfaces as it is in risers. [Ma and Zhu \(1999\)](#) found that the average heat transfer coefficient decreases along the downer. More specifically, they reported that the axial solids hold–up and heat transfer variations follow a three section pattern. They showed that, in the first acceleration section, both

profiles of heat transfer and solid hold-ups decrease sharply. After that, the trend becomes smooth further down the column. For the constant velocity section, the heat transfer coefficient and solids hold-ups becomes almost constant. They claimed that the solids concentration is the dominant factor of the heat transfer. This is the case as a high solids circulating rate or low gas velocity can result in higher solids concentration and thus, higher heat transfer rates. Thus, the decrease of the heat transfer coefficient along the downer was explained given the average measured solids hold-ups from the top to the bottom of the reactor. They also suggested that the heat transfer can also be significantly affected by the gas velocity. On the other hand, these researchers also found that local heat transfer rate also changes with the radial position; showing that the radial changes were in line with the radial distribution of solids hold-ups. In this respect, it was found that approaching the wall region ($r/R=0.85-0.9$), the heat transfer coefficients decreased sharply along the axial direction in the first section. This variation became less significant in the second section and finally became negligible in the third section.

Recently, studies on heat transfer coefficient in downers have been in agreement with previous studies found in the literature. [Yongpan et al. \(2013\)](#) performed numerical simulations and experiments on heat transfer around a probe in the downer reactor for coal gasification. Experimental results revealed that the average heat transfer coefficient decreased with increasing superficial air velocity or decreasing solid mass flux. Furthermore, heat transfer performance near the entrance of the downer was better than that in the developed region. The numerical simulation results showed similar variations in heat transfer coefficients over a broader range of superficial air velocity and solid mass flux. The numerical simulations further revealed that heat transfer coefficients decreased with increasing sand particle size. The authors found the variation of heat transfer coefficients to be directly related to the variation of solid hold-ups, as particle-particle convection was still dominant under the studied cases.

A novel experimental technique to determine the heat transfer coefficient between the bed and particles in a downer was presented by [Yoshie et al. \(2013\)](#). They claimed that the experimental technique of their study was applicable to the measurement of the particle temperature in a binary-solid downflow. The results showed that there is a strong

correlation between the particle-to-bed heat transfer coefficients and the normalized collision frequency under the laminar gas flow conditions.

2.9 Some Industrial Application of Downer Reactor Units

Due to the plug-flow reactor performance, downer reactor units are recognized as being ideal reactors for chemical processes. These have fast reaction systems with intermediates as desired products, such as high temperature catalytic reaction systems, pyrolysis of coal and biomass, plasma reactor, etc (Chuachuensuk et al., 2013; Koratiya et al., 2010; Wu et al., 2009; Maadhah et al., 2008; Shaikh et al., 2008; Fujiyama et al., 2005; Deng et al., 2002; Talman et al., 1999).

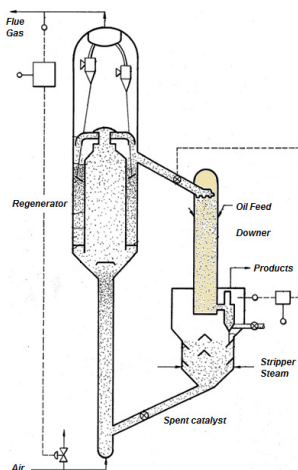
2.9.1 Application of Downers in Fluid Catalytic Cracking (FCC)

The implementation of a downer reactor unit in the fluid catalytic cracking (FCC) process for cracking of petroleum feeds in the presence of a catalyst is claimed to be beneficial. Figure 2-8 and Figure 2-9 show relevant downer design configuration for the FCC process available in the literature.

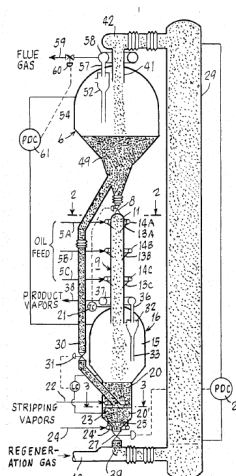
One of the first patents describing the downer reactor configuration was considered to improve the FCC process and dates back to 1983 (Gross and Ramaje, 1983), see Figure 2-8(a). These authors reported that the proposed downflow system ensures uniform distribution of the catalyst throughout the feed, decreases contact time of the catalyst with the feed and reduces the amount of coke made in the process. A comparative graph of gasoline and coke make of the co-current upflow (CCU) riser and co-current downflow (CCD) downer configurations at 600 °F oil preheat temperature is shown in Figure 2-10. These experimental data show a high gasoline selectivity with coke reduction using the in the CCD operation.

Figure 2-8(b) reports another patent, describing a novel catalyst cracking method using both spent catalyst and regenerated catalyst streams. In this patent, Niccum and Bunn (1985) claimed, that the hot freshly regenerated catalyst is contacted with hydrocarbon feedstock in a gravity flow catalytic downer reactor. The spent catalyst from the reactor is

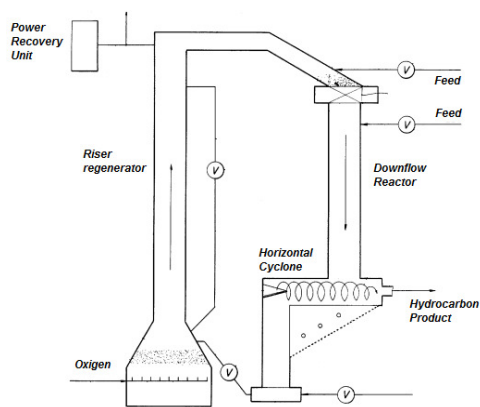
separated from reactants in a ballistic separator and is completely regenerated in a riser regenerator.



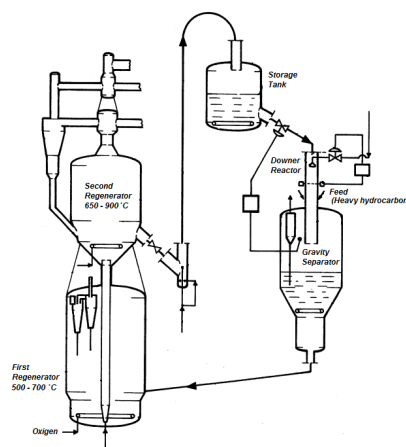
(a) Gross and Ramaje (1983)



(b) Niccum and Bunn (1985)



(c) Dewitz (1989)

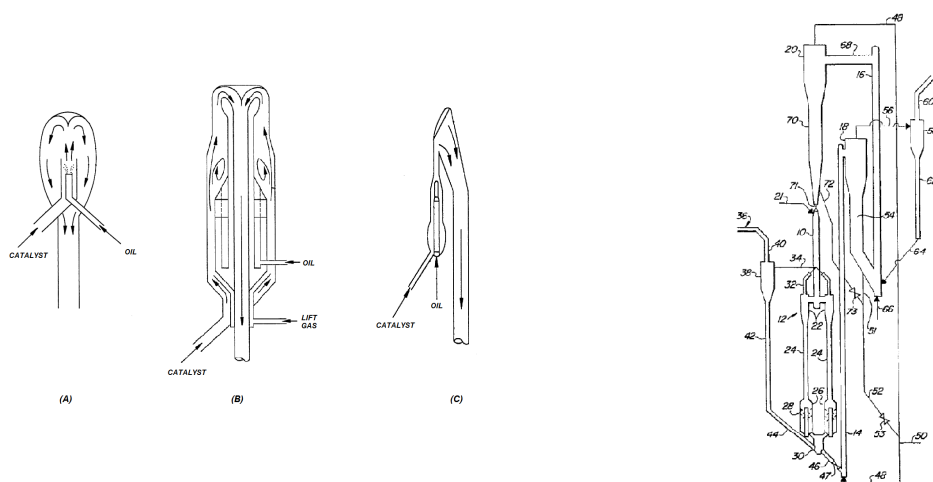


(d) Pontier et al. (1994)

Figure 2–8: Configurations of downer reactors, United States patents in the literature, part 1/2.

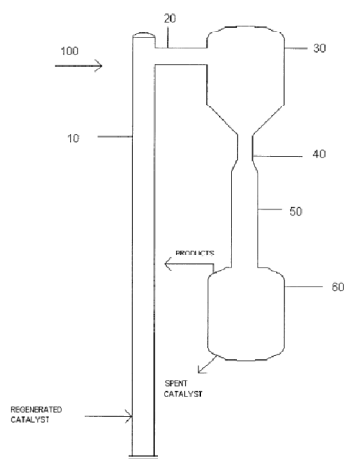
Dewitz (1989) also patented a quick catalyst separation design at the bottom of the downer, see Figure 2–8(c). This author reports an horizontal cyclone separator, to permit the conversion of hydrocarbon material to hydrocarbon products of lower molecular weight in a near zero pressure drop environment.

Pontier et al. (1994) patented an apparatus for a catalytic cracking process, making it possible to treat heavy hydrocarbon oils as described in Figure 2–8(d). This unit includes two regeneration zones and a downflow cracking reactor (dropper). The catalyst is supplied to the downer from a dense bed storage enclosure connected to a rising column coming from the dense bed of the second regenerator. The invention aims to consider simultaneously, the absence of retro mixing, radial homogeneity, and a piston-type flow to obtain optimum conditions.

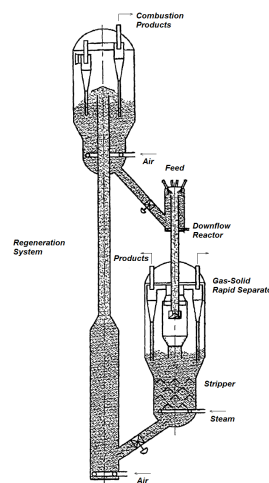


(a) Muldowney (1995)

(b) Zinke and Koves (1996)



(c) de Rezende et al. (2006)



(d) Xu et al. (2006)

Figure 2–9: Configurations of downer reactors, United States patents in the literature, part 2/2.

Muldowney (1995) invented a process and apparatus for short contact time fluidized catalytic cracking of heavy oil feed using a reactor with an upflow cat/oil vaporizer and a downflow reactor. Catalyst slip permitted efficient mixing and limited conversion in the upflow section, while cracking was completed in the downflow reactor with minimal segregation of the catalyst. Total vapour residence times considered were smaller than 5 seconds. Figure 2–9(a) shows this configuration with three FCC reactors as follows: a) an FCC reactor with an upflow internal mixing section connected by a smooth conduit to a downflow cracking section; b) an FCC reactor with an upflow external mixing section connected by a smooth conduit to a downflow cracking section; and c) an FCC reactor with an upflow mixing section, connected to a chamber with a solids impingement surface, which is in turn connected to a down flow cracking section.

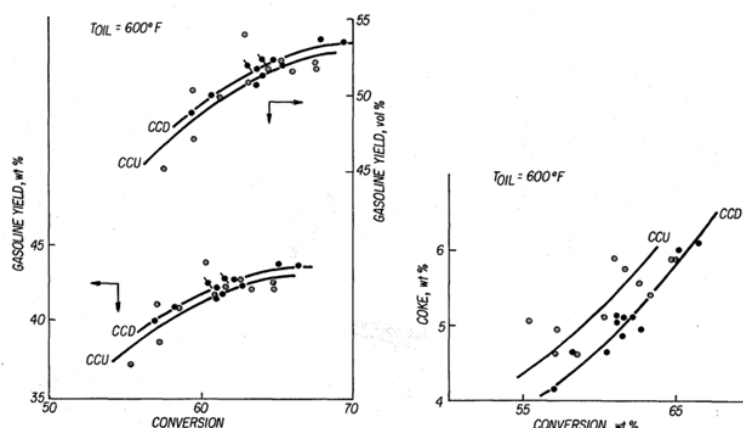


Figure 2–10: Comparison between Co-Current Upflow (CCU) and Co-Current Downflow (CCDF) in gasoline and coke production.

Zinke and Koves (1996) patented an FCC arrangement that uses a two stages upflow conduit combustion and a regenerator cyclone separator to supply catalyst particles from a dip leg, directly into a downflow reaction conduit. The downflow reactor unit provides a stage with quick catalyst and gas product separation at the outlet of the unit, refer to Figure 2–9(b).

de Rezende et al. (2006) designed a downer reactor with feed injectors (nozzles) located in the upper section of the unit. Nozzles atomize the feed so that feed vaporization and

catalyst feed could be optimized. After the cracking reaction in the downflow reactor was completed, reaction products were separated and the spent catalyst was directed to the stripping and regeneration sections as described in Figure 2–9(c).

[Xu et al. \(2006\)](#) patented a downflow catalytic cracking reactor with high oil/catalyst contact efficiency and good reaction performance, refer to Figure 2–9(d). It is claimed that by locating feed nozzles on the reactor top and/or side walls (top section), the feed nozzle jets yield favorable conditions for the vacuum gas oil atomization. This makes the feeding of this downflow reactor adequately atomized to enhance oil/catalyst contact efficiency, and heavy oil cracking. As a result, the yield of products with high added values such as light oil and LPG is increased.

In addition to the FCC patent designs of gas–solid flow in downers, there are several experimental studies that provide important support to downers applications in FCC processes. [Talman et al. \(1999\)](#) developed a downer reactor for the particular case of fluid catalytic cracking. Cracking of cumene (isopropylbenzene), an aromatic organic compound with an aliphatic substituent chain was chosen as the model compound for a test series. At very short contact times in the range of 60–400 ms, conversions up to 70% were obtained.

[Abul–Hamayel \(2004\)](#) summarized their research work comparing downer and riser based FCC processes at high severity conditions in pilot plant experiments. Supported by the pilot plant study and comparing it with the riser, they reported that the downer FCC reduces backmixing, a main cause of gasoline overcracking. These authors also suggested that reduction of backmixing diminishes coke and dry gas formation, resulting in increased yield of gasoline. Typical yields of conventional FCC and the two cases of HSFCC operating modes are listed in Table 2–1.

One can also notice that depending on the operating mode, the HS–FCC can: a) double the amount of light olefins, and b) increase propylene production 2.1–3.6 times. This is achieved at the expense of reducing the olefins content by 50–85wt%. Furthermore,

HS-FCC (case 2) can provide three times more light olefins accompanied with a minimum loss in gasoline.

Table 2–1: Yields of conventional FCC and HS-FCC (Abul-Hamayel, 2004).

Parameter	Conventional FCC	HS-FCC	
		Case 1	Case 2
Reaction temperature (°C)	500	550	600
Conversion (wt%)	75	87	90
Product yield (wt%)			
Ethylene	0.3	0.9	2.3
Propylene	4.2	9.3	15.9
Butylene	5.6	12.2	17.4
Gasoline	53.6	49.5	37.8
Light cycle oil (LCO)	17.6	8.8	6.6
Heavy cycle oil (HCO)	7.7	4.0	3.3
Properties of gasoline (vol%)			
Olefins	13.5	9.6	5.1
Aromatics	28.0	37.0	37.0

Figure 2–11 summarizes the comparative results of downer and riser based FCC processes at high-severity operation in pilot-plant experiments (Abul-Hamayel, 2004). It is observed that at the same conversion, the downer unit requires a smaller catalyst-to-oil ratio, while allowing one to obtain a higher yield of gasoline and lower yields of C₂–C₄ olefins, coke, dry gas and 1,3 Butadiene, refer to Figure 2–11(a–f). Total yields of useful products such as combined gasoline and light olefins are always higher in downers than in risers, see Figure 2–11(g).

An interesting comparison is reported in Figure 2–11(h). At constant yields of total light olefins, the downer can produce more gasoline. On the other hand, at a constant gasoline yield, the downer can produce more light olefins. It is our belief, that these results are persuasive enough to consider larger-scale applications of downers for the FCC process.

One of the first industrial demonstrations of downer reactors in a refinery process can be found in the Jinan Refinery as shown in Figure 2–12. A circulating fluidized bed was built, in which the riser reactor was 0.5 m in diameter and 40 m in height, while the downer was 0.6 m in diameter and 15 m in height. The capacity of this unit was 150,000 ton/year.

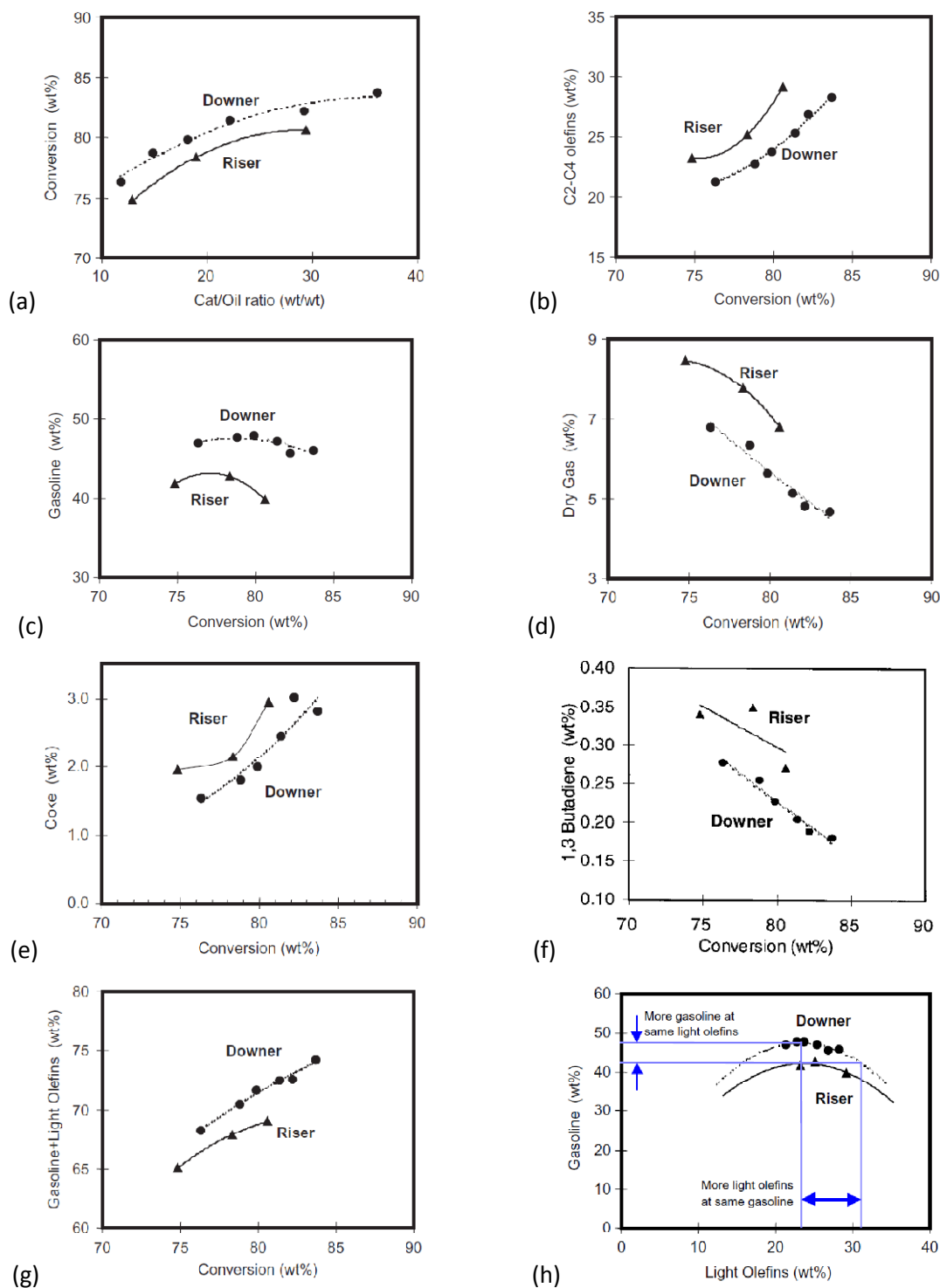


Figure 2–11: Comparison of downer and riser based on High–Severity FCC Process (Abul–Hamayel, 2004).

Different from a single downer design, this demonstration unit adopted an patented configuration (Jin et al., 2014). The basic idea was to utilize the advantages of both the riser and the downer. Two series of experiments were developed in this demonstration unit. The first one used Vacuum Gas Oil (VGO) for high severity catalytic cracking. If one compares the feedstock conversion in the riser, with the feedstock conversion in the downer, one can notice that: a) the dry gas is reduced by 2.27 wt.%, b) the yield of gasoline is increased by 1.06 wt.%, c) the yield of diesel oil is increased by 8.38 wt.%, and d) the yield of propylene is augmented 0.75 wt.%. In summary, the results obtained point towards a downer providing a cleaner gasoline with a 30.7% olefin content in gasoline. This is much less than in the riser using the same feed and catalyst.



Figure 2–12: Industrial demonstration of a downer reactor (Jinan Refinery, SINOPEC).

Thus, given the reported results, it appears that downer reactors in the FCC process provide confidence to move to full scale FCC refinery application.

2.9.2 Application of Downers in Pyrolysis of Biomass and Coal

Biomass has gained much attention as an alternative to fossil fuels in the recent decades, due to its renewability and CO₂ neutrality.

Pyrolysis is attractive in the utilization of biomass given the following: a) raw biomass is difficult and costly to manage, owing to its low energy density; b) bio-oil, gas, and solid char derived from biomass via pyrolysis, are easier to handle, transport and store compared to raw biomass, c) proportions of biomass products can be changed substantially by altering the heating rate, residence time, and temperature to meet market needs; 3) liquid products from biomass pyrolysis contain useful chemicals and can be upgraded to produce transportation fuel (Ding et al., 2012).

Berg et al. (1989) proposed an ultra-rapid fluidized reactor that can be considered for biomass pyrolysis. This unit consists of a mixer, a downer and a gas-solid separator. The mixer unit promotes rapid uniform mixing between a fine particulate heat carrier and a particulate feedstock. This is done in order to achieve high heat transfer rates necessary for fast pyrolysis. These authors reported that the biomass was generally well mixed in the central core of the reactor. Away from the central core, there were increasing three-dimensional flow effects and, in addition, the mixing quality deteriorated. However, and in the smaller time scale of 20–35 ms, the mixing was also quite good and approached that of a random mixture.

Ding et al. (2012) examined the effects of acid washing treatment on the pyrolysis product distribution and product properties in a bench-scale circulating fluidized-bed using wheat straw as a feedstock. Special emphasis was placed on describing the composition, yield, and distribution of pyrolysis products.

Kim et al. (2001) developed a new type of coal gasifier using a downer reactor unit. The heat was supplied from coal combustion in a riser reactor. The circulation of solids within the reactor loop provided energy transfer from the combustion zone (riser) to the gasification zone (downer, gas separator and loop-seal). Experiments were carried out in a 0.1 m internal diameter and 5.0 m high downer. The reaction temperature was in the

750–850 °C range. Results showed that by changing the reactant gas supplied (air or steam) to the loop–seal for solids circulation, both product gas yield and carbon conversion increased. However, the product gas calorific value diminished with reaction temperature.

In the last two decades, extensive work has been conducted to understand biomass pyrolysis (Yongpan et al., 2014, 2013; Dong et al., 2012; Cheng et al., 2008). It is anticipated that a downer reactor with the highest severity operation, would be suitable for coal pyrolysis in thermal plasma processes for acetylene production. This process opens up a new and direct means for producing acetylene. The production of acetylene may occur together with valuable carbon materials in the solid state and with ethylene, methane, hydrogen and carbon monoxide as secondary products (Cheng et al., 2008).

One should also mention that downer reactors are found in processes such as: a) the production of polymeric materials with superior physical properties (Mei et al., 2006); b) the partial oxidation of n–butane to maleic anhydride (MAN) (Vaishali et al., 2010); c) ozone decomposition (Li et al., 2011); and d) carbon dioxide capture (Kongkitisupchai and Gidaspow, 2013).

2.10 Conclusions

- a) A concurrent downward flow circulating fluidized bed, or a downer, has attracted the attention of many researchers given its significant advantages, when compared to other gas–solid systems. Some of these advantages are: a) a relatively homogenous dilute flow structure, b) nearly plug–flow of gas and solid phases, c) low solid hold–ups, d) short residence times and e) a relatively large loading ratio. These advantages are mainly due to the fact that the downward flow is in the same direction as gravity.
- b) Three acceleration zones have been identified in downers. The first acceleration section extends from the entrance of the downer to the axial position where the particle velocity is equal to the gas velocity. The second acceleration zone is located where particles continue to accelerate, under the simultaneous influence of gravity

- and drag forces, with gas velocity becoming lower than particle velocity. The third section occurs where a constant velocity for both particle and gas is reached.
- c) There is some still controversy regarding the hydrodynamics of downer reactors in the radial direction. Some researchers claim that it is mainly uniform, while others argue that there is an annulus with a higher solid concentration in the near wall region.
 - d) Due to the short contact times which are characteristic of downers, it is desirable that the inlet distributor of downers, provide a uniform distribution of phases with quick acceleration of solids, and excellent control of gas–solids mixing. Particle–gas separators located at the downer exit, also need to be especially designed to obtain a fast separation of the particles and products, preventing further reactions and undesired product formation.
 - e) Cluster formation in downers has been reported by experimental and simulation studies. It is reported that particles can aggregate, forming transient structures. These structures can be grouped into two types: a) a dilute phase (more dispersed) and b) a cluster phase (more dense). It is known that the particle clusters limits good multiphase mixing inside the system. Particle agglomeration can have a negative impact on catalytic reactions. Therefore, the study of transient flow structures in downers is valuable to elucidate the mechanisms that control flow behavior in downer units and help considerably with their design, scale–up and overall control.
 - f) There are two schemes adopted for downer modeling and simulation: a) Eulerian–Eulerian or b) Eulerian–Lagrangian. In the Eulerian–Eulerian Method, both phases are treated as continuous, while in the Eulerian–Lagrangian Method, the solid phase is treated with a discrete element method. It is well–acknowledged that input parameters have an important impact on CFD simulation of gas–solid flows. In this respect, drag correlations, wall boundary conditions, and particle–particle collision parameters (restitution coefficient) have to be carefully defined.
 - g) Due to their favorable hydrodynamics, such as relatively homogenous dilute flow structure, nearly plug–flow for gas and solid phases, low solid hold–ups, short residence times and relatively large loading ratios, downer reactor units are considered ideal reactors for catalytic and non–catalytic reactions. An example of this

is fast reaction systems with intermediates as desired products. On this basis, downer reactors are considered as potential units of choice for high temperature catalytic reaction systems, pyrolysis of coal and biomass and plasma reactors.

Chapter 3

3 Scope of the Research

This PhD dissertation seeks to gain understanding on the fluid dynamics of gas–solid concurrent downflow units. More specifically, the purpose of this research is to study the behavior of FCC particles, flowing downwards along with air in a downer reactor. The goal is to achieve this, by means of experimental measurements and computer–based modeling of the particle cluster properties. The novelty of the proposed work lies in the determination of "individual" particle cluster information. The expected outcome of this work is a comprehensive characterization of the gas–solid down fluid flow, allowing the estimation of individual cluster properties such as: a) cluster solid concentrations, b) individual cluster slip velocities, c) individual cluster sizes, and d) cluster size distributions. Another important aspect of the study is to develop a mechanistic based method to calculate cluster drag coefficients. The experimental results will be compared with a computer based simulation analysis using Computational Particle Fluid Dynamics.

3.1 Overall Objectives

a) The measurement and estimation of individual cluster properties such as cluster slip velocities, cluster sizes and cluster holdups, using the CREC–GS–Optiprobe.

It was anticipated that the narrow focal region with high irradiation of the CREC–GS–Optiprobe would allow one to measure, in a downer, along the radius, the individual cluster properties, such as the cluster solid concentrations, the individual cluster slip velocities, the individual cluster sizes and the cluster size distributions. This information should provide valuable insights to describe downer gas–solid hydrodynamics.

b) The establishment of a methodology for the CREC–GS–Optiprobe signal analysis.

The CREC–GS–Optiprobe work in conjunction with an optic electronic data acquisition system. In this system, light changes are converted into digitalized voltage variations. It

was envisioned that a rigorous methodology to analyze the CREC–GS–Optiprobes time–signals, is needed in order to provide precise individual particle cluster dimensioning.

c) The modeling validation using experimental information of gas–solid concurrent evolution in downer reactor units.

Given the status of the development of downer models and the potential interest in scaling them up, one can acknowledge the significance of validation of numerical modeling using experimental data. In this respect, it was planned to perform a gas–solid downflow numerical simulation using the Computational Particle Fluid Dynamics Numerical Scheme (CPFD).

3.2 Accomplishment of Research Objectives

The accomplishments of the research objectives of the present PhD dissertation are reflected in four manuscripts published or to be published in reputable chemical engineering journals as follows:

a) Manuscript 1, entitled "*Particle Clusters and Drag Coefficients in Gas–Solid Downer Units*". This article was published in ***Chemical Engineering Journal***, volumes 200–202, pages 439–451, in June 2012. It considers, as reported in Chapter 5 and 6 of this thesis, “individual” particle cluster information obtained using a Chemical Reactor Engineering Centre Gas–Solid Optical Probe (CREC–GS–Optiprobe).

b) Manuscript 2, entitled "*Particle Cluster Size Distribution in Gas–Solid Downer Units*". This article was published in ***The 14th International Conference on Fluidization – From Fundamentals to Products***, Eds, ECI Symposium Series, volume (2013), in May 2013. http://dc.engconfintl.org/fluidization_xiv/33. It considers, as reported in Chapter 6 of this thesis, individual particle cluster size distributions in gas–solid downflow reactors.

c) Manuscript 3, entitled "*Gas–Solid Fluid Dynamics in a Downflow Reactor: A CPFD Based Model*". This manuscript is still under review. It considers, as reported in Chapter

7 of this thesis, the fluid dynamics in the developed flow region of a concurrent gas–solid downflow fluidized bed unit. Gas–solid flows were simulated using a Computational Particle Fluid Dynamics (CPFD) Numerical Scheme.

d) Manuscript 4, entitled "*Cluster Fluid Dynamics in Gas–Solid Downflow Reactors: Experiments and CPFD Simulations*". This article is still under review. It considers, as reported in Chapter 8 of this thesis, the fluid dynamics in the developed flow region of a 2 inch concurrent gas–solid downflow fluidized bed unit. Gas–solid flows were simulated using a Computational Particle Fluid Dynamics (CPFD) Numerical Scheme. Experimental and simulation results are compared.

Chapter 4

4 Experimental Equipments and FCC Catalyst

This chapter describes the experimental apparatus employed in this PhD research project. Two downer units (one and two inch internal diameters) were used to study the hydrodynamics in gas–solids concurrent downflow reactors. In both cases, the CREC–GS–Optiprobes were implemented to capture the gas–solid fluid dynamics. The details and focal region of the CREC–GS–Optiprobes, are reported in this section, along with a description of the two experimental downer units. A brief description of the FCC catalyst used is also presented. More details regarding to the FCC catalyst used, can be found in Appendix A.

4.1 Chemical Reactor Engineering Centre Gas–Solid Optical Probe (CREC–GS–Optiprobe)

The Chemical Reactor Engineering Gas–Solid Optical Probe (CREC–GS–Optiprobe) was used in the present study, to characterize the gas–solid flow in downer reactors. This fiber optic sensor for sensing particle movement, was designed and patented by [de Lasa et al. \(1998\)](#) at Chemical Reactor Engineering Centre, University of Western Ontario (CREC–UWO). It belongs to the class of fiber optics reflective sensors. An infrared laser beam of 830 nm wavelength from a diode laser was focused on an optical fiber. The constant intensity light beam was collected and transmitted by the optical fiber to its other end. This probe provides a well–defined region of high light intensity. This design minimizes probe intrusion, allowing for detailed resolution of the particle phenomena occurring in the suspension.

To maximize the CREC–GS–Optiprobe performance, an improvement was presented by [Nova et al. \(2004a\)](#), incorporating a GRIN lens. This GRIN lens optimizes the optical characteristics of both the emitter and receiver optical fibers. With the help of a GRIN lens, the emerging light from the back end of the optical fiber is concentrated into a small high intensity irradiated region. The added advantage of the GRIN lens is that it gathers

the light rays into a sensing region far away from the tip of the probe. Here, the probe's intrusion effect on the flowing phases is minimized. Inside this high intensity light region, the light is reflected by moving particles. The reflected light is then collected, and guided from the modulation zone to a semiconductor photodetector with a receiver optical fiber.

In this respect, the use of a GRIN lens in conjunction with optical fiber probes, provide the optical sensor with the capability of changing the depths of the measuring region. This is according to the solid particle concentration in the suspension, focusing the entire incident light into a narrow point, far from the tip of the probe. The advantages of the CREC–GS–Optiprobe, over other reflective sensors, can be summarized as follows: a) the geometric configuration optimizes the optical characteristics of both the emitter and receiver optical fibers, and b) the GRIN lens incorporated into the probe, creates a focal point far from the tip of the sensor. This minimizes flow disturbances in the measurements, resulting from bouncing particles and the boundary layer formed in the front face of the probe.

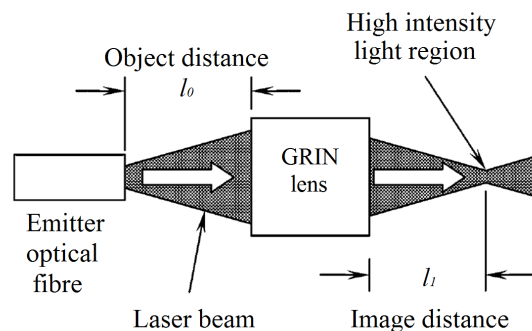


Figure 4-1: Schematics of the emitter side of a CREC–GS–Optiprobe showing the region of high light intensity (Nova et al., 2004a).

As reported by Nova et al. (2004a), the design and operating principles of the CREC–GS–Optiprobe are rather simple, with its main components and features being as follows:

a) An emitter fiber followed by a GRIN lens (Figure 4-1); The emitter fiber is spaced at an optimal object distance (l_o) from the GRIN lens, suitable for producing a sensing region at a desired image distance (l_i) where the beam energy is concentrated. The image

distance can be adjusted, by selecting the adequate object distance. In this way, the sensing region is set sufficiently far from the tip of the sensor.

(b) A receiver fiber positioned adjacent to the GRIN lens, with the adequate numerical aperture, to receive mostly light rays reflected by particles, crossing the sensing region (Figure 4-2). In this manner, light rays reflected by other particles, outside this focal point, are ignored.

(c) A d spacing between the GRIN lens and the receiver optical fiber core (Figure 4-2). The distance d defines the probe visible domain.

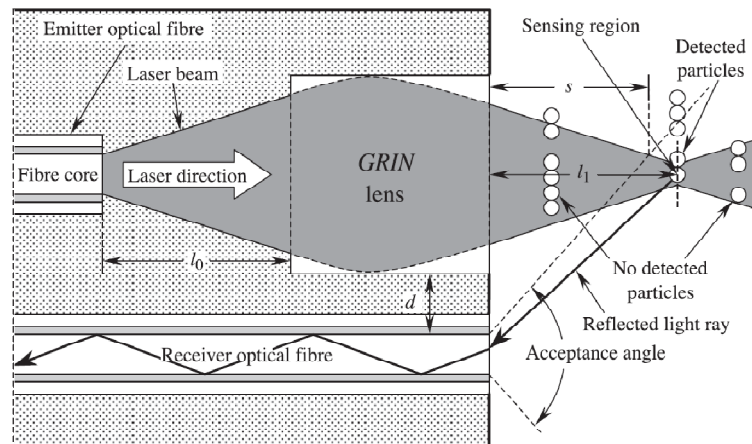


Figure 4-2: Operating principle of the CREC-GS-Optiprobes (Nova et al., 2004b).

Regarding the optoelectronic system, the connections of the optical fibers and the various electronic components used, are described in Figure 4-3. The laser power supply unit provides a voltage between 4.5 and 5.5 V dc to operate the two laser diode assemblies. The laser diode assemblies, used in the present study, emit an infrared laser beam with a wavelength of 830 nm and a power of 20 mW. The upstream signal is obtained as follows: First, a laser beam from one of the laser diode assemblies illuminates one end of an optical fiber. Then, the laser beam is conducted through the fiber and emitted at the other end of CREC-GS-Optiprobe. At this point, the beam strikes a GRIN lens mounted inside the probe head.

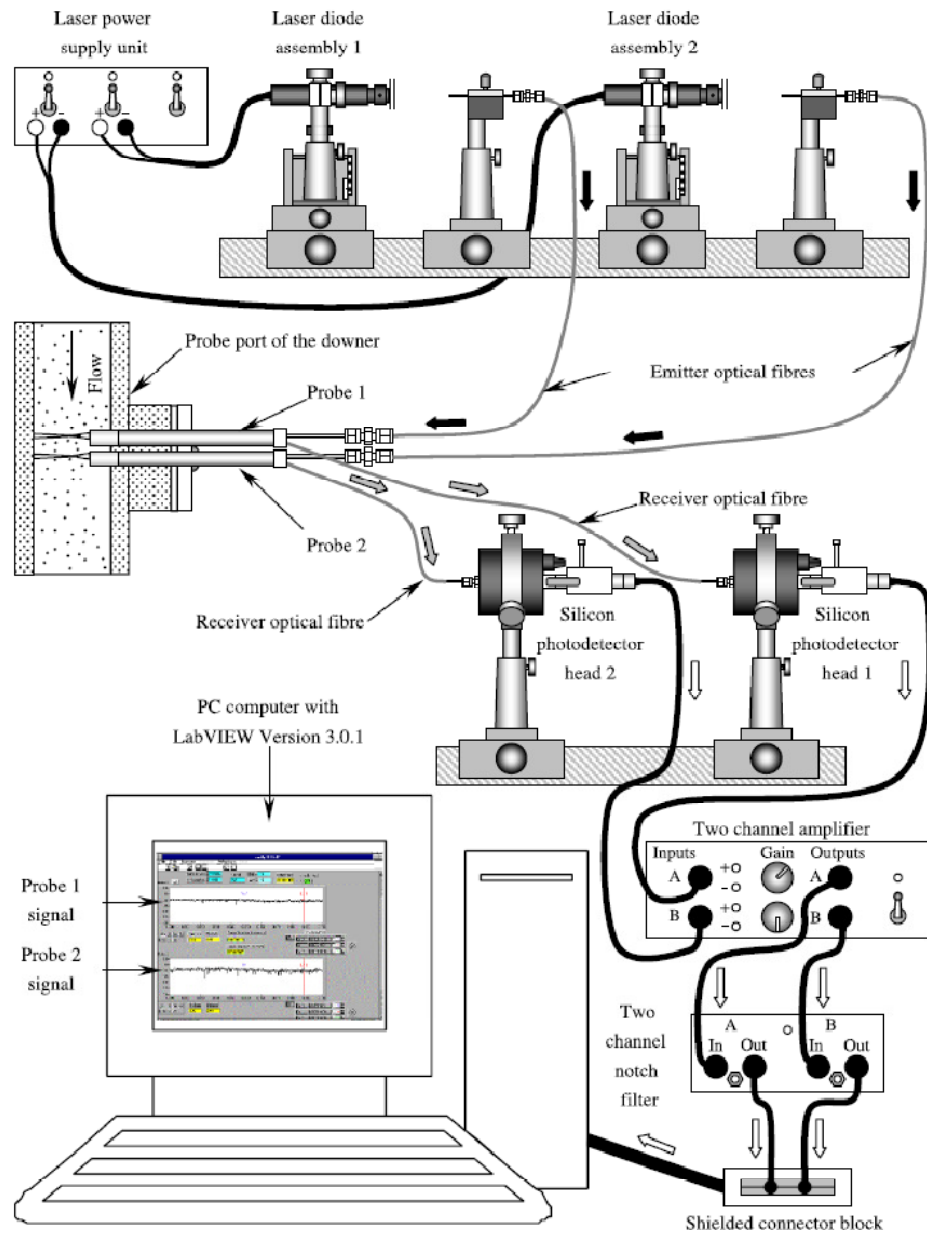


Figure 4-3: Fiber-optic configuration system for cross-correlation analysis (Nova et al., 2004b).

As mentioned previously, the laser beam emerging from the GRIN lens is focused into a point, far from the tip of the probe within the gas-solid flow. Only the particles crossing through this detection region, reflect enough light to be collected by the receiver optical fiber. The collected light is then transmitted through the receiver fiber and sent to a

silicon photodetector, where the optical signal is converted into an electrical signal. The downstream signal is obtained in the same way.

Next, both the upstream and downstream signals are sent to a two channel voltage amplifier and a two channel notch filter for signal conditioning. The electrical signals require amplification because the signals coming from the photodetectors are too weak for signal processing and analysis. The notch filter eliminates periodic interferences modulating the flow, from the compressed-air system. Once the signal conditioning is completed, the signals are sent to a PC computer via a shielded I/O connector block, to be processed and analyzed with the LabVIEW software package. The measurement of particle velocities is achieved, by obtaining the cross-correlation function, of a pair of time series signals from two sensors spaced axially along the flow stream.

The CREC-GS-Optiprobes in a gas-solid fluidized bed, measure the particle/cluster velocities as well as cluster sizes. In the context of cluster size measurement, the characterization of a high irradiance focal region size is crucial. It is important to mention that given the miniature size of the probe, with component dimensions in the range of a few millimeters, machining of the probe with deviations smaller than 20% is challenging to achieve. In order to obtain more accurate measurements and better probe performance, it is a good practice to measure precisely the probe effective focal region location, l_1 .

[Islam et al. \(2011\)](#) proposed that the CREC-GS-Optiprobes image distance (l_1) as described in Figure 4-2, can be determined by direct measurement using a Charge Coupled Device (CCD) Camera Beam Profiler. A beam profiler is a diagnostic device which can measure the whole optical intensity profile of a laser beam, i.e., not only the beam radius but also the detailed shape and intensity distribution (refer to Appendix B for more details regarding the CCD-Camera Beam Profiler). These researchers used a CCD-Camera Beam Profiler to study the CREC-GS-Optiprobe sensing region. The Camera Beam Profiler was placed on the propagation path of a laser beam at 2.0, 3.5, 5.2, 7.5 and 12.5 mm away from the GRIN lens face. The authors analyzed the color code shown between 2D and 3D images. It was observed that high intensity laser beams converged into a narrow region at around a 5.2 mm separation from the GRIN lens back

face. This direct visualization of the high intensity irradiated spot is in agreement with the location calculated for the image or sensing region (5.2 mm) by geometrical optics. The reader is referred to [Islam et al. \(2011\)](#) for a more detailed explanation of the geometrical estimation of the image distance (l_1).

A similar procedure was followed in the present study, to determine the CREC–GS–Optiprobes image distance (l_1). a CCD–Camera Beam Profiler was used to study the CREC–GS–Optiprobe sensing region. However, this time, instead of studying color code changes, a Graphical User Interface (GUI) was implemented for the CCD–Camera Based Beam Profiler. Signal analysis using this device is shown in Appendix C. This method allows individual views of the X and Y beam cross sections, 2D projections, and 3D profiles in gray scale or color mode as well as the numerical parameters in separate windows. Details like peak and centroid position, Gaussian approximations of the X and Y profiles, and elliptical fits of the beam’s cross section can be superimposed, faded out, or displayed in many different variations.

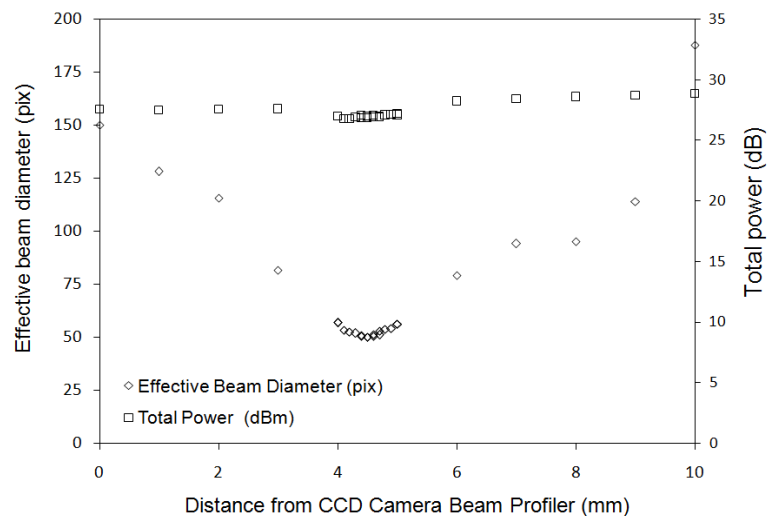


Figure 4-4: CREC–GS–Optiprobe beam profile characterization results.

In this respect, a CCD camera was placed in front of the probe at several known positions, in order to determine the effective beam diameter and total power at each position using a Graphical User Interface. Figure 4-4 reports CREC–GS–Optiprobe beam profile characterization results. One can notice that, as expected, the total power can be

considered constant at all positions. However, there is a clear minimum effective beam diameter, where it is inferred that the CREC–GS–Optiprobes high intensity region image distance (l_1) is located.

To determine the minimum effective beam diameter position, a curve fitting analysis was performed. Figure 4-5 reports the results. In this analysis, the information of the effective beam diameter in the range of 4 to 5 mm distance away from the sensor tip, was considered. It was estimated that the minimum Effective Beam Diameter is located at 4.5 mm from the CCD Camera Beam Profiler. This value of 4.5 mm is very close to the 5.2 mm value reported by [Islam et al. \(2011\)](#).

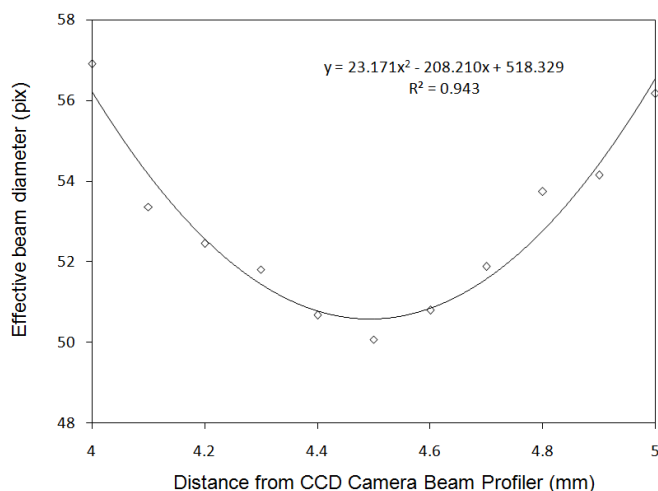


Figure 4-5: Curve fitting analysis of the beam profile.

The second important parameter of the CREC–GS–Optiprobes to study particle cluster characteristics is the effective focal region diameter. [Islam et al. \(2011\)](#) and [Islam \(2010\)](#) established a focal region diameter for the calculation of cluster size considering the following factors: 1) Accurate placement of receiver fiber for optimal visible domain, 2) Minimal signal distortion at receiver fiber end, as well as 3) Minimum errors during data acquisition and data processing. A total of 60 experimental conditions were studied using different combinations of gas and solid flows in a downer reactor unit. They reported that

CREC–GS–Optiprobes have an effective focal region diameter average value of 118 μm with a standard deviation of 34 μm .

4.2 Gas–solid Co–current Flow Downer Units

The experimental data obtained from two independent downer reactor units was used to study the hydrodynamics of concurrent gas–solid flows over several operating conditions. Both acrylic units were designed and built at the Chemical Reactor Engineering Center Laboratory of The University of Western Ontario. The main difference between them is that the first one has a one inch internal diameter, while the second unit has roughly the double (two inch internal diameter).

4.2.1 One inch Internal Diameter Downer Unit

A schematic diagram of the one inch (2.57 cm) internal diameter downer unit is presented in Figure 4-6. The solids in this unit are fed in a batch mode. This unit is operated at ambient conditions. Initially, the Fluid Catalytic Cracking (FCC) catalyst particles from a fluidized bed, are fed to the riser section through a feeding tube and a “Valve 1” located at the bottom of the riser section. A ball vibrator assists the ball valve, “Valve 1”, in supplying a constant amount of solids to the riser section. Regarding the catalyst particles, they are pneumatically transported upwards, using air fed through the combined action of a single orifice hole distributor and a ring gas distributor. The single orifice hole distributor is located at the bottom of the riser section and supplies the air to propel the catalyst particle upwards to the ring gas distributor.

The ring gas distributor is situated at a height of 34 cm above the single orifice hole distributor and contains twelve 0.5 mm holes distributed evenly around the ring distributor. These holes are also angled to 45 degrees from the vertical. This provides good and relatively uniform gas flow in the riser section.

At the top of the riser section (downer entry), the solid particles are disengaged from the air stream through the “Cyclone 2”. The air exiting the top of the cyclone passes through a bag filter where the remaining catalyst particles are collected. Moreover, the catalyst particles exiting the bottom of the “Cyclone 2” move downwards towards the downer

section. This occurs, as a result of the combined effect of gravity and some gas entrained with solid particles.

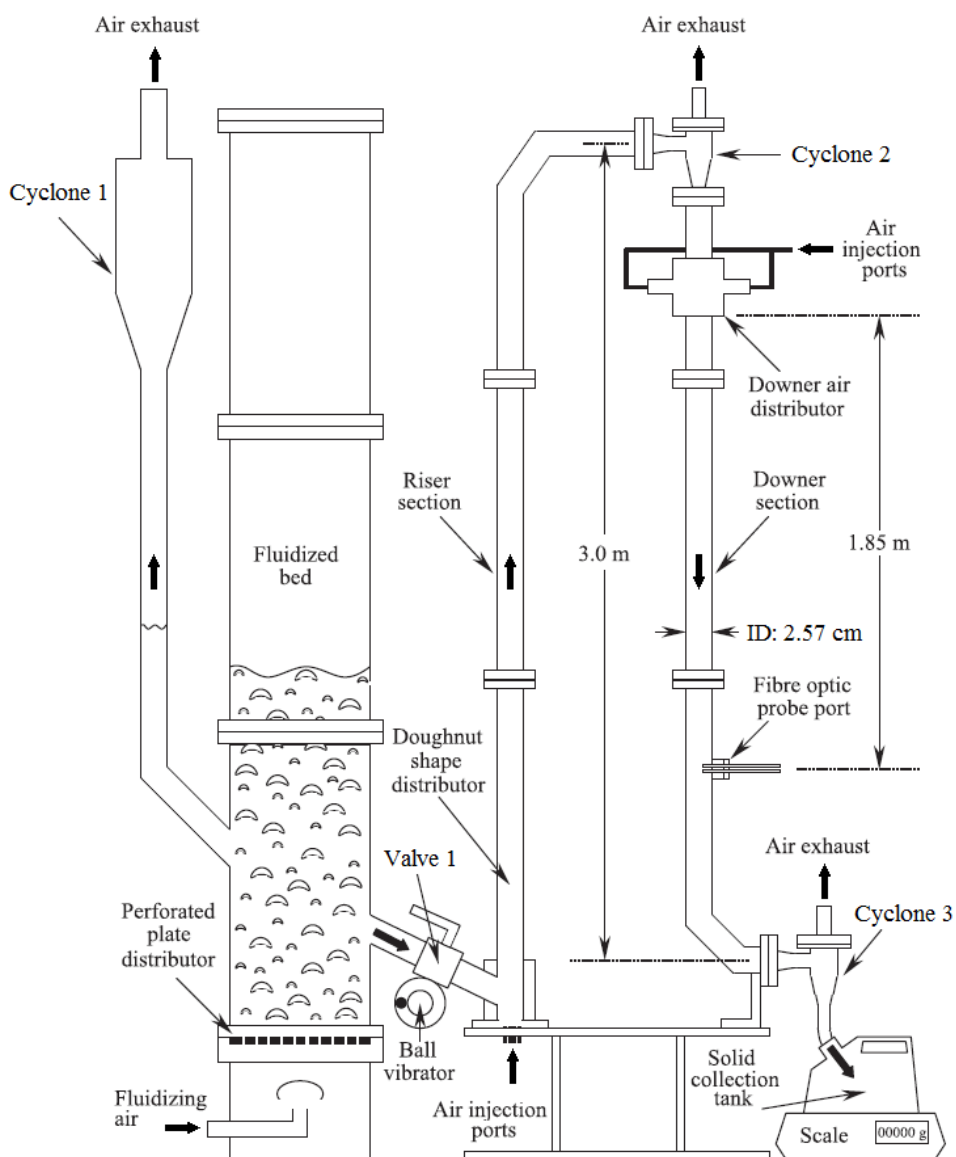


Figure 4-6: Schematic diagram of the one inch internal diameter downer unit showing the fiber optic port, adapted from Nova (2005).

The gas distributor is located 24 cm downstream from the downer top cyclone. This provides additional air to the downer section to complete the required gas flow rate. This air injection simulates the reactant injection and the intense mixing at the entrance region

of a downer unit. To secure a good particle–fluid mixing in the feeding section, the downer top air distributor is configured with sixteen 0.5 mm holes distributed evenly around the circumference of the column and angled downwards 45 degree with respect to the vertical wall.

From this point onwards, the FCC catalyst particles continue their circulation down with the air stream, past the probes, until they reach another cyclone located at the bottom of the downer (Cyclone 3) where they are disengaged from the air stream and collected in a storage tank. This tank is placed on a scale for continuous weighing and monitoring of the catalyst flow rate. Moreover, the air coming from the cyclone 3 is directed to a filter to eliminate remaining solids and then to a rotameter to measure the gas flow in the downer section. More details regarding maintenance, adjustments and standard functioning of this experimental unit can be found in [Islam \(2010\)](#) and [Nova \(2005\)](#).

4.2.2 Two inch Internal Diameter Downer unit

A schematic diagram of the new downer unit is reported in Figure 4-7. Regarding pressure and temperature, this unit is also operated at ambient conditions. The main differences of this new downer unit when compared with the previous one are the following: 1) The internal diameter is almost two times larger, it has a two inch (5.08 cm) internal diameter instead of one inch. 2) The FCC catalyst particles follow a continuous loop 3) Two risers are used to secure a continuous solid loop circulation.

Initially, the FCC catalyst particles from a fluidized bed are fed to the first riser section through a feeding tube and a valve (Valve 1) located at the bottom of the riser section. The catalyst particles are pneumatically transported upwards, using air fed through the combined action of a single orifice hole distributor and a ring gas distributor. The single orifice hole distributor is located at the bottom of the riser section, and supplies the air to propel the catalyst particle upwards to the ring gas distributor.

At the top of the first riser section (downer entry), the solid particles are disengaged from the air stream by the Cyclone Separator 2. Moreover, the catalyst particles exiting the

bottom of the cyclone move downwards towards the downer section, as a result of the combined effect of gravity and gas entrained with the solid particles.

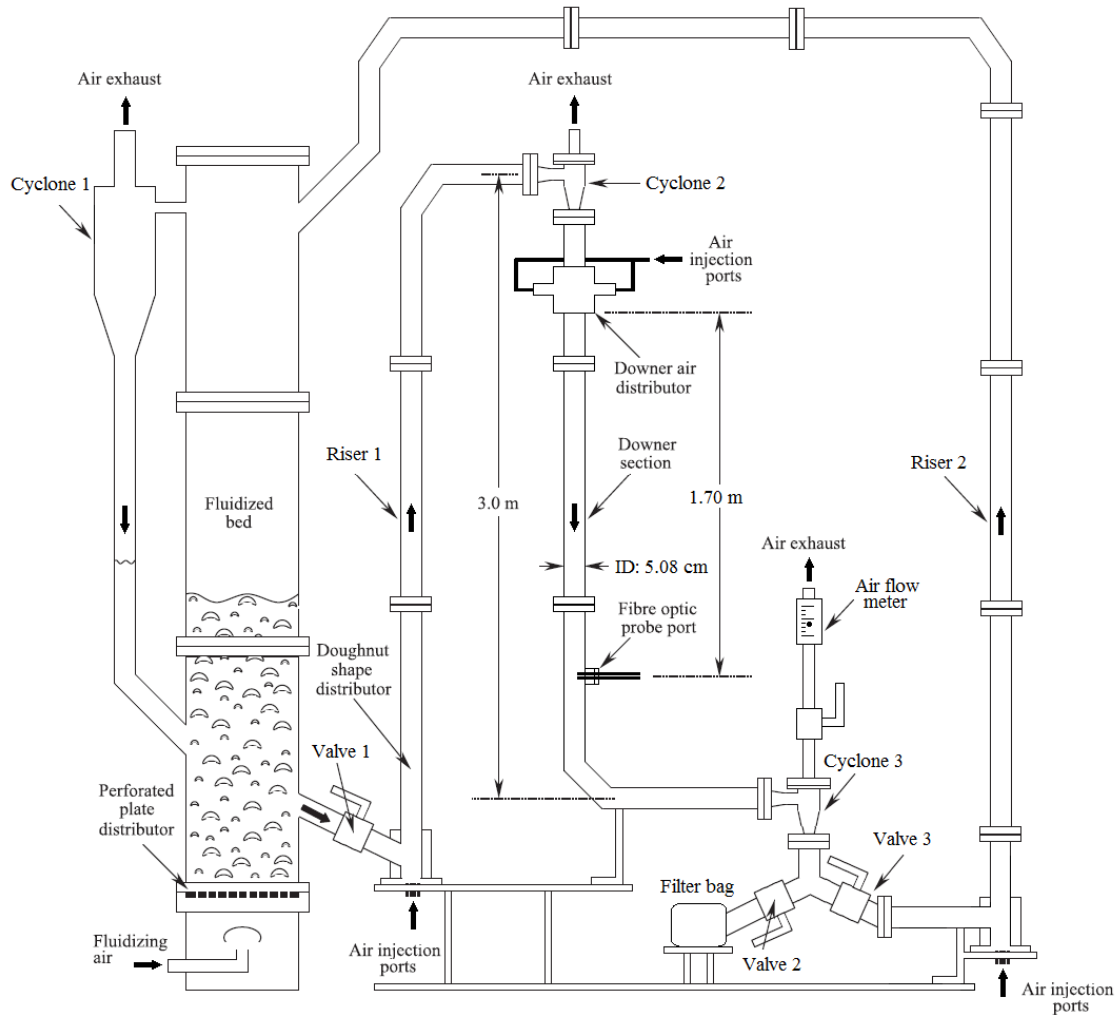


Figure 4-7: Schematic diagram of the two inch internal diameter downer unit.

The gas distributor is placed below the downer top cyclone (Cyclone 2). This provides air to the downer section, in order to achieve the required gas flow rate. This air injection simulates the reactant injection and the intense mixing at the entrance region of a downer unit. To secure a good particle–fluid mixing in the feeding section, the downer top air distributor is configured with sixteen 0.5 mm holes distributed evenly around the

circumference of the column and angled downwards 45 degree with respect to the vertical wall.

From this point onwards, the FCC catalyst particles continue circulating down with the air stream. They pass the probes, and continue onwards until they reach a two ways valve located at the bottom of the downer where: 1) they can continue and flow toward the second riser and then close the loop by going into the fluidized bed or, 2) the solids can be collected in a bag filter. The bag filter is then placed on a scale for weighing and monitoring the catalyst flow rate. Moreover, the air coming from the Cyclone 3, can be directed to a filter to retain the remaining solids and then, to a rotameter to measure the gas flow in the downer section.

A scaled representation of the two inch internal diameter downer unit is presented in Figure 4-8.

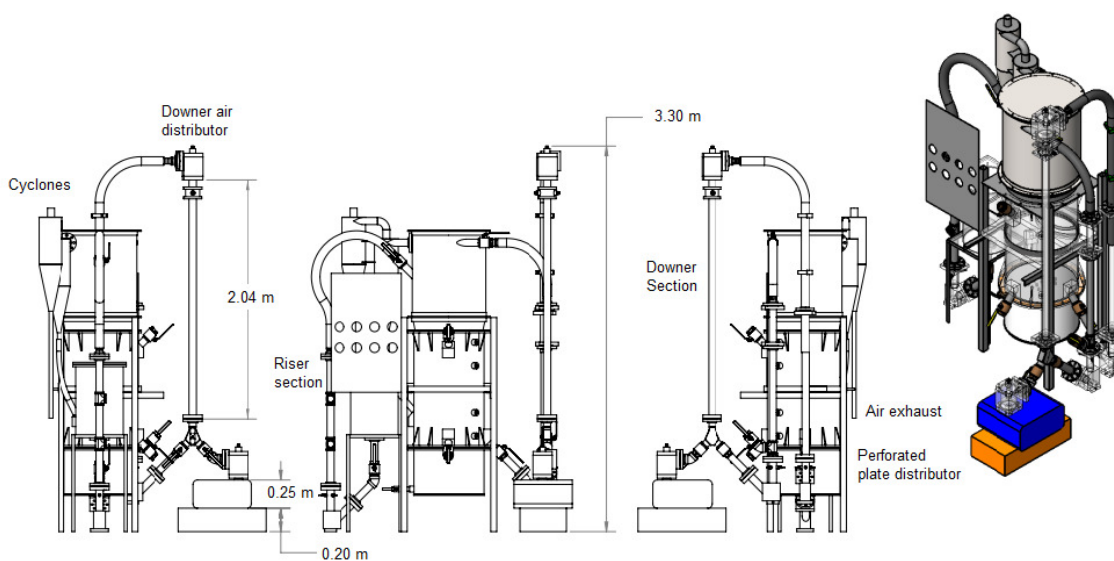


Figure 4-8: Scaled representation of the 2 inch internal diameter downer unit.

4.3 FCC Catalyst Particles Used

The FCC particles used in the experiments, had the same characteristics as those employed by [Islam et al. \(2010\)](#) and [Islam \(2010\)](#). They have a mean particle diameter of

84.42 μm with a standard deviation of 33.62 μm , and an apparent particle density of 1,722 kg/m^3 . Figure 4-9 shows the particle size distribution (PSD) curve.

The fluidization gas used was air, at close to ambient pressure and temperature. To minimize electrostatic charges and fouling, 0.01 m^3 of ammonia hydroxide (ammonium hydroxide, 28–30wt%, CAS 1336–21–6) were added per 1 m^3 of FCC catalyst in the fluidized bed. The experimental set up was electrically grounded as well, to discharge electrostatic charges during operation.

More details regarding to the FCC catalyst used in the present PhD dissertation can be found in Appendix A.

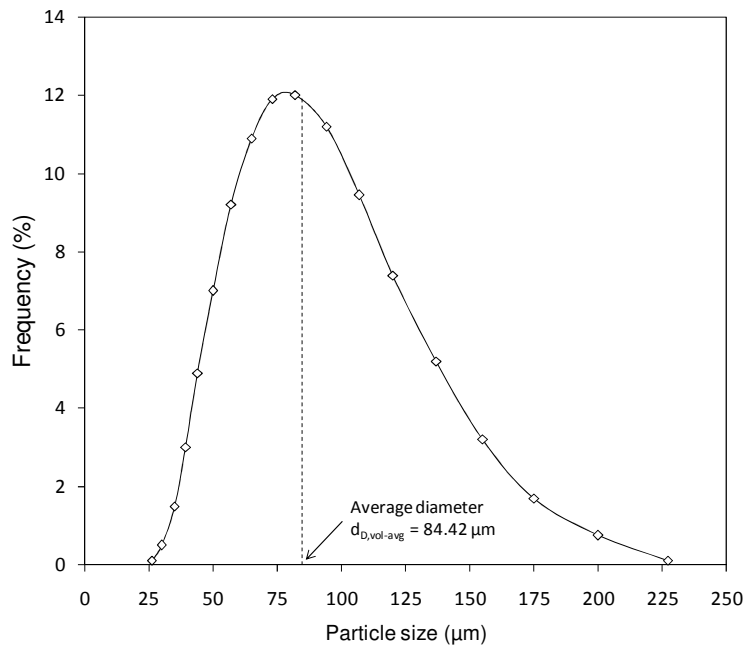


Figure 4-9: Volume weighted particle size distribution of FCC particles used in the present study.

4.4 Conclusions

- a) Four equipments/components were described in this chapter, used in the experimental set-up: 1) the CREC–GS–Optiprobes, 2) a one inch internal diameter downer unit, 3)

- a two inch internal diameter downer unit, and 4) the FCC catalyst. All these elements were used in the present PhD dissertation.
- b) The CREC–GS–Optiprobes were employed given the following advantages over other reflective sensors: a) they have a geometric configuration which optimizes the optical characteristics of both the emitter and receiver optical fibers, 2) they incorporate a GRIN lens into the probe which creates a focal point far from the tip of the sensor, minimizing flow disturbances in the measurements, and 3) they involve a simple design and operating principle.
 - c) A Camera Beam Profiler was used to determine CREC–GS–Optiprobes optimal image distance. It was estimated that the high intensity region image distance (l_1) is located at 4.5 mm from the tip of the CREC–GS–Optiprobes. In addition, the CREC–GS–Optiprobes have an effective focal region diameter average value of 118 μm with a standard deviation of 34 μm .
 - d) A one inch internal diameter downer unit operating in a batch mode, was employed in the present study. The total height of the downer column was 2 m. The CREC–GS–Optiprobes were placed at 1.85 m from the air feeding distributor.
 - e) A two inch internal diameter downer unit with continuous solid recirculation was used in the present research. The total height of the downer column was 2 m . This also involved two risers to achieve continuous particulate recirculation. The CREC–GS–Optiprobes were placed at 1.70 m from the downer air distributor.
 - f) The FCC particles used in both downer units, have a mean particle diameter of 84.42 μm with a standard deviation of 33.62 μm , and an apparent particle density of 1,722 kg/m^3 .

Chapter 5

5 Methodology Proposed for Signal Analysis

In this chapter, a rigorous methodology is proposed to determine the position of the so called "baseline" in order to be able to develop signal analysis. A detailed explanation of the baseline concept and its importance, along with the details of the new proposed methodology are presented as follows.

5.1 Baseline Concept and its Importance for Signal Analysis

The CREC–GS–Optiprobes work in conjunction with an optic–electronic data acquisition system where light changes are converted in digitalized voltage variations (Islam, 2010). Each of the two CREC–GS–Optiprobes recorded data at a frequency of 100 kHz. A sample of the time signals recorded by both the upper and lower probes is reported in Figure 5–1. For data acquisition, a program called ‘‘Probe Signal Sampling.vi’’ originally developed by Nova (2005), was employed.

Data reported along the vertical axis of Figure 5–1 represents the signal time series expressed in volts (Sharma et al., 2000). Each operational condition was recorded during at least 1 s period or 100,000 data points. However, for a clear illustration of the signals, this graph reports only 7.55 ms of signal duration, as recorded by one of the CREC–GS–Optiprobes at the radial position $r/R=0.1$.

One can notice that there is a delay time between both signals, which represents the time shift between the upper to the lower optiprobes. This is the time displacement required for the particle cluster to move from one detection volume to the other. In the case reported in Figure 5–1, the time displacement is 2.4 ms, this time displacement is estimated using a cross–correlation function as is explained further in this PhD dissertation. Regarding Δt_i as reported in Figure 5–1, this represents the detection time for each cluster. This detection time Δt_i , is used to estimate cluster size.

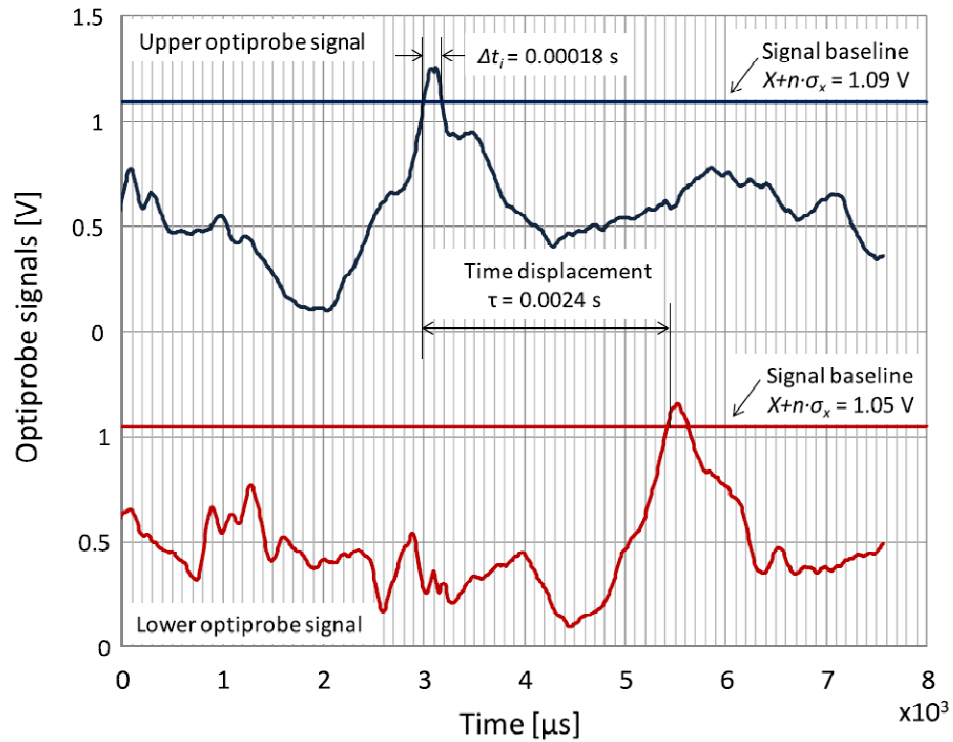


Figure 5–1: CREC–GS–Optiprobe signals for the upper and lower probes: conditions, 1 inch downer, $G_s=60.2 \text{ kg/m}^2/\text{s}$, $U_g=1.29 \text{ m/s}$, $r/R=0.1$.

In order to analyze the optiprobe signals, it is required to set signal baselines. Each signal baseline is defined in the present study as,

$$X + n \cdot \sigma_x \quad (5-1)$$

where X is the signal average; σ_x is the signal standard deviation; and n is a baseline reference factor.

The important influence of n on signal analysis can be noticed in Figure 5–1, where it is advisable to set a signal baseline as high as possible to avoid particle secondary reflections or noise contribution. Nevertheless, the higher the baseline, the larger the lost of relevant cluster data.

For the selection of the signal baseline, different researchers used various empirical approaches for setting the n values. For example, [Soong et al. \(1993\)](#) suggested that the

baseline for clusters identification must comply with three conditions: a) the solid concentration must be significantly larger than the time-average solid concentration at the point of measurement, b) the perturbation in solid concentration due to clusters must be greater than the random background fluctuation of solid fraction, and c) the concentration perturbation should be sensed within a sampling volume with a characteristic length greater than one to two orders of magnitude of the particle diameter. To comply with these conditions, [Soong et al. \(1993\)](#) proposed that the local instantaneous solid volume fraction for a cluster must exceed the signal average solid concentration by at least two times of the standard deviation, $X + 2\sigma_x$.

On the other hand, [Sharma et al. \(2000\)](#) used optiprobos to investigate the parametric effects of particle size and superficial gas velocity on cluster characteristics in a 15 cm diameter and 11 m height fluidized bed. Based on visual observations these investigators proposed a reasonable but arbitrary criterion, to determine solid concentration in a cluster. They suggested that a cluster, once surpassing the $X + 2\sigma_x$ level, is considered to exist and survive as long as its solid concentration remains above X . They also noticed that by using a different baseline (e.g. $X + 3\sigma_x$) they could alter the results quantitatively with however no changes being noticed in the overall cluster characteristics.

Other baseline criterion was assumed by [Nova et al. \(2007\)](#) for the evaluation of the cluster sizes in downer reactors. These authors considered as cluster related data the signal peaks which were complied with the constraint of being at least as tall as 95% of the highest peak in the signal train. Then peak widths were measured at a reference level, crossing the signal at 50% of the height of the highest peak in the signal train.

Moreover, [Islam et al. \(2010\)](#) and [Islam \(2010\)](#) based the cluster size determination on measurements of the signal-peak widths sets at $X + 3\sigma_x$. This baseline was selected in order to reduce the likely uncorrelated signals present. Thus, peaks surpassing $X + 3\sigma_x$, were considered appropriate for cluster size calculations, while the rest of signals was discarded for further analysis.

Manyele et al. (2002) studied the dynamic properties of clusters in a concurrent downer reactor using optical probes. A value of $n = 0.5$ was used by these researchers. This value of n was based on the interception of two straight lines drawn above a graph of n versus the time average radial solid concentration, ε_s .

5.2 Baseline Setting Methodology

In the present PhD dissertation, a more rigorous methodology to set the data baseline is proposed. To achieve this, instead of using an arbitrary and fixed level definition, the position of the baseline has to be selected for every downer level and operational condition in compliance with solid mass balance. Using this approach noise resulting from secondary reflection is eliminated and all valuable data is kept in the time series.

Regarding the cross-sectional solid mass flux, G_s , can be defined at every downer axial position as,

$$G_s = \frac{\rho_s}{A} \int_0^A U_s \varepsilon_s dA \quad (5-2)$$

where ρ_s is the particle density, A is the total internal area of the downer reactor, U_s is the time weighted average radial cluster velocity, and ε_s is the time average radial solid concentration.

It can be noticed that both U_s and ε_s depend on the baseline position. Therefore, changes in the baseline level lead to different solid velocities and solid fractions. Thus, according to the methodology proposed, one can iterate using different baseline levels until the calculated U_s and ε_s gives values that comply with Equation (5-2).

Regarding this iterative calculation, for the first iteration, the baseline is set at the highest peak position of the probe signal. Following this, U_s and ε_s are estimated at this baseline level, and then the calculated G_s is compared with the experimental G_s value. If it is judged that there is a significant deviation between the calculated and measured solid fluxes, a new iteration is initiated where a new baseline is set at a lower position. The iteration process continues until G_s estimated converge with Equation (5-2) becoming

essentially identical to the measured G_s . Converged U_s and ε_s results, at every radial position, are identified as the ones corresponding to the operating condition studied.

Thus, in accordance with the methodology proposed in this PhD dissertation, for the upper optiprobe signal of Figure 5–1 case, the value of n obtained is 2.087, the signal average X in this optiprobe signal is 0.671 V, and the standard deviation $\sigma_x=0.201$ V. Therefore, the baseline reference factor for the upper optiprobe signal analysis can be estimated as:

$$X + n \cdot \sigma_x = 0.671 + 2.0870 \cdot 0.201 = 1.09V$$

For each baseline level set, during the iteration process, both U_s and ε_s were calculated. For instance, the local solid concentration, ε_s , was estimated as follows.

$$\varepsilon_s = \frac{\sum_{i=1}^m \Delta t_i}{t} \quad (5-3)$$

where m is the total number of clusters detected surpassing the selected baseline level in a t observation period; Δt_i is the detection time determined for each cluster ($\Delta t_i = t_{2i} - t_{1i}$ with t_{1i} being the starting time of the cluster i detection and t_{2i} the end of cluster detection).

One should notice that Equation (5–3) hypothesizes that there are two possible operating conditions while using the CREC–GS–Optiprobe: a) the focal region is filled completely with solid particles; and b) the focal region is devoid of solids. This is a reasonable assumption if one considers the expected 118 ± 34 μm focal region size, the FCC–particle size used, and the expected cluster size.

In the present study, the typical total recording signal period in each one of the CREC–GS–Optiprobe was set to 1 s or 100,000 data points. At least 5 signal trains of 1 s, or 500,000 data points, were recorded at every radial position and for each operating condition. As a result, it was judged that the data acquired in conjunction with Equation (5–3) provides an adequate assessment of the local averaged solid concentration at various radial downer positions.

It is important to mention that even though the CREC–GS–Optiprobes were placed at 11 radial positions, only the information obtained from 10 of them was used for calculations with the center one being excluded. This was needed to be able to define the solid flux using an area–weighted method. Therefore, the downer tube cross–section was divided into 10 concentric annulus and the solid mass flux, G_s , was determined in each circular strip of cross–section area. A detailed explanation of this area–weighted method can be found in either [Qi et al. \(2008\)](#) or [Herbert et al. \(1994\)](#).

Likewise, the particle cluster velocity, U_s , was calculated using the delay time presented between the upper and lower optisensors signals, Figure 5–1. To estimate the delay time a cross–correlation is obtained with the voltages of both signals (x and y , respectively) ([Ye et al., 2009](#); [Nova et al., 2004b](#); [Zhang et al., 1998](#); [Aguillon et al., 1996](#); [Culshaw, 1984](#)).

$$R_{xy}(\tau) = \lim_{T \rightarrow \infty} \frac{1}{T} \int_0^T x(t) \cdot y(t + \tau) \cdot dt \quad (5-4)$$

where τ is the time displacement or delay time.

A numerical approximation was used for discrete cross–correlation calculations of pair of time series “ x ” and “ y ” digitalized signals obtained from the upper and the lower sensors for every particle cluster. The calculation implemented returns the cross–correlation sequence R_{xy} .

$$R_{xy}(j) = \sum_{i=0}^{n-1} x_i \cdot y_{i+j} \quad (5-5)$$

For $j = -(n - 1), -(n - 2), \dots, -2, -1, 0, 1, 2, \dots, m - 1$

where n is the number of elements x_j in the sequence X , m is the number of elements y_j in the sequence Y , and $R_{xy}(j)$ are the elements in the sequence R_{xy} with length $n+m-1$. In Equation (5–5), when the indexed elements x_i or y_{i+j} fall outside the range of X or Y , their value is set equal to zero according to the following:

$$x_j = 0, \text{ for } j < 0 \text{ or } j \geq n \quad (5-6)$$

and

$$y_j = 0, \text{ for } j < 0 \text{ or } j \geq m \quad (5-7)$$

An example of the cross-correlation calculation with normalized sequence R_{xy} is reported in Figure 5-2. A value of $R_{xy} = 1$ means that the signals are identical. For all the conditions studied in the present PhD dissertation the maximum value of R_{xy} was larger than 0.4. Signals with maximum value of cross-correlation sequence $R_{xy} \leq 0.4$ were discharged.

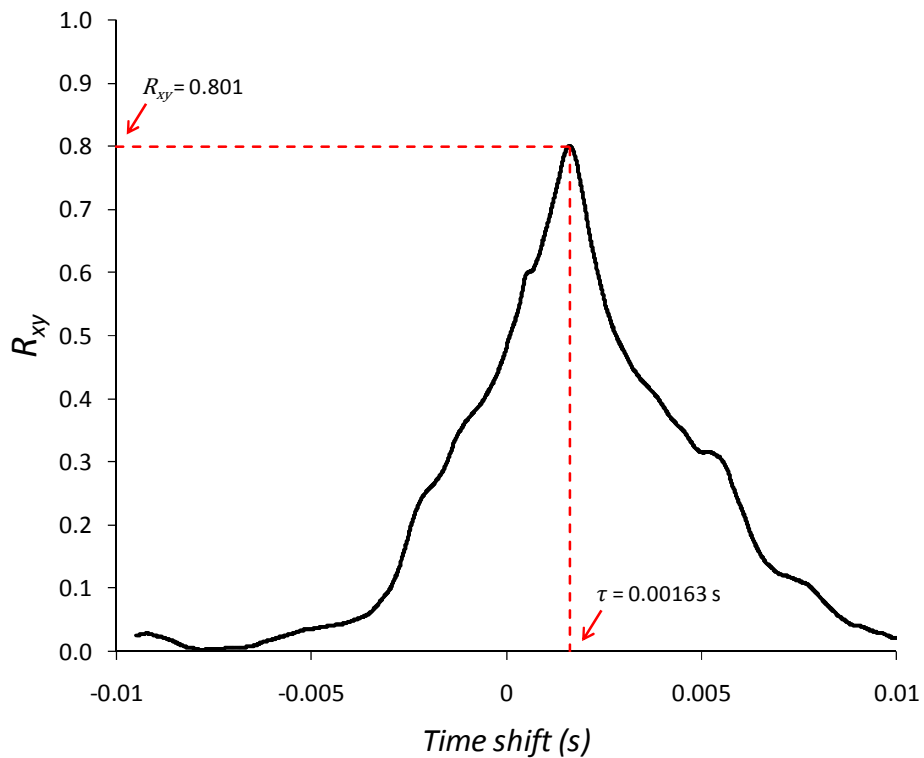


Figure 5-2: Example of the cross-correlation sequence R_{xy} for one cluster, 2 inch downer, $G_s=50 \text{ kg/m}^2/\text{s}$, $U_g=1.5 \text{ m/s}$, $r/R=0$.

Once the time shift obtained via signal cross-correlation and considering the 0.006 m spacing between the upper and lower focal sensor regions the cluster velocity is

calculated. In the case reported in Figure 5–1, the time displacement is 0.0024 s, the individual cluster velocity, U_s , can thus be determined as: $U_s=0.006 \text{ m}/0.0024 \text{ s} =2.456 \text{ m/s}$.

Regarding cluster calculations, it has to be pointed out that in the present study it was preferred to establish time delays for each individual cluster signal. This represents a more rigorous approach versus cluster properties defined as an average value by [Islam et al. \(2010\)](#). In this manner, the actual velocity of each individual cluster at a specific radial location was obtained.

In addition and concerning cross–correlation, there are a number of factors that may reduce cross–correlation. For instance, some clusters may be detected by one probe and may not be detected by the other. In some instances secondary reflections may contribute with background noise. Therefore, uncorrelated or poor correlated data have to be eliminated for further signal analysis.

In this study, in order to consider data as acceptable for further analysis two conditions had to be satisfied:

$$U_s \geq U_{sg} \quad (5-8)$$

and

$$U_s \leq 3 + U_{sg} \quad (5-9)$$

With interstitial and superficial gas velocities approximated with superficial gas velocity given the low average solid concentration.

$$U_g = \frac{U_{sg}}{1 - \varepsilon_s} \quad (5-10)$$

Regarding Equation (5–8), it states that a cluster to be considered as such, has to have a velocity in the downer unit always greater than or equal to the superficial gas velocity. This is the case given various forces applied on flowing particles in motion are dominated by gravity, and the probe is located in a position where the gas-solid flow is fully

developed. As a result, it is expected that all particles shall display a positive slip with respect to the superficial gas velocity.

The second inequality, as given by Equation (5–9), considers that the solid velocity has to be less than or equal to the superficial gas velocity plus 3 m/s. This condition is based on experimental results found in the technical literature. For similar reactor sizes, particle size, and operational conditions, the slip velocity was found always smaller than 3 m/s (Islam et al., 2010; Nova, 2005; Nova et al., 2004b).

In summary, once the measured particle velocities passed the two tests, as given by Equations (5–8) and (5–9), they were considered as acceptable cluster velocity data. These data were further used for developing frequency weighted average cluster size distribution and circulating average cluster velocities at each radial location.

Furthermore, and as described above, the established average local solid hold up and average cluster velocities associated to 10 concentric annular section strips of the downer were considered for solid mass flux, G_s calculations, as described in Equation (5–2). It is important to mention that under the entire experimental conditions of this study, and once the iterative calculations were completed, the error obtained while comparing the G_s estimated with the measured experimental G_s , was always less than 0.1% in all cases.

Considering the large amount of data available, a computational program was created in Matlab[®] Version 7.6.0.324 (R2008a). This program was designed with three main subprograms. The first subprogram estimates the velocity of solids by cross–correlation function. The second subprogram estimates the solid concentration. And, the third subprogram determines the solid mass flux.

5.3 Conclusions

- a) The particle cluster velocity, U_s , was calculated using the delay time presented between the upper and lower CREC–GS–Optiprobe signals. This calculation was done using a discrete cross–correlation approach.

- b) A rigorous methodology for setting the data baseline is considered in this PhD dissertation. The author is not aware of similar methodology reported in the technical literature. It is proposed following this approach that the position of the baseline has to be determined for every downer level and operating condition in compliance with solid mass balance.
- c) To accomplish this, an iterative calculation is needed to determine the baseline position. Changes in the baseline level lead to different solid velocities, U_s , and solid fractions, ε_s . Thus, according to the methodology proposed, an iteration calculation using different baseline levels is needed until the calculated U_s and ε_s gives values that comply with the corresponding solid mass flux.
- d) Solid fluxes were estimated using an area-weighted method considering 10 of the 11 radial measures with the center one being excluded. The downer tube cross-section was divided into 10 concentric annulus and the solid mass flux, G_s , was determined in each circular strip of cross-section area.
- e) The total recording signal period in each one of the CREC-GS-Optiprobes was set to 1 s or 100,000 data points. Five signal trains of 1 s, or 500,000 data points, were recorded at every one of the 11 radial position and for each operating condition. Therefore, 5 million and 5 hundred data points were recorded for each sensor and for each operating condition.
- f) Under the entire experimental conditions of this study, and once the iterative calculations were completed, the error obtained while comparing the G_s estimated with the measured experimental G_s , was always less than 0.1% in all cases.

Chapter 6

6 Experimental Results Obtained with the 1 inch Internal Diameter Downer Unit

In this chapter, “individual” particle cluster information obtained using the CREC–GS–Optiprobes is reported.

Experiments were carried out in the 1 inch internal diameter circulating fluidized bed downer cold model unit of 3.0 m height. The solids used were a fluid catalytic cracking (FCC) catalyst with a mean particle diameter of 84.42 μm and a particle density of 1,722 kg/m^3 . The velocity and solid mass fluxes are varied from 0.95 to 2.53 m/s and from 10 to 106 $\text{kg/m}^2\text{s}$, respectively in this case.

Table 6–1: Operating conditions used in the 1 inch internal diameter downer unit.

Operational Condition #	Gas Velocity (U_g , m/s)	Solid Mass Flux (G_s , $\text{kg/m}^2/\text{s}$)
1	0.95	10
2	1.43	15
3	1.18	50
4	1.72	28
5	2.54	46
6	1.25	65
7	1.85	57
8	2.53	76
9	1.16	106
10	1.68	82
11	2.52	91

Analysis of the data obtained involves a rigorous methodology for setting the data baseline in compliance with solid mass balances. The application of this method allows the simultaneous measurement of a) baseline reference factor results, b) cluster solid concentrations, c) individual cluster slip velocities and d) individual cluster sizes. These data also allow calculation of cluster size frequency distribution at various radial positions in the downer unit. On the strength of these experimental data, particle cluster drag coefficients are calculated as a function of the cluster Reynolds’ number and average particle number in the cluster. Drag coefficients determined using the proposed

method, provide close range values. These findings support a particle string configuration for clusters in downer units.

Two CREC–GS–Optiprobess were placed at 1.85 m height below the injection port in the 1 inch internal diameter downer unit, and separated axially 0.006 m. It was considered that at 1.60 m the particles reached terminal velocity. A confirmation of the fully developed flow pattern (clusters evolving at terminal velocity), as shown via the pressure along the downer, is provided in [Islam et al. \(2010\)](#).

Experiments were carried out under a wide range of operating conditions as described in Table 6–1. To ensure both the validity and reproducibility of the data, measurements were repeated at least 5 times for each radial position, and their time–averaged values were adopted as the measured results. For each operational condition, the two CREC–GS–Optiprobess were aligned at 11 equally–divided radial positions. Thus, with this combination of number of samples and radial positions, the full spectra of hydrodynamic signals of interest along the radius were captured from the downer unit.

6.1 Baseline Reference Factor from Experimental Results

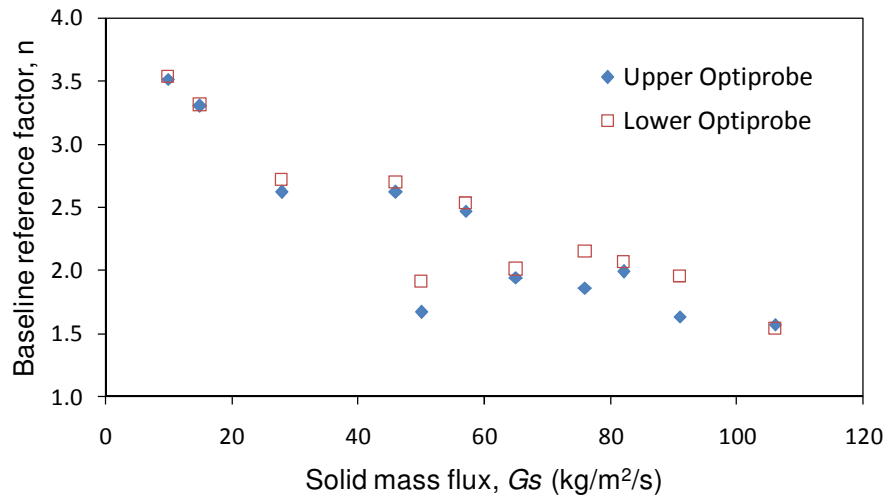
The experimental results of the baseline reference factor estimated using the new methodology proposed in the present study are reported in Table 6–2. As it can be seen in this table, the values of n estimated with the signal data recorded by the upper and the lower CREC–GS–Optiprobess are very close. These results also show the validity and applicability of proposed baseline determination method as described in Equation (5–2).

Figure 6–1 and Figure 6–2 provide a graphical representation of the baseline reference factor n of Equation (5–1), as reported in Table 6–2. It can be noticed that n , decreases when the solid mass flux, G_s , is increased.

Table 6–2: Baseline reference factor experimental results.

Operational Condition #	Gas Velocity (U_g , m/s)	Solid Mass Flux (G_s , kg/m ² /s)	Upper Optiprobe	Lower Optiprobe
			Baseline Reference Factor, n	Baseline Reference Factor, n
1	0.95	10	3.51	3.53
2	1.43	15	3.30	3.31
3	1.18	50	1.67	1.91
4	1.72	28	2.62	2.72
5	2.54	46	2.62	2.70
6	1.25	65	1.94	2.01
7	1.85	57	2.47	2.53
8	2.53	76	1.86	2.15
9	1.16	106	1.57	1.54
10	1.68	82	1.99	2.07
11	2.52	91	1.63	1.95

The gas velocity, on the other hand, did not have such a significant influence on the n parameter. To explain this behavior of n with G_s one can argue that larger G_s may lead to more secondary ray reflections from particles or particle clusters increasing both the signal average, X , and the standard deviation σ_x (Lanza et al., 2013).

**Figure 6–1: Baseline reference factor as a function of the solid mass flux.**

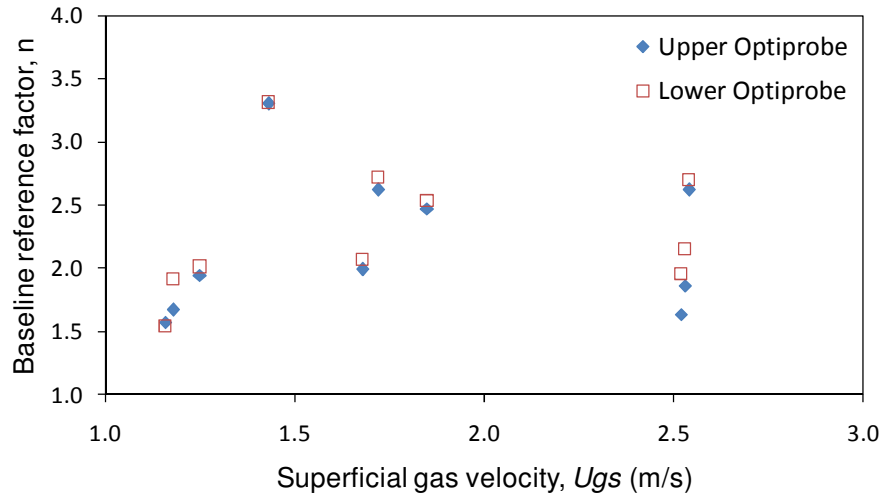


Figure 6–2: Baseline reference factor as a function of the superficial gas velocity.

6.2 Cluster Slip Velocity from Experimental Data

Radial cluster slip velocity and radial cluster solid concentration are reported in four groups of graphs as follows: a) low solid flux (10 and 15 kg/m²/s); b) low–intermediate solid flux (28, 46, and 49 kg/m²/s); c) high–intermediate solid flux (57, 65, and 76 kg/m²/s); and d) high solid flux (82, 92, and 106 kg/m²/s). Cluster slip velocities, u_{slip} , were estimated with the following Equation (6–1), and are reported in Figure 6–3. The error bar for the experimental results are presented in Chapters 7 and 8 of the present PhD dissertation.

$$U_{slip} = U_s - U_g \quad (6-1)$$

where U_{slip} is the local slip velocity; U_s is the measured local particle or cluster velocity; U_g is the interstitial gas velocity.

Regarding the data, one can see that the radial slip velocity profiles are relatively flat, presenting mild increases for the higher values of gas velocity at the position $r/R=0.5$. Flat slip velocity profiles in downers have been found by other researchers as well (Wu et al., 2010; Li et al., 2004; Talman et al., 1999). It is noticeable that the cluster radial slip velocity shows however, an increase when the gas superficial velocity augments.

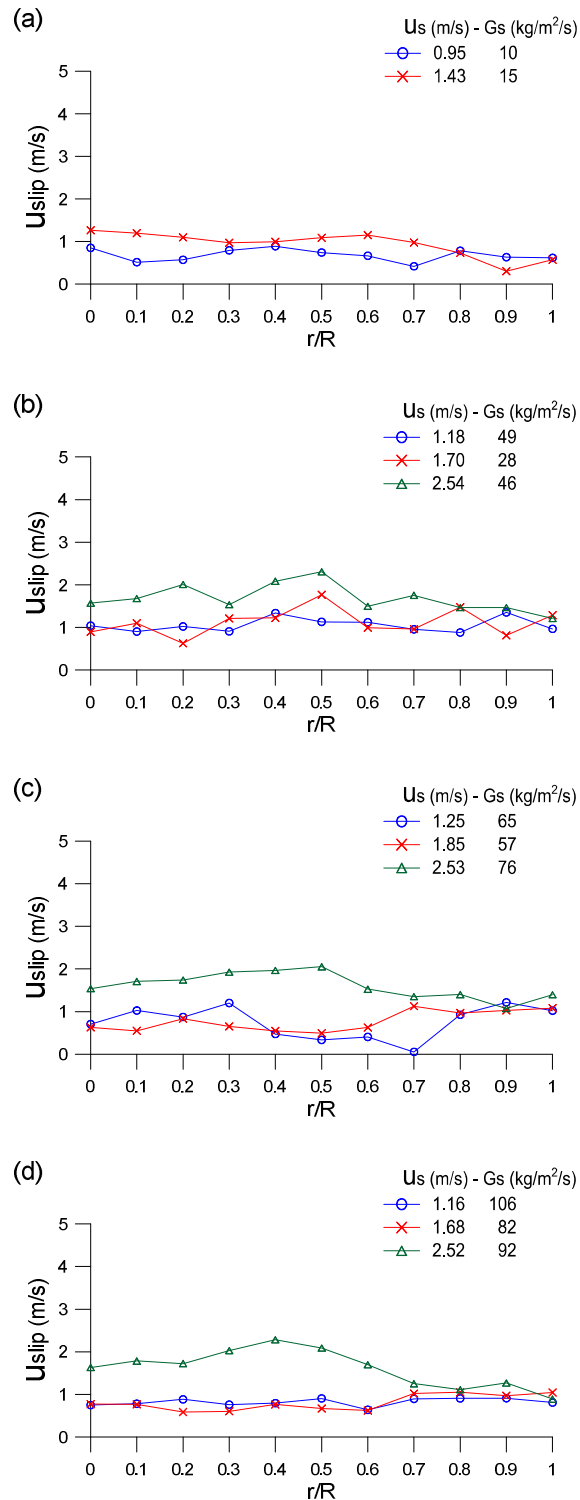


Figure 6–3: Radial cluster slip velocity profiles. Figures (a) to (d) show lower, lower intermediate, higher intermediate, and higher solid mass flux respectively.

This behavior can be assigned to the fact that higher superficial gas velocities enhance particle interaction, and may facilitate larger particle clusters formation. One should notice that formation of large clusters yields a reduced drag force and increased particle slip velocity (Nova et al., 2004b).

6.3 Radial Solid Concentration Profiles

The radial solid concentration profile is another important parameter for fluid dynamic description of solid flows in the fully developed region in downer units. Radial solid concentrations were calculated with Equation (5-3), and are reported in Figure 6-4. The average of five samples of 1 s data duration was considered for each position.

It can be seen that the solid concentration profiles for both the upper and lower Optiprobe are close. This also provides evidence of good correlation between the signals recorded from both upper and lower CREC-GS-Optiprobos. One can also notice that the solid concentration radial profiles are quite flat with this being particularly true at the lower solid mass fluxes. Radial solid concentration profiles present a fluctuation in the radial position $r/R=0.6$ with this becoming more pronounced at the higher the solid mass fluxes.

It can be also observed that for similar gas superficial velocities, the solid concentration increases with solid mass flux. An increase in gas velocity is found to have an important influence as well on solid concentration, making the solid flow less uniform, as reported in Figure 6-4d and h.

Regarding radial solid concentration profile in the near wall region, it appears that the gathered results are in good agreement with other studies (Manyele et al., 2003). It can be observed that in the downer fully developed flow region radial profiles are rather flat with no significant changes close to the wall. These observations are valid for a wide range of operating conditions. Additionally, it is found that the solid concentrations increase with G_s and decrease with U_g with these findings being consistent with the other publications in the technical literature (Manyele et al., 2002, 2003).

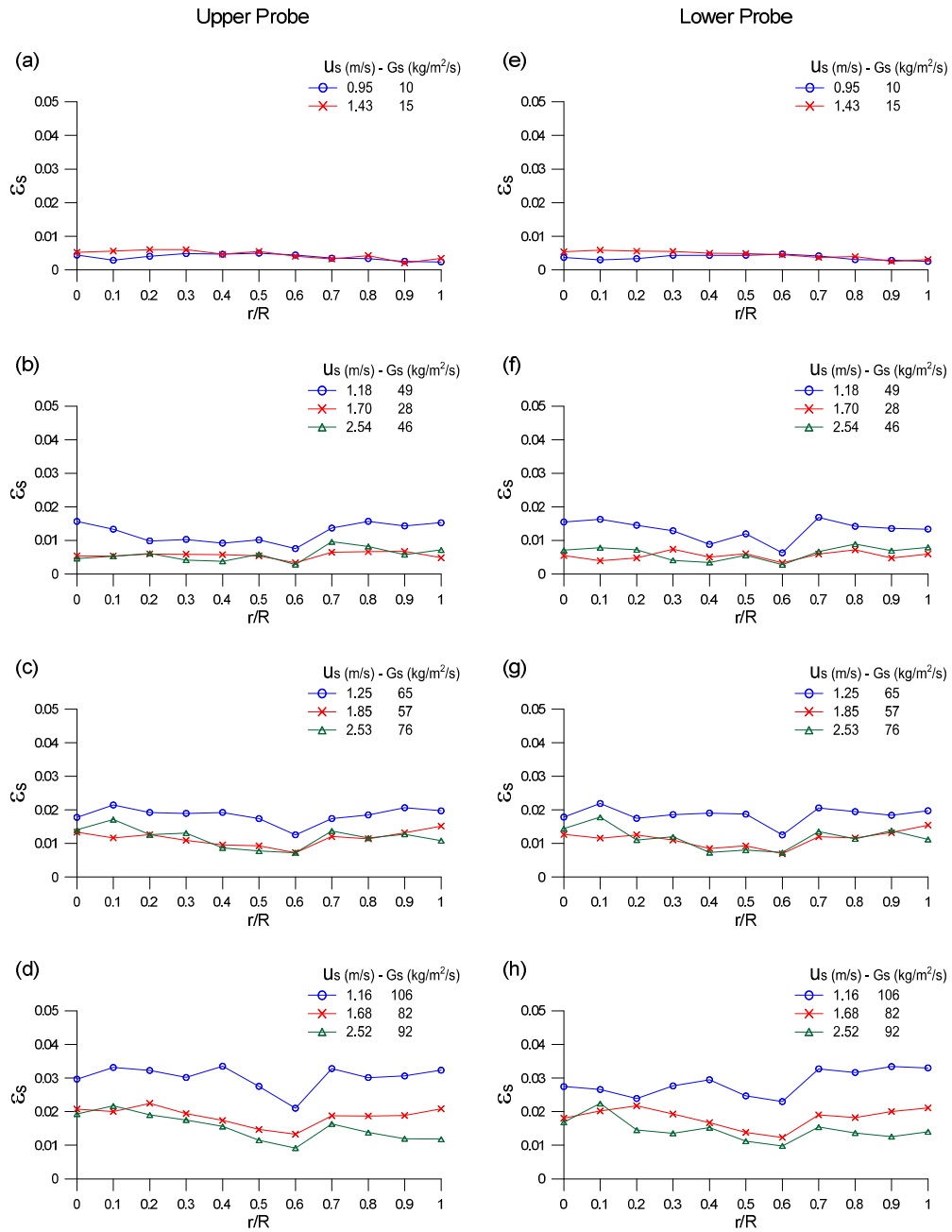


Figure 6–4: Radial cluster solid concentration profiles. Figures from (a) to (d), show results of the upper optiprobe; (e) to (h) show results of the lower optiprobe. Four groups are presented, lower, lower intermediate, higher intermediate, and higher solid mass flux.

6.4 Cluster Size and Cluster Slip Velocity Calculations

Figure 6–5 reports the changes of cluster slip velocity with the expected number of particles in clusters. This analysis was performed for the set of U_{sg} and G_s of 0.95 m/s and 10 kg/m²/s respectively, including 899 cluster data points. Figure 6–5 reports three observations: a) there is a wide distribution of cluster sizes and cluster velocities for a given operation condition, b) there is a wide distribution of cluster sizes for a given slip velocity, and c) there is a significant variation of slip velocity for a given cluster size.

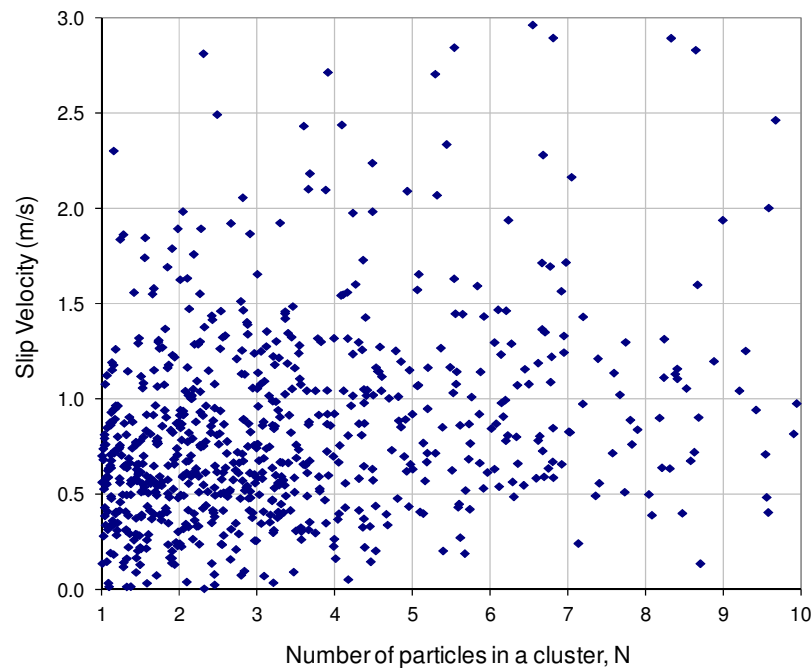


Figure 6–5: Slip velocities of particles as a function of number of particles in the 1 inch internal diameter downer unit. Operating condition: $U_g=0.95$ m/s, $G_s=10$ kg/m²/s. Data points included: 899 clusters.

Moreover, this data analysis is further enhanced in the present study as reported in Figure 6–6. These data sets correspond to 1.16 m/s gas velocity, 106 kg/m²/s solid flux, and 3272 clusters. Figure 6–6 reports the cluster slip velocity distribution for two groups of clusters co-existing in the same cluster population. In the first group, the clusters have 1 or 2 particles. In the second group the clusters have 7 or 8 particles. It can be noticed that

the slip velocity of clusters are consistently higher for the clusters containing a larger number of particles.

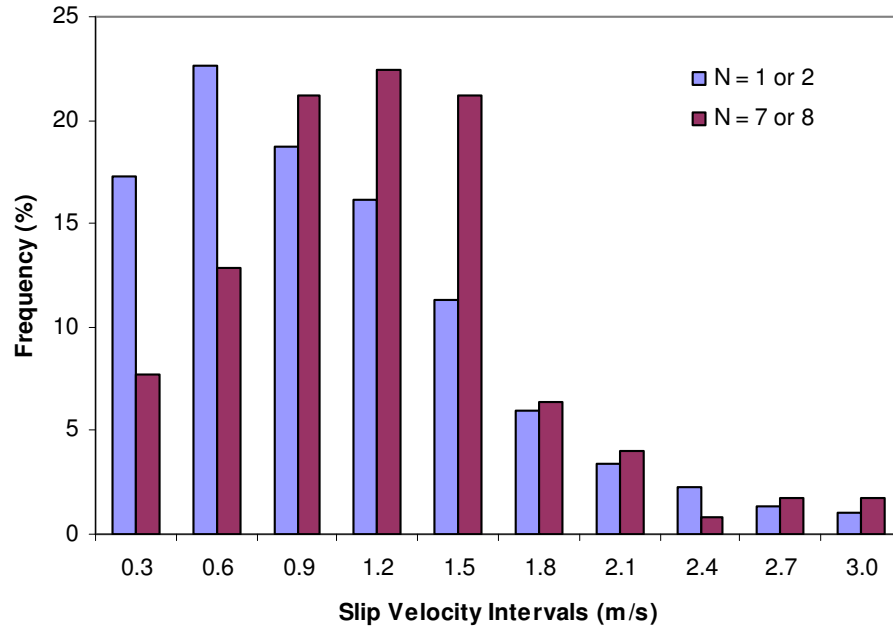


Figure 6–6: Cluster slip velocity distribution: $U_g=1.16$ m/s, $G_s=106$ kg/m²/s.

Table 6–3 summarizes the total number of clusters studied at the various operating conditions of the present study, one can notice that more than 20,000 clusters were studied.

6.5 Particle Cluster Size Distribution Results

This section reports individual particle cluster size distributions results, the experimental data was obtained from the 1 inch internal diameter gas–solid downflow reactor. To accomplish this, local cluster particle characteristics are determined using a significantly enhanced data analysis. It is proven that for all conditions considered, cluster particle size distributions are consistently asymmetric, with cluster sizes varying from 1 to 9 average size particles, and with the smaller clusters being the most abundant.

Table 6–3: Operating conditions and number of clusters studied.

Operational Condition #	Gas Velocity (U_g , m/s)	Solid Mass Flux (G_s , kg/m ² /s)	Number of Cluster Studied
1	0.95	10	899
2	1.43	15	1,209
3	1.18	50	1,355
4	1.72	28	1,896
5	2.54	46	1,509
6	1.25	65	2,823
7	1.85	57	1,675
8	2.53	76	1,442
9	1.16	106	3,272
10	1.68	82	2,444
11	2.52	91	2,143

To establish cluster sizes, the string cluster configuration proposed by [Krol et al. \(2000\)](#) was assumed as applicable in the present study. Thus, we can assume that particles agglomerate on the basis of a number of leading particles, which are followed by a number of trailing particles. This vertical chain of N number of particles in contact with each other is a hydrodynamically favored cluster shape. This favored cluster shape offers a configuration where drag forces are minimized. Therefore, the cluster shape is assumed to be a vertical chain of N number of spherical particles in contact with each other. The numbers of particles in each one of these clusters can be estimated according to the Equation (6–2) as follows,

$$N_i = \frac{(U_{si}\Delta t_i) - h + d_p}{d_p} \quad (6-2)$$

where U_{si} represents the terminal velocity of the cluster i , at the corresponding pair of time series; Δt_i is the time that cluster i needs to move down into the sensing region of the upper optiprobe; h is the characteristic transversal dimension of the optiprobe sensing region (focal point); and d_p is the particle diameter ([Nova et al., 2004b](#)).

Therefore, to estimate a cluster size, it is necessary to first determine the cluster velocity U_s , with Equation (6–3),

$$U_{si} = \frac{d}{\tau_i} \quad (6-3)$$

where d is the distance between the upper and lower focal sensor regions; and τ_i represents the time shift or time displacement between both signals for the cluster i .

Once the time shift is obtained via signal cross-correlation, as proposed by [Lanza et al. \(2012\)](#), and given that the spacing d between the upper and lower focal regions equals 0.006 m, the cluster velocity can be calculated. For instance, in the case of Figure 5–1, the time displacement is 0.0024 s. The cluster velocity, U_{si} , can, thus, be determined to be 2.456 m/s. Therefore, for the upper optiprobe signal (Figure 5–1), the number of particles can be estimated as:

$$\begin{aligned} N_i &= \frac{(U_{si}\Delta t_i) - h + d_p}{d_p} \\ &= \frac{\left(2.456 \frac{m}{s}\right) (0.00018 s) - (118 \cdot 10^{-6} m) + (84.42 \cdot 10^{-6} m)}{(84.42 \cdot 10^{-6} m)} \\ &= 4.84 \approx 5 \text{ particles} \end{aligned}$$

Given that for every cluster in a size distribution, the calculated particle number is most likely to be a decimal number, one can approximate the size of every cluster using the closest integer class.

Table 6–4 summarizes the operating conditions considered for the present cluster size distribution study. Information obtained at 10 radial positions was used for calculations. The downer tube cross-section was divided into 10 concentric annuli and the solid mass flux, G_s , was determined in each circular strip of cross-section area as proposed by [Qi et al. \(2008\)](#). It was judged that these data in conjunction with the enhanced data analysis, provide an adequate evaluation of the local averaged solid concentration at various radial downer positions.

Table 6–4: Operating conditions and number of clusters considered for cluster size distribution study.

Operational Condition #	Gas Velocity (U_g , m/s)	Solid Mass Flux (G_s , kg/m ² /s)	Number of Cluster Studied
1	0.95	10	899
2	1.43	15	1,209
3	1.18	50	1,355
4	1.85	57	1,675
5	1.25	65	2,823
6	2.53	76	1,442
7	1.68	82	2,444
8	2.52	91	2,143
9	1.16	106	3,272

On the other hand, Figure 6–7 describes the observed individual particle cluster size distributions. In this figure, the total number of clusters observed for each operational condition in the complete downer cross-sectional area is reported. The vertical axis of Figure 6–7 reports particle cluster size distributions on a percentage basis while the horizontal axis reports the operational conditions studied (e.g. solid mass flux, G_s , and gas velocities, U_g). The side legend in Figure 6–7 describes the cluster sizes established as a number of 84.42 μm average particles: from 1 to 10 average particle sizes.

It can be noticed in Figure 6–7 that, for a given operational condition and cluster population, the cluster size distribution is asymmetric with smaller particle clusters being more dominant than larger clusters. Figure 6–8 reports a zoom of the $G_s=91.2$ kg/m²/s, and $U_g=2.5$ m/s condition where more than 28% of clusters have only one particle. Moreover, the sum of all clusters with an N value larger than 6 is, in this case, smaller than 15%. These strongly asymmetric distributions of cluster size and cluster slip velocity were found to be a characteristic cluster feature for all operating conditions considered in the present PhD dissertation cluster size study. This means that clusters with a large number of particles are less likely to survive. One can argue that this behavior is the result of the collision between clusters, with this collision tending to break larger clusters in smaller ones.

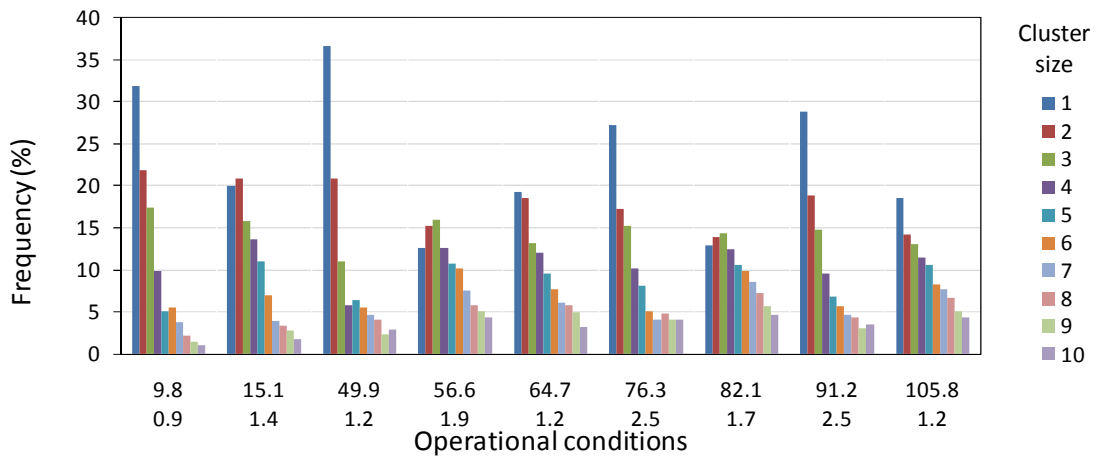


Figure 6–7: Individual particle cluster size distributions at various solid fluxes and gas velocities.

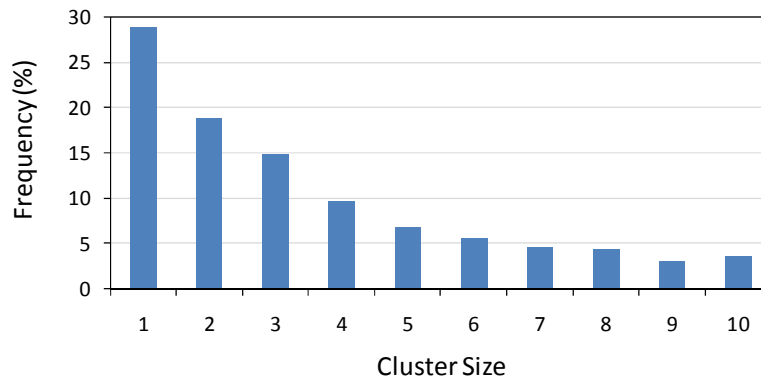


Figure 6–8: Distribution of the number of particles in clusters for $U_g=2.5$ m/s, $G_s=91.2$ kg/m²/s.

Figure 6–9 provides a weighted average of individual particle cluster size distributions for the complete set of operational conditions. The error bars represent the weighted standard deviation. As a result, one can conclude that for all operational conditions considered, the cluster size distributions are asymmetric with smaller particle clusters being more dominant than larger particle clusters.

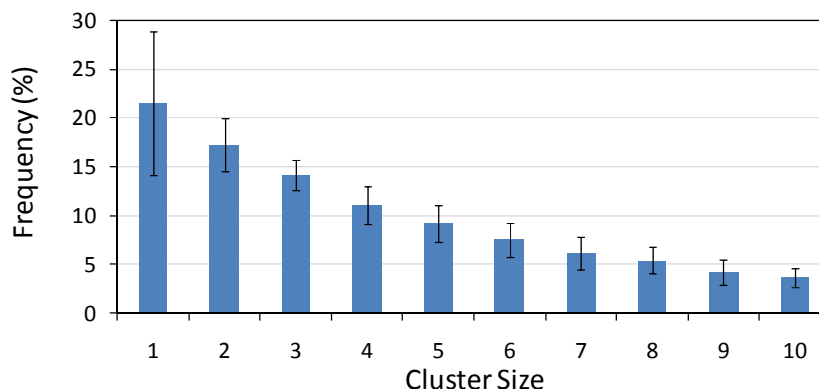


Figure 6–9: Individual particle cluster size distribution averages.

To gain a better understanding of the particle cluster size distributions in downers reactors, the radial position influence on cluster size distribution was also considered. Figure 6–10 reports cluster size distribution changes with radial positions having $r/R=0$ as the column center and $r/R=1$ as the internal downer wall, the legend in this figure describes cluster sizes established on the basis of the number of average particle sizes (e.g., from 1 to 10). Values of the distributions reported in Figure 6–10, correspond to weighted average distributions with error bars representing weighted standard deviations.

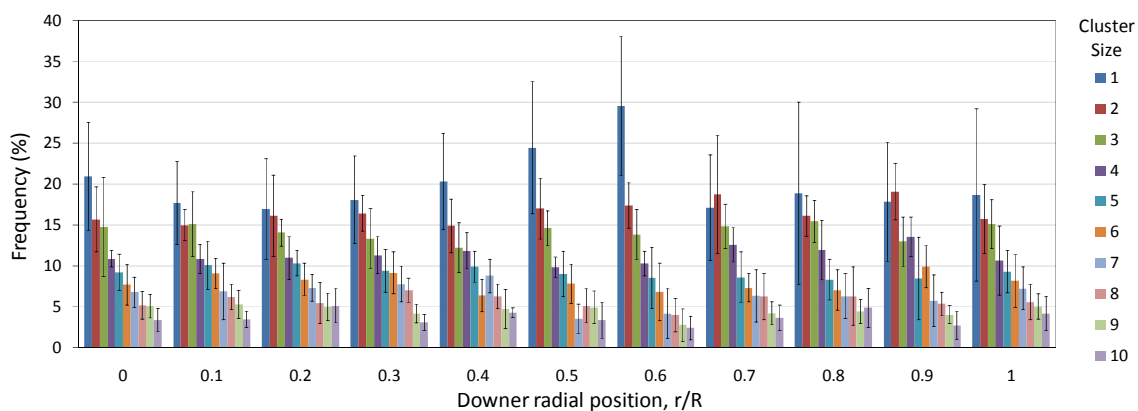


Figure 6–10: Individual particle cluster size distribution weighted averages for all operational conditions studied.

Figure 6–11 reports a zoom of the individual cluster size distribution weighted averages at $r/R=0$ in Figure 6–10. One can notice that the cluster size distributions in downers are in agreement with the total average distributions as described in Figure 6–9. This provides confirmation that it is more likely to find clusters in a downer with just a few particles, than to find clusters with a large number of particles.

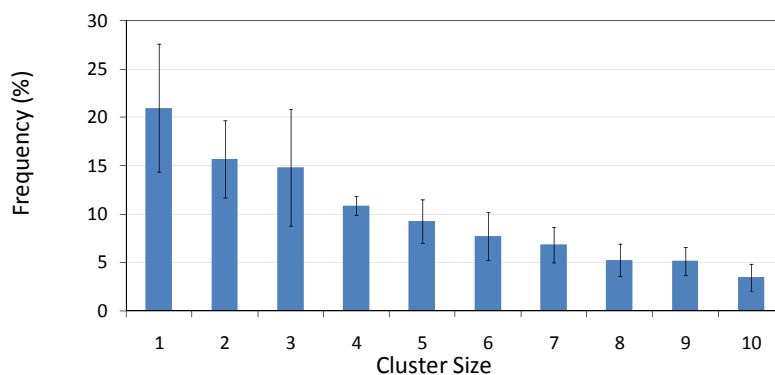


Figure 6–11: Individual cluster size distribution averages at $r/R=0$ radial position.

Thus, as shown in Figure 6–10 the cluster size distributions found in this study are consistently asymmetric, with smaller particle clusters being the most dominant with this trend being independent of the radial position. It is our view that these typical cluster size distributions are of great importance for the fluid dynamic simulation and design of downer reactors for industrial applications.

6.6 Mechanistic Model for the Cluster Drag Coefficient Calculation

A key fluid dynamic parameter in downer units is the cluster drag coefficient. A generally recognized fundamental expression for calculating the particle drag coefficient can be based on a balance of forces, as described in Figure 6–12 (Sommerfeld, 2010; Gibilaro, 2001; Kunii et al., 1991). One can thus, refer to the net effect of gravity and buoyancy on a particle as the effective weight, w_e :

$$w_e = f_g + f_b = -V_p(\rho_s - \rho_g)g \quad (6-4)$$

where V_p is the particle volume.

At equilibrium conditions, the drag force, f_d , equates to this effective particle weight, w_e such as

$$f_d = -w_e \quad (6-5)$$

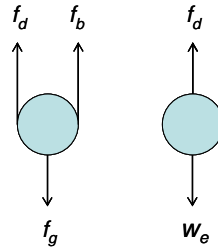


Figure 6–12: Main forces acting on single particles.

Furthermore, for a single particle, the drag force can be expressed in term of the drag coefficient, C_d , using the following equation,

$$f_d = \frac{1}{2} \rho_g A_s C_d U_{slip}^2 \quad (6-6)$$

where A_s is the cross-section area of a spherical particle.

Bearing in mind that the cluster configuration proposed by [Krol et al. \(2000\)](#) was assumed as applicable, an adaptation of the drag force was considered using: a) cluster cross-section area equivalent to the cross-section area of the first spherical particle, and b) cluster volume defined as one characteristic particle volume multiplied by the N numbers of particles present in the cluster under consideration,

$$A_c = A_s = \frac{\pi d_s^2}{4} \quad (6-7)$$

$$V_c = NV_s = N \frac{\pi d_s^3}{6} \quad (6-8)$$

Thus, replacing the corresponding terms, for the cluster configuration assumed, Equation (6-4) can be expressed as:

$$\frac{1}{2} \rho_g \left(\frac{\pi d_s^2}{4} \right) C_d U_{slip}^2 = N \left(\frac{\pi d_s^3}{6} \right) (\rho_s - \rho_g) g \quad (6-9)$$

And solving for C_d , one can obtain,

$$C_d = \frac{4}{3} \left(\frac{\rho_s - \rho_g}{\rho_g} \right) g d_s \frac{N}{U_{slip}^2} \quad (6-10)$$

As it frequently encountered in the technical literature (Sommerfeld, 2010; Islam et al., 2010; Islam, 2010; Chhabra et al., 1999; Gibilaro, 2001; Haider and Levenspiel, 1989; Kunii et al., 1991; Zhou et al., 1995), it is convenient to express the drag coefficient in terms of the particle Reynolds' number, a dimensionless parameter relating inertial and viscous forces. In this study, the characteristic length involved in the viscous forces term was assumed to be the equivalent particle diameter of a sphere with the same cluster volume.

$$Re = \frac{U_{slip} \rho_g d_s}{\mu_g} \quad (6-11)$$

Consequently, solving Equation (6-11) for U_{slip} and replacing it in Equation (6-10), one can obtain a mechanistic expression to estimate the drag coefficient in downer reactors.

$$C_d = \frac{4d_s^3 (\rho_s - \rho_g) \rho_g g N}{3\mu_g^2 Re^2} \quad (6-12)$$

Thus, for any cluster configuration and Reynolds number the following plot as reported in Figure 6-13 can be obtained.

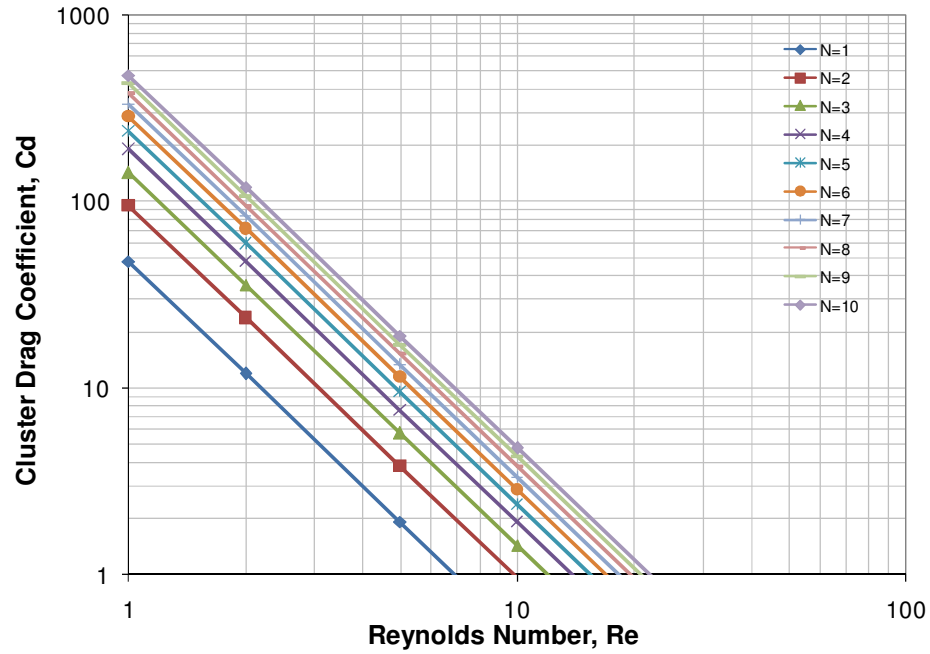


Figure 6–13: Cluster drag coefficient dependence with Reynolds number according with Equation (6–12).

Haider and Levenspiel (1989) developed an empirical equation to determine the drag coefficient for nonspherical particles as follows:

$$C_d = \frac{24}{Re} \left[1 + e^{(2.3288 - 6.4581\Phi + 2.4486\Phi^2)} \cdot Re^{(0.0964 + 0.5565\Phi)} \right] + \frac{Re \cdot e^{(4.905 - 13.8944\Phi + 18.4222\Phi^2 - 10.2599\Phi^3)}}{Re + e^{(1.4681 + 12.2584\Phi - 20.7322\Phi^2 + 15.8855\Phi^3)}} \quad (6-13)$$

where Φ is the cluster sphericity, and it can be obtained as:

$$\Phi = \frac{s}{S} \quad (6-14)$$

and s is the surface of a sphere having the same volume as the cluster and S is the actual surface area of the cluster (Chhabra et al., 1999).

In the present study the cluster sphericity is considered equal to:

$$\Phi = N^{-1/3} \quad (6-15)$$

Thus, combining Equation (6–13) with Equation (6–12), one solution for each cluster configuration can be obtained for various N values. Figure 6–14 reports the solution points for each value of N . In this respect, one can notice that it is possible to have clusters with same length but with different drag coefficients. This apparent ambiguity can be explained using Equation (6–10), where the key variable is the particle size. This is certainly of significance given that in the present study there is a distribution of FCC particle sizes, as reported by Islam (2010).

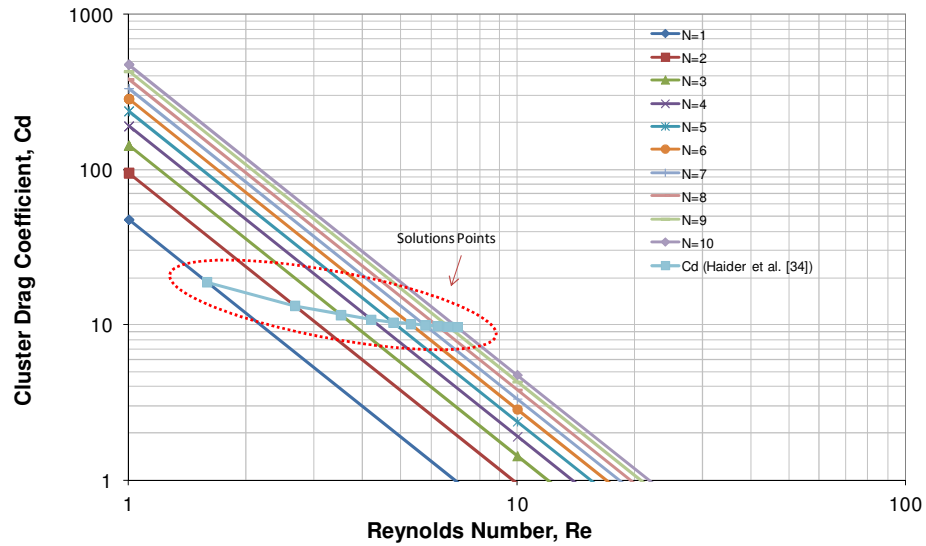


Figure 6–14: Change of the CD with Re. Solution Points for Equations (6–12) and (6–13).

Thus, based on the particle size distribution, and following the methodology proposed in the present PhD dissertation, it is possible to estimate both a maximum and a minimum C_d as follow:

$$C_{d,min} = \frac{4\gamma_{min}d_s^3(\rho_s - \rho_g)\rho_g g N}{3\mu_g^2 Re^2} \quad (6-16)$$

and,

$$C_{d,max} = \frac{4\gamma_{max}d_s^3(\rho_s - \rho_g)\rho_g g N}{3\mu_g^2 Re^2} \quad (6-17)$$

where γ_{min} and γ_{max} are correction factors that can be calculated according to the cluster particle size configuration as considered using Eqs (6-18) and (6-19).

$$\gamma_{min} = \frac{3}{2d_s} \left(\frac{V_c}{A_p} \right)_{min} \quad (6-18)$$

$$\gamma_{max} = \frac{3}{2d_s} \left(\frac{V_c}{A_p} \right)_{max} \quad (6-19)$$

In this respect, it is necessary to estimate γ_{min} with the particle cluster configuration that provides a minimum ratio between the cluster volume, V_c , and the cluster projected area, A_s . As well one has to estimate γ_{max} for the cluster configuration that provides a maximum ratio between cluster volume, V_c , and cluster projected area, A_s . In both cases d_s is the diameter of an equivalent sphere with the same volume that the particles in the cluster.

To enhance the estimation of the drag coefficient two approaches were studied. In Figure 6-15 the Equation (6-13) proposed by [Haider and Levenspiel \(1989\)](#) was used, while in Figure 6-16 the Equation (6-20) proposed by [Ganser \(1993\)](#) was employed.

$$C_d = \left\{ \frac{24}{ReK_1K_2} [1 + 0.1118(ReK_1K_2)^{0.6567}] + \frac{0.4305}{1 + \frac{3305}{ReK_1K_2}} \right\} K_2 \quad (6-20)$$

$$Re = \frac{2\rho_f U_{slip}}{\mu_f} \left(\frac{3V_c}{4\pi} \right)^{1/3} \quad (6-21)$$

$$K_1 = \frac{3}{1 + \frac{2}{\sqrt{\phi}}} \quad (6-22)$$

$$K_2 = 10^{K_3} \quad (6-23)$$

$$K_3 = 1.8148(-\log\Phi)^{0.5743} \quad (6-24)$$

Regarding Equation (6–20), the applicability of this type of correlation was suggested by [Islam et al. \(2010\)](#), [Chhabra et al. \(1999\)](#), [Zhou et al. \(1995\)](#), [Ganser \(1993\)](#), and [Haider and Levenspiel \(1989\)](#). This correlation can be applied to a cluster–based drag coefficient and within a restricted range of Reynolds numbers ($4 < Re < 12$).

Figure 6–15 and Figure 6–16 report C_d for particle clusters with different configurations (e.g. $N=1, 2, 3, 4$). One can notice that [Ganser \(1993\)](#) or [Haider and Levenspiel \(1989\)](#) correlations can be used along with Eqs. (6–16) and (6–17) as proposed in the present study. Both correlations provide very close C_d values and as a result either one could be used for assessing cluster slip velocities.

In order to explain this cluster behavior one can consider for instance a five particle cluster ($N=5$) led by a 50 micron particle. It is quite apparent that the drag coefficient for this cluster is quite different than if the same five particle cluster is led by a 100 micron particle. Thus, these various configurations inevitably lead to particle clusters of the same length displaying however significant cluster drag coefficients variation, as shown in Figure 6–15 and Figure 6–16.

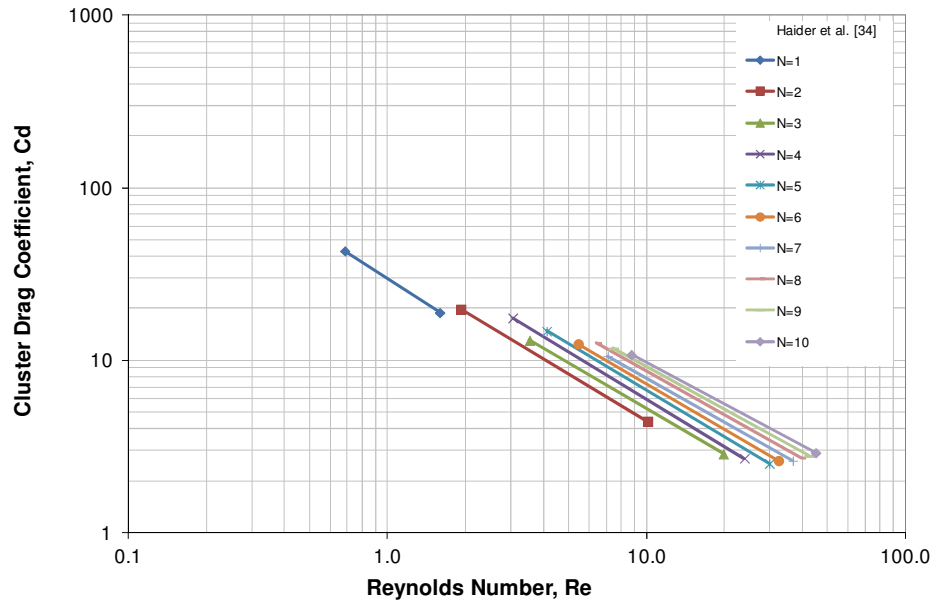


Figure 6–15: Maximum and minimum cluster drag coefficients estimated with Haider and Levenspiel (1989) correlation.

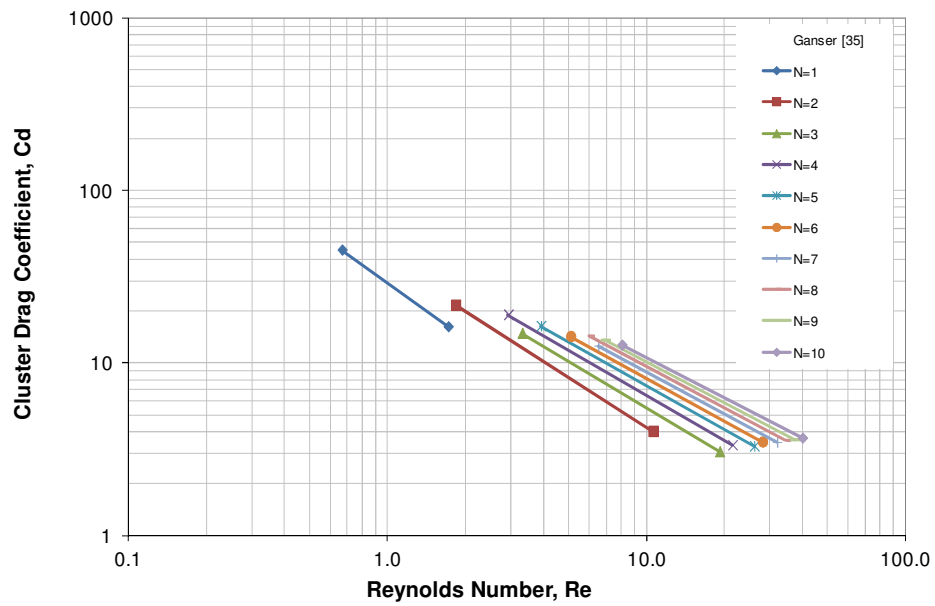


Figure 6–16: Maximum and minimum cluster drag coefficients estimated with Ganser (1993) correlation.

Figure 6–17 reports a 2D distribution diagram showing frequency of cluster slip velocity versus number of particles combination for a total population of 20,667 clusters, as detected using the CREC–GS–Optiprobe. The color–bar represents a fraction of the population sharing a same cluster slip velocity and number of particles combination. For instance, one can see that the dark red–orange zones show a higher abundance of particle clusters with 2–3 particles and cluster velocities varying in the 0.5–1 m/s range.

Moreover, broken lines in Figure 6–17 report the expected maximum and minimum slip velocity obtained using the methodology proposed in this manuscript along with the [Ganser \(1993\)](#) or [Haider and Levenspiel \(1989\)](#) correlations.

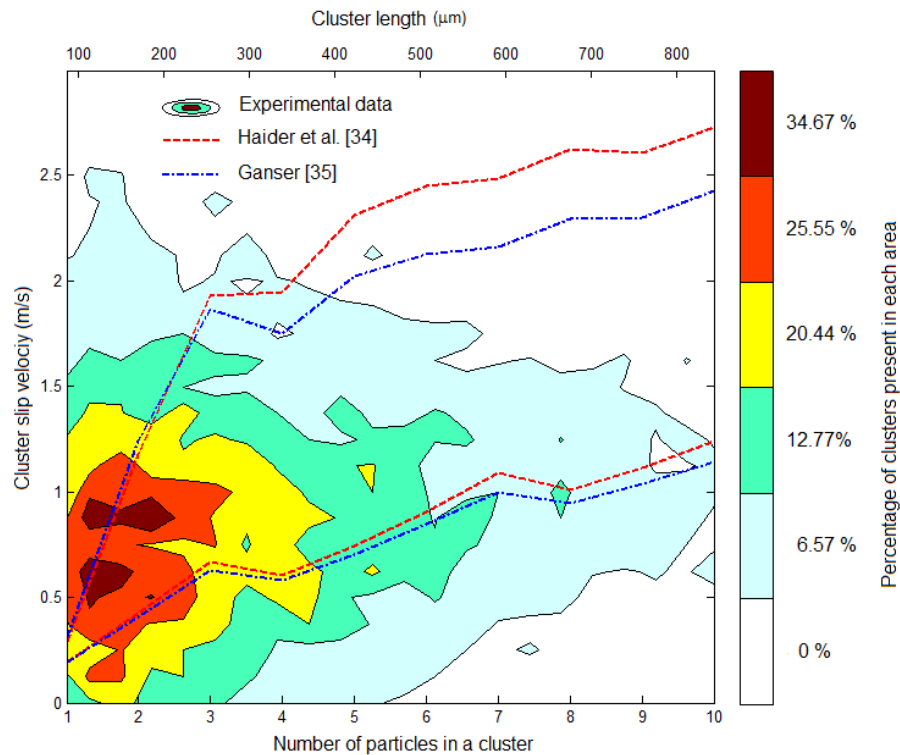


Figure 6–17: Theoretical and experimental cluster slip velocities for various cluster lengths. Experimental data are reported in color zones. Color zones represent fractions of the 20,667 total clusters population sharing the same cluster slip velocity and number of particles.

Results shown in Figure 6–17 demonstrate that equations [Ganser \(1993\)](#) or [Haider and Levenspiel \(1989\)](#) provide good cluster slip velocity predictions for various N parameters. One can notice that more than 78% of the reported clusters fall between the maximum and minimum slip velocity theoretical ranges, which are represented by the broken lines. This means that a high fraction of experimentally observed clusters (78%) display a fluid dynamic behavior in good agreement with the theoretical expected values.

6.7 Conclusions

As a summary of this section, the following conclusions can be highlighted:

- a) Data obtained with a CREC–GS–Optiprobe was successfully applied to characterize cluster fluid dynamic of the gas solid concurrent flow in a down flow reactor.
- b) A new methodology using data obtained using the CREC–GS–Optiprobe and targeted to set the time series signal baseline is proposed. The reported results show that the baseline reference factor, n , decreased when solid mass flux, G_s , increased. Additionally, the gas velocity does not have a strong influence on the baseline reference factor. With this new methodology one can calculate cluster velocities and cluster sizes with increased confidence.
- c) Particle cluster size distributions show that particle clusters display asymmetric distributions with smaller particle clusters being the most dominant. This finding was true for all operating conditions and various radial positions considered.
- d) Using this data, the fluid dynamic of the gas–solid two phase flow in downer unit is established and this for a wide range of superficial gas velocities and solid mass fluxes. Reported results include: cluster solid concentrations, individual cluster slip velocities, cluster sizes and cluster drag coefficients.
- e) A mechanistic based method is proposed to calculate cluster drag coefficients with the cluster drag coefficient being a function of the cluster length and cluster particles size configuration contained in each cluster. A well defined range of possible drag coefficient is reported in this manuscript for each cluster length.

Chapter 7

7 Computational Particle Fluid Dynamics Modeling of the One inch Internal Diameter Downer unit.

Given the status of the development of downer models and the potential interest in scaling them up, one can acknowledge the significance of specific model validation using experimental data.

Consequently, in this section a gas–solid downflow comparative study is reported. Calculations are developed using the CPFDF numerical scheme with an cluster size distribution for each operating condition, the cluster size distribution was calculated as the particle size distribution times the weighted average number of average particle determined as reported in [Lanza et al. \(2013\)](#). The simulation conditions are selected so that the calculated results could be directly compared with experimental results. It is observed that the successful comparison of experimental and simulated results provides strong support for a phenomenologically based model for downer units. This is the first study in the technical literature that we are aware of, where such a model using solid hold–ups and cluster velocities is validated with experimental data.

7.1 Computational Method

The fluid dynamics in the developed flow region of a concurrent gas–solid downflow fluidized bed unit was simulated using a Computational Particle Fluid Dynamics (CPFDF) numerical scheme. The CPFDF model includes particles represented as clusters. This model is validated with experimental data obtained in a 1 inch internal diameter downer unit. In this downer unit, air and solid particles are fed at the top of the downer with experimental data being collected at its bottom. Observed time–averaged axial and radial velocities and solid concentration profiles are successfully simulated by CPFDF calculations. These findings support; a) a narrow distribution of particle cluster catalyst residences, b) the characteristic particle “forward” mixing, c) the relatively flat radial solid concentrations and solid cluster velocities.

Using the CPFD methodology the gas and particle equations are solved in three dimensions. The gas phase dynamics is described by averaged Navier–Stokes equations (mass and momentum) with a strong coupling to the particle phase. The particle momentum equation follows the multi–phase particle–in–cell (MP–PIC) formulation (Snider et al., 2011, 1998; Snider and Banerjee, 2010; O’Rourke and Snider, 2010; O’Rourke et al., 2009; Anderson, 2009; Amsden et al., 1989; Auzerais et al., 1988).

7.1.1 Gas Phase Model

In a downer reactor, the averaged mass and momentum equations for the gas phase are:

$$\frac{\partial(\varepsilon_g \rho_g)}{\partial t} + \nabla \cdot (\varepsilon_g \rho_g \mathbf{U}_g) = 0 \quad (7-1)$$

$$\frac{\partial(\varepsilon_g \rho_g \mathbf{U}_g)}{\partial t} + \nabla \cdot (\varepsilon_g \rho_g \mathbf{U}_g \mathbf{U}_g) = -\nabla p - \mathbf{F} + \varepsilon_g \rho_g \mathbf{g} + \nabla \cdot (\varepsilon_g \boldsymbol{\tau}_g) \quad (7-2)$$

where ε_g is the gas volume fraction, ρ_g is the gas density, t is the time, \mathbf{U}_g is the gas velocity vector, p is the gas pressure, $\boldsymbol{\tau}_g$ is the gas stress tensor, \mathbf{g} is the gravitational acceleration, and \mathbf{F} is the rate of momentum exchange per volume between the gas and particle phases.

In Equation (7-2), there is a non–hydrostatic component of the stress, $\boldsymbol{\tau}_g$. The value of this term depends on the rate of deformation, which for a Newtonian fluid it can be represented as follows:

$$\tau_{g_{ij}} = 2\mu S_{ij} - \frac{2}{3} 2\mu_g \delta_{ij} \frac{\partial U_i}{\partial U_j} \quad (7-3)$$

and

$$S_{ij} = \frac{1}{2} \left(\frac{\partial U_i}{\partial x_j} + \frac{\partial U_j}{\partial x_i} \right) \quad (7-4)$$

where μ_g is the coefficient of dynamic viscosity which depends only on the thermodynamics state of the gas, δ_{ij} is the Dirac delta function ($\delta_{ij}=1$ if $i=j$ and $\delta_{ij}=0$ if $i \neq j$).

Furthermore, the mass and momentum balances as per Eqs (7–1) and (7–2) can be considered isothermal and compressible. In addition, the total pressure of the system is close to atmospheric pressure. Thus, the density can be related through the ideal gas equation of state.

$$p = \frac{\rho_g RT}{Mw_g} \quad (7-5)$$

where R is the universal gas constant, T is the temperature (300 K constant), ρ_g is the gas density, and Mw_g is the gas molecular weight. There is no mass transfer between the gas and particle phases, neither a potential contribution of the chemical reactions.

One should mention that \mathbf{F} , the rate of momentum exchange between phases, is reported later in this manuscript in section 7.1.3 (coupling gas and particle phases).

7.1.2 Particle Phase Model

To make numerical computations tractable in a multiparticle system, the physics of the particle phase is predicted by solving a transport equation for an “*ensemble of particles*” (Snider et al., 1998). In this manner, the dynamics of the particle phase can be represented by a Particle Distribution Function (PDF) f .

This PDF f represents a number of particles per unit volume with similar local properties. Thus, in our case, f is a function of: a) the particle ensemble spatial location \mathbf{x} , b) the particle ensemble velocity \mathbf{U}_s , c) the particle ensemble mass m_p , and d) the time t . Possible dependencies of f on particle temperature and composition are neglected given isothermal conditions in the downer with neither mass transfer between phases, nor particle vaporization. Therefore, $f(\mathbf{x}, m_s, \mathbf{U}_s, t) dm_s d\mathbf{U}_s$ is the average number of particles per unit volume with velocities in the interval $(\mathbf{U}_s, \mathbf{U}_s + d\mathbf{U}_s)$, and masses in the interval $(m_s, m_s + dm_s)$.

Thus, the time rate of change of the particle distribution function f , can be calculated using a transport conservation equation in the multi-dimensional space. This transport equation includes a particle collision damping term as suggested by [O'Rourke and Snider \(2010\)](#) and [O'Rourke et al. \(2009\)](#).

$$\frac{\partial f}{\partial t} + \frac{\partial(f\mathbf{U}_s)}{\partial \mathbf{x}} + \frac{\partial(f\mathbf{a}_s)}{\partial \mathbf{U}_s} = \left(\frac{\partial f}{\partial t}\right)_{coll}^D \quad (7-6)$$

With the collision damping term given by,

$$\left(\frac{\partial f}{\partial t}\right)_{coll}^D = \frac{f_D - f}{\tau_D} \quad (7-7)$$

where τ_D is the collision damping time, f_D is the PDF obtained by collapsing the velocity dependency of f to a delta function centered about the mass-averaged particle velocity $\bar{\mathbf{u}}_s$, the reader is referred to [O'Rourke and Snider \(2010\)](#) for more details.

The particle acceleration \mathbf{a}_s in Equation (7-6), can be expressed as follows:

$$\mathbf{a}_s = \frac{d\mathbf{U}_s}{dt} = D_s(\mathbf{U}_g - \mathbf{U}_s) - \frac{1}{\rho_s} \nabla p + \mathbf{g} - \frac{1}{\varepsilon_s \rho_s} \nabla \tau_s + \frac{\bar{\mathbf{U}}_s - \mathbf{U}_s}{\tau_D} \quad (7-8)$$

where, \mathbf{U}_g is the local mean gas velocity; ε_s is the solid volume fraction; \mathbf{U}_s is the particle velocity; ρ_s is the particle density; \mathbf{g} is the gravitational acceleration; D_s is the drag function which depends on the particle size, velocity, position, and time. D_s is further described in section 0 (drag model) of this manuscript. τ_{sp} is the particle contact stress, which depends on spatial location; and $\bar{\mathbf{U}}_s$ is the local mass-averaged particle velocity.

The particle velocity is defined as,

$$\mathbf{U}_s = \frac{d\mathbf{x}}{dt} \quad (7-9)$$

with the particle normal stress exerted by particle–particle collisions in Equation (7–8), calculated as proposed by [Auzerais et al. \(1988\)](#).

$$\tau_s = \frac{P_s \varepsilon_s^\gamma}{\varepsilon_{cp} - \varepsilon_s} \quad (7-10)$$

where P_s is a positive constant with pressure units, ε_{cp} is the particle volume fraction at close packing, and γ is a parameter with recommended values between 2 to 5 ([Auzerais et al., 1988](#)).

One should note that τ_s within particle agglomerates cannot exceed the compressive yield stress. Otherwise, the particle cluster collapses forming a higher close packing with ε_{cp} being capable of bearing the load. In addition, the volume filled by spherical particles is the one of random close packing and cannot exceed a density limit of 63.4%. It is advisable that the particle normal stress denominator be calculated as in Equation (7–11) to avoid a zero singularity where the solids volume fraction equals ε_{cp} ([Andrews and O'Rourke, 1996](#)). Thus,

$$\tau_s = \frac{P_s \varepsilon_s^\gamma}{\max[(\varepsilon_{cp} - \varepsilon_s), \epsilon (1 - \varepsilon_s)]} \quad (7-11)$$

where ϵ is a small number in the order of 10^{-6} .

7.1.3 Coupling Gas and Particle Phases

The addition of fluid and particle volume fractions must be equal to one. This is required given there are no other phases forming the entire gas–solid system.

$$\varepsilon_s + \varepsilon_g = 1 \quad (7-12)$$

The particle volume fraction is related to the PDF f by:

$$\varepsilon_s = \iiint f V_s dV_s d\rho_s d\mathbf{U}_s \quad (7-13)$$

The inter–phase momentum transfer in Equation (7–2) is defined as ([Snider et al., 2011](#)):

$$\mathbf{F} = \iiint f V_s \rho_s \left[D_s(\mathbf{U}_g - \mathbf{U}_s) - \frac{1}{\rho_s} \nabla p \right] dV_s d\rho_s d\mathbf{U}_s \quad (7-14)$$

7.1.4 Turbulence model

The default mathematical model for turbulence used in Barracuda is Large Eddy Simulation (LES). In the LES model, the large eddies are calculated from the flow equations and the subgrid turbulence is captured with a model. As with other turbulence models, there is no accepted choice for a subgrid turbulence model for dense particle flow. Barracuda uses the [Smagorinsky \(1963\)](#) subgrid scale (SGS) model which calculates an eddy viscosity based on the notion that the effect of the SGS Reynolds stress is increased transport and dissipation. The form of subgrid scale eddy viscosity is:

$$\mu_t = C_s \Delta^2 |\bar{s}| \quad (7-15)$$

$$S_{ij} = \frac{1}{2} \left(\frac{\partial u_i}{\partial x_j} + \frac{\partial u_j}{\partial x_i} \right) \quad (7-16)$$

where Δ is the filter length. The common choice of filter length scale is $\Delta = (\delta x \delta y \delta z)^{1/3}$. The constant C_s may be a function of Reynolds number, geometry, and solids volume fraction. For channel flow, it is on the order of 0.005 and can be larger or smaller with a typical value on the order of 0.01.

7.1.5 Experimental Set-up and Simulation Conditions

The experimental data used to validate the CPFD simulations, were obtained in the first experimental riser-downer covering various radial positions and a broad range of experimental conditions. In the case of the present study, a 2.0 m high and 0.0257 m (1 inch) internal diameter column was used. Two CREC-GS-Optiprobes were placed at a 1.85 m distance in the downer below the injection port, and separated axially by 0.006 m. A schematic diagram of the experimental unit is presented in Figure 4-6. A detailed explanation regarding the design of this unit is reported in section 4.2.1 of the present PhD dissertation.

The FCC particles used in the experiments had a mean particle diameter of 84.42 μm with a standard deviation of 33.62 μm , and an apparent particle density of 1,722 kg/m^3 . Figure 7–1 shows the particle size distribution (PSD) curve. The fluidization gas was air close to ambient pressure and temperature. More details regarding to the FCC particles used can be found in section 4.3 of the present manuscript.

For Barracuda simulations in the downer unit, a CAD model of 2 m high and 0.0257 m column diameter has to be defined prior to any calculation. In the case of the present study, a particle free empty downer tube filled with air at standard pressure and temperature was used. In addition and consistent with the experimental data, air and solid particles were considered to be fed at the top of the downer with flow parameters (cluster particle concentration, cluster velocity) matching the ones observed at the exit of the downer.

The gas and solid high mixing feeder used in both downer units of the present PhD dissertation involves: a descending solid stream emerging from the bottom of a cyclone. This solid stream meets sixteen 0.5 mm impinging high velocity gas jets (30–50 m/s) angled at 45 degrees. It is expected, given the significant gas and solid momentum dissipation, that at the outlet of this feeder a uniform gas velocity and a cluster velocity in the 0.1–0.2 m/s range is obtained.

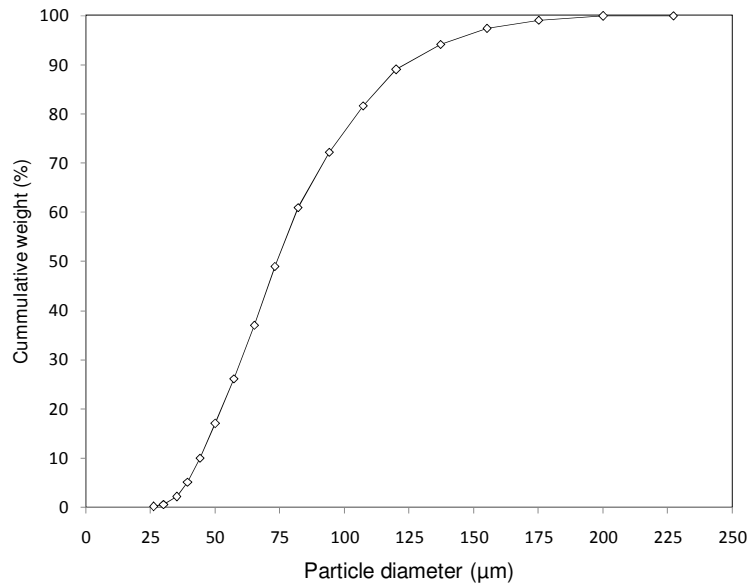


Figure 7–1: Particle Size Distribution (PSD) for the FCC particles of the present study.

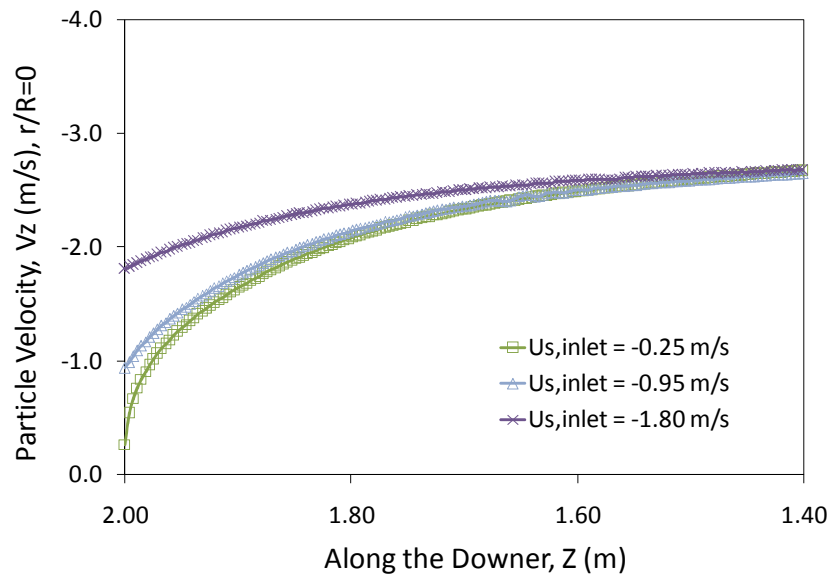


Figure 7–2: Inlet particle velocity sensitivity analysis.

Figure 7–2 reports the lack of influence of the particle velocity at the feeding point on the cluster velocity in the stabilized flow region. It is observed that even if a 0.25 m/s to 1.8 m/s initial particle velocity is assigned to clusters, after 0.4 m all clusters reach an

essentially identical stabilized velocity. As a result one can consider that at 1.85 m from the feeding point the cluster velocity is unaffected by the initial velocity. Thus, a 0.3–0.5 m/s initial cluster velocity, as adopted in the present study, is fully adequate for calculations in the stabilized flow region.

A chain like cluster geometry is considered in the simulations. This is in agreement with particle suspension conditions where there is a much higher influence of drag versus electrostatic forces. This “drag force dominated regime” was achieved using ammonia pretreated beds (0.01 m³ of ammonia hydroxide per 1 m³ of FCC catalyst), which lead to clusters with a “chain of particles” configuration (Krol et al., 2000).

A particle cluster can be formed in downer units when one cluster/particle falls in the wake of another cluster/particle. Alternatively, a cluster can break into two fragments, as result of hydrodynamic instability (Krol et al., 2000). Thus, the observed time signals from the CREC optiprobes reflect dynamic conditions with clusters being broken and reformed continuously.

7.2 Discretization Sensitivity Analysis

Barracuda is a computational particle fluid dynamics software package based on the multiphase particle-in-cell (MP-PIC) numeric method. This computational method is specifically formulated for coupled fluid-particle motion. To accomplish this, governing equations for the gas phase are treated as a continuum in the framework of an Eulerian grid, while the particles are modeled as discrete entities, or computational particles (clouds) in a Lagrangian framework.

Thus, on one hand, discretization for the fluid phase is performed on a spatial grid and the sensitivity of the solution to the grid size must be considered. On the other hand, the particulate phase is modeled as a discrete phase constituted by Lagrangian particles. Using this approach, particles are grouped into integral parcels or particle clouds. A particle cloud is an integer number of particles with all of them sharing the same properties. Thus, the use of particle clouds in downers to decrease the computational time and memory required in a fully-coupled, gas/particle flow calculations is possible. As a

result, physical models, such as particle drag applicable to individual particle clusters, can be considered to mimic the physics of the system. In other words, a “particle cloud” in a downer can be visualized as a group of particle clusters, following the motion of individual particle clusters. Therefore, discretization sensitivity with respect to “particle cloud” resolution must also be considered.

It is important to mention that the sensitivity of a solution to particle cloud resolution in downer units is a new topic to Barracuda users. This involves investigating the validity of the modeling assumptions whereby a number of actual particle clusters are represented by a lesser number of particle clouds. This is typically referred to as an average number of particle clouds per cell.

In summary, when using Barracuda, coarse to fine resolution studies have to be performed on both the number of ‘computational cells’ and the particle clusters fed per average volume. As a result, in this manuscript, this discretization analysis was developed as follows: i) First, a grid of $7 \times 7 \times 557$ (27,293) cells was set, ii) This grid was chosen given that it was considered reasonably coarse and providing a fast-running computational model. Then, a computational particle resolution study was developed increasing successively ten times the number of computational particles per average unit volume, n_p , going from 30 to 30,000. In this respect, the minimum number of computational particles per unit cell that is able to properly capture the fluid dynamics in the downer unit was established. Once the computational particle analysis was completed, a grid resolution study was also considered by approximately doubling the grid size from $7 \times 7 \times 557$ (27293) to $9 \times 9 \times 702$ (56,862) cells.

It can also be noticed that CPFDD involves the selection of a number of numerical particles. If this number is too large the CPFDD calculation may become very slow. On the other hand, if the number of numerical particles chosen is too small the simulation may become inaccurate. To address this issue, Table 7–1 reports the results of increasing the number of particles fed per average unit volume or n_p , from 30 to 30,000 having a relatively constant total number of particles of 2 million. One can observe that the total number of computational particles (clouds) in various runs increases from 13,257 up to

294,353 or about 1/8 of the total number of particles. Thus, one can notice that even for cases 3 and 4, there is significant savings in calculations in terms of both memory and computational time.

Table 7–1: Particle discretization analysis. Operating condition: $U_g=1.68$ m/s, $G_s=82$ kg/m²s.

Run #	Grid size	np (input value)	Number of particles	Number of clouds	Particles/Cell	Clouds/Cell	Particle/Clouds
1	7x7x557	30	1,897,585	12,257	69.5	0.49	143.1
2	7x7x557	300	2,089,276	115,107	76.5	4.22	18.2
3	7x7x557	3,000	2,141,667	256,744	78.5	9.41	8.3
4	7x7x557	30,000	2,139,651	294,353	78.4	10.78	7.3

In the present discretization analysis, the following conditions were used: $U_g=1.68$ m/s, $G_s=82$ kg/m²s. These conditions are typically representative of all the conditions which include an average value for both the gas superficial velocity and the solid flux. Furthermore, the drag model used is given in section 0 while particle cluster size distribution is reported in Table 7–5.

Figure 7–3, Figure 7–4, and Figure 7–5 report the estimated values for cluster particle velocity, particle volume fraction, and pressure along the downer. One can see that Run 1 which has the coarsest particle resolution, differs considerably from the calculated values of Runs 2, 3 and 4. On the other hand, one can also notice that Runs 2, 3 and 4 provide close values for particle cluster velocity, particle volume fraction and pressure. As a result, this shows that the 3,000 particles fed per average unit volume, provide acceptable value calculations, capturing the fluid dynamics in the down flow reactor of the present study.

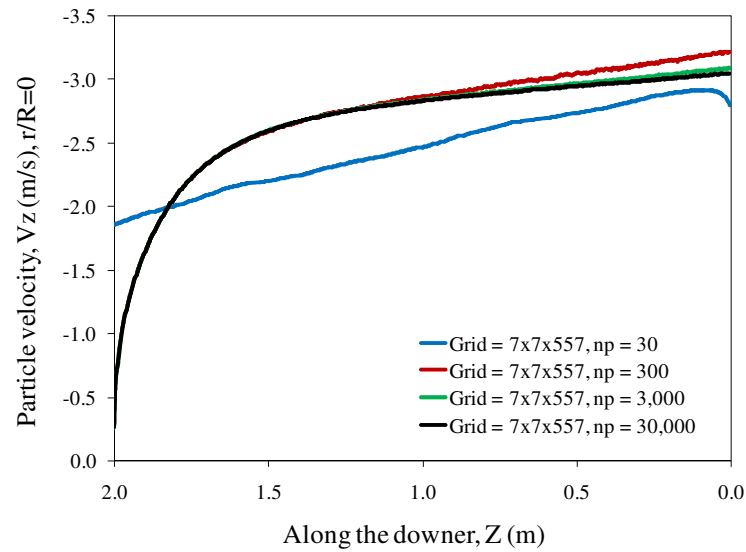


Figure 7–3: Effect of particle resolution on the calculated cluster particle velocity at the center line of the downer unit. Operating condition: $U_g=1.68$ m/s, $G_s=82$ kg/m²s.

Note: four different grids with n_p changing from 30–30,000 were used in the calculations.

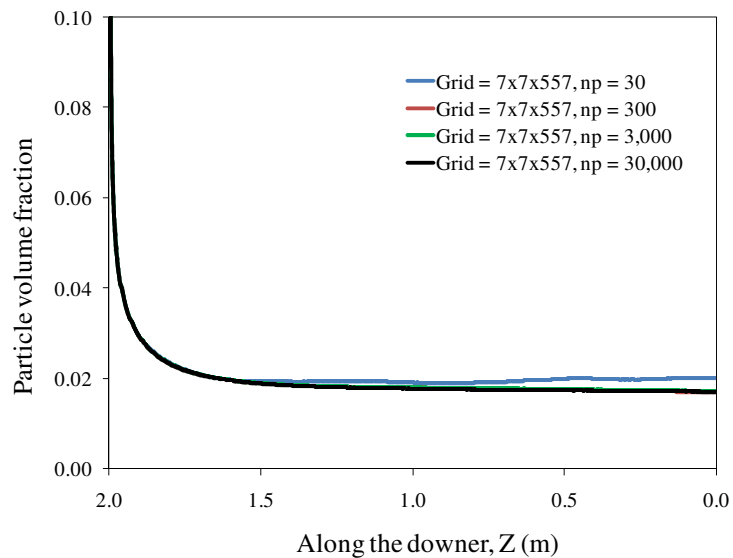


Figure 7–4: Effect of particle resolution on particle volume fraction at the center line in the downer unit. Operating condition: $U_g=1.68$ m/s, $G_s=82$ kg/m²s. Note: four different grids with n_p changing from 30–30,000 were used in the calculations.

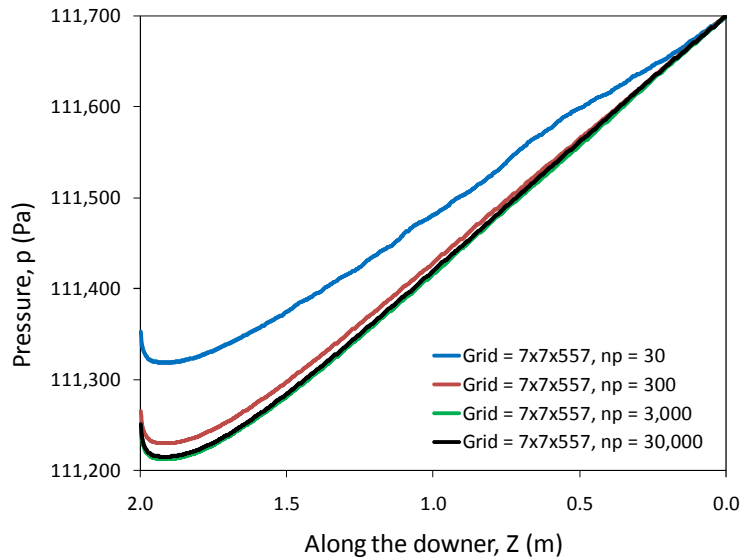


Figure 7–5: Effect of particle resolution on pressure in a downer unit of this study. Operating condition: $U_g=1.68$ m/s, $G_s=82$ kg/m²s. Note: four different grids with n_p changing from 30–30,000 were used in the calculations.

In regard to Figure 7–3, it reports the effect of particle resolution on the calculated cluster particle velocity at the center line of the downer unit. Figure 7–3 provides an indication that n_p has to be larger than 30 to yield a sound numerical solution given that: a) $n_p=30$ leads to particle/cluster velocities without physical meaning at the reactor entrance, and b) the calculated axial particle/cluster velocity differs significantly in shape from axial cluster velocity profiles calculated with larger n_p values.

To study the spatial discretization, the grid cells were roughly doubled. A new mesh with $9 \times 9 \times 702$ (56,862) cells was used. Table 7–2 reports the details. In addition, a third mesh of $21 \times 7 \times 557$ is also studied due to having eleven values along the downer radius from the CPFD simulations, makes it more convenient to compare them with the reported experimental data (Lanza et al., 2012) avoiding interpolations. Table 7–2 reports the details.

Table 7–2: Mesh discretization details

Run #	Grid size	np (input value)	Number of particles	Number of clouds	Particles/Cell	Clouds/Cell	Particle/Clouds
1	7x7x557	3,000	2,141,667	256,744	78.5	9.41	8.3
2	9x9x702	3,000	2,135,686	295,006	37.6	5.19	7.2
3	21x7x557	3,000	2,180,633	558,498	26.6	6.82	3.9

Doubling the number of cells and keeping the number of particles fed per average volume, n_p , constant, roughly decreases the number of clouds per cells by half. 2 million particles are modeled with less than 300,000 computational particles.

Figure 7–6, Figure 7–7, and Figure 7–8 report very similar cluster particle velocity, particle volume fraction and pressure changes using 7x7x557 and 9x9x702 grids. Therefore, the smaller number of cells 7x7x557 (27,293) with n_p of 3,000 particles was considered satisfactory for gas–particle fluid dynamic calculations.

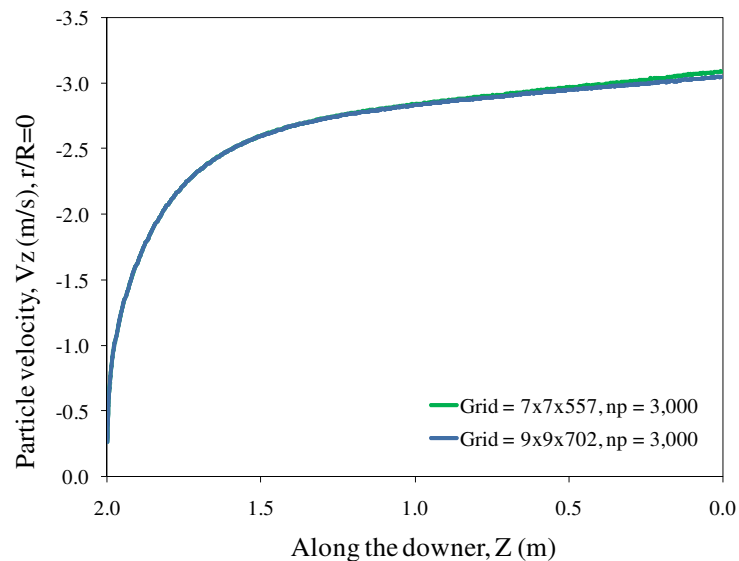


Figure 7–6: Effect of spatial resolution on cluster particle velocity at the center line of the downer unit. Operating condition: $U_g=1.68$ m/s, $G_s=82$ kg/m²s. Note: $n_p=3,000$, 7x7x557 and 9x9x702 grids were used in the calculations.

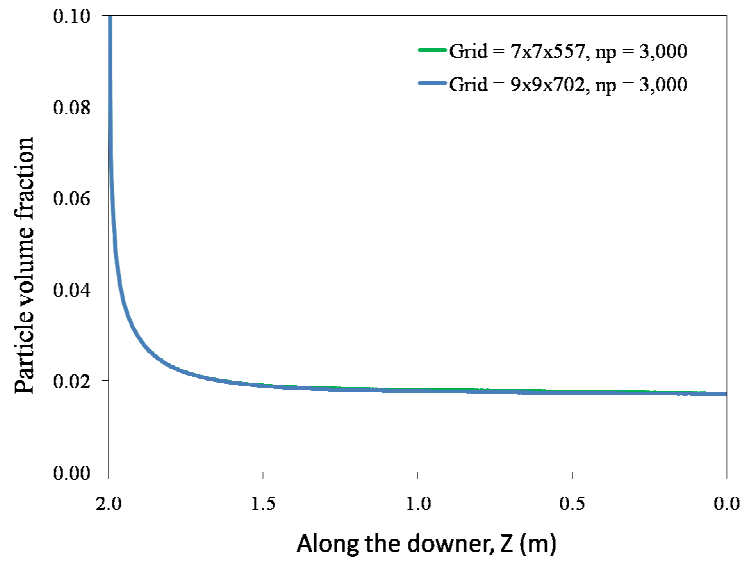


Figure 7–7: Effect of spatial resolution on particle volume fraction at the center line of the downer unit. Operating condition: $U_g=1.68$ m/s, $G_s=82$ kg/m²s. Note: $n_p=3,000$, $7 \times 7 \times 557$ and $9 \times 9 \times 702$ grids were used in the calculations.

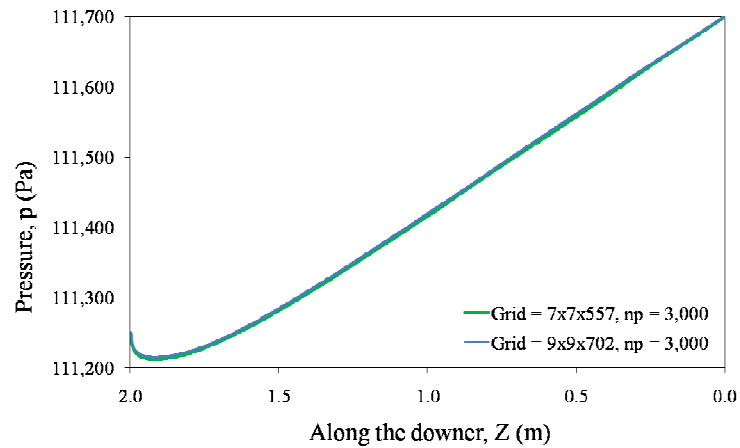


Figure 7–8: Effect of spatial resolution on pressure. Operating condition: $U_g=1.68$ m/s, $G_s=82$ kg/m²s. Note $n_p=3,000$, $7 \times 7 \times 557$ and $9 \times 9 \times 702$ grids were used in the calculations.

To validate the proposed model avoiding interpolations, the experimental results obtained by [Lanza et al. \(2012\)](#) are compared with the results of the CPFD simulations of the present study. Furthermore, the reported data have eleven values along the downer radius.

Thus a finer mesh in the radial direction versus the one considered in Table 7–1 was used to effectively compare data. To accomplish this, a 21x7x557 grid with 81,879 cells is considered instead.

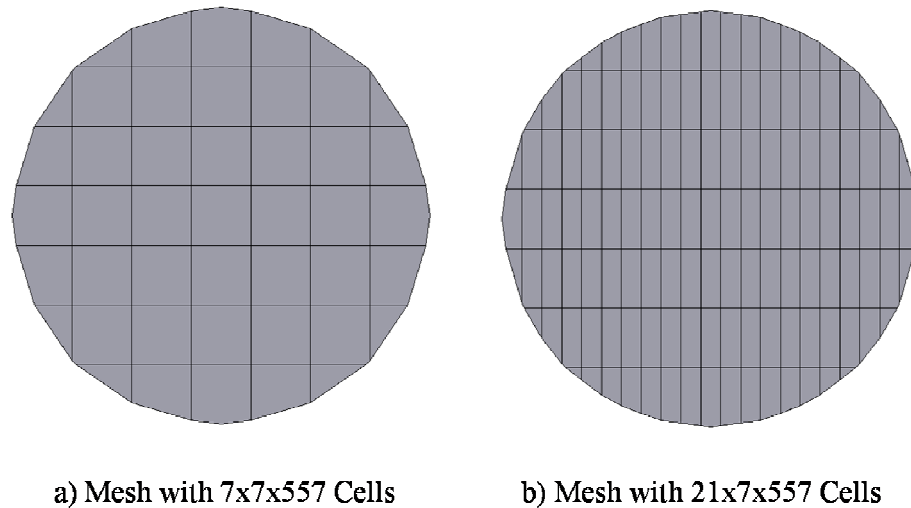


Figure 7–9: X–Y Grids used in the CPFD simulations.

Figure 7–9 reports the details of two different grids considered. The left hand Figure 7–9(a) represents the reference grid selected for the discretization analysis, while the right hand grid Figure 7–9(b) represents the grid used in the present study. One can notice that the grid Figure 7–9(b) has eleven cells along the radial position from $r/R=0$ (the center), to $r/R=1$ (the wall), as required for effective comparison with experimental data.

7.3 Boundary Conditions and Input Values

CPFD simulations require gas velocity and particle fluxes. Table 7–3 reports the operating conditions studied in the present manuscript. These conditions were the same as the ones reported in [Lanza et al. \(2012\)](#). This was done in order to have the identical conditions and being able to develop a thorough comparison of CPFD simulations and experimental results.

Regarding boundary conditions, one should consider that: a) at the wall surface no slip condition, $U_g=0$, U_s =terminal velocity, U_{slip} =terminal velocity, b) At the near wall region $U_g < U_s$, U_s =terminal velocity, and $U_{slip}=U_s-U_g$ with both U_g and U_s being larger than zero, having a turbulent gas velocity predicted with a 1/6 power model for predicting gas velocity in the near wall region. Once outside the near wall region, the U_s becomes progressively larger than the U_g .

Table 7–3: Operating conditions used in this study.

Operating condition #	Solid Mass Flux, Gs (kg/m ² s)	Gas Velocity, Ug (m/s)
1	10	0.95
2	15	1.43
3	46	2.54
4	50	1.18
5	57	1.85
6	65	1.25
7	76	2.53
8	82	1.68
9	91	2.52
10	106	1.16

The normal and tangential-to-wall momentum particle components in the near wall region are given by equation (7–8) with 0.95 restitution coefficients (refer to Table 7–4) (Abbasi et al., 2013). These two restitution coefficients were selected as recommended by Zhao et al. (2010).

Furthermore, Table 7–4 reports the various input parameters required for the CPFD simulation.

Table 7–4: Input parameters in the CPFD Simulation.

	Geometry	Cylinder 2.632 (cm) diameter 2 (m) height
	Mesh	21x7x557
Heat transfer	Isothermal flow	300 (K)
Gravity	Z Gravity	-9.8 (m/s ²)
	Gas density, ρ_g	1.17285 (kg/m ³)
	Gas molecular weight	28.9652 (g/mol)
	Gas viscosity, μ_g	1.84951e-05 (Pa·s)
	Solid density, ρ_s	1,722 (kg/m ³)
	Solid molecular weight	60.0843 (g/mol)
	Solid sphericity	See Table 7–5
	Solid emissivity	1
Particle–to–particle interaction	Close pack volume fraction	0.5
	Maximum momentum redirection from collision	40%
Particle normal stress model	Harris–Crighton's model	
	Ps constant	10
	B constant	3
	Eps constant	1e-08
	Factor of average velocity	0.5
Particle–to–wall interaction	Normal–to–wall momentum retention	0.95
	Tangent–to–wall momentum retention	0.95
	Diffuse bounce	0
Initial conditions	Gas velocity	0
	Gas pressure	111700 (Pa)
	Solids	0
Pressure boundary conditions	Outlet pressure (downer bottom)	111700 (psi)
	Particle out flow	To be calculated
Flow boundary conditions	Particle feed (Slip and mass flow)	See Table 7–5
	Particle feed per average volume	3,000
Solver settings	Maximum volume iteration	2
	Volume residual	1e-07
	Maximum pressure iteration	2000
	Pressure residual	1e-08
	Maximum velocity iteration	50
	Velocity residual	1e-07
	Maximum energy iteration	100
	Energy residual	1e-06
	Friction coefficient	0.1
Time controls	Time step	0.002 (s)
	End time	10 (s)
	Beginning time for average	5 (s)

7.4 Drag Model

There are two drag models in the commercial CPFD Barracuda software that consider non-sphericity. These models are the Ganser and Haider and Levenspiel models (Chhabra et al., 1999). Given the string cluster configuration as proposed by Krol et al. (2000), it was considered that a non-spherical drag model was needed in the present study. A cluster is likely to be formed by a single leading particle followed by several trailing particles. This vertical chain of N number of particles in contact with each other is a hydrodynamically favored cluster. This favored cluster offers a configuration where drag forces are minimized. Figure 7–10 reports the inter-phase drag coefficients calculated by the two different drag models for different sphericity values that represent one, two, an three particles traveling together. The results show very close values of the drag coefficients for low Reynolds numbers. In the present study low Reynolds number are expected ($Re < 15$). In this respect, both drag models can be equally used in the present research. However, in order to have an invariable criteria for the calculations, the Ganser's model was used under all operating conditions.

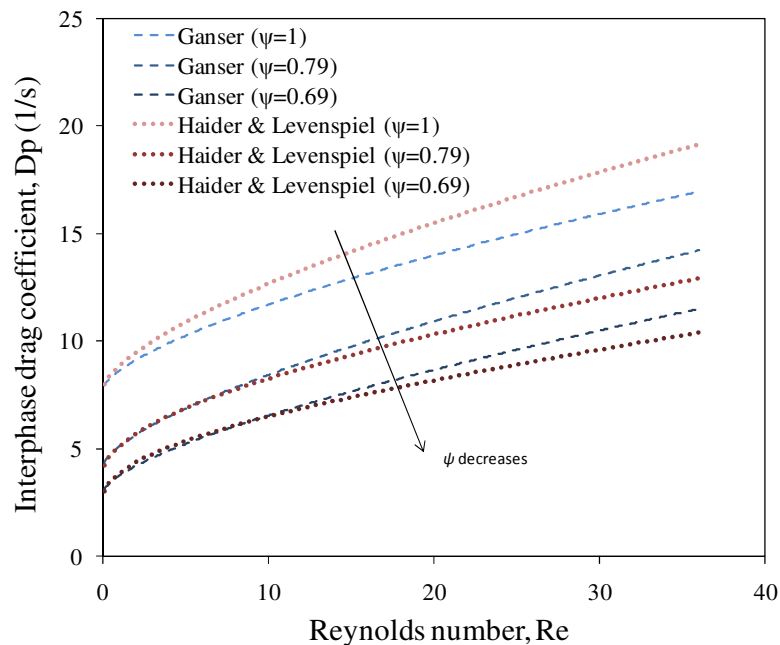


Figure 7–10: Drag coefficients for various drag models including non-spherical particles.

The [Ganser \(1983\)](#) model is given by:

$$F_s = m_s d_s (U_g - U_s) \quad (7-17)$$

$$d_s = 0.375 C_D \frac{\rho_g |U_g - U_s|}{\rho_s r_{eq}} \quad (7-18)$$

$$r_{eq} = \left(\frac{3 \cdot V_c}{4 \cdot \pi} \right)^{1/3} = N^{1/3} \cdot r_p \quad (7-19)$$

$$C_D = (1 - \varepsilon_s)^{-2.65} K_2 \left\{ \frac{24}{Re K_1 K_2} [1 + 0.1118 (Re K_1 K_2)^{0.6567}] + \frac{0.4305}{1 + \frac{3305}{Re K_1 K_2}} \right\} \quad (7-20)$$

$$K_1 = \frac{3}{1 + \frac{2}{\sqrt{\psi}}} \quad (7-21)$$

$$K_2 = 10^\alpha \quad (7-22)$$

$$\alpha = 1.8148 (-\log \psi)^{0.5743} \quad (7-23)$$

7.5 Particle Cluster Sizes and Sphericity

A cluster size average was established in the present research for each one of the operating conditions studied. With this end, the method reported by [Lanza et al. \(2013\)](#) was adopted, by calculating average cluster size from their characteristic asymmetric distribution in downers.

The sphericity definition proposed by [Chhabra et al. \(1999\)](#) was adopted.

$$\psi = \frac{s}{S} \quad (7-24)$$

where ψ is the cluster sphericity, s is the surface of a sphere having the same volume as the cluster and S is the actual surface area of the cluster. In the present study, the cluster sphericity is considered equal to:

$$\psi = \frac{s}{S} = \frac{4\pi r_e q^2}{N \cdot 4\pi r_p^2} = \frac{4\pi(N^{1/3}r_p)^2}{N \cdot 4\pi r_p^2} = N^{-1/3} \quad (7-25)$$

where N represent the average cluster size (number of particles having the same volume weighted average diameter)

The following table reports the average cluster size and sphericity used.

Table 7–5: Average particle cluster size and sphericity.

Operating condition #	G_s (kg/m ² ·s)	U_g (m/s)	Avg. Cluster Size, (μm)	Sphericity, ψ
1	10	0.95	247.0	0.70
2	15	1.43	301.2	0.65
3	46	2.54	356.9	0.62
4	50	1.18	468.3	0.56
5	57	1.85	339.2	0.63
6	65	1.25	375.4	0.61
7	76	2.53	306.6	0.65
8	82	1.68	363.7	0.61
9	91	2.52	388.6	0.60
10	106	1.16	292.3	0.66

7.6 Results and Discussion

The results reported in this section are based on the conditions previously considered for simulation in this manuscript. Cluster particle velocity profiles and particle volume fractions predicted with the CPFD model are compared with the experimental data already published by [Lanza et al. \(2012\)](#).

Regarding the proposed model, Figure 7–11 reports the model predicted average pressure profile along the downer for $U_g=2.53$ m/s and $G_s=76$ kg/m²s. It can be noticed that close to the inlet downer section, there is a quick pressure drop, where particles are accelerated by gravity and gas drag; with particle velocity quickly increasing. However, when particle velocity equals the gas velocity value, the gas drag acting on the particles become zero, the pressure reaches a minimum, and the pressure gradient becomes zero.

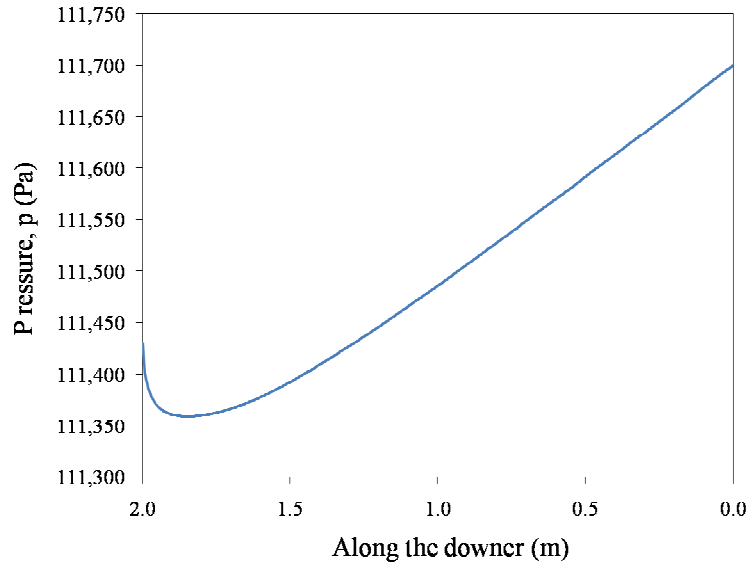


Figure 7–11: Simulated average pressure profile along the downer. Operating condition: $U_g=2.53$ m/s; $G_s=76$ kg/m²s.

Regarding pressure gradients and cluster particle velocities, they are reported in Figure 7–12 and Figure 7–13, respectively. One can observe that there is a downer entry region, so-called “first particle cluster acceleration” section. It is in this “particle cluster acceleration” region where the pressure decreases continuously to compensate for the drag on particles and the friction between the wall and the gas–solid flow. This can be represented by,

$$\left(\frac{\partial p}{\partial h}\right)_{U_g, G_s} < 0, U_g > U_s$$

This region ends with the zero pressure gradient condition and particle velocity being equal to the gas velocity (Wang et al., 1992).

$$\left(\frac{\partial p}{\partial h}\right)_{U_g, G_s} = 0, U_g = U_s$$

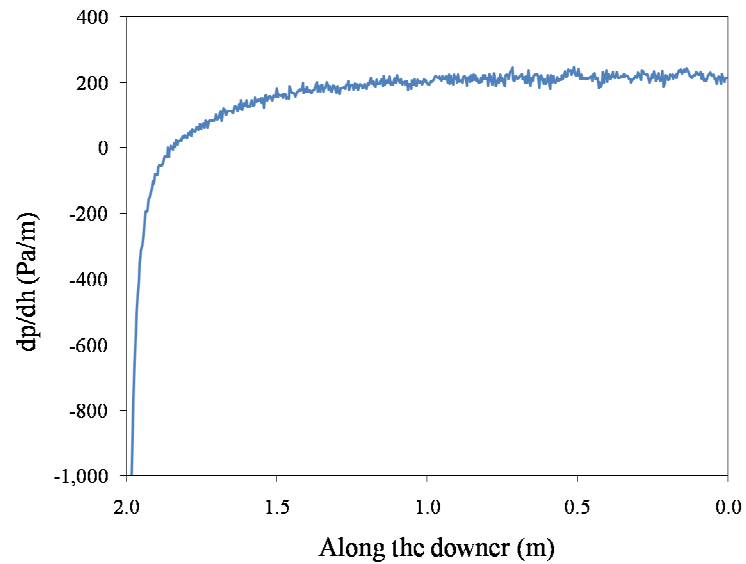


Figure 7–12: Average pressure gradient profile along the downer. Operating conditions: $U_g=2.53$ m/s; $G_s=76$ kg/m²s.

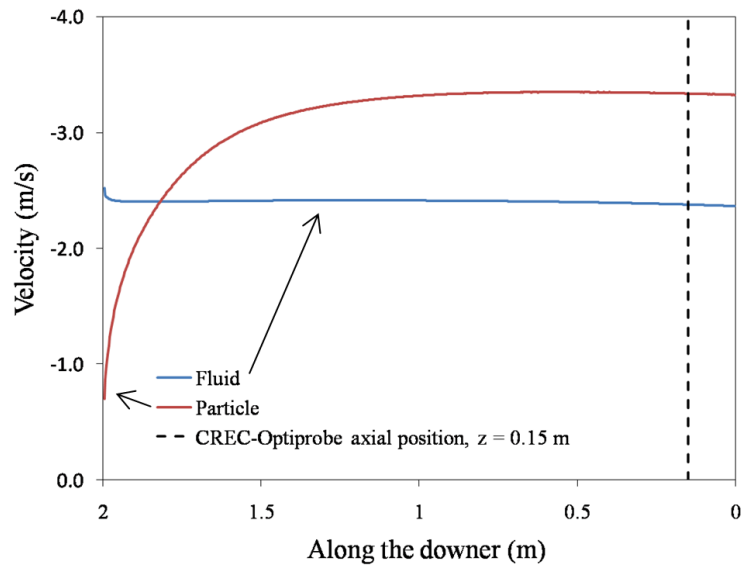


Figure 7–13: Average axial velocity profile along the downer. Operating conditions: $U_g=2.53$ m/s; $G_s=76$ kg/m²s.

Moreover and further down the unit, there is as reported in Figure 7–12 and Figure 7–13, “a second particle cluster acceleration’ section. It is in this region where the cluster particle velocity continues to increase exceeding the gas velocity. It is in this section,

where gas drag acts in opposite direction than gravity and total pressure increases in the flow direction displaying a positive pressure gradient. In summary, particle clusters keep accelerating while gas drag remains smaller than gravity such as:

$$\left(\frac{\partial p}{\partial h}\right)_{U_g, G_s} > 0, U_g < U_s$$

Finally, particle cluster evolving in a downer reach a “third constant velocity region”. It is in this region where gas drag forces become equal to gravity forces with cluster particle velocity reaching a maximum value. In this section pressure steadily increases in the direction of the gas–solid flow, with the pressure gradient being positive and constant, such as:

$$\left(\frac{\partial p}{\partial h}\right)_{U_g, G_s} > 0, \left(\frac{\partial^2 p}{\partial h^2}\right)_{U_g, G_s} = 0, U_g < U_s, U_s = \text{constant}$$

One can thus notice that the proposed cluster particle model describes the pressure changes in downers as reported in previous publications (Li et al., 2013; Abbasi et al., 2012; Zhao et al., 2010; Zhang et al., 2003; Zhu et al., 2001; Zhu et al., 1995; Wang et al., 1992).

Figure 7–13 shows that the location of the CREC optiprbes and thus, the related measurements of cluster particle velocity and particle volume fraction were in the developed downer flow region and as a result one can safely compare modeling predictions (which include this assumption) and experimental results as attempted in the upcoming sections of this manuscript.

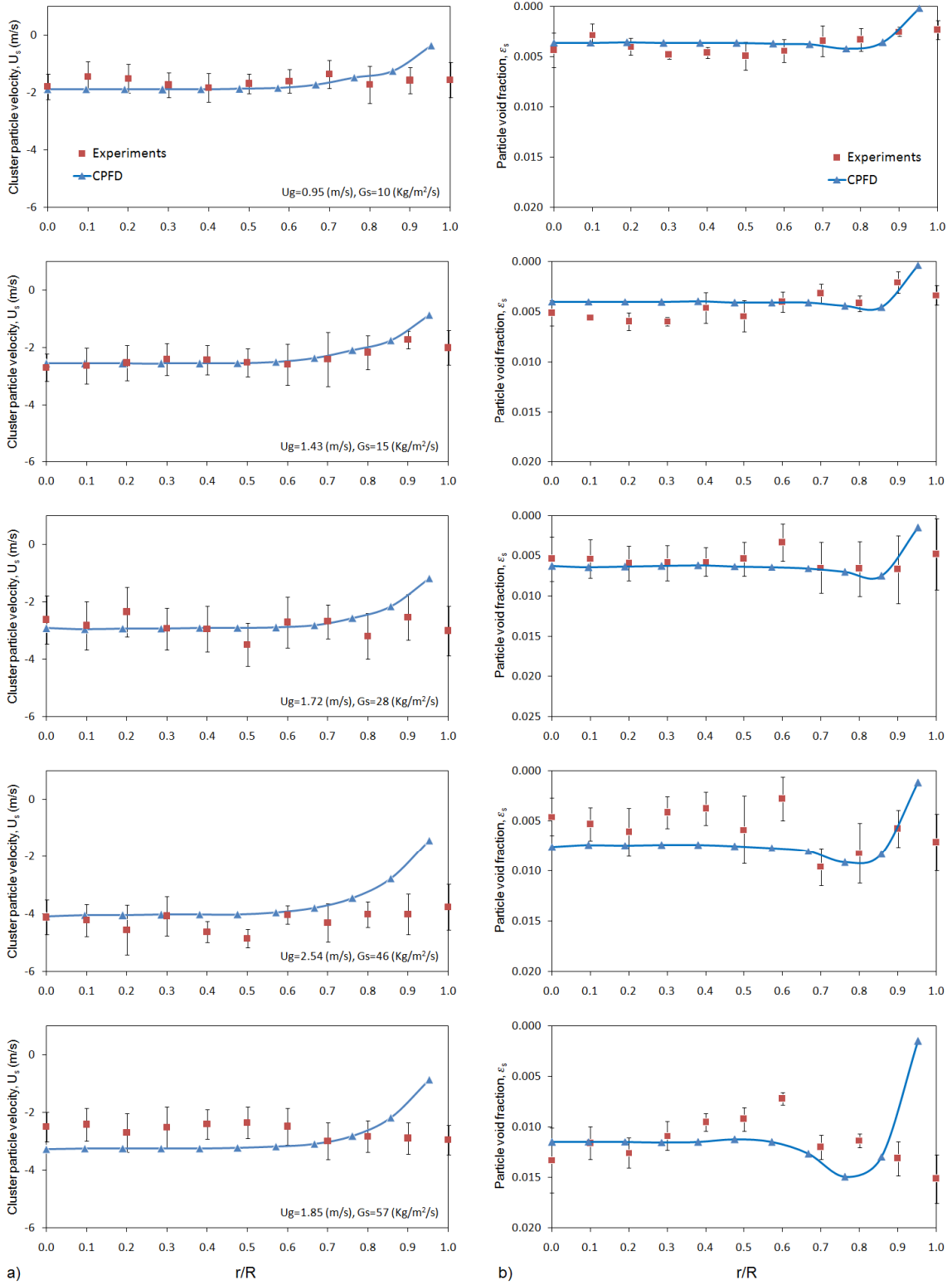


Figure 7–14: Radial profiles for a) cluster particle velocity profile, and b) particle void fraction profile. Axial position of the CREC–GS–Optprobe $z=0.15$ m, (1/2).

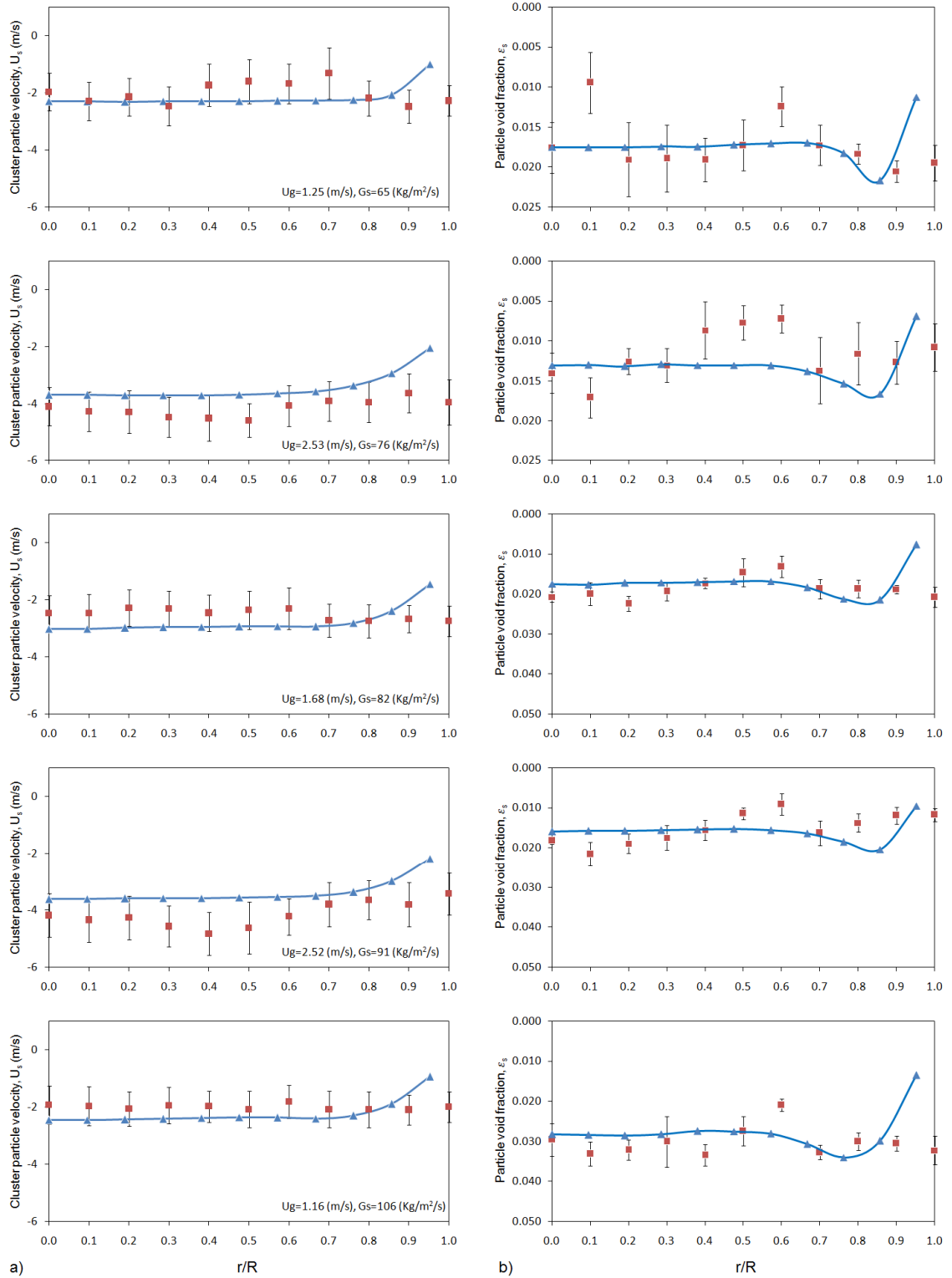


Figure 7–15: Radial profiles for a) cluster particle velocity profile, and b) particle void fraction profile. Axial position of the CREC–GS–Optprobe $z=0.15\text{m}$, (2/2).

In order for the proposed model to be rigorously validated, one has to consider both the experimentally measured and model predicted cluster particle velocity and volume solid fractions. In this respect, Figure 7–14 and Figure 7–15 report the cluster particle velocity profiles and particle void fractions of three of the eleven operating conditions studied. It can be observed that the CPFD simulations show good agreement with the experimental data for both cluster particle velocity profiles and particle volume fractions with a difference observed in the vicinity of the wall. One can observe that for all operating conditions, there is a dominant flat velocity profile, predicted both by CPFD and observed experimentally. Differences, however, are noticed in the near wall region. Regarding this finding, one should note that the CPFD computational model uses a zero gas velocity at the wall surface. This selected boundary condition may lead to the observed differences at the vicinity of the wall.

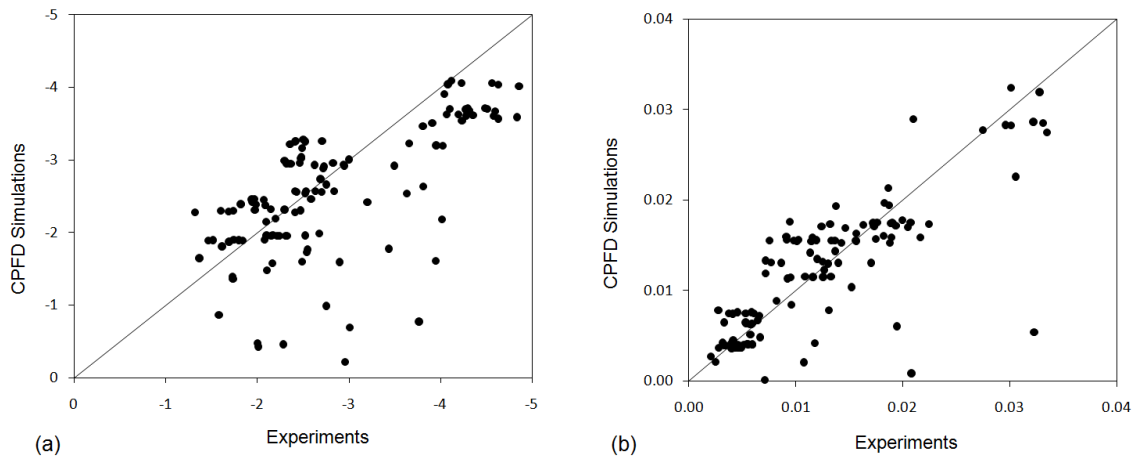


Figure 7–16: Comparison of between CPFD simulations and experimental results for cluster particle velocity and particle volume fraction. a) Cluster particle velocity (m/s), b) Particle volume fraction.

A comparison between the CPFD simulations and the experimental results is reported in Figure 7–16. The calculated errors reported for both cluster particle velocity and particle volume fraction can be in some cases greater than 100%. As was previously described, the major contributors to this, are the differences observed in the vicinity of the wall, with the CPFD Barracuda simulation assigning a zero gas velocity at the near wall surface.

On the other hand, Figure 7–17 reports the same results, omitting, however, the data in the near wall region. The calculated error decreases now to 15.7% for cluster particle velocity and to 22.1% for particle volume fraction. Thus, it appears that further research is required to improve the CPFD simulation results in the vicinity of the wall.

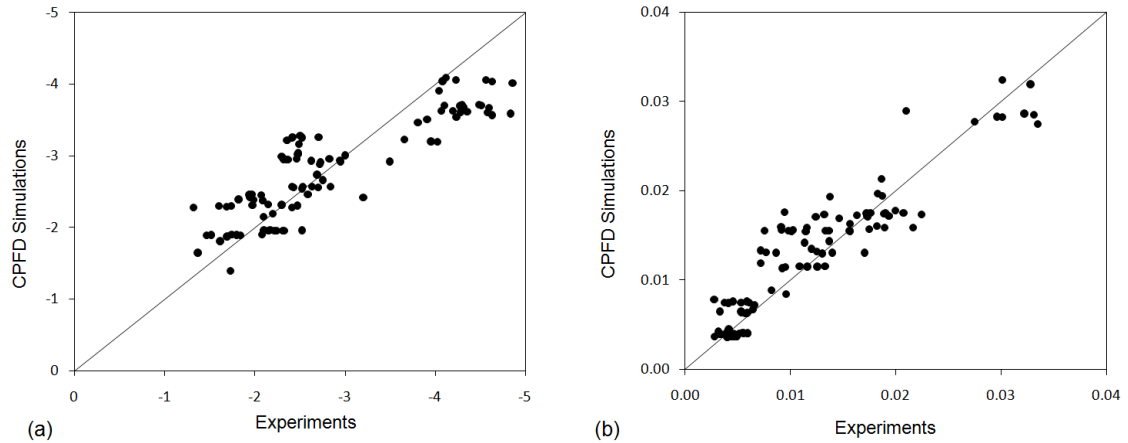


Figure 7–17: Comparison between CPFD simulations and experimental results omitting the data in the near wall region. (a) Cluster particle velocity (m/s), (b) Particle volume fraction.

Figure 7–18 (a) reports the simulated radial velocity profiles for the gas and particle clusters in the downer. One can observe similarity for each z position considered, with changes noticed along the downer. For instance, at the inlet section, a flat radial profile is observed. This can be anticipated, given the homogeneous assumption of the gas–particle mass flow at the near inlet conditions. However and once, the flow is established, the wall starts having an increasing role on the radial velocity profile.

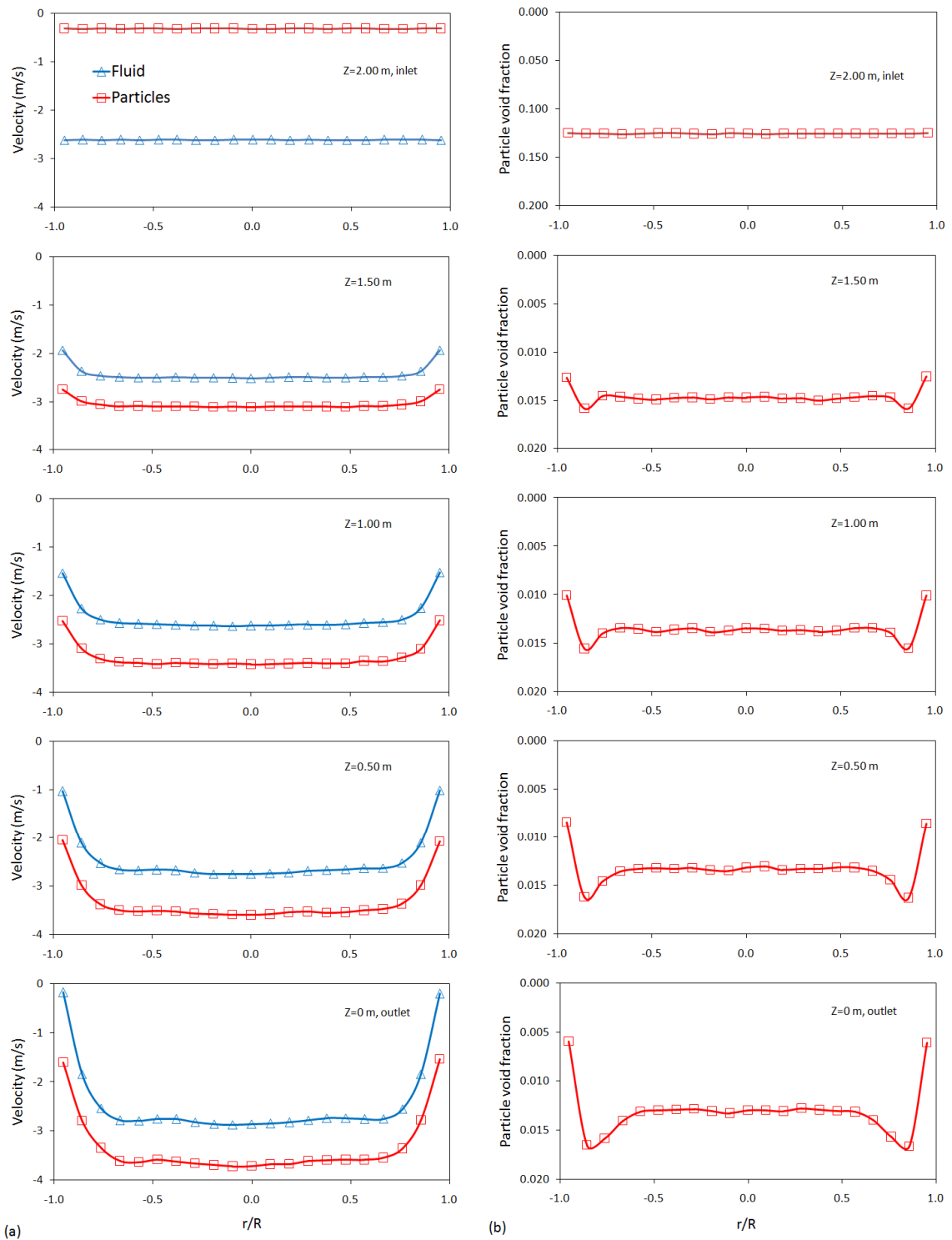


Figure 7–18: (a) Radial velocity profile, (b) Particle volume fraction. Operating conditions: $U_g=2.53$ m/s; $G_s=76$ kg/m²s.

Figure 7–18(b) describes the particle volume fraction in the downer at various axial positions. It can be observed that there is an important effect of the wall on the particle volume fraction. For example, from $Z=0.5\text{m}$, an annular region of high solids concentration develops near the wall, from $r/R=0.65$ to 0.85 . On the other hand, particle concentrations remain fairly constant in the centre core region up to $r/R=0.65$, increasing thereafter with a peak at around $r/R=0.75$ and decreasing in the near wall region. Similar results were found by [Zhu et al. \(1995\)](#) and [Wang et al. \(1992\)](#).

Both model and experimental data show good agreement in the core region of the downer and some discrepancy in the near wall region.

Thus, it appears that further research in this area is still required to elucidate the gas–solid fluid dynamics in the near wall downer region. These clarifications may considerably help, making the cluster model simulations applicable to the entire reactor unit. It is expected, however, that the wall effect will be of significantly smaller importance in larger diameter downers where there is a much more limited wall influence on the entire gas–solid fluid dynamics.

In summary, the present study shows the value of CPFDD simulations for modeling the fluid dynamics of downer units, this is the first manuscript in the technical literature that we are aware of, where such a CPFDD model is validated using experimentally measured solid holdups and cluster velocities. This is accomplished by validating the proposed particle cluster model with experimental data obtained using CREC–Optiprobes. One can, thus, conclude that CPFDD simulations of downer units provide a valuable modeling tool for the future development and scale–up of these units.

7.7 Conclusions

- a) CPFDD numerical simulations of downer units are successfully developed using CPFDD Barracuda based models.
- b) Grid mesh and numerical particles are established considering the influence of meshing on both particle volume fraction and cluster particle velocities.

- c) CPFD simulations include average particle cluster sizes obtained from experimentally measured cluster size distributions. Drag coefficients in these simulations are accounted for by using average cluster sizes.
- d) Cluster particle acceleration regions and particle cluster constant velocity regions are successfully captured by the CPFD calculations.
- e) Experimentally measured radial cluster particle velocities and radial particle holdups show flat profiles in the central downer region with this being consistent with the CPFD simulations. This provides strong support to the phenomenologically based CPFD models of downer units of the present study.
- f) Experimentally measured radial cluster particle velocities and radial particle holdups display differences in the near-wall region. While significant, the near-wall region effect is considered of less importance for scaling up of larger diameter downer reactors.

Chapter 8

8 Experimental Results and CPFD Simulations Obtained with the Two Inch Internal Diameter Downer Unit.

This chapter reports “individual” particle cluster information obtained using the CREC–GS–Optiprobos. Experiments were carried out in a two inch internal diameter downer unit. The fluid catalytic cracking (FCC) catalysts were the same ones used in a one inch internal diameter downer unit, with a mean particle diameter of 84.42 μm and a particle density of 1,722 kg/m^3 . The gas velocity and solid mass fluxes were varied from 1.1 to 2.0 m/s and from 7 to 50 $\text{kg}/\text{m}^2\text{s}$, respectively. The analysis of the data obtained, involved a rigorous methodology for setting the data baseline in compliance with solid mass balances explained in Chapter 5. As mentioned in Chapter 5, the application of this method allows the simultaneous measurement of a) baseline reference factor results, b) cluster solid concentrations, c) individual cluster slip velocities and d) individual cluster sizes. These data also allow the calculation of cluster size frequency distributions at various radial positions in the downer unit. These findings support a particle string configuration for clusters in downer units. Additionally, a Computational Particle Fluid Dynamics (CPFD) approach, was used to solve numerically, the system equations using the operating conditions proposed in the present chapter. Results of the simulation were compared with the experimental results. Good agreements were observed in almost all of the cases studied.

Two CREC–GS–Optiprobos were placed at a 1.70 m height, below the injection port in the two inch internal diameter downer unit, and separated axially by 0.006 m. It was considered that at 80 cm from the injection port, the particles reached terminal velocity. A confirmation of the fully developed flow pattern (clusters evolving at terminal velocity), as shown via the pressure profile along the downer, is provided in Figure 8–19.

Experiments were carried out under a wide range of operating conditions as described in Table 8–1. The same experimental methodology was implemented as in the experiments with the one inch internal diameter downer unit. Thus, both the data adequacy and the

reproducibility were ensured by repeating the measurements at least 5 times, for each radial position. Their time-averaged values were considered as the measured results.

For each operational condition, the two CREC-GS-Optiprobes were aligned at 11 equally-divided radial positions. Therefore, with this combination of a number of samples and radial positions, the full spectra of hydrodynamic signals of interest along the downer radius, were obtained. In addition, it can be observed in Table 8-1, that experiments were developed with three types of gas superficial velocities and mass fluxes: low, intermediate, and high values. This was done to be able to obtain data under a wide range of operating conditions.

Table 8-1: Operating conditions used in the 2 inch internal diameter downer unit.

Operational Condition #	Gas Velocity (U_g , m/s)	Solid Mass Flux (G_s , kg/m ² /s)
1	1.1	11
2	1.1	28
3	1.1	44
4	1.5	11
5	1.5	34
6	1.5	50
7	2	7
8	2	37
9	2	45

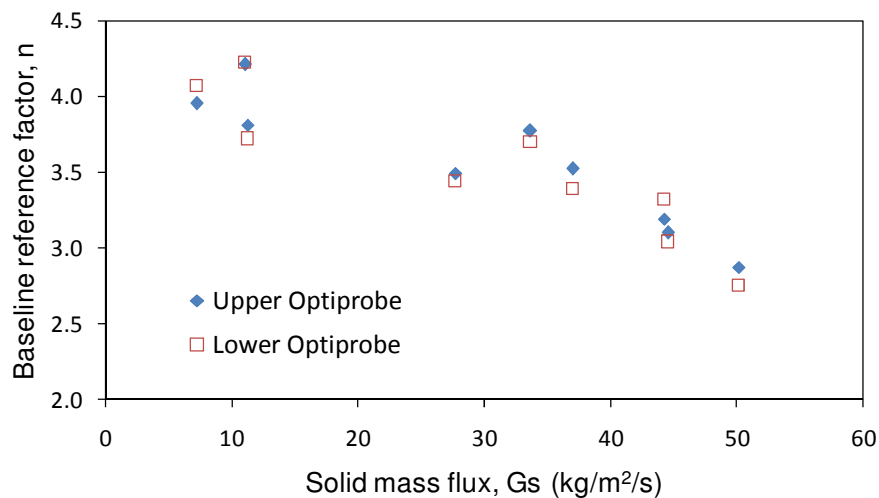
8.1 Baseline Reference Factor from Experimental Results

Table 8-2 reports the experimentally calculated baseline reference factor for various conditions and for two CREC-GS-Optiprobes. As can be noticed in this table, the values of n , estimated with the signal data and those recorded by the upper and the lower CREC-GS-Optiprobes were very close. These results also show the validity and applicability of the proposed baseline determination method as described in Equation (5-2) of Chapter 5.

Table 8–2: Baseline reference factor experimental results.

Operational Condition #	Gas Velocity (U_g , m/s)	Solid Mass Flux (G_s , kg/m ² /s)	Upper Optiprobe	Lower Optiprobe
			Baseline Reference Factor, n	Baseline Reference Factor, n
1	1.1	11	3.81	3.72
2	1.1	28	3.49	3.44
3	1.1	44	3.19	3.32
4	1.5	11	4.21	4.22
5	1.5	34	3.77	3.70
6	1.5	50	2.87	2.75
7	2.0	7	3.95	4.07
8	2.0	37	3.52	3.39
9	2.0	45	3.10	3.04

Figure 8–1 and Figure 8–2 report a graphical representation of the baseline reference factor n , as reported in Table 8–2. It can be noticed that n , decreases when the solid mass flux, G_s , is increased. One should notice that a similar behavior was found for the one inch internal diameter downer unit. The gas velocity, on the other hand, did not have such a significant influence on the n parameter, in neither the one nor the two inch internal diameter downer units. To explain this behavior of the n with the G_s , one can indicate that the larger G_s may lead to more secondary ray reflections from particles or particle clusters increasing both the signal average, X , and the standard deviation σ_x (Lanza et al., 2013).

**Figure 8–1: Baseline reference factor as a function of the solid mass flux.**

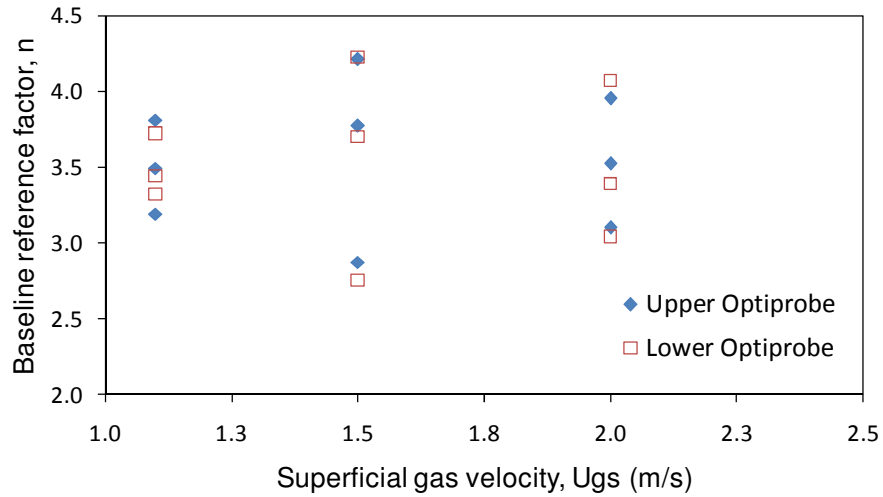


Figure 8–2: Baseline reference factor as a function of the gas velocity.

8.2 Cluster Slip Velocity from Experimental Data

Radial cluster slip velocity and radial cluster solid concentration are reported in three groups of graphs in Figure 8–3 as follows: a) low gas velocity (1.1 m/s); b) intermediate gas velocity (1.5 m/s); and c) high gas velocity (2 m/s). Local cluster slip velocities, U_{slip} , were estimated with the following Equation (8–1), and are reported in Figure 8–3.

$$U_{slip} = U_s - U_g \quad (8-1)$$

where U_{slip} is the local slip velocity; U_s is the measured local particle or cluster velocity; U_g is the interstitial gas velocity.

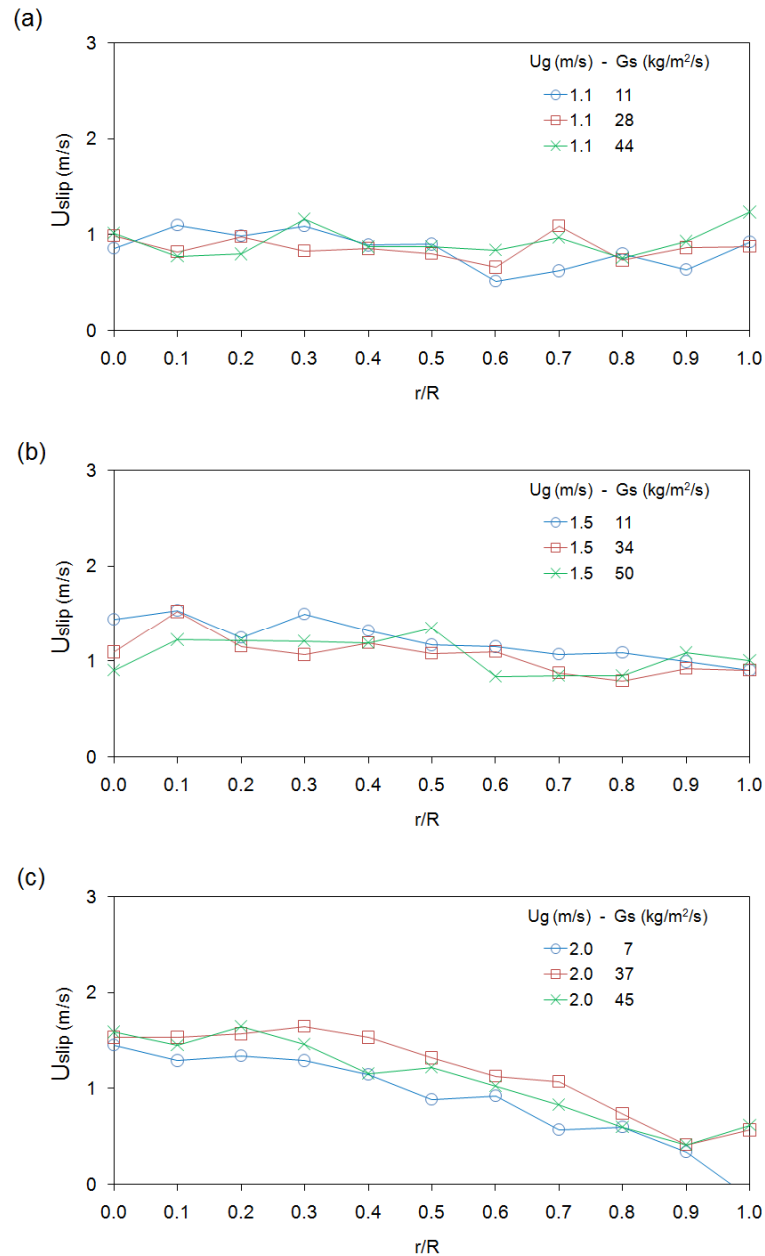


Figure 8–3: Radial cluster slip velocity profiles. Figures (a) to (c) show lower, intermediate, and higher gas velocity, respectively.

Regarding the data presented above, one can see that the radial slip velocity profiles are relatively flat, becoming less uniform at the higher values of gas velocity. Flat slip velocity profiles in downers have been found by other researchers as well (Wu et al., 2010; S. Li et al., 2004; Talman et al., 1999). It is also noticeable however, that the

cluster slip velocity shows an increase when the gas superficial velocity augments. This behavior can be assigned, to the fact that higher superficial gas velocities enhance particle interaction, and may facilitate larger particle clusters formation. One should also notice that the formation of large clusters yields a reduced drag force and an increased particle slip velocity.

8.3 Radial Solid Concentration Profiles

The radial solid concentration profile is another important parameter for the fluid dynamic description of solid flows in the fully developed region in downer units. Radial solid concentrations were calculated with Equation (5.3) of Chapter 5, and are reported in Figure 8-4. The average of five samples with each of them being 1 second of data records was considered for each position.

It can be seen that the solid concentration profiles for both the upper and lower optiprubes were close in value. This also provides evidence of good correlation between the signals recorded from both upper and lower CREC-GS-Optiprubes. One can also notice that the solid concentration radial profiles are quite flat, with this being particularly true at the lower solid mass fluxes. For solid concentration, the radial profiles present, however, a fluctuation at $r/R=0.75$ and for the intermediate value of the gas velocity.

It can also be observed that for similar gas superficial velocities, the solid concentration increases with solid mass flux. An increase in gas velocity is found to have an important effect on solid concentration as well, making the solid flow less uniform, as reported in Figure 8-4b, e and f.

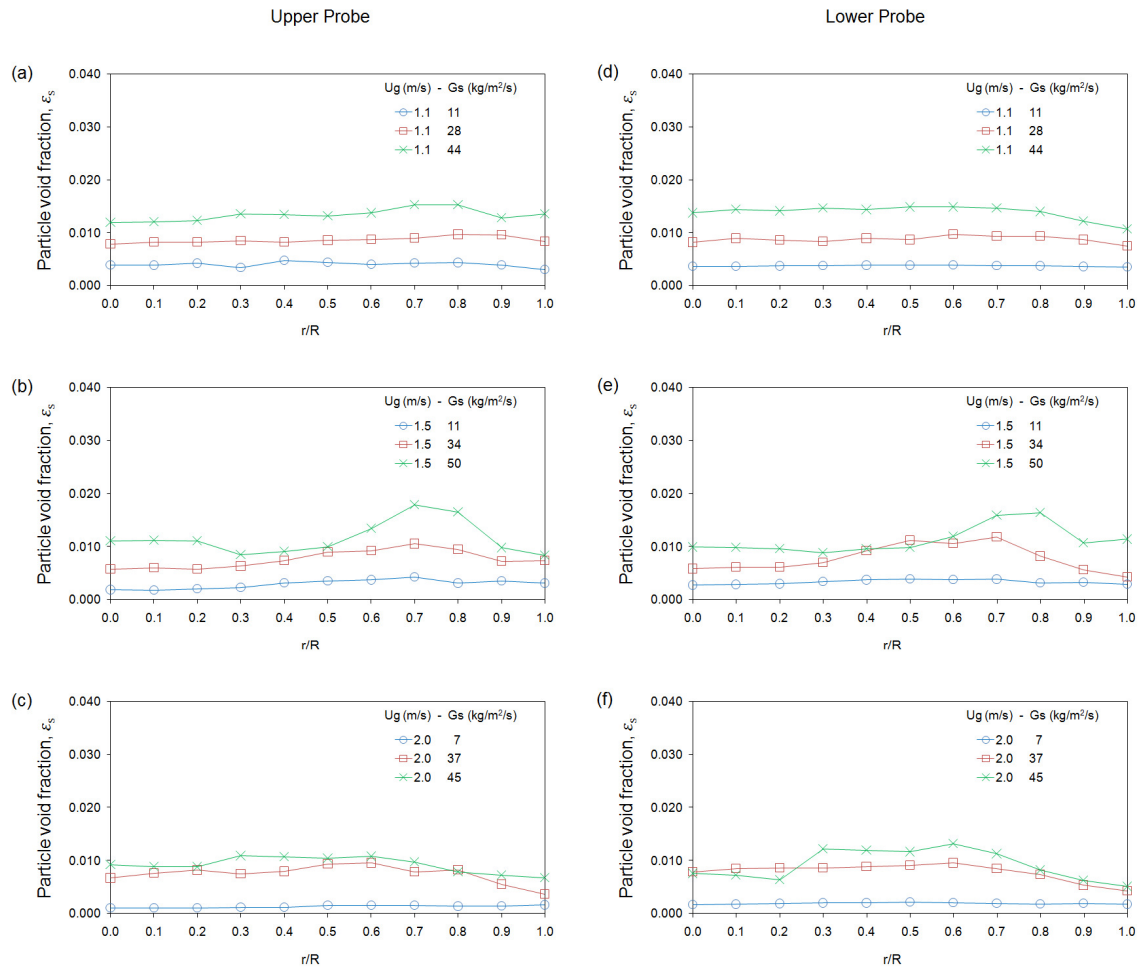


Figure 8–4: Radial cluster solid concentration profiles. Figures from (a) to (c), show results of the upper optiprobe; (d) to (f) show results of the lower optiprobe. Three groups are presented, lower, intermediate, and higher gas velocity.

Regarding the radial solid concentration profile in the near-wall region, it appears that the gathered results are in good agreement with other studies (Manyele et al., 2003). It can be observed that in the downer fully developed flow region, radial profiles are rather flat with no significant changes close to the wall. These observations are valid for a wide range of operating conditions. Additionally, it is found that the solid concentrations increase with G_s and decrease with U_g , with these findings being consistent with the other publications in the technical literature (Manyele et al., 2003).

8.4 Cluster Size and Cluster Slip Velocity Calculations

Figure 8–5 reports the changes in cluster slip velocity, with the expected number of particles in each cluster. This analysis was performed for the set of U_g and G_s , with these being 1.5 m/s and 34 kg/m²/s respectively, and including 533 cluster data points. Figure 8–5 reports three observations: a) that there is a wide distribution of cluster sizes and cluster velocities for a given operational condition, b) that there is a wide distribution of cluster sizes for a given slip velocity, and c) that there is a significant variation of slip velocity for a given cluster size.

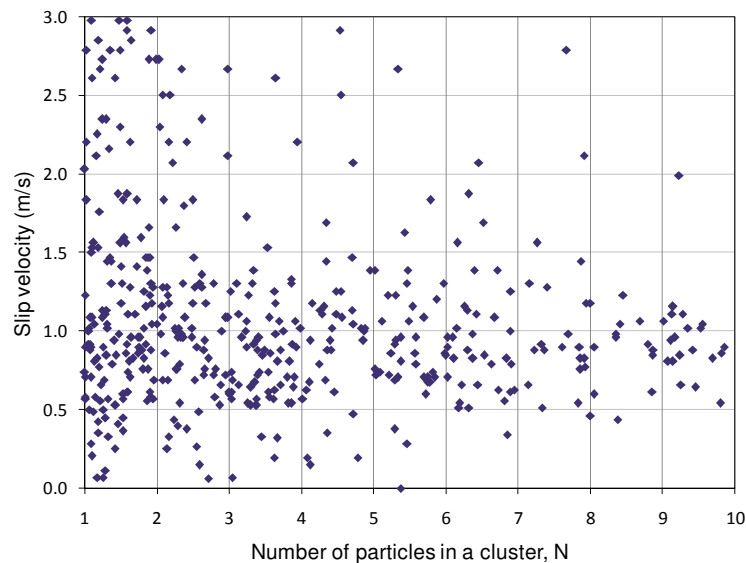


Figure 8–5: Slip velocities of particles as a function of the number of particles in the 2 inch internal diameter downer unit. Operating condition: $U_g=1.5$ m/s, $G_s=34$ kg/m²s. Data points included: 533 clusters.

Moreover, this data analysis is further enhanced in the present study, as reported in Figure 8–6. These data sets correspond to the same operating condition. Figure 8–6 reports the cluster slip velocity distribution for two groups of clusters, co-existing in the same cluster population. In the first group, the clusters have 1 or 2 particles. In the second group, the clusters have 7 or 8 particles. It can be noted that the slip velocity of clusters

with a low number of particles, has a slightly lower frequency than the clusters with a larger number of particles. In the one inch internal diameter downer unit, this study was also performed, showing a larger difference between small and larger cluster velocities. One can argue that this behavior is the result of the two inch internal diameter downer unit displaying a Reynolds Number twice the value of that of the 1 inch internal diameter downer unit for the same gas velocity. Thus, it is likely that clusters evolve in a more turbulent media, with larger clusters breaking up more rapidly. Therefore, it is expected that this increased turbulence may facilitate collision between clusters, with these collisions tending to break the larger clusters in smaller ones. As a result, the larger clusters may not be able to reach their corresponding terminal velocity values.

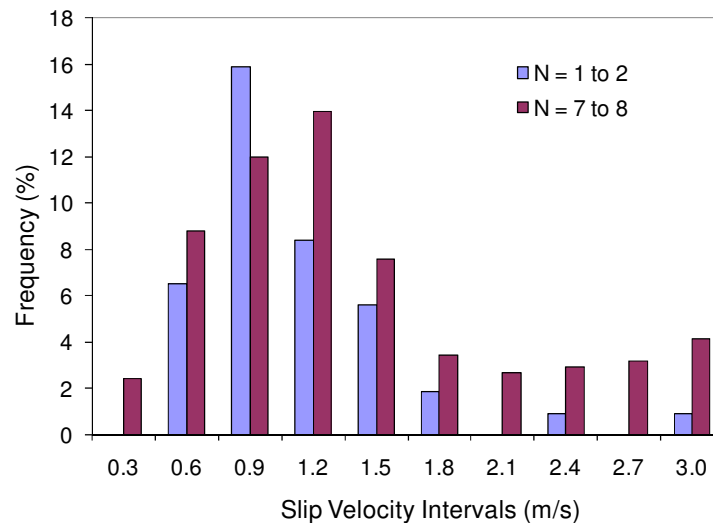


Figure 8–6: Cluster slip velocity distribution. For N=1 to 2, 250 clusters are considered; For N=7 to 8, 43 clusters are accounted. Operating condition: $U_g=1.5$ m/s, $G_s=34$ kg/m²s.

The following Table 8–3 summarizes the total number of clusters studied at the various operating conditions of the present study. One can notice that in total, more than 5,000 clusters were studied.

Table 8–3: Operating conditions and number of clusters studied

Operational Condition #	Gas Velocity (U_g , m/s)	Solid Mass Flux (G_s , kg/m ² /s)	# of Clusters Studied
1	1.1	11	478
2	1.1	28	511
3	1.1	44	535
4	1.5	11	483
5	1.5	34	533
6	1.5	50	471
7	2	7	839
8	2	37	632
9	2	45	610

8.5 Particle Cluster Size Distribution Results

This section reports individual particle cluster size distributions results, with the experimental data obtained, in a two inch gas–solid downflow reactor. To accomplish this, local cluster particle characteristics were determined using a significantly enhanced data analysis. It was proven that for all conditions considered, cluster particle size distributions are consistently asymmetric, with clusters containing from 1 to 9 average size particles, and with clusters having the smallest number of particles (e.g. 1 to 2) being the most abundant.

To determine cluster sizes, the string cluster configuration proposed by [Krol et al. \(2000\)](#) was assumed as applicable in the present study. Thus, we can assume that particles agglomerate, on the basis of a number of leading particles, which are followed by a number of trailing particles. This vertical chain of N number of particles, in contact with each other, is a hydrodynamically favored cluster shape. This favored cluster shape offers a configuration where drag forces are minimized. Therefore, the cluster shape is assumed to be a vertical chain of an N number of spherical particles, in contact with each other. A detailed explanation of the methodology used to determine the cluster size distribution is presented in Chapter 6.

Figure 8–7 describes the observed individual particle cluster size distributions. In this figure, the total number of clusters observed, for each operational condition, in the complete downer cross–sectional area, is reported. The vertical axis of Figure 8–7 reports

particle cluster size distributions on a percentage basis, while the horizontal axis reports the operational conditions studied (e.g. solid mass flux, G_s , and gas velocity, U_g). The side legend in Figure 8–7, describes the cluster sizes established for FCC particle of 84.42 μm average size and containing from 1 to 10 average size particles.

It can be noticed in Figure 8–7 that, for a given operational condition and cluster population, the cluster size distribution is asymmetric with smaller particle clusters being more dominant than larger clusters. Figure 8–8 reports a zoom of the $U_g=1.5$ m/s and $G_s=34$ kg/m²s operating condition, where more than 27% of clusters have only one particle. Moreover, the sum of all clusters with an N value larger than 6 particles is, in this case, smaller than 15%. These strongly asymmetric distributions of cluster size and cluster slip velocity were found to be a characteristic cluster feature, for all operating conditions considered, in the present PhD dissertation, in both 1 inch ID and 2 inch ID downer units. This means that clusters with a large number of particles are less likely to survive. One can thus, state that this behavior is the result of the collision between clusters, with this collision tending to break down larger clusters in smaller ones.

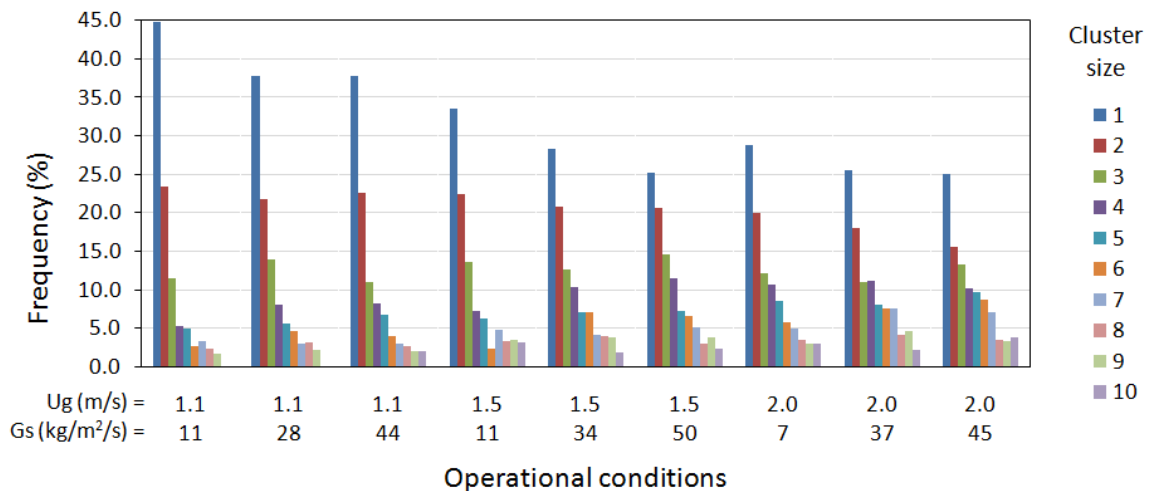


Figure 8–7: Individual particle cluster size distributions at various solid fluxes and gas velocities.

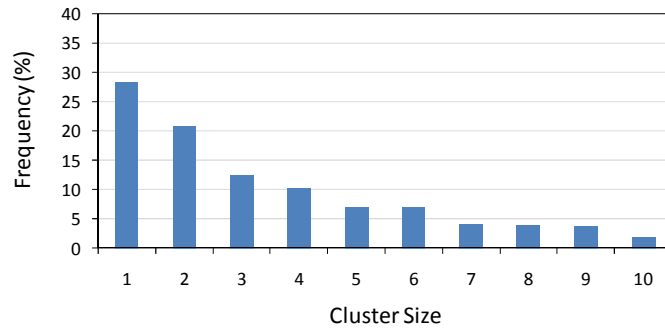


Figure 8–8: Distribution of the number of particles in clusters for $U_g=1.5$ m/s, $G_s=34$ kg/m²s.

Figure 8–9 provides a weighted average of individual particle cluster size distributions for the complete set of operational conditions. The error bars represent the weighted standard deviation. As a result, one can conclude that for all operational conditions considered, the cluster size distributions are asymmetric with smaller particle clusters being more dominant than larger particle clusters.

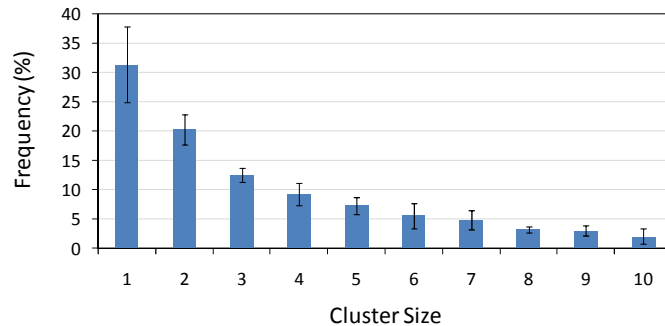


Figure 8–9: Individual particle cluster size distribution averages.

To gain a better understanding of the particle cluster size distributions in downer reactors, as was also done for the 1 inch ID downer unit, the influence of the radial position on cluster size distributions was also considered. Figure 8–10 reports cluster size distribution changes from radial position $r/R=0$ (column center) to $r/R=1$ (internal downer wall). The legend in this figure, describes cluster sizes established on the basis of the number of

average size particles per cluster (e.g. from 1 to 10). Values of the distributions reported in Figure 8–10, correspond to weighted average distributions with error bars representing weighted standard deviations.

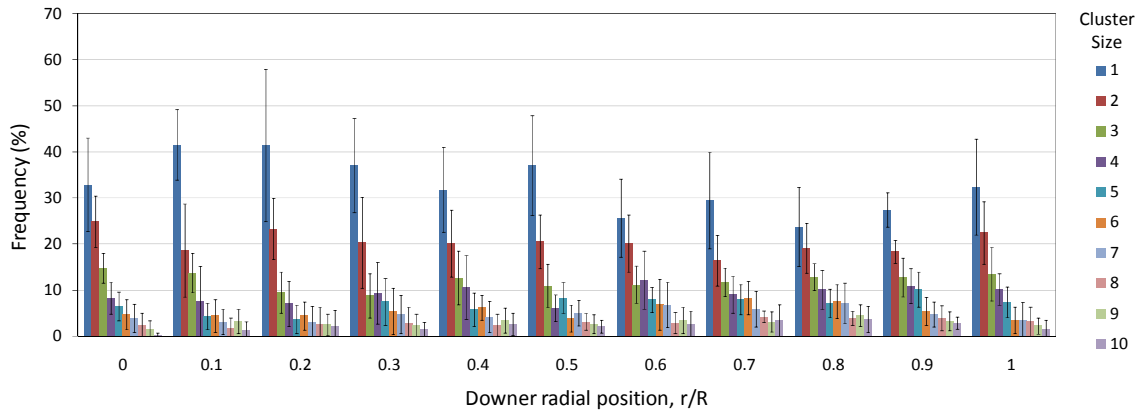


Figure 8–10: Individual particle cluster size distribution weighted averages for all operational conditions studied.

Figure 8–11 reports an expanded view of the individual cluster size distribution weighted averages at $r/R=0.9$ of the data reported in Figure 8–10. One can note that the cluster size distributions in downers, are in agreement with the total average distributions as described in Figure 8–9. This provides confirmation that it is more likely to find clusters in a downer with just a few particles, than to find clusters with a large number of particles.

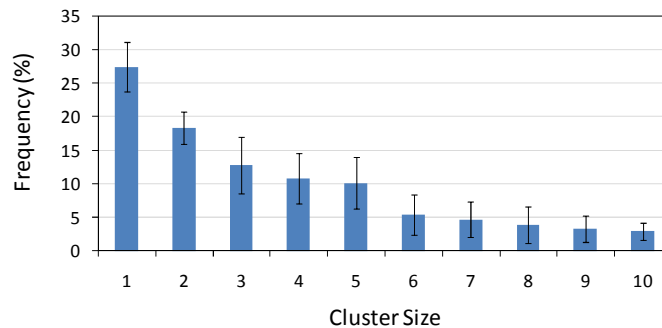


Figure 8–11: Individual cluster size distribution averages at $r/R=0.9$ radial position.

Thus, as shown in Figure 8–10, the cluster size distributions, found in this study, are consistently asymmetric, with smaller particle clusters being the most dominant configuration. This trend also appears to be independent of the radial position. It is our view, that identification of these typical cluster size distributions is of great importance for the fluid dynamic simulation and design of downer reactors for industrial applications.

8.6 Computational Particle Fluid Dynamics Modeling of the Downward Gas–Solid Flow.

Calculations were also developed, using the CPFDP numerical scheme, for the two inch diameter downer. The simulation conditions were selected, in order that the calculated results could be directly compared with experimental results. It was observed that the successful comparison of experimental and simulated results provides a strong support for a phenomenologically based model for downer units.

8.6.1 Computational Method

The fluid dynamics in the developed flow region of the two inch concurrent gas–solid down flow fluidized bed unit was also simulated using a Computational Particle Fluid Dynamics (CPFDP) Numerical Scheme.

The CPFDP model includes particles represented as clusters. This model is validated with experimental data obtained from the two inch internal diameter downer unit (2.04 m height and 5.08 cm internal–diameter downer column), reported in section 8.5. As in the one inch internal diameter downer unit, air and solid particles were fed at the top of the downer with experimental data being collected at its bottom.

Using the CPFDP methodology, the gas and particle equations are solved in three dimensions. A detailed explanation of the CPFDP numerical method was reported in Chapter 7.

One can notice that the observed time–averaged axial and radial velocities and solid concentration profiles were in agreement with CPFDP calculations. As a result, these

findings support: a) a narrow distribution of particle cluster catalyst residences, b) the characteristic particle “forward” mixing, c) the relatively flat, radial solid concentrations and solid cluster velocities.

8.6.2 Experimental Set-up and Simulation Conditions.

A detailed explanation regarding the design of the 2 inch ID diameter downer unit is reported in Chapter 4 of the present PhD dissertation.

The same FCC particles used in the one inch internal diameter downer experiments, were also used in the two inch downer unit experiments. FCC particles have a mean particle diameter of 84.42 μm with a standard deviation of 33.62 μm , and an apparent particle density of 1,722 kg/m^3 . Figure 7–1 in Chapter 7 shows the particle size distribution (PSD) used for Barracuda simulations. More details regarding to the FCC particles used, can also be found in Appendix A of the present manuscript. The fluidization gas was air, close to ambient pressure and temperature.

For Barracuda simulations, in the 2 inch ID downer unit, a Computer–Aided Design (CAD) model of 2.04 m height and 5.08 cm column diameter was defined prior to any calculation. As with the one inch internal diameter downer unit, a particle free empty downer tube, filled with air, at standard pressure and temperature was used. In addition, and consistent with the experimental data, air and solid particles were assumed to be fed at the top of the downer, with the exit located at the bottom of the downer.

8.6.3 Discretization Sensitivity Analysis

As was mentioned in Chapter 7, Barracuda is a Computational Particle Fluid Dynamics software package based on the Multiphase Particle–In–Cell (MP–PIC) numeric method. This computational method is specifically developed for coupled fluid–particle motion. To accomplish this, governing equations for the gas phase, are treated as a continuum in the framework of an Eulerian grid. The particles are modelled as discrete entities, or computational particles (clouds) in a Lagrangian framework. This formulation requires a discretization sensitivity analysis in two dimensions. This includes coarse to fine resolution studies, using various numbers of ‘computational cells’ and particle clusters

fed per average volume. A detailed discussion of the need of such two dimensional sensitivity analyses while using CPFDD is reported in Chapter 7 of the present PhD dissertation.

In this case, the discretization analysis was developed as follows: a) first, a grid of $11 \times 11 \times 453$ (54,813) cells was set; b) this grid was chosen, given that it was considered reasonably coarse and provided a fast-running computational model; c) then, a computational particle resolution study was developed, increasing ten times successively, the number of computational particles per average unit volume, n_p , going from 30 to 300,000. In this respect, the minimum number of computational particles per unit cell, that is able to properly simulate the fluid dynamics in the downer unit was established. Once the computational particle analysis was completed, a grid resolution study was also considered, by approximately increasing the grid size by 1.5 times, from $11 \times 11 \times 453$ (54,813) to $13 \times 13 \times 518$ (87,524) cells.

It can also be noticed that CPFDD involves the selection of a number of numerical particles. If this number is too large, the CPFDD calculation may become very demanding from a computational point of view. On the other hand, if the number of numerical particles chosen is too small, the simulation may become inaccurate. To address this issue, Table 8–4 reports the results of increasing the number of particles fed, per average unit volume or n_p , from 30 to 300,000, and having a relatively constant total number of particles of about 500 million. One can observe that for $n_p=30,000$, the total number of computational particles (clouds) in the system, is 5 million or about 1/100 of the total number of particles. Thus, one can notice that there is significant savings in calculations, in terms of both memory and computational time.

In the present discretization analysis, the operation condition number 5 (refer to Table 8–4) was used: $U_g=1.5$ m/s, $G_s=34$ kg/m²s. This operating condition is representative of all the conditions, given that it includes an intermediate value for both the gas superficial velocity and the solid flux. Furthermore, the drag model used, is given section 7.4 of Chapter 7.

**Table 8–4: Particle discretization analysis. Operating condition: $U_g=1.5$ m/s,
 $G_s=34$ kg/m²s.**

Run #	Grid Size	n_p (Input Value)	Number of Particles	Number of Clouds	Particles/Cell	Clouds/Cell	Particle/Clouds
1	11x11x453	30	393,795,560	14,923	7,184	0.3	26,388.5
2	11x11x453	300	455,248,780	173,773	8,306	3.2	2,619.8
3	11x11x453	3,000	489,133,470	1,690,105	8,924	30.8	289.4
4	11x11x453	30,000	490,892,560	5,051,600	8,956	92.2	97.2
5	11x11x453	300,000	486,319,190	6,045,267	8,872	110.3	84.4

Figure 8–12, Figure 8–13, and Figure 8–14 report the estimated values for cluster particle velocity, particle volume fraction, and pressure along the downer. One can see that run 1 and 2, which have the coarsest particle resolution, differ considerably from the calculated values of runs 3, 4 and 5. On the other hand, one can also notice that runs 3, 4 and 5 provide close values for particle cluster velocity, particle volume fraction and pressure. As a result, this shows that the 30,000 particles fed per average unit volume, provide acceptable value calculations, describing the fluid dynamics in the down flow reactor of the present study.

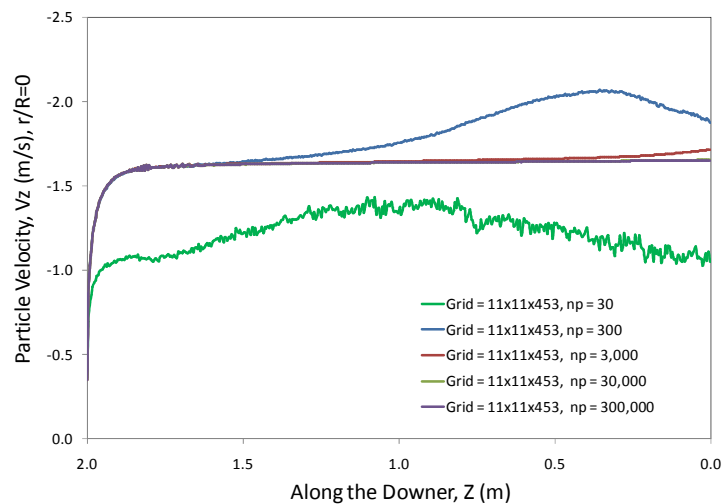


Figure 8–12: Effect of particle resolution on the calculated cluster particle velocity at the center line of the downer unit. Operating condition: $U_g=1.5$ m/s, $G_s=34$ kg/m²s. Note: five different grids with n_p changing from 30–300,000 were used in the calculations.

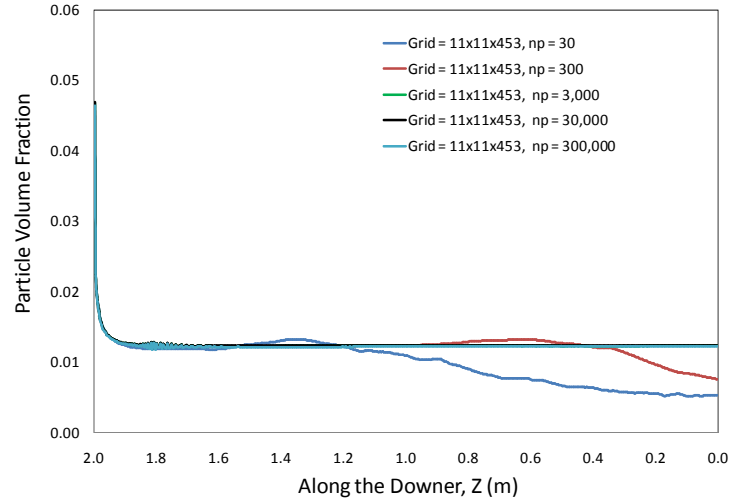


Figure 8–13: Effect of particle resolution on particle volume fraction at the center line in the downer unit. Operating condition: $Ug=1.5$ m/s, $Gs=34$ kg/m²s. Note: five different grids with n_p changing from 30–300,000 were used in the calculations.

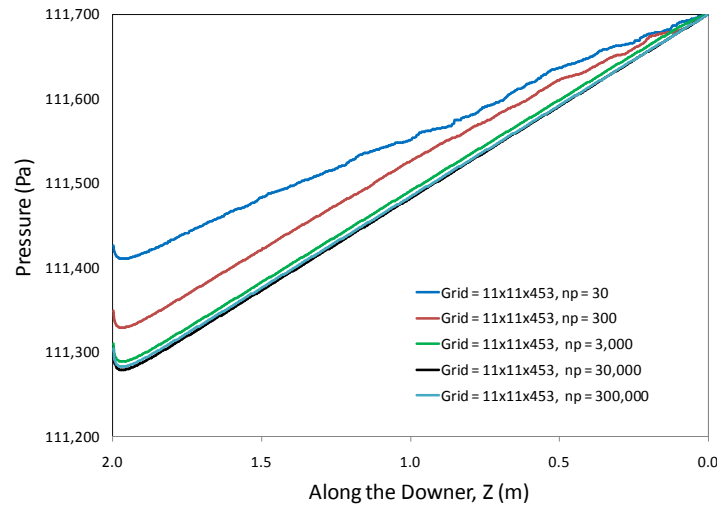


Figure 8–14: Effect of particle resolution on pressure in a downer unit of this study. Operating condition: $Ug=1.5$ m/s, $Gs=34$ kg/m²s. Note: five different grids with n_p changing from 30–300,000 were used in the calculations.

To study the spatial discretization, the grid cells were increased by 1.5 times. A new mesh with 13x13x518 (87,524) cells was used. Table 8–5 reports the details.

Table 8–5: Mesh discretization details

Run #	Grid Size	n_p (Input Value)	Number of Particles	Number of Clouds	Particles/Cell	Clouds/Cell	Particle/Clouds
1	11x11x453	30,000	490,892,560	5,051,600	8,956	92.2	97.2
2	13x13x518	30,000	485,231,070	6,166,924	5,543	70.4	78.7

Increasing the number of cells by 1.5 and keeping the number of particles fed per average volume, n_p , constant, roughly decreases the number of clouds per cells by 1.3. 500 million particles are modelled with less than 6.2 million computational particles.

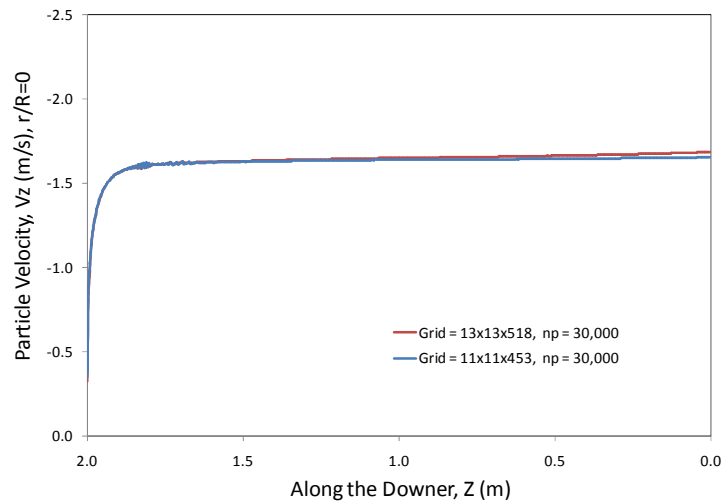


Figure 8–15: Effect of spatial resolution on cluster particle velocity at the center line of the downer unit. Operating condition: $Ug=1.5$ m/s, $Gs=34$ kg/m²s. Note: $n_p=30,000$, 11x11x453 and 13x13x518 grids were used in the calculations.

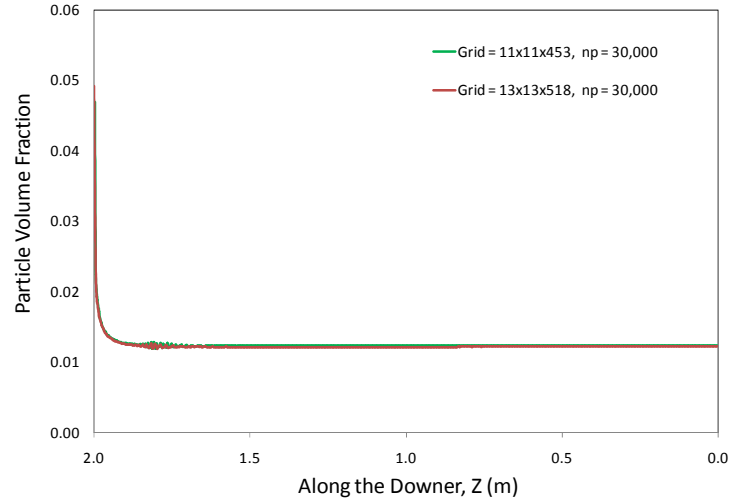


Figure 8–16: Effect of spatial resolution on particle volume fraction at the center line of the downer unit. Operating condition: $U_g=1.5$ m/s, $G_s=34$ kg/m²s. Note: $n_p=30,000$, 11x11x453 and 13x13x518 grids were used in the calculations.

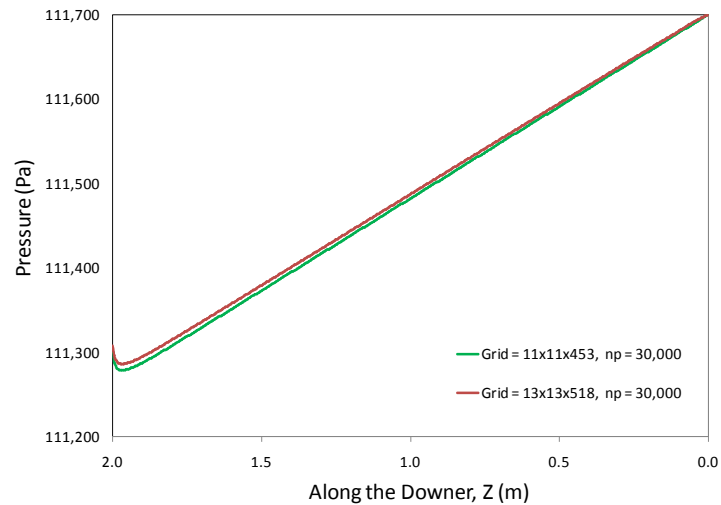


Figure 8–17: Effect of spatial resolution on pressure. Operating condition: $U_g=1.5$ m/s, $G_s=34$ kg/m²s. Note: $n_p=30,000$, 11x11x453 and 13x13x518 grids were used in the calculations.

Figure 8–15, Figure 8–16, and Figure 8–17 report very similar cluster particle velocities, particle volume fractions and pressure changes using 11x11x453 and 13x13x518 grids. Therefore, the smaller number of cells 11x11x453 (54,813) with an n_p of 30,000 particles was considered satisfactory for gas–particle fluid dynamic calculations.

8.6.4 Boundary Conditions and Input Values

CPFD simulations require superficial gas velocities and particle fluxes as in the various experiments developed with the two inch downer column. Table 8–6 reports the operating conditions studied using CPFD. This was done in order to match the experimental operating conditions and being able to develop a thorough comparison of CPFD simulations and experiments.

Regarding boundary conditions at the near wall region, the turbulent gas velocity model with a 1/6 power function was chosen. A zero gas velocity assigned at the wall surface. Concerning cluster particle velocities in the vicinity of the downer wall, equation (9) establishes particle normal and tangential–to–wall momentum components using 0.95 (refer to Table 7–1) restitution coefficients. These two restitution coefficients were selected as recommended by [Zhao et al. \(2010\)](#).

Table 8–6: Input parameters in the CPFD Simulation.

	Geometry	Cylinder 5.08 (cm) diameter 2.04 (m) height
	Mesh	11x11x453
Heat transfer	Isothermal flow	300 (K)
Gravity	Z Gravity	-9.8 (m/s ²)
	Gas density, ρ_g	1.17285 (kg/m ³)
	Gas molecular weight	28.9652 (g/mol)
	Gas viscosity, μ_g	1.84951e-05 (Pa·s)
	Solid density, ρ_s	1,722 (kg/m ³)
	Solid molecular weight	60.0843 (g/mol)
	Solid sphericity	See Table 8–7
	Solid emissivity	1
Particle-to-particle interaction	Close pack volume fraction	0.5
	Maximum momentum redirection from collision	40%
Particle normal stress model	Harris–Crighton's model	
	Ps constant	10
	B constant	3
	Eps constant	1e-08
	Factor of average velocity	0.5
Particle-to-wall interaction	Normal-to-wall momentum retention	0.95
	Tangent-to-wall momentum retention	0.95
	Diffuse bounce	0
Initial conditions	Gas velocity	0
	Gas pressure	111700 (Pa)
	Solids	0
Pressure boundary conditions	Outlet pressure (downer bottom)	111700 (psi)
	Particle out flow	To be calculated
Flow boundary conditions	Particle feed (Slip and mass flow)	See Table 8–7
	Particle feed per average volume	30,000
Solver settings	Maximum volume iteration	2
	Volume residual	1e-07
	Maximum pressure iteration	2000
	Pressure residual	1e-08
	Maximum velocity iteration	50
	Velocity residual	1e-07
	Maximum energy iteration	100
	Energy residual	1e-06
	Friction coefficient	0.1
Time controls	Time step	0.002 (s)
	End time	10 (s)
	Beginning time for average	5 (s)

8.6.5 Drag Model

As mentioned in Chapter 7, there are two drag models in the Commercial CPFDP Barracuda Software that consider non-sphericity. These are the Ganser Model, and Haider and Levenspiel Model (Chhabra et al., 1999). In the present study, the Ganser Model was used under all operating conditions. A detailed explanation of why this model was chosen, as well as a description of each model was presented in Chapter 7 of the present PhD dissertation.

8.6.6 Particle Cluster Sizes and Sphericity

The cluster size average determined previously in this chapter, was considered for each one of the operating conditions studied. Table 8–7 shows the average cluster size, used in each of the CPFDP Barracuda calculations. The sphericity definition proposed by Chhabra et al. (1999) was adopted. This definition is presented in Chapter 7 of the present PhD dissertation.

Table 8–7: Average particle cluster size and sphericity.

Operating Condition #	Ug (m/s)	Gs (kg/m ² ·s)	Avg. Cluster Size, N (μm)	Sphericity, ψ
1	1.1	11	2.3	0.76
2	1.1	28	2.7	0.72
3	1.1	44	3.0	0.69
4	1.5	11	4.1	0.63
5	1.5	34	4.0	0.63
6	1.5	50	3.9	0.64
7	2	7	6.6	0.53
8	2	37	5.1	0.58
9	2	45	4.9	0.59

8.7 Results and Discussion

The results reported in this section, are based on the conditions previously considered for simulation in this chapter. Cluster particle velocity profiles and particle volume fractions, predicted with the CPFDP model are compared with the experimental data.

Regarding the proposed model, Figure 8–18 reports the model predicted average pressure profile along the downer for $Ug=1.5$ m/s and $Gs=34$ kg/m²·s. It can be noticed that close to the inlet downer section, there is a quick pressure drop, where particles are accelerated

by gravity and gas drag; with particle velocity quickly increasing. However, when particle velocity equals the gas velocity value, the gas drag acting on the particles becomes zero, the pressure reaches a minimum, and the pressure gradient becomes zero.

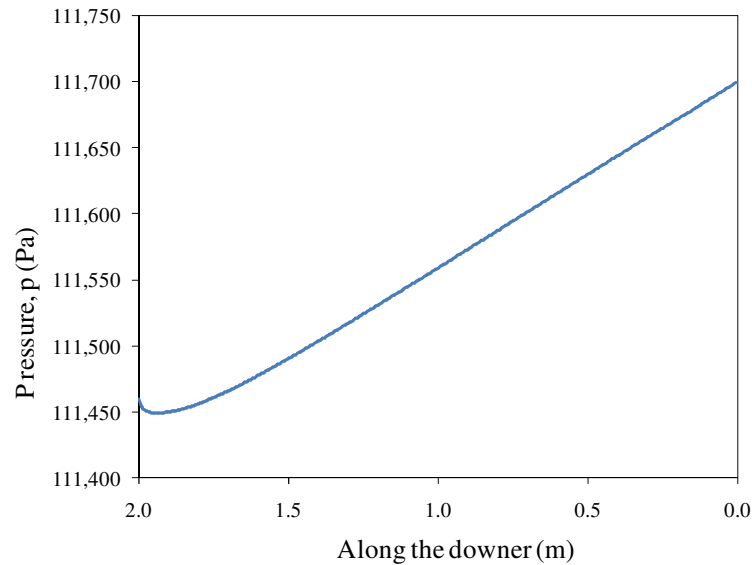


Figure 8–18: Simulated average pressure profile along the downer. Operating condition: $U_g=1.5$ m/s, $G_s=34$ kg/m²s.

Concerning pressure gradients and cluster particle velocities, they are reported in Figure 8–19 and Figure 8–20, respectively. As it was mentioned in Chapter 7, one can observe that there is a downer entry region, called the “first particle cluster acceleration” section. It is in this “particle cluster acceleration” region, where the pressure decreases continuously to compensate for the drag on particles and the friction between the wall and the gas–solid flow. This can be represented by,

$$\left(\frac{\partial p}{\partial h}\right)_{U_g, G_s} < 0, U_g > U_s$$

This region ends with the zero pressure gradient condition and particle velocity being equal to the gas velocity (Wang et al., 1992).

$$\left(\frac{\partial p}{\partial h}\right)_{U_g, G_s} = 0, U_g = U_s$$

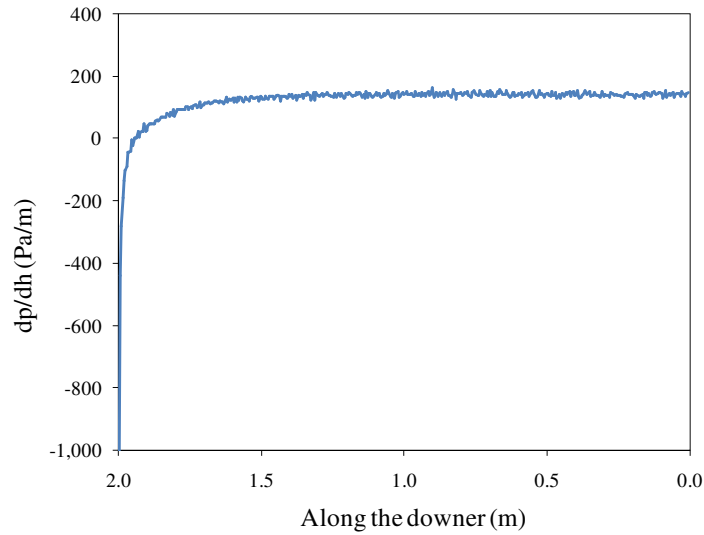


Figure 8–19: Average pressure gradient profile along the downer. Operating condition: $U_g=1.5$ m/s, $G_s=34$ kg/m²s.

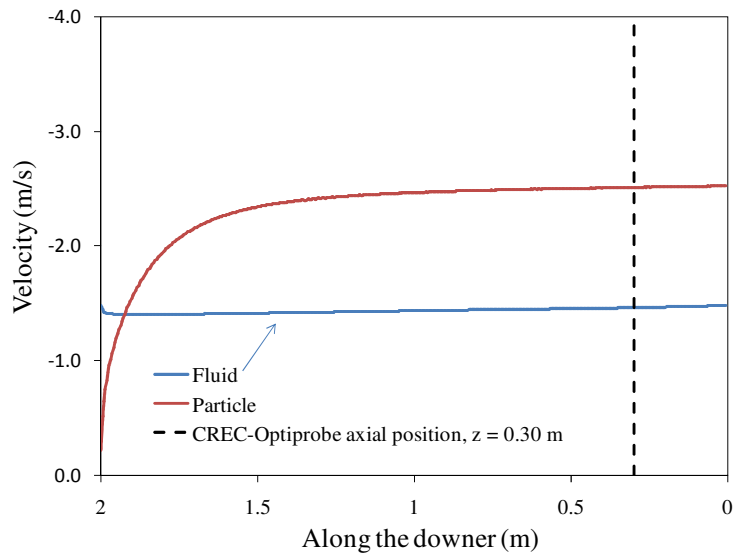


Figure 8–20: Average axial velocity profile along the downer. Operating condition: $U_g=1.5$ m/s, $G_s=34$ kg/m²s.

Moreover and further down the unit, there is, as reported in Figure 8–19 and Figure 8–20, "a second particle cluster acceleration" section. It is in this region, where the cluster particle velocity continues to increase, exceeding the gas velocity. It is in this section,

where gas drag acts in the opposite direction than gravity. Total pressure increases in the flow direction, displaying a positive pressure gradient. In summary, particle clusters keep accelerating, while gas drag remains smaller than gravity such as:

$$\left(\frac{\partial p}{\partial h}\right)_{U_g, G_s} > 0, U_g < U_s$$

Finally, particle clusters evolving in a downer reach a “third constant velocity region”. It is in this region, where gas drag forces become equal to gravity forces, with cluster particle velocity reaching a maximum value. In this section, pressure steadily increases, in the direction of the gas–solid flow, with the pressure gradient being positive and constant, as follows:

$$\left(\frac{\partial p}{\partial h}\right)_{U_g, G_s} > 0, \left(\frac{\partial^2 p}{\partial h^2}\right)_{U_g, G_s} = 0, U_g < U_s, U_s = \text{constant}$$

One can thus notice, that the proposed cluster particle model describes the pressure changes in downers as reported in previous publications (Li et al., 2013; Abbasi et al., 2012; Zhao et al., 2010; Zhang et al., 2003; Zhu et al., 2001; Zhu et al., 1995; Wang et al., 1992).

Figure 8–20 shows that the location of the CREC–GS–Optiprobes, and thus, the related measurements of cluster particle velocity and particle volume fraction are in the developed downer flow region. As a result, one can safely compare modeling predictions (which include this assumption) and experimental results, as attempted in the upcoming sections of this chapter.

In order to rigorously validate the proposed model, one has to consider both the experimentally measured and model predicted cluster particle velocity and volume solid fractions. In this respect, Figure 8–21, Figure 8–22 and Figure 8–23 report the cluster particle velocity profiles and particle volume fractions for the nine operating conditions studied (refer to Table 8–7). It can be observed that the CPDF simulations show good agreement with the experimental data. This is the case for both cluster particle velocity profiles and particle volume fractions with some differences between simulated and

observed values in the vicinity of the wall. One can observe that for all operating conditions, there is a dominant flat velocity profile, predicted both by CPFDF and observed experimentally. Differences, however, are noticed in the near wall region. Regarding this finding, one should note that the CPFDF computational model uses a zero gas velocity at the wall surface. This selected boundary condition may lead to the observed differences at the vicinity of the wall.

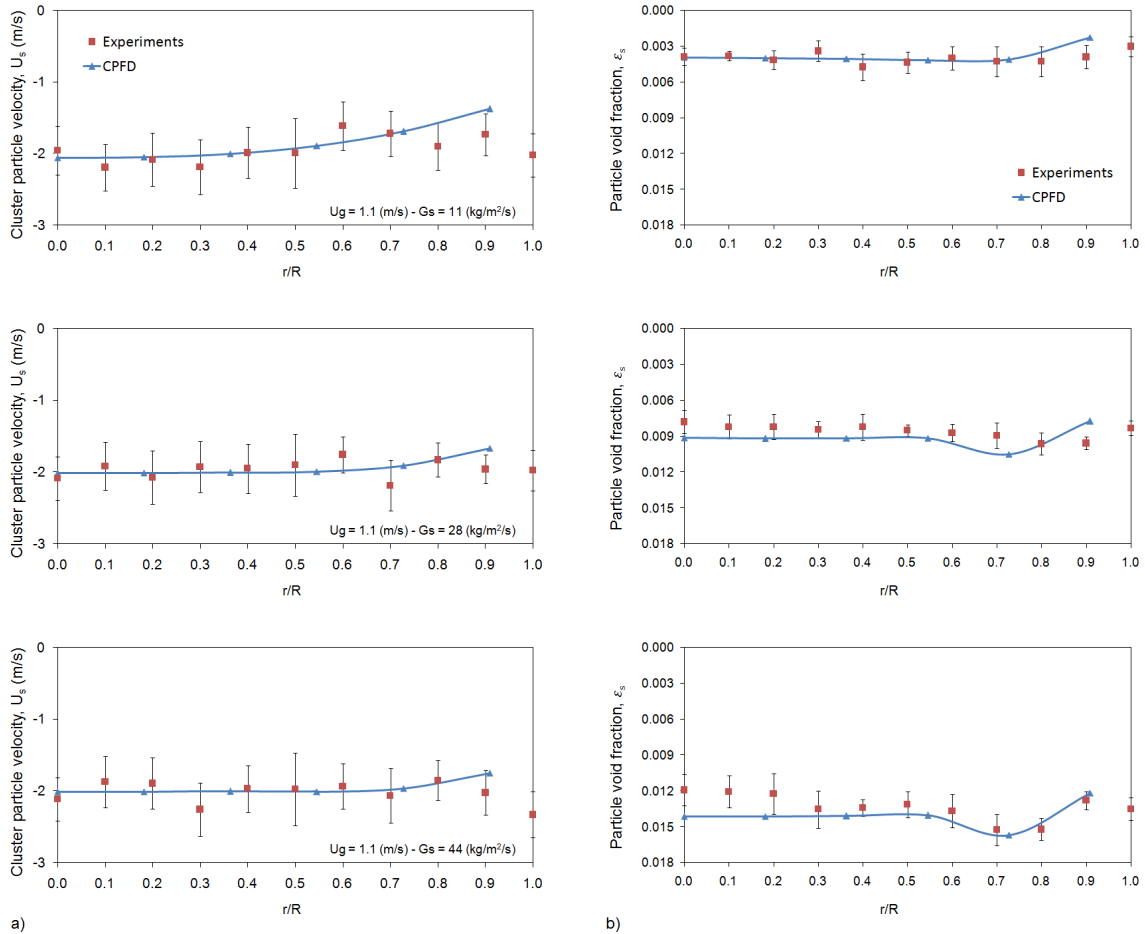


Figure 8–21: Radial profiles for a) cluster particle velocity profile, and b) particle volume fraction profile. Low gas velocities. Axial position of the CREC–GS–Optiprobes $z=0.30$ m.

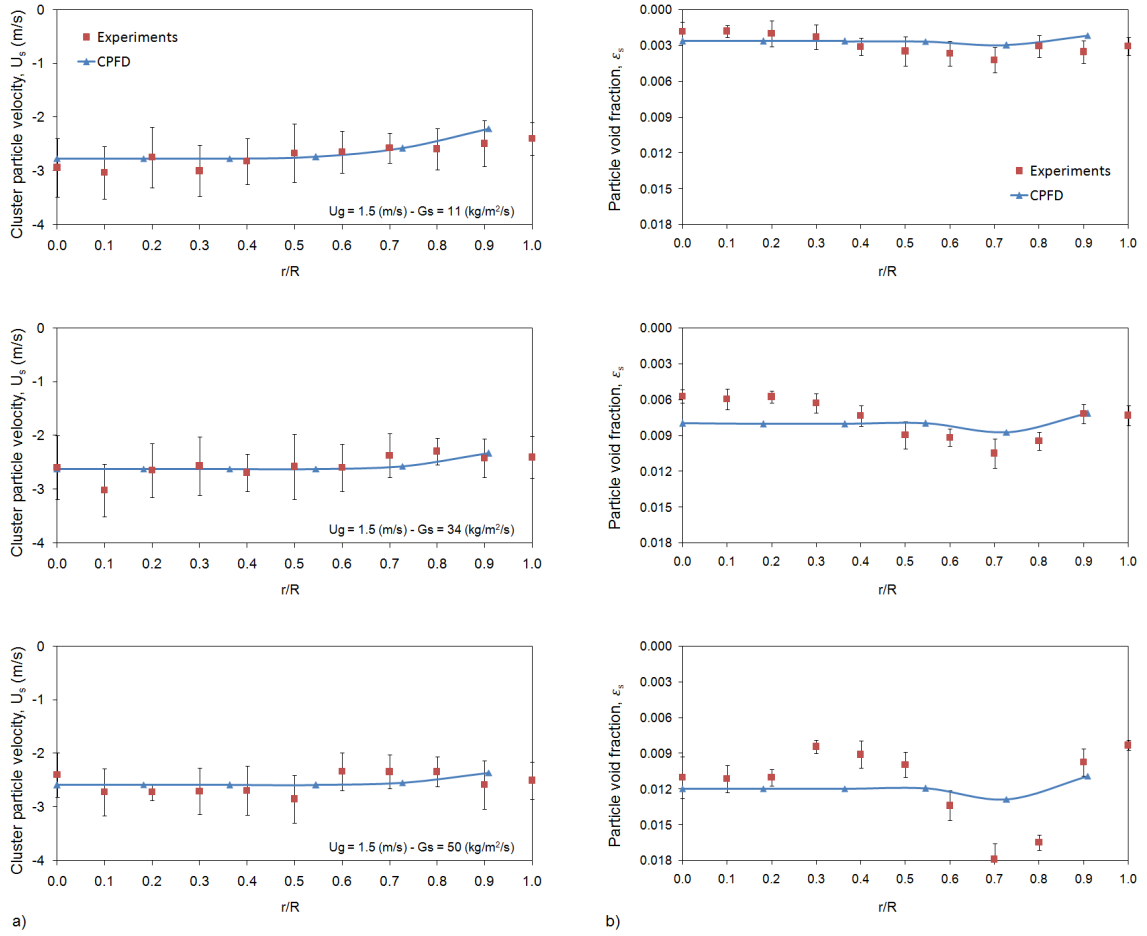


Figure 8–22: Radial profiles for a) cluster particle velocity and b) particle volume fraction. Intermediate gas velocities. Axial position of the CREC–GS–Optprobes $z=0.30$ m.

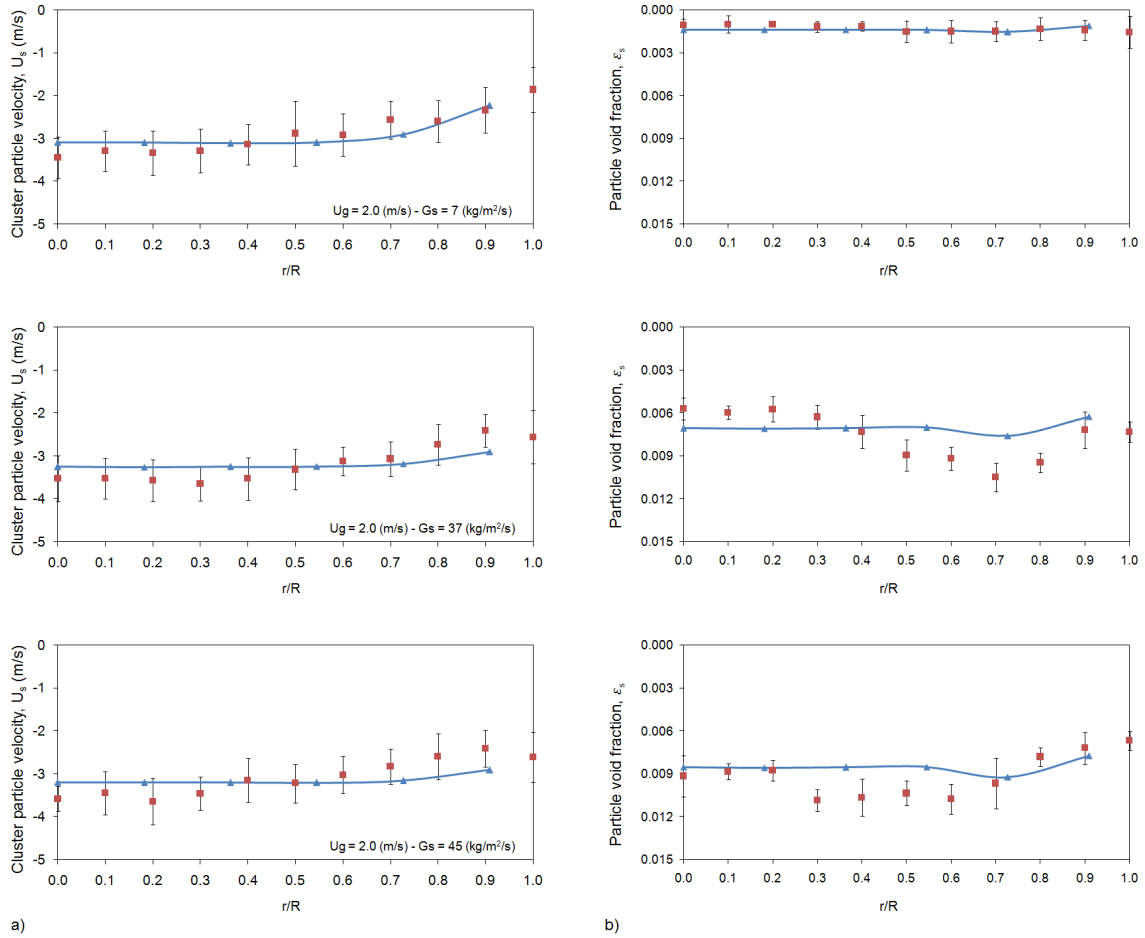


Figure 8–23: Radial profiles for a) cluster particle velocity and b) particle volume fraction. High gas velocities. Axial position of the CREC–GS–Optprobes $z=0.30$ m.

A comparison between the CFPD simulations and the experimental results for $r/R=0$ to $r/R=0.9$ is reported in Figure 8–24. The calculated deviations are: a) cluster particle velocity deviations: 8.1%, and b) particle volume fraction deviations: 19.4%.

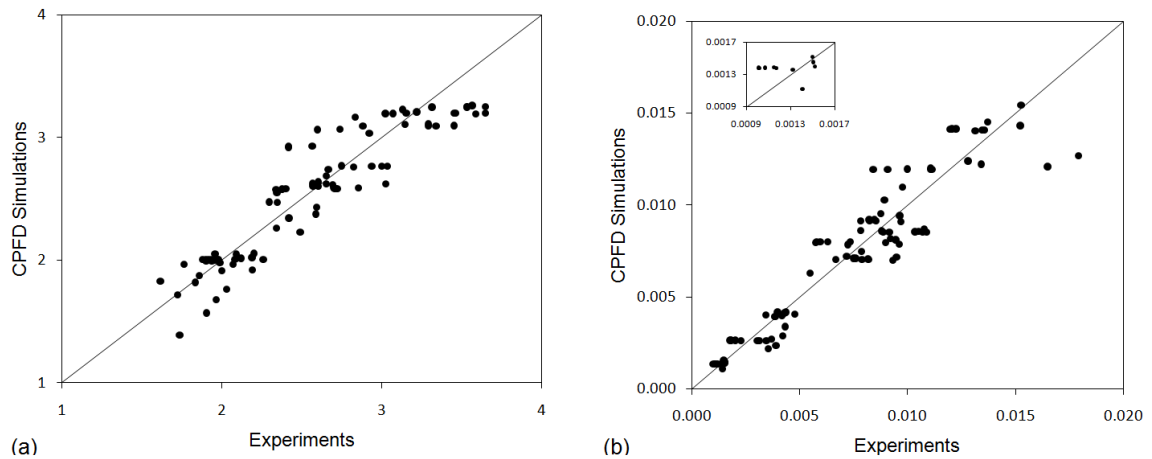


Figure 8–24: Comparison between CPFDF simulations and experimental results for cluster particle velocity and particle volume fraction. (a) Cluster particle velocity (m/s), and (b) Particle volume fraction.

Figure 8–25(a) shows the simulated radial velocity profiles for the gas and particle clusters in the downer. One can observe a similarity for each z position considered, with changes noticed along the downer. For instance, at the inlet section, a flat radial profile is observed. This can be anticipated, given the homogeneous assumption of the gas–particle mass flow at the near inlet conditions.

However, and once the flow is established, the wall starts having an increasing role on the radial velocity profile. One should notice that in the vicinity of the wall, a common practice is to calculate the slip velocity, from the experimental results, using a constant fluid velocity. This creates, as a result, an issue of uncertainty and need of model validation. On the other hand, in CPFDF simulations, the radial particle slip velocity, in the near wall regions is calculated using a more accurate estimation of fluid radial velocity. Thus, model results are likely more reliable.

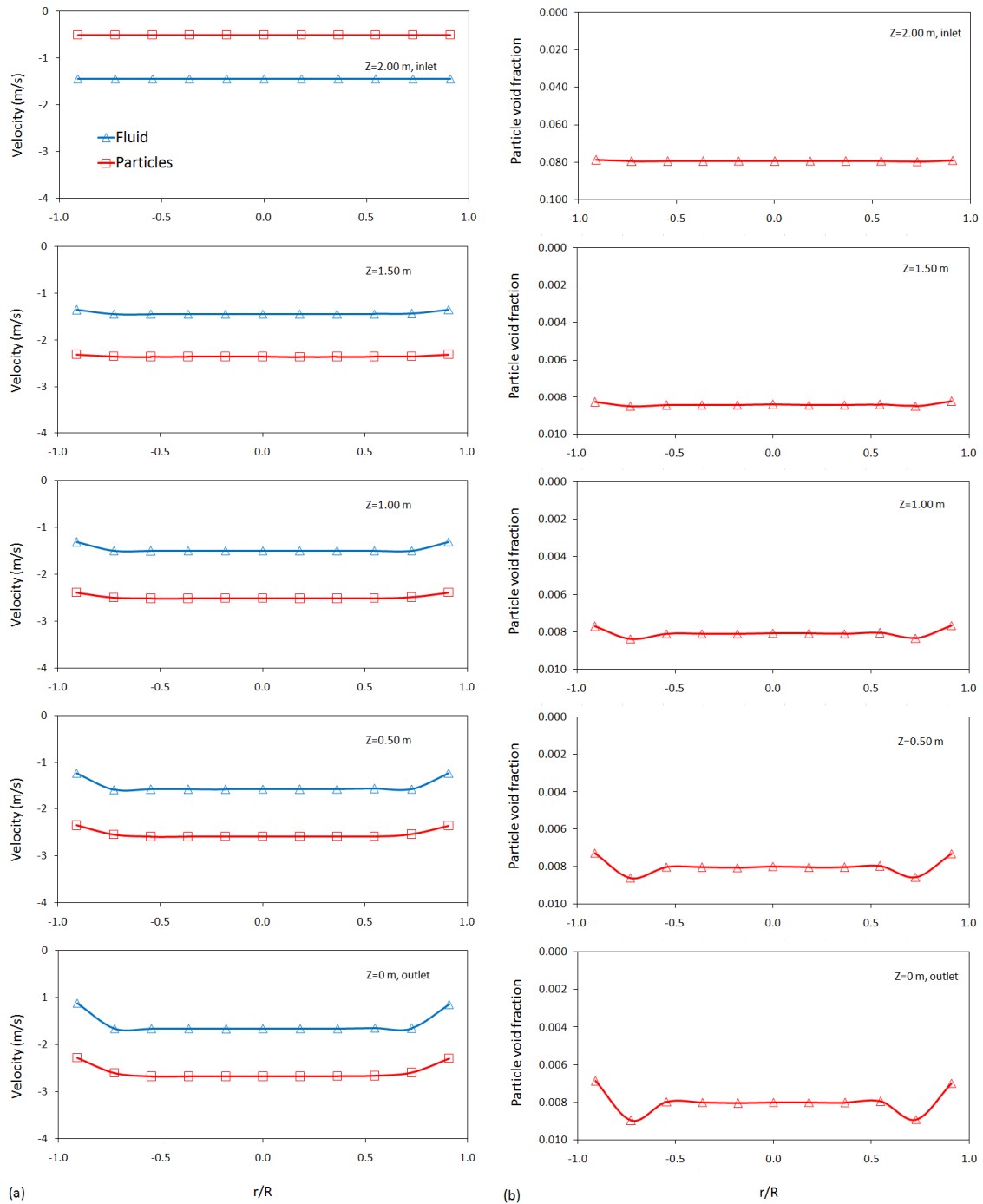


Figure 8–25: (a) Radial velocity profile, (b) Particle volume fraction. Operating condition: $U_g=1.5$ m/s, $G_s=34$ kg/m²s.

Figure 8–25(b) describes the particle volume fraction in the downer, at various axial positions. It can be observed, that there is an important effect of the wall on the particle

volume fraction. For example, starting at $Z=1.0$ m, an annular region of higher solid concentration develops near the wall, in the $r/R=0.65$ to 0.85 region. On the other hand, particle concentration remains fairly constant, in the centre core region, for up to $r/R=0.65$. Thereafter, it increases with a peak at around $r/R=0.75$ and decreases in the near wall region. Similar results were found by Wang et al. (1992) and Zhu et al. (1995).

Thus, both model and experimental data show good agreement, in the core region of the downer, with some discrepancy observed in the near wall region. It appears that further research in this area is still required, to elucidate the gas–solid fluid dynamics in the near wall downer region. These clarifications may considerably help, making the cluster model simulations applicable to the entire reactor unit.

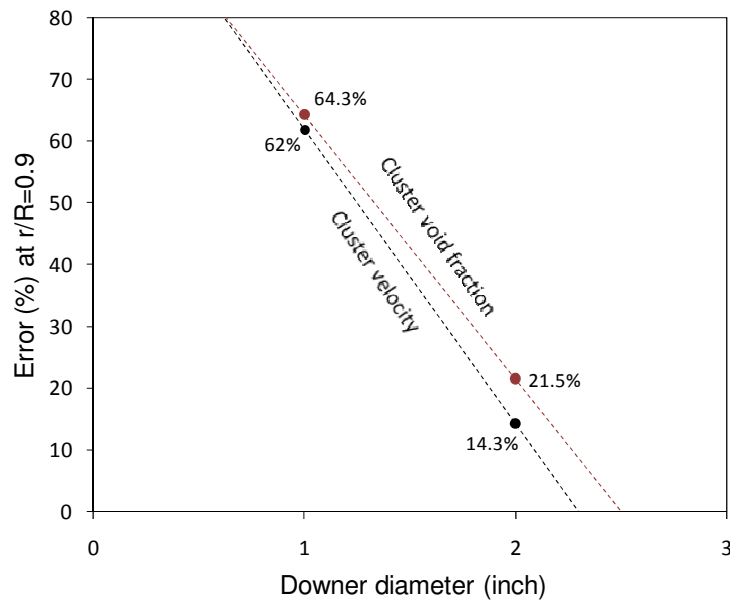


Figure 8–26: Comparison of the CPFD simulations and experimental data for the cluster void fraction and the cluster velocity based on the deviations (error %) at $r/R=0.9$ of the downer units studied.

Figure 8–26 compares the CPFD simulations, with experimental data, for both cluster void fractions and cluster velocity, based on their deviations (errors %) at $r/R=0.9$ position. One should notice that each point in Figure 8–26, represents more than 5,000 clusters. One can thus, observe that errors close to the wall are reduced when increasing

column diameters from one inch ID to two inch ID. Thus, it is expected, that the wall effect will be of significantly smaller importance in larger diameter downers where there is a much more limited near wall influence on the entire gas–solid fluid dynamics. We believe that this finding provides a significant contribution towards the design of industrial scale downers of larger diameter (e.g. 40 in ID).

In summary, the present study shows the value of CPDF simulations for modeling the fluid dynamics of downer units. This is accomplished by validating the proposed particle cluster model with experimental data obtained using the CREC–GS–Optiprobes. One can, thus, conclude that CPDF simulations using downer units, provide a most valuable modeling tool for the future development and scale–up of these units.

8.8 Conclusions

The following points are the main conclusions of this chapter:

- a) Data obtained with a CREC–GS–Optiprobes was successfully applied, to characterize the cluster fluid dynamics of the gas–solid concurrent flow in a 2 inch down flow reactor. This sensor belongs to the reflective type and has an incorporated GRIN lens. This GRIN lens allows measuring particle flow in downers, far away from the tip of the sensor, resulting in minimum intrusion effects in the gas–solid flow.
- b) The new methodology using data obtained with the CREC–GS–Optiprobes and targeted to set the time series signal baselines as proposed in Chapter 5, was successfully implemented. The reported results showed that the baseline reference factor, n , decreased when solid mass flux, G_s , increased. Additionally, it was observed that gas velocity does not have a strong influence on the baseline reference factor. This result was also found for the one inch internal diameter downer unit. With this new methodology, one can calculate cluster velocities and cluster sizes with increased confidence.
- c) Particle cluster size distributions showed that particle clusters display asymmetric distributions with smaller particle clusters being the most dominant. This finding was true for all operating conditions and various radial positions considered for both 1 inch ID and 2 inch ID downers units.

- d) Using this data, the fluid dynamics of the gas–solid two phase flow in downer units was established. This was the case for a wide range of superficial gas velocities and solid mass fluxes. Reported results include: cluster solid concentrations, individual cluster slip velocities, cluster sizes and cluster drag coefficients.
- e) CPFD numerical simulations of downer units were successfully developed using CPFD Barracuda based models. Grid meshes and numerical particles were set, considering the influence of meshing on both particle volume fraction and cluster particle velocities.
- f) CPFD simulations included average particle cluster sizes obtained from experimentally measured cluster size distributions. Drag coefficients, in these simulations, were accounted for by using average cluster sizes.
- g) Cluster particle acceleration regions and particle cluster constant velocity regions were successfully described by the CPFD calculations.
- h) CPFD simulated radial cluster particle velocities and radial particle hold-ups show flat profiles in the central downer region, with this being consistent with the experimental data. This agreement provides strong support to the phenomenologically based CPFD models of downer units of the present study.
- i) Experimentally measured radial cluster particle velocities and radial particle hold-ups, display differences in the near–wall region. This difference was smaller in the 2 inch diameter column than in the 1 inch diameter unit. It is considered that model and experimental discrepancies will be of less importance in larger diameter downer reactor units.

Chapter 9

9 Conclusions and Recommendations

This PhD dissertation reports a comprehensive characterization of the gas–solid fluid flow in two downer units. The studies developed include a) experimental data obtained using the CREC–GS–Optiprobes, and b) numerical modeling of gas–solid flows using a CPFD software. Individual cluster properties, such as: a) cluster solid concentrations, b) individual cluster slip velocities, c) individual cluster sizes and d) cluster size distributions are established and calculated. The following is a summary of the main conclusions and recommendations of the present research study.

9.1 Conclusions

- a) Data obtained with the CREC–GS–Optiprobes was successfully applied to characterize the cluster fluid dynamics of the gas–solid concurrent flow in two down flow reactors. This sensor belongs to the reflective type and has an incorporated GRIN lens. This GRIN lens allows measuring particle flow in downers far away from the tip of the sensor, resulting in minimum intrusion effects in the gas–solid flow.
- b) A rigorous methodology to analyze the CREC–GS–Optiprobes time–signals was successfully established. It was proposed that the position of the baseline has to be selected for every downer level and for operational conditions in compliance with solid mass balances. Using this approach, the noise resulting from secondary reflections is eliminated and all valuable data are kept in the time series. The reported results show that the baseline reference factor, n , decreases with the increase of the mass solid flow. Additionally, it is found that the gas velocity does not have a strong influence on the baseline reference factor. With this new methodology, one can calculate cluster velocities and cluster sizes with increased confidence.
- c) A mechanistic based method is proposed, to calculate cluster drag coefficients. The cluster drag coefficient is a function of the cluster length and cluster particles size

configuration. A well-defined range of possible drag coefficients is reported in this PhD dissertation for each cluster length.

- d) Cluster sizes and cluster size distributions are studied by adopting a particle cluster string configuration. Particle cluster size distributions show that particle clusters display asymmetric distributions with smaller particle clusters being the most dominant. This finding was true for all operating conditions and various radial positions considered.
- e) A computer based modeling validation using experimental information of gas–solid concurrent evolution in downer reactor units was performed. It is shown that the hydrodynamics of the gas–solid flow in downer reactors, modelled with the Barracuda Computational Particle Fluid Dynamics Numerical Scheme, was successfully simulated.
- f) When using the CPFD Barracuda, grid mesh sizes and number of numerical particles need to be established. This is required in order to obtain a numerical solution that is independent of both mesh and numerical particles. Furthermore, average particle cluster sizes obtained from experimentally measured cluster size distributions are considered in the CPFD simulations. Thus, drag coefficients, in these simulations, are accounted for by using average cluster sizes.
- g) CPFD calculations successfully simulated the cluster particle acceleration regions and particle cluster constant velocity region.
- h) CPFD simulations are consistent with the experimentally measured radial profiles of cluster particle velocities and particle hold-ups. These show flat profiles in the central downer region. These findings provide strong support to a phenomenologically based CPFD model for the downer units of the present study.
- i) CPFD simulations display important variations in the near wall region when comparing them with experimentally measured properties (cluster particle velocities and radial particle profiles of hold-ups). Furthermore, the proposed CPFD model, has

a limited ability to describe these changes. It is anticipated, however, that this model limitation is less of an issue when designing larger diameter downer reactors.

9.2 Recommendations

The following are the recommendation for future studies:

- a) To use a high speed miniaturized video camera system to develop an independent method for studying individual particle clusters in down flow reactors. This should give additional information about particle cluster sizes and shapes and should allow confirmation of cluster flow structures.
- b) To study a larger range of fluid dynamic conditions, including the study of higher solid fluxes and higher air velocities, extending the application of the CREC–GS–Optiprobes. This is important to fully establish the characteristics of clusters under conditions of potential industrial interest.
- c) To place several CREC–GS–Optiprobes at various axial and radial locations of the downer section, in order to perform simultaneous measurements in different acceleration sections of the downer. This is important in order to obtain experimental information that should allow the characterization of these sections.
- d) To study the impact of different gas/solid distributor designs, using fiber optic probes positioned at the downer inlet section, to validate the particle cluster behavior presented in this PhD dissertation.

References

- Abbasi, A., Islam, M., Ege, P., de Lasa, H. (2012). Downer reactor flow measurements using CREC–GS–Optiprobos. *Powder Technology*, 224, 1–11.
- Abbasi, A., Islam, M., Ege, P., de Lasa, H. (2013). CPFD flow pattern simulation in downer reactors. *AIChE Journal*, 59(5), 1635–1647.
- Abul–Hamayel, M. (2004). Comparison of downer and riser based fluid catalytic cracking process at high severity condition: A pilot plant study. *Petroleum Science and Technology*, 22(5–6), 475–490.
- Aguillon, J., Shakourzadeh, K., Guigon, P. (1996). A new method for local solid concentration measurement in circulating fluidized bed. *Powder Technology*, 86, 251–255.
- Amsden, A., O’Rourke, P., Butler, T. (1989). KIVA–II: A computer program for chemically reactive flows with sprays, Los Alamos – National Laboratory, report LA–11560–MS. New Mexico.
- Anderson, J. (2009). *Computational Fluid Dynamics*. McGraw–Hill. 3er ed. pp. 15–51. ISBN: 0–07–001685–2. New York.
- Andrews, M., O’Rourke, P. (1996). The multiphase particle–in–cell (MP–PIC) method for dense particulate flows. *International Journal of Multiphase Flow*, 22(2), 379–402.
- Arsenijević, Z., Kaluđerović, T., Garić–Grulović, R., Đuriš, M., Grbavčić, Ž. (2014). Hydrodynamic modeling of downward gas–solid flow. Part II: Co–current flow. *Powder Technology*, 256, 416–427.
- Auzerais, F., Jackson, R., Russel, W. (1988). The resolution of shocks and the effects of compressible sediments in transient settling. *Journal of Fluid Mechanics*, 195, 437–462.

- Berg, D., Briens, C., Bergougnou, M. (1989). Reactor development for the ultrapyrolysis process. *The Canadian Journal of Chemical Engineering*, 67(1), 96–101.
- Bieberle, M., Barthel, F., Hampel, U. (2012). Ultrafast X-ray computed tomography for the analysis of gas–solid fluidized beds. *Chemical Engineering Journal*, 189–190, 356–363.
- Bolkan, Y., Berruti, F., Zhu, J. –X., Milne, B. (2003). Modeling circulating fluidized bed downers. *Powder Technology*, 132(2–3), 85–100.
- Brust, H., Wirth, K. (2004). Residence time behavior of gas in a downer reactor. *Industrial and Engineering Chemistry Research*, 43(18), 5796–5801.
- Cao, C., Weinstein, H. (2000a). Characterization of downflowing high velocity fluidized beds. *AIChE Journal*, 46(3), 515–522.
- Cao, C., Weinstein, H. (2000b). Gas dispersion in downflowing high velocity fluidized beds. *AIChE Journal*, 46(3), 523–528.
- Chalermssinsuwan, B., Chanchuey, T., Buakhao, W., Gidaspow, D., Piumsomboon, P. (2012). Computational fluid dynamics of circulating fluidized bed downer: Study of modeling parameters and system hydrodynamic characteristics. *Chemical Engineering Journal*, 189–190, 314–335.
- Chalermssinsuwan, B., Gidaspow, D., Piumsomboon, P. (2013). Comparisons of particle cluster diameter and concentration in circulating fluidized bed riser and downer using computational fluid dynamics simulation. *Korean Journal of Chemical Engineering*, 30(4), 963–975.
- Chen, Y. –M. (2003). Applications for Fluid Catalytic Cracking. In: *Handbook of Fluidization and Fluid–Particles Systems*, Yang W. ed. Shell Global Solutions, Houston, Texas, USA.

- Cheng, Y., Chen, J., Ding, Y., Xiong, X., Jin, Y. (2008). Inlet effect on the coal pyrolysis to acetylene in a hydrogen plasma downer reactor. *The Canadian Journal of Chemical Engineering*, 86(3), 413–420.
- Cheng, Y., Guan, G., Ishizuka, M., Fushimi, C., Tsutsumi, A., Wang, C. –H. (2013). Numerical simulations and experiments on heat transfer around a probe in the downer reactor for coal gasification. *Powder Technology*, 235, 359–367.
- Cheng, Y., Wang, C. –H. (2014). Numerical study on coal Gasification in the Downer Reactor of a Triple–Bed Combined Circulating Fluidized Bed. *Industrial and Engineering Chemistry Research*, 53, 6624–6635.
- Cheng, Y., Wei, F., Guo, Y., Jin, Y. (2001). CFD simulation of hydrodynamics in the entrance region of a downer. *Chemical Engineering Science*, 56(4), 1687–1696.
- Cheng, Y., Wu, C., Zhu, J. –X., Wei, F., Jin, Y. (2008). Downer reactor: From fundamental study to industrial application. *Powder Technology*, 183(3), 364–384.
- Cheng, Y., Zhang, W., Guan, G., Fushimi, C., Tsutsumi, A., Wang, C. –H. (2014). Numerical studies of solid–solid mixing behaviors in a downer reactor for coal pyrolysis. *Powder Technology*, 253, 722–732.
- Chhabra, R., Agarwal, L., Sinha, N. (1999). Drag on non–spherical particles: An evaluation of available methods. *Powder Technology*, 101(3), 288–295.
- Chuachuensuk, A., Paengjuntuek, W., Kheawhom, S., Arpornwichanop, A. (2013). A systematic model–based analysis of a downer regenerator in fluid catalytic cracking processes. *Computers and Chemical Engineering*, 49, 136–145.
- Collin, A., Wirth, K. –E., Stroeder, M. (2009). Characterization of an annular fluidized bed. *Powder Technology*, 190(1–2), 31–35.
- Culshaw, B. (1984). *Optical fibre sensing and signal processing*. Institution Of Engineering and Technology. Peter Peregrinus Ltd. ISBN: 9780906048993. UK.

- Dang, N., Gallucci, F., van Sint Annaland, M. (2014). Micro-structured fluidized bed membrane reactors: Solids circulation and densified zones distribution. *Chemical Engineering Journal*, 239, 42–52.
- Dang, T., Gallucci, F., van Sint Annaland, M. (2014). Gas back-mixing study in a membrane-assisted micro-structured fluidized bed. *Chemical Engineering Science*, 108, 194–202.
- de Lasa, H., Young, B., Krol, S. (1998). Fiber optic sensor for sensing particle movement in a catalytic reactor. United States Patent 5740291.
- de Rezende, A., Furtado, J., Kenso, W., Machado, C., Silva, M., Medina, A., Junior, N., Medeiros, J., Freire, P., Nunes, W., Moreira, P. (2006). Apparatus and process for down fluid catalytic cracking. United States Patent 7087154.
- Deng, R., Wei, F., Liu, T., Jin, Y. (2002). Radial behavior in riser and downer during the FCC process. *Chemical Engineering and Processing: Process Intensification*, 41(3), 259–266.
- Dewitz, T. (1989). Downflow fluidized catalytic cracking system. United States Patent 4797262.
- Ding, T., Li, S., Xie, J., Song, W., Yao, J., Lin, W. (2012). Rapid pyrolysis of wheat straw in a bench-scale Circulating Fluidized Bed downer reactor. *Chemical Engineering and Technology*, 35(12), 2170–2176.
- Dong, P., Wang, Z., Li, Z., Li, S., Lin, W., Song, W. (2012). Experimental study on pyrolysis behaviors of coal in a countercurrent downer reactor. *Energy and Fuels*, 26(8), 5193–5198.
- Fan, C., Zhang, Y., Bi, X., Song, W., Lin, W., Luo, L. (2008). Evaluation of downer reactor performance by catalytic ozone decomposition. *Chemical Engineering Journal*, 140(1–3), 539–554.

- Fujiyama, Y., Redhwi, H., Aitani, A., Saeed, M. (2005). Demonstration plant for new FCC technology yields increased propylene. *Oil and Gas Journal*, 103 36, 54
- Ganser, G. (1993). A rational approach to drag prediction of spherical and nonspherical particles. *Powder Technology*, 77, 143–152.
- Gartside, R. (1989). QC – A new reaction system. In *Fluidization VI*, J. Grace, L. Bergougnou, M. Shemilt Eds. pp. 25–32. New York.
- Gartside, R., Ellis, A. (1983). Thermal regenerative cracker: A development update. *Chem Eng Prog*, 79(3), 82–85.
- Ge, W., Wang, W., Yang, N., Li, J., Kwauk, M., Chen, F., Chen, J., Fang, X., Guo, Li., He, X., et al. (2011). Meso-scale oriented simulation towards virtual process engineering (VPE)—The EMMS paradigm. *Chemical Engineering Science*, 66, 4426–4458.
- Geldart, D. (1973). Types of gas fluidization. *Powder Technology*, 7, 285–292.
- Gibilaro, L. (2001). *Fluidization dynamics*. Elsevier B.V. ISBN: 978-0-7506-5003-8.
- Grace, J. R., Bi, H. (2003). Circulating Fluidized Beds, In: *Handbook of Fluidization and Fluid-Particle Systems*, Yang W. C. eds. pp. 15–40.
- Gross, B., Ramaje, M. (1983). FCC Reactor with a downflow reactor riser. United States Patent 4385985.
- Haider, A., Levenspiel, O. (1989). Drag coefficient and terminal velocity of spherical and nonspherical particles. *Powder Technology*, 58, 63–70.
- Herbert, P., Gauthier, T., Briens, C., Bergougnou, M. (1994). Application of fiber optic reflection probes to the measurement of local particle velocity and concentration in gas-solid flow. *Powder Technology*, 80, 243–252.

- Herbert, P., Gauthier, T., Briens, C., Bergougnou, M. (1998). Flow study of a 0.05 m diameter downflow circulating fluidized bed. *Powder Technology*, 96, 255–261.
- Huard, M., Berruti, F., Briens, C. (2010). Experimental study of a novel fast gas–solid separator for pyrolysis reactors. *International Journal of Chemical Reactor Engineering*, 8, Article A134.
- Hudec, P. (2011). FCC Catalyst – key element in refinery technology. In: 45th International Petroleum Conference, pp. 1–11. Bratislava, Slovak Republic.
- Islam, M. (2010). Fluid dynamic studies in downer reactors with the CREC–GS–Optiprobes, PhD thesis dissertation, The University of Western Ontario.
- Islam, M., Krol, S., de Lasa, H. (2010). Slip velocity in downer reactors: Drag coefficient and the influence of operational variables. *Industrial and Engineering Chemistry Research*, 49(15), 6735–6744.
- Islam, M., Krol, S., de Lasa, H. (2011a). Radial distribution of particle clusters in a downer reactor unit. In: The 13th International Conference on Fluidization – New Paradigm in Fluidization Engineering, ECI Conference. Korea.
- Islam, M., Krol, S., de Lasa, H. (2011b). The CREC–GS–Optiprobes and its focal region. *Chemical Engineering Science*, 66, 1671–1684.
- Jiao, S. –Y., Zhu, J. –X., Bergougnou, M. A., Ikura, M., Stanciulescu, M. (1998). Investigation and modeling of the thermal cracking of waste plastic derived oil in a downer reactor. *Institution of Chemical Engineers*, 76, 319–331.
- Jin, Y., Wei, F., Cheng, Y., Wang, Z. (2014). Gas and solid parallel–flow folding type quick fluidized–bed reactor. Patent CN 1113689C.
- Johnston, P., de Lasa, H., Zhu, J. –X. (1999). Axial flow structure in the entrance region of a downer fluidized bed: Effects of the distributor design. *Chemical Engineering Science*, 54, 2161–2173.

- Johnston, P., Zhu, J. -X., de Lasa, H., Zhang, H. (1999). Effect of distributor designs on the flow development in downer reactor. *AIChE Journal*, 45, 1587–1592.
- Karimipour, S., Mostoufi, N., Sotudeh-Gharebagh, R. (2006). Modeling the hydrodynamics of downers by cluster-based approach. *Industrial and Engineering Chemistry Research*, 45, 7204–7209.
- Khongprom, P., Aimdilokwong, A., Limtrakul, S., Vatanatham, T., Ramachandran, P. (2012). Axial gas and solids mixing in a down flow circulating fluidized bed reactor based on CFD simulation. *Chemical Engineering Science*, 73, 8–19.
- Kim, Y., Bang, J., Kim, S. (1999). Bed-to-wall heat transfer in a downer reactor. *The Canadian Journal of Chemical Engineering*, 77, 207–212.
- Kim, Y., Lee, S., Kim, S. (2001). Coal gasification characteristics in a downer reactor. *Fuel*, 80, 1915–1922.
- Kim, Y., Wu, C., Cheng, Y. (2011). CFD simulation of hydrodynamics of gas–solid multiphase flow in downer reactors: revisited. *Chemical Engineering Science*, 66, 5357–5365.
- Kongkitisupchai, S., Gidaspow, D. (2013). Carbon dioxide capture using solid sorbents in a fluidized bed with reduced pressure regeneration in a downer. *AIChE*, 59, 4519–4537.
- Koratiya, V., Kumar, S., Sinha, S. (2010). Modeling, simulation and optimization of FCC downer reactor. *Petroleum and Coal*, 52, 183–192.
- Krol, S., Pekediz, A., de Lasa, H. (2000). Particle clustering in down flow reactors. *Powder Technology*, 108, 6–20.
- Kunii, D., Levenspiel, O., Brenner, H. (1991). *Fluidization engineering*. 2nd Edition, ISBN 0–409–90233–0. Boston, USA.

- Lanza, A., Islam, M., de Lasa, H. (2012). Particle clusters and drag coefficients in gas–solid downer units. *Chemical Engineering Journal*, 200–202, 439–451.
- Lanza, A., Islam, M., de Lasa, H. (2013). Particle cluster size distribution in gas–solid downer units. In: *The 14th International Conference on Fluidization – From Fundamentals to Products* eds, ECI Symposium Series, Volume (2013). The Netherlands.
- Lehner, P., Wirth, K. –E. (1999). Characterization of the flow pattern in a downer reactor. *Chemical Engineering Science*, 54, 5471–5483.
- Li, D., Ray, M., Ray, A., Zhu, J. –X. (2013). A comparative study on hydrodynamics of circulating fluidized bed riser and downer. *Powder Technology*, 247, 235–259.
- Li, D., Zhu, J. –X., Ray, M., Ray, A. (2011). Catalytic reaction in a circulating fluidized bed downer: Ozone decomposition. *Chemical Engineering Science*, 66, 4615–4623.
- Li, S., Lin, W., Yao, J. (2004). Modeling of the hydrodynamics of the fully developed region in a downer reactor. *Powder Technology*, 145, 73–81.
- Lim, E., Zhang, Y., Wang, C. –H. (2006). Effects of an electrostatic field in pneumatic conveying of granular materials through inclined and vertical pipes. *Chemical Engineering Science*, 61, 7889–7908.
- Liu, Y., Liu, X., Kallio, S., Zhou, L. (2011). Hydrodynamic predictions of dense gas–particle flows using a second–order–moment frictional stress model. *Advanced Powder Technology*, 22, 504–511.
- Lu, X., Li, S., Du, L., Yao, J., Lin, W., Li, H. (2005). Flow structures in the downer circulating fluidized bed. *Chemical Engineering Journal*, 112, 23–31.
- Ma, Y., Zhu, J. –X. (1999). Experimental study of heat transfer in a co–current downflow fluidized bed (downer). *Chemical Engineering Science*, 54, 41–50.

- Maadhah, A., Fujiyama, Y., Redhwi, H., Abul-Hamayel, M., Aitani, A., Saeed, M., Dean, C. (2008). A new catalytic cracking process to maximize refinery propylene. *The Arabian Journal for Science and Engineering*, 33, 17–28.
- Manyele, S., Pärssinen, J., Zhu, J. (2002). Characterizing particle aggregates in a high-density and high-flux CFB riser. *Chemical Engineering Journal*, 88, 151–161.
- Manyele, S., Zhu, J. –X., Zhang, H. (2003). Analysis of the microscopic flow structure of a CFB downer reactor using solids concentration signals analysis. *International Journal of Chemical Reactor Engineering*, 1, Article A55.!!
- Matsuno, Y., Yamaguchi, H., Oka, T., Kage, H., Higashitanp, K. (1983). The use of optic fiber probes for the measurement of dilute particle concentrations: Calibration and application to gas-fluidized bed carryover. *Powder Technology*, 36, 215–221.
- Mei, G., Herben, P., Cagnani, C., Mazzucco, A. (2006). The spherizone process: A new PP manufacturing platform. *Macromolecular Symposia*, 245–246, 677–680.
- Muldowney, G. (1995). FCC Process with upflow and downflow reactors. United States Patent 5468369.
- Niccum, P. K., Bunn, D. P. (1985). Catalytic cracking system. United States Patent 4514285.
- Nova, S. (2005). Optical sensor for particle clustering studies in downflow reactors. PhD thesis dissertation, The University of Western Ontario.
- Nova, S., Krol, S., de Lasa, H. (2004a). CREC fiber-optic probes for particle velocity and particle clustering: design principles and calibration procedures. *Industrial and Engineering Chemistry Research*, 43, 5620–5631.
- Nova, S., Krol, S., de Lasa, H. (2004b). Particle velocity and particle clustering in down-flow reactors. *Powder Technology*, 148, 172–185.

- Nova, S., Krol, S., de Lasa, H. (2007). Radial distribution of particle clusters in down flow reactors. In: The 12th International Conference on Fluidization – New Horizons in Fluidization Engineering eds. ECI Symposium Series.
- O'Rourke, P., Snider, D. (2010). An improved collision damping time for MP-PIC calculations of dense particle flows with applications to polydisperse sedimenting beds and colliding particle jets. *Chemical Engineering Science*, 65, 6014–6028.
- O'Rourke, P., Zhao, P., Snider, D. (2009). A model for collisional exchange in gas/liquid/solid fluidized beds. *Chemical Engineering Science*, 64, 1784–1797.
- Pantzali, M., B., L., Heynderickx, G., Marin, G. (2013). Three-component solids velocity measurements in the middle section of a riser. *Chemical Engineering Science*, 101, 412–423.
- Peng, G., Dong, P., Li, Z., Wang, J., Lin, W. (2013). Eulerian simulation of gas–solid flow in a countercurrent downer. *Chemical Engineering Journal*, 230, 406–414.
- Pontier, R., Hoffmann, F., Galtier, P. (1994). Down fluid catalytic cracking process and apparatus. United States Patent 5344554.
- Prajongkan, Y., Piumsomboon, P., Chalermssinsuwan, B. (2012). Computation of mass transfer coefficient and Sherwood number in circulating fluidized bed downer using computational fluid dynamics simulation. *Chemical Engineering and Processing: Process Intensification*, 59, 22–35.
- Qi, X., Zhang, H., Zhu, J. –X. (2008). Solids concentration in the fully developed region of circulating fluidized bed downers. *Powder Technology*, 183(3), 417–425.
- Qian, L., Lu, Y., Zhong, W., Chen, X., Ren, B., Jin, B. (2013). Developing a novel fibre high speed photography method for investigating solid volume fraction in a 3D spouted bed. *The Canadian Journal of Chemical Engineering*, 91, 1793–1799.
- Reh, L. (1971). Fluidized Bed Processing. *Chem Eng Prog*, 67, 58–63.

- Ropelato, K., Meier, H., Cremasco, M. (2005). CFD study of gas–solid behavior in downer reactors: An Eulerian–Eulerian approach. *Powder Technology*, 154, 179–184.
- Samruamphianskun, T., Piumsomboon, P., Chalermssinsuwan, B. (2012). Computation of system turbulences and dispersion coefficients in circulating fluidized bed downer using CFD simulation. *Chemical Engineering Research and Design*, 90, 2164–2178.
- Shaikh, A., Al–Mutairi, E., Ino, T. (2008). Modeling and simulation of a downer–type HS–FCC Unit. *Industrial and Engineering Chemistry Research*, 47, 9018–9024.
- Sharma, A., Tuzla, K., Matsen, J., Chen, J. (2000). Parametric effects of particle size and gas velocity on cluster characteristics in fast fluidized beds. *Powder Technology*, 111, 114–122.
- Shu, Z., Peng, G., Wang, J., Zhang, N., Li, S., Lin, W. (2014). Comparative CFD analysis of heterogeneous gas–solid flow in a countercurrent downer reactor. *Industrial and Engineering Chemistry Research*, 53, 3378–3384.
- Smagorinsky, J. (1963). General circulation experiments with the primitive equations, Part I: the basic experiment. *Monthly Weather Review*, 91:99-164.
- Snider, D., Banerjee, S. (2010). Heterogeneous gas chemistry in the CPFD Eulerian–Lagrangian numerical scheme (ozone decomposition). *Powder Technology*, 199, 100–106.
- Snider, D., Clark, S., O’Rourke, P. (2011). Eulerian–Lagrangian method for three–dimensional thermal reacting flow with application to coal gasifiers. *Chemical Engineering Science*, 66, 1285–1295.
- Snider, D., O’Rourke, P., Andrews, M. (1998). Sediment flow in inclined vessels calculated using a multiphase particle–in–cell model for dense particle flows. *International Journal of Multiphase Flow*, 24, 1359–1382.

- Sommerfeld, M. (2010). Two-phase gas-solid flow – Particle motion in fluids. In VDI Heat Atlas, 2nd Edition, pp. 1181–1185. ISBN 978-3-540-77876-9. Germany.
- Song, X., Bi, X., Bolkan, Y. (2005). Hydrodynamics of high-density downer reactors using a novel solids feeder. *International Journal of Chemical Reactor Engineering*, 3, Article A52.
- Soong, C., Tuzla, K., Chen, J. (1993). Identification of particle clusters in circulating fluidized beds. In: *Fluidized Bed Technology IV Engineering Foundation*, Avidan A. A. ed. pp. 615–620. New York.
- Squires, A. (1994). Origins of the fast fluidized bed. In: *Fast Fluidization Advances in Chemical Engineering*, Kwauk M. eds. 20, 1–37.
- Talman, J., Geier, R., Reh, L. (1999). Development of a downer reactor for fluid catalytic cracking. *Chemical Engineering Science*, 54, 2123–2130.
- Tuzla, K., Sharma, A., Chen, J., Schiewe, T., Wirth, K., Molerus, O. (1998). Transient dynamics of solid concentration in downer fluidized bed. *Powder Technology*, 100, 166–172.
- Vaishali, S., Roy, S., Mills, P. (2008). Hydrodynamic simulation of gas-solids downflow reactors. *Chemical Engineering Science*, 63, 5107–5119.
- Vaishali, S., Roy, S., Mills, P. (2010). Modeling of partial oxidation in gas-solids downer reactors. *AIChE*, 56, 2150–2162.
- Wang, Z., Bai, D., Jin, Y. (1992). Hydrodynamics of cocurrent downflow circulating fluidized bed (CDCFB). *Powder Technology*, 70, 271–275.
- Weber, J., Layfield, K., Van Essendelft, D., Mei, J. (2013). Fluid bed characterization using Electrical Capacitance Volume Tomography (ECVT), compared to CPFD Software's Barracuda. *Powder Technology*, 250, 138–146.

- Werther, J. (1999). Measurement techniques in fluidized beds. *Powder Technology*, 102, 15–36.
- Wu, C., Cheng, Y., Ding, Y., Jin, Y. (2010). CFD–DEM simulation of gas–solid reacting flows in fluid catalytic cracking (FCC) process. *Chemical Engineering Science*, 65, 542–549.
- Wu, C., Cheng, Y., Jin, Y. (2009). Understanding riser and downer based Fluid Catalytic Cracking processes by a comprehensive two–dimensional reactor model. *Industrial and Engineering Chemistry Research*, 48, 12–26.
- Xu, K., Hou, S., Long, J., Zhong, J., Zhang, J., Zhang, Z., Li, S., Wu, X., He, J. (2006). Downflow catalytic cracking reactor and its application. United States Patent 7153478 B2.
- Yan, Y. (1996). Mass flow measurement of bulk solids in pneumatic pipelines. *Measurement Science Technology*, 7, 1687–1706.
- Ye, S., Qi, X., Zhu, J. –X. (2009). Direct measurements of instantaneous solid flux in a CFB riser using a novel multifunctional optical fiber probe. *Chemical Engineering and Technology*, 32, 580–589.
- Yoshie, Y., Ishizuka, M., Guan, G., Fushimi, C., Tsutsumi, A. (2013). A novel experimental technique to determine the heat transfer coefficient between the bed and particles in a downer. *Advanced Powder Technology*, 24, 487–494.
- Zhang, H. (1999). Hydrodynamics in downflow fluidized beds (1): solids concentration profiles and pressure gradient distributions. *Chemical Engineering Science*, 54, 5461–5470.
- Zhang, H., Johnston, P., Zhu, J. –X., de Lasa, H., Bergougnou, M. (1998). A novel calibration procedure for a fiber optic solids concentration probe. *Powder Technology*, 100, 260–272.

- Zhang, H., Zhu, J. -X. (2000). Hydrodynamics in downflow fluidized beds (2): Particle velocity and solids flux profiles. *Chemical Engineering Science*, 55, 4367–4377.
- Zhang, H., Zhu, J. -X., Bergougnou, M. (1999a). Flow development in a gas–solids downer fluidized bed. *The Canadian Journal of Chemical Engineering*, 77, 194–198.
- Zhang, H., Zhu, J. -X., Bergougnou, M. (1999b). Hydrodynamics in down flow fluidized beds (1): solids concentration profiles and pressure gradient distributions. *Chemical Engineering Science*, 54, 5461–5470.
- Zhang, M., Chu, K., Wei, F., Yu, A. (2008). A CFD–DEM study of the cluster behavior in riser and downer reactors. *Powder Technology*, 184, 151–165.
- Zhang, M., Qian, Z., Yu, H., Wei, F. (2003). The solid flow structure in a circulating fluidized bed riser/downer of 0.42–m diameter. *Powder Technology*, 129, 46–52.
- Zhang, Y., Lan, X., Gao, J. (2012). Modeling of gas–solid flow in a CFB riser based on computational particle fluid dynamics. *Petroleum Science*, 9, 535–543.
- Zhang, Y., Wang, Z. -W., Jin, Y. (2013). Simulation and experiment of gas–solid flow field in short–contact cyclone reactors. *Chemical Engineering Research and Design*, 91, 1768–1776.
- Zhao, T., Liu, K., Cui, Y., Takei, M. (2010). Three–dimensional simulation of the particle distribution in a downer using CFD–DEM and comparison with the results of ECT experiments. *Advanced Powder Technology*, 21, 630–640.
- Zhao, Y., Cheng, Y., Wu, C., Ding, Y., Jin, Y. (2010). Eulerian–Lagrangian simulation of distinct clustering phenomena and RTDs in riser and downer. *Particuology*, 8, 44–50.
- Zhao, Y., Ding, Y., Wu, C., Cheng, Y. (2010). Numerical simulation of hydrodynamics in downers using a CFD–DEM coupled approach. *Powder Technology*, 199, 2–12.

- Zheng, Y., Liu, Q. (2010). Review of certain key issues in indirect measurements of the mass flow rate of solids in pneumatic conveying pipelines. *Measurement*, 43, 727–734.
- Zhou, J., Grace, J., Lim, C., Brereton, C. (1995). Particle velocity profiles in a circulating fluidized bed riser of square cross-section. *Chemical Engineering Science*, 50, 237–244.
- Zhu, J. -X., Li, G. -Z., Qin, S. -Z., Li, F. -Y., Zhang, H., Yang, Y. -L. (2001). Direct measurements of particle velocities in gas-solids suspension flow using a novel five-fiber optical probe. *Powder Technology*, 115, 184–192.
- Zhu, J. -X., Yu, Z. -Q., Jin, Y., Grace, J., Issangya, A. (1995). Cocurrent downflow circulating fluidized bed (downer) reactors – A state of the art review. *The Canadian Journal of Chemical Engineering*, 73, 662–677.
- Zinke, R., Koves, W. (1996). Downflow FCC reaction arrangement with upflow regeneration. United States Patent 5582712.

Appendices

Appendix A: Fluid Catalytic Cracking (FCC) Catalyst

The particulate phase used in the present PhD dissertation is a Catalyst used in Fluid Catalytic Cracking (FCC) units with a mean particle diameter of 84.42 μm and a particle density of 1,722 kg/m^3 . Table A–1 reports the corresponding Particle Size Distribution of this product.

Table A–1: Fluid Catalytic Cracking (FCC) Catalyst Particle Size Distribution.

Particle diameter (μm)	Frequency (%)	Cumulative Weight (%)
26	0.1	0.1
30	0.5	0.6
35	1.5	2.1
39	3.0	5.1
44	4.9	10.0
50	7.0	17.0
57	9.2	26.2
65	10.9	37.1
73	11.9	49.0
82	12.0	61.0
94	11.2	72.2
107	9.5	81.7
120	7.4	89.1
137	5.2	94.3
155	3.2	97.5
175	1.7	99.2
200	0.7	99.9
227	0.1	100.0

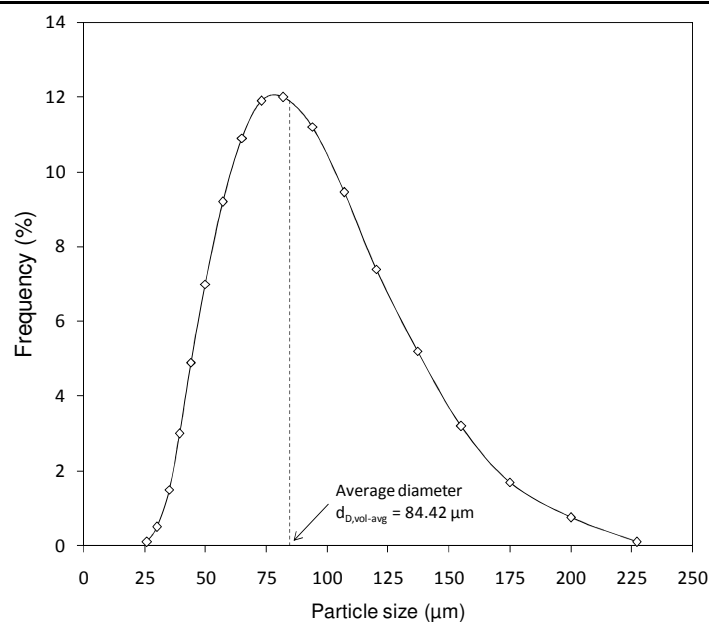


Figure A–1: Volume weighted particle size distribution of the FCC catalyst.

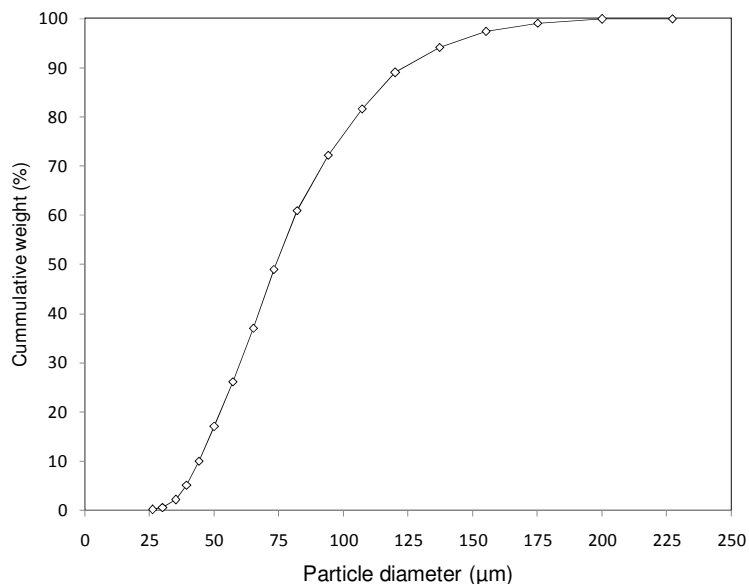


Figure A-2: Cumulative weight of the catalyst used in the present study.

Figures A-1 and A-2 report the volume weighted particle size distribution and the cumulative weight of the catalyst used in the present study according with Table A-1.

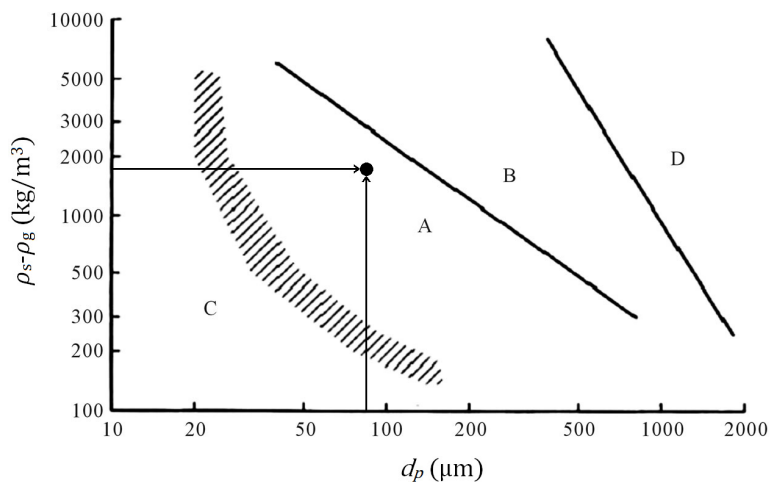


Figure A-3: Geldart's classification of the FCC Catalyst used.

Figure A-3 reports that the used FCC Catalyst belongs to class A according with the Geldart's classification (Geldart, 1973), where, A is Aeratable ($U_{mb} > U_{mf}$), the material has significant deaeration time, e.g. FCC Catalyst; B is Bubbles above U_{mf} ($U_{mb} = U_{mf}$),

e.g. 500 μm sand; C is Cohesive, e.g. flour, and fly ash; and D is Spoutable, e.g. wheat, 2000 μm polyethylene pellets.

This catalyst was provided by the Canadian petroleum company Imperial Oil Limited. The precise chemical composition is property of Imperial Oil Limited. However, a modern FCC catalyst has four major components: crystalline Zeolite, matrix, binder, and filler, see Figure A–4.

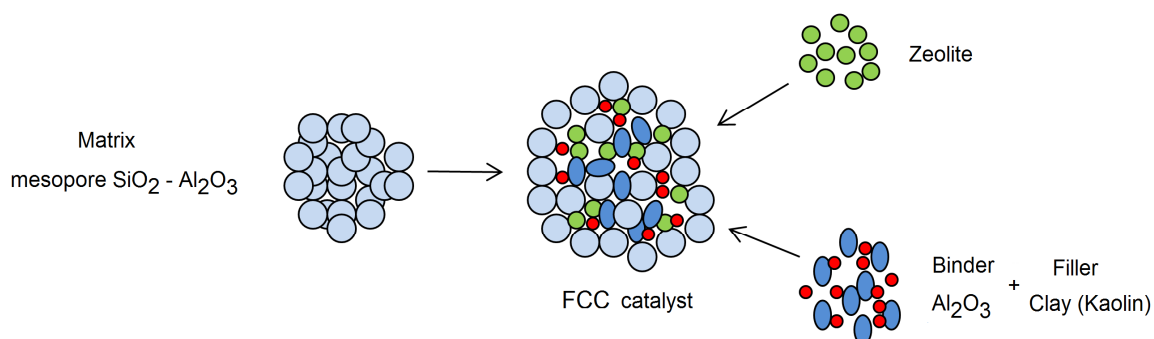


Figure A–4: Components of a typical FCC catalyst.

The Zeolite is the primary active component and can range from about 15 to 50 weight percent of the catalyst. The Zeolite used in FCC catalysts is referred to as faujasite or as Type Y and is composed of silica and alumina tetrahedra with each tetrahedron having either an aluminum or a silicon atom at the center and four oxygen atoms at the corners. It is a molecular sieve with a distinctive lattice structure that allows only a certain size range of hydrocarbon molecules to enter the lattice. The matrix component of an FCC catalyst contains amorphous alumina which may also provides catalytic activity sites and larger pores that allows entry for larger molecules. The binder and filler components provide the physical strength and integrity of the catalyst. The binder is usually silica and the filler is usually a clay (kaolin).

As reported by [Hudec \(2011\)](#), the philosophy of the preparation of the new generation of FCC–catalyst is to have a) weak acid centers in macroporous matrix to insure the cracking of larger molecules of residue, b) medium acidity in mesopores (synthetic silica–alumina) where the molecules previously cracked in macroporous could enter, and

c) strong acid centers in Zeolite micropores where products of cracking in mesopores could finally enter and be cracked into smaller molecules, mainly gasoline fraction, see Figure A–5.

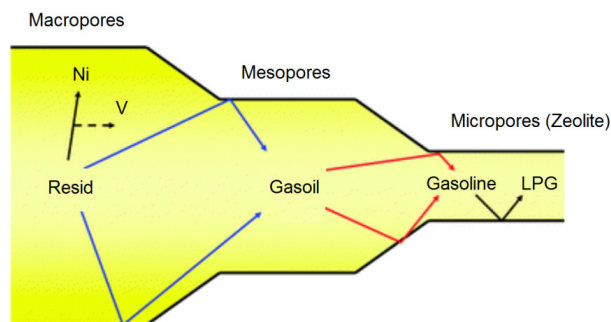


Figure A–5: Role of different pore sizes in FCC Catalyst.

As a reference, Table A–2 reports the physical and chemical properties of a typical modern FCC Catalyst.

Table A–2: Physical and chemical properties of a typical modern FCC Catalyst.

Physical Properties	
Davison Attrition Index	4.2
Celda parameter, Å,	24.6
Total Area, m ² /g	380.0
Zeolite Area, m ² /g	291.0
Matrix Area, m ² /g	89.0
Zeolite/Matrix Ratio	3.3
After hydrothermal deactivation 7 hr 1500 °F	
Total Area, m ² /g	136
Zeolite Area, m ² /g	84
Matrix Area, m ² /g	52
Chemical Properties	
Alumina or aluminum trioxide (Al ₂ O ₃), %w	38.0
Silica or silicon dioxide (SiO ₂), %w	56.0
Sodium oxide (Na ₂ O), %w	0.24
Iron trioxide (Fe ₂ O ₃), %w	0.9
Titanium dioxide (TiO ₂), %w	2.4
Phosphorus (P), ppm	728.00
Zinc (Zn), ppm	0.01
Cerium trioxide (Ce ₂ O ₃), %w	0.03
Lanthanum trioxide (La ₂ O ₃), %w	3.20
+ Rhenium trioxide (Re ₂ O ₃), %w	3.23

Appendix B: Camera Beam Profiler

A charge coupled device (CCD) Camera Beam Profiler (BC106–VIS) with a wavelength range of 350–1100 nm was used in the present study. A CCD is an integrated circuit etched onto a silicon surface forming light sensitive elements called pixels. Photons incident on this surface generate charge that can be read by electronics and turned into a digital copy of the light patterns falling on the device. CCDs come in a wide variety of sizes and types and are used in many applications from cell phone cameras to high–end scientific applications.

The CCD Camera Beam Profiler (BC106–VIS) used is a full featured, high–precision instrument that can analyze the power distribution and effective beam diameter of laser beams with diameters from 30 μm – 6.6 mm. This allows complex mode patterns (like flat top and donut) to be identified while optimizing laser systems. Table B–1 summarizes the features of the CCD camera based beam profiler used in the present study.

Table B–1: CCD Camera Beam Profiler features.

Specification	CCD Camera Beam Profiler
Wavelength Range	350 – 1100 nm
Power Range	50 fW – 1 W
Aperture Size	8.77 mm x 6.6 mm
Beam Diameter	30 μm – 6.6 mm
Resolution	1.3 megapixels
ND Filters	10, 20, 30, and 40 dB

The measurement head has a USB 2.0 interface, which allows the user to easily operate the device with the included Beam Profile Software.

Appendix C: Beam Profiler Software

A Graphical User Interface (GUI) was designed for the CCD camera based beam profiler device, which allows individual views of the X and Y beam cross sections, 2D projections, and 3D profiles in gray scale or color mode as well as the numerical parameters in separate windows. Many details like peak and centroid position, Gaussian approximations of the X and Y profiles, and elliptical fits of the beam's cross section can be superimposed, faded out, or displayed in many different variations.

The beam diameter is calculated according to the ISO 11146 standard ISO 11146-1:2005(E), or at any user-defined clip level. GUI images and calculated data can be saved to different file formats.

The appearance of the beam profiler software can be arranged according to user's requirements and taste. All small windows can be sized and positioned very flexible. Figure C-1 reports an example of arranging some small windows.

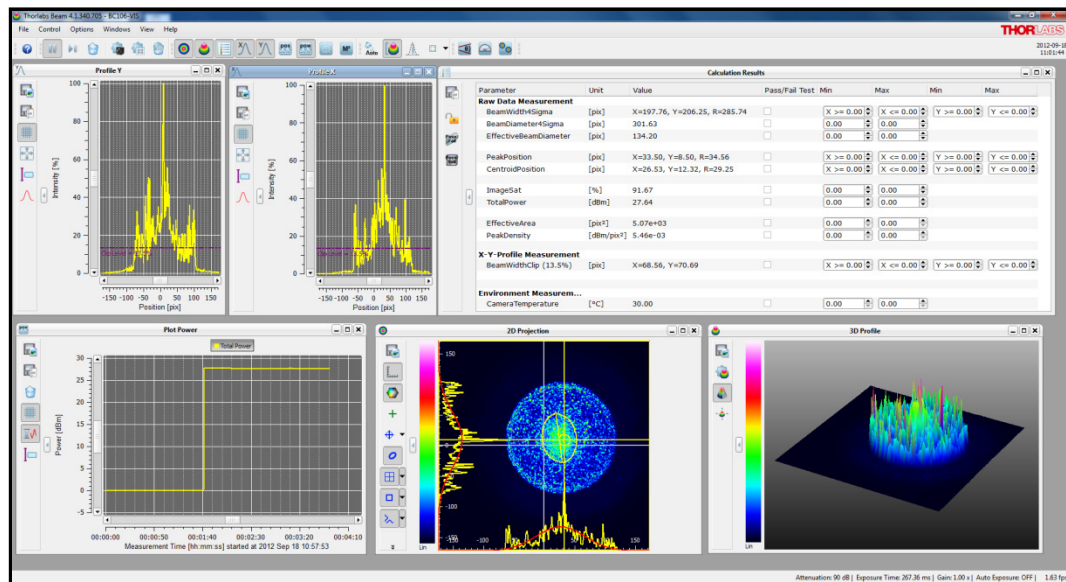


Figure C-1: Thorlabs beam profiler software appearance.

A brief description of each small window is presented as follows.

C.1 2D Projection

The 2D Projection graph, presented in Figure C–2, shows the image from the Beam Profiler indicating the power intensity distribution within the selected Region of Interest (ROI).

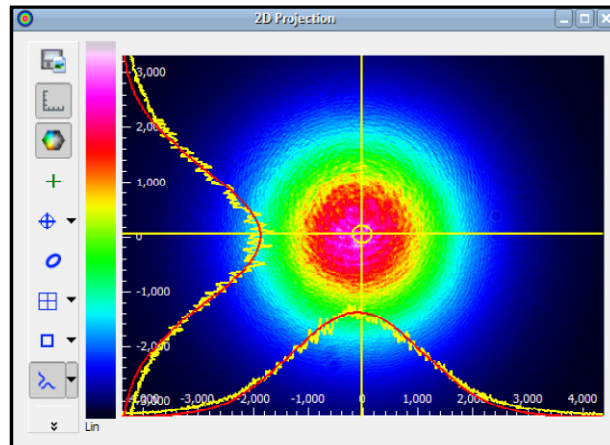


Figure C–2: 2D Projection Window.

It is important to notice that the calculation area must not cut off also lower intensity parts of the beam profile. This may cause improper calculation results. The following Figure C–3, shows an example of chosen ROI and Calculation Area.

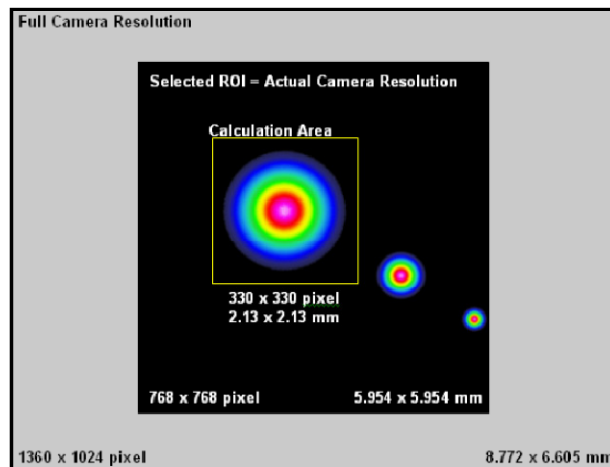


Figure C–3: Region of Interest (ROI).

In Figure C-3's example, a beam is entering the Beam Profiler once directly and in addition multiple reflections of it. The ROI is selected to 768 x 768 pixels so that all 3 beams are visible within the 2D Projection window. But, in order to limit the image interrogation to the main beam the calculation area was chosen much smaller.

Within this 2D Projection panel, coordinates X and Y are defined as follows:

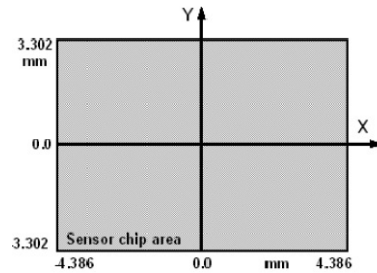


Figure C-4: Coordinates X and Y.

C.2 3D Profile

The 3D Profile illustrates the power density distribution of the measured optical beam. Whereas the beam's cross-section is parallel with the x-y-plane the relative power intensity is shown in the z direction (Pseudo 3D).

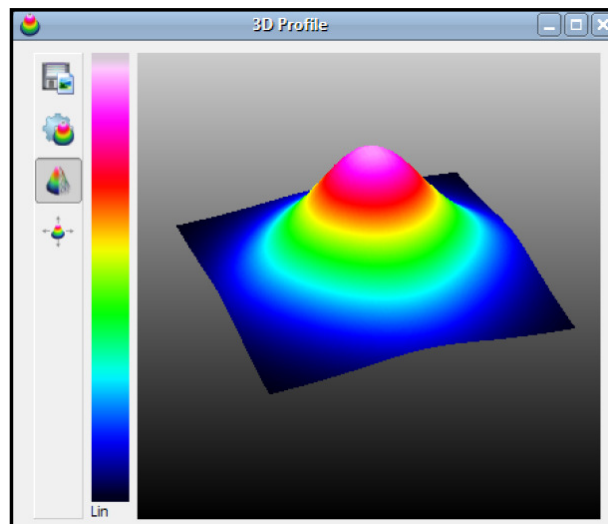


Figure C-5: 3D Profile.

C.3 X,Y Profiles

Even though in Figure C–6 only the X profile is shown, it is also possible to display the Y profile, as reported in Figure C–7. The X profile displays a single pixel row taken from the received camera image, whereas the Y profile shows a single pixel column. The column and row is defined by the position of cross hair within the 2D Projection graph. The yellow graph shows the measured profile, while the red curve shows the approximated Gaussian fit function. The horizontal scale is displayed in μm and its range refers to the selected Region of Interest (ROI).

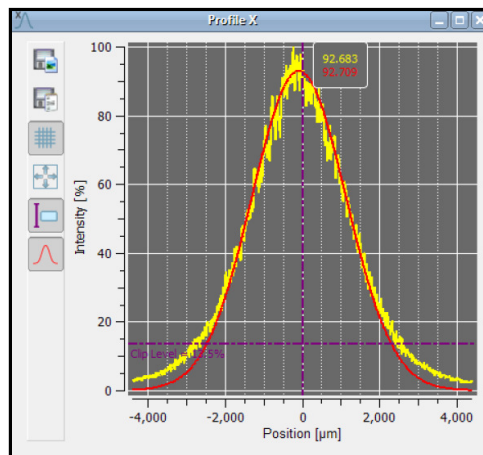


Figure C–6: X profile.

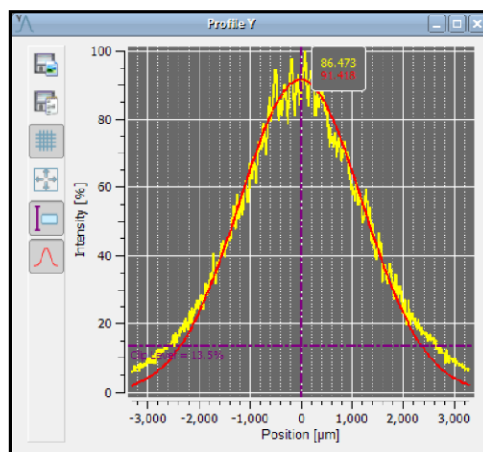


Figure C–7: Y profile.

C.4 Plot Power

Thorlabs Beam software offers some additional plot windows to show the beam behavior, they are: Plot Positions, Plot Power, Beam Stability, Plot Gaussian Fit, and Plot Orientation. Figure C–8 reports an example of the plot power graph where the total power measured by the beam profiler vs. time is displayed.

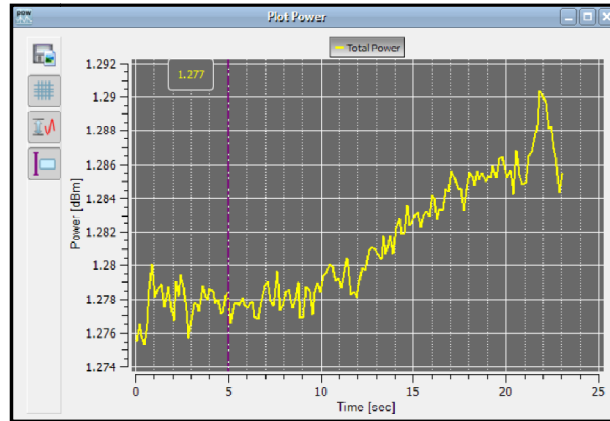


Figure C–8: Plot Positions.

Parameter	Unit	Value	Pass/Fail Test	Min.	Max.	Min.	Max.
Raw Data Measurement							
Beam Width (4-Sigma)	[μm]	X=5821.69, Y=5463.23, R=7983.66	<input type="checkbox"/>	X >= 0	X <= 0	Y >= 0	Y <= 0
Beam Diameter (1-Sigma)	[μm]	6057.77	<input type="checkbox"/>	0	0		
Effective Beam Diameter	[μm]	5602.62	<input type="checkbox"/>	0	0		
Peak Position	[μm]	X=-77.40, Y=-32.25, R=83.85	<input type="checkbox"/>	X >= 0	X <= 0	Y >= 0	Y <= 0
Centroid Position	[μm]	X=-43.10, Y=77.47, R=48.59	<input type="checkbox"/>	X >= 0	X <= 0	Y >= 0	Y <= 0
AD Saturation	[%]	92.44	<input type="checkbox"/>	0	0		
Total Power	[dBm]	3.36	<input type="checkbox"/>	0	0		
Effective Area	[μm^2]	10619889.05	<input type="checkbox"/>	0	0		
Peak Density	[dBm/ μm^2]	0.00	<input type="checkbox"/>	1	1		
Ellipse (fitted)							
Diameter (13.5%)	[μm]	min= 5462.59, max= 5532.86, mean= 5497.73	<input type="checkbox"/>	Min >= 0	Min <= 0	Max >= 0	Max <= 0
Ellipticity	[%]	98.73	<input type="checkbox"/>	0	0		
Eccentricity	[%]	15.89	<input type="checkbox"/>	0	0		
Orientation	[deg]	32.10	<input type="checkbox"/>	0	0		
X-Y-Profile Measurement							
Beam Width Clip (13.5%)	[μm]	X=5503.30, Y=5542.23	<input type="checkbox"/>	X >= 0	X <= 0	Y >= 0	Y <= 0
Gaussian Fit Measurement							
Gaussian Intensity	[%]	X=96.24, Y=96.24	<input type="checkbox"/>	X >= 0	X <= 0	Y >= 0	Y <= 0
Gaussian Diameter	[μm]	X=5152.20, Y=5121.97	<input type="checkbox"/>	X >= 0	X <= 0	Y >= 0	Y <= 0

Figure C–9: Calculation Results.

C.5 Calculation Results

In this small window the result of the calculations are displayed. Effective Beam Diameter and Total Power were the most important parameters used to characterize the beam profile in the present study.

C.6 Filter Wheel

The Thorlabs BC106 Camera Beam Profiler is equipped with a filter wheel containing four absorptive neutral density (ND) optical attenuation filters made from glass, that is why they are applicable only for the visible and near infrared wavelength range 350–1100 nm. These filters are designated for a quick and easy adaptation of the light source power (which may exceed the saturation power of the camera) to a power level within the dynamic range of the CCD camera.

In the present study an attenuation of the light source was necessary because with the nominal source power level the camera beam Profiler software displayed an error that said "Power too high, camera saturated!" Therefore, the light intensity exceeded the maximum detectable power of the CCD camera beam profiler. In this respect, in order to prevent damage to the camera, and also have reliable measurement results, a configuration of three attenuation filters was required (total of 90 dB). It is important to mention that 90 dB was the lowest possible attenuation. It is recommended to work with the lowest possible attenuation in order to minimize beam distortions by the ND filters.

The beam profiler software allows the user to indicate the chosen ND filter loss configuration in dB as a precondition for proper power measurement results.

Curriculum Vitae

Angel Virgilio Lanza Soto

EDUCATION

- | | |
|-----------|--|
| 2011–2015 | Doctor of Philosophy in Engineering Sciences
The University of Western Ontario, Canada
Grade Point Average of 95.3% |
| 2001–2007 | Master of Science in Mechanical Engineering
Simón Bolívar University, Venezuela
Grade Point Average of 96.6% |
| 1995–2001 | Bachelor of Science in Mechanical Engineering (Hon)
Carabobo University, Venezuela
Grade Point Average of 80.02% (first highest score) |

SCHOLARSHIPS AND AWARDS

- | | |
|------------------|---|
| 2013 | Ontario Graduate Scholarships (OGS/QEIIGSST)
The University of Western Ontario, Canada |
| 2011–2014 | Western Research Graduate Scholarship
The University of Western Ontario, Canada |
| 2011–2014 | CREC Lab Scholarship
The University of Western Ontario, Canada |
| 2011 | Graduate Student Teaching Award
The University of Western Ontario, Canada |
| 2006 | Best Oil&Gas Well Drilling Poster Award
III Scientific and Quality Journal, Cuba |
| 2001 | Postgraduate studies Scholarship
Carabobo University, Venezuela |
| 2001 | Undergraduate Best Grade Award
Carabobo University, Venezuela |
| 1995, 1996, 1998 | Best Student of the Term Award
Carabobo University, Venezuela |

RELATED WORK EXPERIENCE

- 2011–2014 Graduate Teaching Assistant (seven times consecutively)
Chemical and Biochemical Engineering Department
The University of Western Ontario, Canada
- 2010 Research Teaching Assistant
Chemical and Biochemical Engineering Department
The University of Western Ontario, Canada
- 2004–2010 Drilling Engineer
Department of Construction and Maintenance of Oil Wells
Petroleum of Venezuela Research Institute, Venezuela
- 2001–2004 University Professor
Energy Department
Carabobo University, Venezuela
- 1997–2001 Teaching Assistant
Physics and Energy Department
Carabobo University, Venezuela

SELECTED CONTRIBUTIONS TO RESEARCH

- 2014 (Presentation) Gas–Solid Fluid Dynamics in a Down Flow Reactor Validation of a CPFDF Numerical Simulation, Canadian Chemical Engineering Journal.
- 2014 (Paper) **A. Lanza**, H. de Lasa, Cluster Fluid Dynamics in Gas–Solid Downflow Reactors: Experiments and CPFDF Simulations. This article is still under revision.
- 2014 (Paper) **A. Lanza**, M. Islam, H. de Lasa, Gas–solid Fluid Dynamics in a Down Flow Reactor Validation of a CPFDF Numerical Simulation. This article is still under revision..
- 2013 (Poster) Particle Cluster Properties and Size Distribution and in Gas–Solid Downer Units, Sarnia Research Bridges, Canada.
- 2013 (Presentation) Particle Cluster Properties and Size Distribution in Gas–Solid Downer Units, Fluidization XIV, The Netherlands.
- 2013 (Poster) Cluster Size Distribution in Gas–Solid Downer Units, Fluidization XIV, The Netherlands.

- 2013 (Paper) **A. Lanza**, M. Islam, H. de Lasa, Particle Cluster Size Distribution in Gas–Solid Downer Units, ECI, Fluidization XIV From Fundamentals to Products.
- 2012 (Paper) **A. Lanza**, M. Islam, H. de Lasa, Particle Clusters and Drag Coefficients in Gas–Solid Downer Units, Chemical Engineering Journal.
- 2007 (Paper) J. Blanco, D. Ocando, **A. Lanza**, R. Rendon, F. Rodriguez, A. Caligiore, J. Acosta, N. Carrero, Viscoelastic System as an Alternative to UBD for Drilling a Severely Fractured Limestone Reservoir, SPE 109203.
- 2007 (M.Sc. Thesis) Modeling and Simulation of Gasified Drilling with Concentric Casing Injection, Simón Bolívar University, Venezuela.
- 2006 (Poster) Underbalance Drilling in Oilfields: Design and Evaluation of Hydraulic. III Scientific and Quality Journal, Cuba.